

**OVALLING OSCILLATIONS OF SHELLS IN CROSS FLOW:  
AN ANALYTICAL AND EXPERIMENTAL INVESTIGATION**

by

**SIOW-YIANG ANG**

**A Thesis Submitted to the Faculty Of Graduate  
Studies and Research in Partial Fulfillment  
of the Requirements for the Degree of  
Master of Engineering**

**Department of Mechanical Engineering  
McGill University  
Montreal, Quebec, Canada**

**August 1983** ©

### ABSTRACT

This thesis investigates and aims to uncover the cause of ovaling oscillations of cylindrical shells in cross flow.

Experiments were conducted with thin-walled cylindrical shells clamped at both ends and subjected to cross flow. The natural frequencies and modal damping of the system were measured. A systematic investigation of the wake characteristics of a rigid cylinder, in the presence of a splitter plate, confirmed that the splitter plate is effective in suppressing periodic vortex shedding, but not in suppressing ovaling oscillations. Experiments on a cylindrical shell with a glued-on insert and another shell with a "wake eliminator" in place have clearly demonstrated the importance of wake flow on the stability of the system.

A refined quasi-static aeroelastic theory was developed, to predict the threshold for ovaling oscillations of a clamped-clamped shell in cross flow. It was found that the system may develop oscillatory instabilities associated with negative aerodynamic damping. Consistently with experimental observations, the theory also shows the importance of pressure fluctuations in the wake, in predicting the threshold flow velocities for ovaling.

Lastly, utilizing measured pressure distributions of (static) deformed shell shapes and the phase relation between shell vibration and the induced pressure, an entirely new analytical model was developed for predicting the onset of ovaling; it was shown that the system is capable of extracting energy from the flow field, and a reasonably good prediction of the threshold flow velocity for ovaling was obtained.

## SOMMAIRE

Cette thèse analyse et vise à trouver les causes du flottement des coques cylindriques soumises à un écoulement transversal.

Des essais ont été conduits sur des coques cylindriques mimes fixées aux extrémités, et soumises à un écoulement transversal. Les fréquences naturelles et l'amortissement modal du système ont aussi été mesurés. Une étude systématique des caractéristiques du sillage d'un cylindre rigide en présence d'une ailette séparatrice, a confirmé que celle-ci est efficace pour la suppression du décrochement tourbillonnaire périodique, mais non à prévenir le flottement de la coque. Des essais sur une coque cylindrique munie d'un pièce insérée collée ainsi que sur une autre munie d'un "suppresseur de sillage" ont clairement démontré l'importance de l'écoulement dans le sillage sur la stabilité du système.

Un modèle théorique quasi-statique amélioré a été développé pour prédire le seuil du flottement pour des coques fixes aux extrémités, soumises à un écoulement transversal. On a ainsi constaté que des instabilités oscillatoires associées à un amortissement aérodynamique négatif sont possibles. Conformément aux observations expérimentales, le modèle théorique démontre aussi l'importance des fluctuations de pression dans le sillage quand à la prédiction du seuil des vitesses de flottement.

Finalement, en utilisant des distributions de pression expérimentales sur des coques déformées (statiquement), ainsi que la relation de phase entre la vibration de la coque et la pression induite, un modèle analytique entièrement nouveau a été développé pour prédire le seuil du flottement; il fut démontré que le système peut extraire de l'énergie de la zone d'écoulement, et une prédiction raisonnablement bonne du seuil du flottement a été obtenue.

### ACKNOWLEDGEMENTS

The author is grateful to Prof. M.P. Paidoussis for his guidance, and Prof. S.J. Price for his advice, throughout the course of this work. Their assistance in proof-reading the manuscript and suggestions for improvement were extremely helpful.

The author is indebted to Prof. B.G. Newman who has made available the facilities of the Low-Speed Aerodynamic Laboratory.

The help offered by Mr. J. Dubik for various mechanical work and Mr. J.O. Gagnon for many useful discussions, are deeply appreciated.

Sincere thanks are due to Messrs. L. Curling, D. Mavriplis and S. Chan, for their helpful comments, and to Mrs. A. Cerrone-Mancini for typing the manuscript.

Last, but not the least, the author also acknowledges the Natural Sciences and Engineering Research Council of Canada and Le Programme FCAC of Quebec for the financial support which has made this research possible.



## TABLE OF CONTENTS

	<u>PAGE</u>
ABSTRACT . . . . .	ii
SOMMAIRE . . . . .	iii
ACKNOWLEDGEMENTS . . . . .	iv
TABLE OF CONTENTS . . . . .	v
NOMENCLATURE . . . . .	viii
1. <u>INTRODUCTION</u> . . . . .	1
1.1 Preliminary Remarks . . . . .	1
1.2 The Present Thesis . . . . .	4
2. <u>DESCRIPTION OF THE APPARATUS</u> . . . . .	7
2.1 The Wind Tunnel . . . . .	7
2.2 The Epoxy Shell . . . . .	8
2.3 Basic Experimental Set-Up . . . . .	8
2.4 Experimental Procedure . . . . .	9
3. <u>NATURAL FREQUENCY AND MODAL DAMPING MEASUREMENTS</u> . . . . .	11
3.1 A Survey of Experimental Techniques . . . . .	11
3.2 Description of the Experiment . . . . .	13
3.3 Testing Procedure . . . . .	14
3.4 Results and Discussion . . . . .	15
4. <u>FIRST PHASE OF WIND TUNNEL TESTING</u> . . . . .	19

	<u>PAGE</u>
4.1 Preliminary Remarks . . . . .	19
4.2 Oavlling Results for the Insert-Less Clamped-Clamped Shell . . . . .	20
4.3 Shell With an Insert . . . . .	21
4.4 Wake Characteristics Without and With a Splitter Plate . . . . .	24
5. <u>SECOND PHASE OF WIND TUNNEL TESTING</u> . . . . .	27
5.1 Flow Around the Shell with Wake Eliminator . . . . .	27
5.2 Wind Effects on the System . . . . .	30
6. <u>FLUTTER ANALYSIS OF A CLAMPED-CLAMPED SHELL</u> . . . . .	32
6.1 Equations of Motion . . . . .	33
6.2 The Fluid Pressure on the Shell . . . . .	34
6.3 Boundary Condition . . . . .	37
6.4 Determination of the Velocity Potential . . . . .	38
6.5 Pressure Fluctuations . . . . .	42
6.6 Solution of the Equations . . . . .	47
6.7 Theoretical Results . . . . .	54
7. <u>ENERGY INPUT TO THE SHELL</u> . . . . .	61
7.1 Preliminary Remarks . . . . .	61
7.2 The Energy Expression . . . . .	63
7.3 Static Pressure Measurements . . . . .	66
7.3.1 Brief description of the experimental set-up . . . . .	66
7.3.2 Pressure coefficient of various models . . . . .	69
7.4 Computation of Work Done by the Fluid Flow . . . . .	71
7.5 Results . . . . .	75

	<u>PAGE</u>
8. DISCUSSION AND CONCLUSION . . . . .	78
8.1 On Vortex Shedding as the Excitation Mechanism for Ovalling	78
8.2 In Search of a New Cause . . . . .	80
8.3 Conclusion . . . . .	81
REFERENCES . . . . .	85
TABLES . . . . .	88
FIGURES . . . . .	98
APPENDICES . . . . .	199
A. AUXILIARY INSTRUMENTS . . . . .	199
B. THE NATURAL FREQUENCIES AND MODAL DAMPING OF SHELL A . . . . .	200
C. THE BEHAVIOUR OF SHELL A (WITHOUT AND WITH) AN INSERT . . . . .	209
D. BERNOULLI EQUATION FOR A NON-STATIONARY SOLID-FLUID BOUNDARY . .	216
E. PHASE RELATION BETWEEN SHELL DEFORMATION AND THE INDUCED PRESSURE	218
E.1 Experimental Set-Up to Measure Phase . . . . .	218
E.2 Experimental Results . . . . .	219
E.3 Calculation of Phase for $\theta = 0$ to 85 Degrees . . . . .	222
E.4 Results . . . . .	227
F. THEORY FOR OVALLING WITH A NODE FACING THE FREE STREAM . . . . .	246
G. LISTING OF THE COMPUTER PROGRAMS . . . . .	253
H. EFFECT OF BOUNDARY LAYER GUARDS . . . . .	273

NOMENCLATURE

Unless otherwise specified, the notation used is as follows:

$a$	Shell radius
$D$	Shell diameter
$E$	Young's modulus for the shell material
$f_{n,m}$	Ovalling frequency of the shell without an insert in the (n,m)-mode
$f_{n,m}^i$	Ovalling frequency of the shell with an insert in the (n,m)-mode
$f_{vs}$	Vortex shedding frequency
$f(\theta)$	Normalized tangential surface flow velocity, $(V_\theta/U) _{r=a}$
$h$	Wall thickness of the shell
$L$	Length of the shell
$m$	Axial mode number
$n$	Circumferential mode number
$(n,m)$	Mode identification, for a mode with $n$ circumferential waves and $m$ axial half waves
$p$	Pressure
$r$	Ratio $f_{n,m}/f_{vs}$ for the shell without an insert
$r^i$	Ratio $f_{n,m}^i/f_{vs}$ for the shell with an insert
$U$	Mean approach flow velocity
$U_{cr}$	Threshold flow velocity for the onset of ovalling of the shell (without an insert) for the mode occurring first with increasing flow
$U_{cr}^i$	Threshold flow velocity for the onset of ovalling of the shell (with an insert) for the mode occurring first with increasing flow
$U_{thr}$	Threshold flow velocity for the onset of a particular mode of ovalling of the shell (without an insert) - but not necessarily the first to occur with increasing flow

$U_{thr}^1$ 

Threshold flow velocity for the onset of a particular mode of ovaling of the shell (with an insert) - but not necessarily the first to occur with increasing flow.

 $u, v, w$ 

Displacements of the shell middle surface in the axial, circumferential and radial directions, respectively

 $V_\theta, V_r, V_x$ 

Tangential, radial and axial flow velocities

 $W$ 

Energy extracted from fluid flow, per cycle

 $W_d$ 

Energy dissipated by structural damping, per cycle

 $\gamma$ 

$\rho_s a^2 (1 - \nu^2) / E$

 $\delta_{n,m}$ 

Modal logarithmic decrement for dissipation in the shell without an insert, in the (n,m)-mode

 $\delta_{n,m}^1$ 

Modal logarithmic decrement for dissipation in the shell with an insert, in the (n,m)-mode

 $\kappa$ 

$(h/a)^2 / 12$

 $\nu$ 

Poisson's ratio

 $\rho$ 

Density of the fluid

 $\rho_s$ 

Density of the shell material

 $\Phi$ 

Total velocity potential of the fluid

 $\phi_0$ 

Velocity potential of the mean flow

 $\phi^*$ 

Perturbation velocity potential

 $\psi_m$ 

$m^{th}$  axial comparison function of the shell

## CHAPTER 1

### INTRODUCTION

#### 1.1 Preliminary Remarks

After erection of thin metal chimney stacks in Moss Landing, California in the 1950's, ovaling oscillation (a relatively new phenomenon) was seen to develop in a steady wind of moderate velocity. Unlike the more common swaying oscillation of chimney stacks, "breathing" or "ovaling" vibrations are characterized by periodic deformation of the cross-sectional shape of the stack. The deformed shape at any cross-section may be described by its radial component which varies circumferentially proportionately to  $\cos n\theta$ , where  $\theta$  is the usual (azimuthal) angle and  $n$  is the circumferential wave number; i.e.,  $n$  is equal to the number of full sinusoidal waves around the circumference, so that the number of nodal points are twice  $n$  (see Figure 1.1). For example, beam-like swaying motion is characterized by  $n=1$ , whilst for  $n=2$ , the second mode of ovaling, there are four nodal points and two full sine waves around the periphery of the stack. In common usage, "ovaling" refers to all shell modes of oscillation for which  $n \geq 2$ , but strictly speaking it should be restricted to the second circumferential mode.

The Moss Landing incident prompted Dickey and Woodruff [1] and Dockstader *et al.* [2] to investigate the cause of the vibration; they conducted some on-site full scale tests on the stacks. In their studies, the vortex shedding frequency was inferred by assuming a Strouhal number ( $S = f_{vs} D/U$ ) of  $S \approx 0.22$ , rather than being actually measured. They found

that the second-mode ovaling frequency occurred at, or close to, the natural frequency of the stack and that it corresponded to approximately twice the vortex shedding frequency. Since it is well established that swaying oscillation of chimneys is caused by the alternating forces induced by the periodic shedding of vortices in the wake of the stack, Dockstader *et al.* proposed that a similar mechanism was responsible for ovaling oscillation, where now periodic vortices would excite ovaling at double their own frequency, such that the chimney would go through two cycles of oscillation for each pair of vortices shed.

Having questioned [3] the necessity of a 2:1 relationship between the ovaling natural frequency and the vortex shedding frequency, Sharma and Johns [4] conducted an extensive series of wind tunnel experiments on metallic cylindrical shells. They concluded that ovaling oscillations were induced subharmonically by vortex shedding [5], such that there was a more general integral relationship (ratio) between the ovaling frequency and the vortex shedding frequency, and that this integral ratio,  $r$ , ranged from 1 to 6. Again it should be noted that Sharma and Johns also did not measure the vortex shedding frequency, but calculated it by assuming a constant Strouhal number of either  $S = 0.20$  or  $S = 0.166$ . They then extended the Dockstader *et al.* argument, and proposed a mechanism whereby a cylindrical shell would undergo a number of full cycles (for  $r = 2, 4, 6$ , respectively), or a number of half cycles (for  $r$  odd), of oscillation for each vortex shed. Since the vortex shedding frequency was not known precisely, the hypothesis that ovaling was induced subharmonically by vortex shedding could not be said to have incontrovertibly been established.

To test this hypothesis further, Paidoussis and Helleur [6] conducted experiments in which they measured both the vortex shedding and ovaling frequencies. They found that an integral relationship between the two existed only close to the onset of ovaling. With increasing flow, beyond the threshold of ovaling, there was no form of lock-in or synchronization between the vortex shedding frequency,  $f_{vs}$ , and the shell ovaling frequency,  $f_o$ , in contrast to what is usually found in the case of swaying oscillations. Hence it was tentatively concluded that, although vortex shedding may trigger the ovaling oscillation, it is not essential for the maintenance of the oscillation. Nevertheless, further experiments with a long splitter plate mounted behind the cylindrical shell, to suppress periodicity in the wake [7], showed that ovaling still occurred. This suggested periodic vortex shedding neither initiated nor sustained ovaling!

The dispute over the cause of ovaling led to a series of investigations by Aaron [8], Wong [9], and Suen [10]. They confirmed that ovaling was a phenomenon independent of periodic vortex shedding. Other findings by the three authors, similar to those reported in Ref. [6], were: (i) ovaling occurred at essentially one of the shell natural frequencies; (ii) there was no lock-in of the vortex-shedding frequency to the shell frequency, of the type common in the swaying type of oscillation; (iii) at onset, it was not always true that  $f_o/f_{vs} = \text{integer}$ . Hence, these investigators concluded that even the sub-multiple relationship between  $f_{vs}$  and  $f_o$  is not an essential prerequisite for the onset of ovaling.

Experiments conducted by Wong on a clamped-clamped cylindrical shell spanning the height of the working section of the wind tunnel showed that ovaling could occur in two-dimensional flow. Paidoussis and Wong



[9,11] then developed an analytical model for the aeroelastic instability of an infinitely long cylindrical shell in cross flow. It was found that, at sufficiently high flow velocity, certain types of shell motion lead to flutter, of the single-degree-of-freedom, negative-aerodynamic-damping type. The mode shapes<sup>†</sup> leading to instability as predicted by theory agree with experimental observations; however, quantitative agreement between predicted and measured thresholds of instability is poor.

By utilizing three-dimensional shell equations, the theory was extended to deal with cylindrical shells of finite length and clamped ends [10,12]. Even though the new theory gave a better representation of the actual experimental system [10,29], it was found to still greatly overestimate the critical flow velocities for the onset of ovaling.

Everything so far indicated that alternate vortex shedding was not the cause of ovaling. However, one last possibility remained: that of synchronous symmetric vortex shedding, such as that observed for in-line oscillations of cylinders [13]. However, in a special study of this question with shells in cross flow, no symmetric vortex shedding was detected, either before or after the onset of ovaling [14]. The same study also ruled out acoustic coupling as a mechanism for initiating or sustaining ovaling oscillation.

## 1.2 The Present Thesis

It seems that the mechanism underlying ovaling is far more complex than had previously been supposed. Hence, the objective of this thesis is

---

<sup>†</sup>I.e., the orientation of the modes *vis-à-vis* the upstream flow-velocity vector.

to further examine and hopefully uncover the "true" cause of this intriguing phenomenon.

The experimental part of this thesis includes modal damping measurements and wind tunnel tests involving a clamped-clamped cylindrical shell in cross wind. The apparatus is described in Chapter 2. An improved and refined technique, as described in Chapter 3, was developed for measuring shell damping, which is an essential prerequisite for the theory to predict the threshold flow velocity for the onset of ovaling instability.

Chapter 4 describes a specific set-up where shell motion was restricted over part of the shell circumference, the ultimate aim being to immobilize that part of the shell which lies in the wake; this would then correspond better to the theoretical model of Refs. [9-12], where the wake was viewed as a dead region and as having no effect on the stability of the system - thus enabling a better comparison of the analytical and experimental results. To evaluate the effectiveness of the splitter plate, the periodicity in the wake of a rigid circular cylinder with and without a splitter plate was thoroughly investigated. As will be seen in Chapter 4, the experimental evidence indicates that wake flow does play an important role in precipitating ovaling oscillation. For this reason, a special wake eliminator was constructed, and further tests were conducted, as will be described in Chapter 5. In the same Chapter, the problems encountered while attempting to simulate a fully potential flow around the cylindrical shell will be discussed.

Chapter 6 presents an analytical model for the aeroelastic instability of a clamped-clamped shell in cross flow. The theory of references [10,12] was extended to account for a moving fluid-solid

boundary and the pressure fluctuations in the wake due to shell motion.

Chapter 7 is devoted to the calculation of energy input to the system from the air-stream. The calculation is based on quasi-static analysis, utilizing measured time-average pressures of certain permanently deformed (static) shell shapes. For this analysis, the phase difference between the perturbation pressure field and the shell displacement has to be known. The determination of this phase is discussed in Appendix E.

Finally, the major findings of this work are discussed and summarized in Chapter 8.



## CHAPTER 2

### DESCRIPTION OF THE APPARATUS

A number of different experiments were designed to explore the mechanism of ovaling oscillations of a thin cylindrical shell in cross flow. In this Chapter, only the main experimental set-up and instrumentation will be described; other special set-ups which serve specific functions will be described in subsequent Chapters, which makes for more meaningful and interesting reading.

#### 2.1 The Wind Tunnel

The experiments were conducted in a low speed, open return wind tunnel (see Figure 2.1) with a closed working section of 0.91 m (3.0 ft.) wide and 0.61 m (2.0 ft.) high. The wind speed range is about 0-45 m/s and the longitudinal turbulence is certainly less than 0.5% [15]. The boundary layers on the top and bottom walls of the tunnel working section are about 31.8 mm (1.25 in.) thick while those on the side walls are about 50.8 mm (2.00 in.) thick.

The flow velocity was determined by measuring the pressure difference between the atmospheric pressure and a reference pressure, upstream of the working section. With this pressure difference, the actual wind speed at the working section was inferred from a calibration curve [15]. When the model was in place, the wind speed was corrected for blockage effects [16]. For a circular cylinder of 76.2 mm (3.00 in.) in diameter, spanning the height of the tunnel, a 5% correction was calculated.

## 2.2 The Epoxy Shell

The test shells were spin-cast from low viscosity epoxy material. The dimensions and geometry of the shells tested are tabulated in Table 2.1. Measurements around the periphery of the cylindrical shell indicated that there was approximately a 5% variation in wall thickness.

In some tests, the test models used (as shown in Figure 2.2) had an aluminium insert glued onto the inner surface of the shell. The purpose of the insert, which has the form of part of a cylinder, was to restrict the motion over that portion of the flexible shell. The ultimate aim was to have a rigid body in the wake, with only the front part, lying in the unseparated flow region, being flexible. This would then provide a crucial test for the theory, where the flow in the wake was ignored, as will be explained in due course.

## 2.3 Basic Experimental Set-Up

The flexible cylindrical shell (of length approximately 584 mm (23.0 in.), see Table 2.1) was mounted at the center of the working section, spanning the height of the wind tunnel, as shown diagrammatically in Figure 2.3. It was clamped at both ends, resulting in an effective length of 533 mm (21.0 in.); precautions were taken to avoid any axial loading on the shell.

Shell vibration caused by wind excitation was sensed by a fibre-optic "fotonic" sensor. Noting that ovalling in the second mode occurred with a node facing the free stream, while in the third mode there was an antinode facing the flow, for most experiments the fotonic sensor was

positioned at an angle of  $45^\circ$  to the flow-velocity vector and 127 mm (5.00 in.) above the tunnel floor. The light beam emitted from the fonic probe was first projected onto a mirror and then reflected onto the cylindrical shell (see Figure 2.3). The intensity of the ray reflected from the shell surface back onto the sensor determines the instantaneous position of the surface. A shiny metallic tape acting as a reflector was attached to the shell surface.

The periodicity in the wake was sensed by a hot wire anemometer. The hot wire was positioned near the free shear layer and a few diameters downstream of the cylinder (typically in between positions 15 and 16 of Figure 4.6), and at a height of 203 mm (8.00 in.) above the tunnel floor.

Both the hot wire and fonic sensor signals were processed by a Hewlett-Packard 5420A FFT signal analyzer. The dominant frequencies could be identified and measured from power-spectral-density analysis of the signals.

The type and make of instruments used are listed in Appendix A.

## 2.4 Experimental Procedure

To study the wind effects on the cylindrical shell, the procedure was to start the wind tunnel at a low flow velocity, approximately 2 m/s, and gradually increase the wind speed in steps of roughly 2 m/s, up to around the critical velocity for the onset of ovalling. From then on, the flow velocity was increased in smaller steps of about 1 m/s. The behaviour of the shell was observed from the top and through a side window in the working section, and thus the ovalling mode shape could be identified with

( the aid of a stroboscope. For each flow condition, the wind speed, shell response, and vortex shedding frequency were recorded. The flow velocity was then incremented and the same procedure repeated.

## CHAPTER 3

### NATURAL FREQUENCY AND MODAL DAMPING MEASUREMENTS

The main objective of the experiments presented here was to accurately measure the modal damping of the shell. This information is necessary for the theory<sup>†</sup>, to be able to predict the threshold flow velocity for the onset of instability of the cylindrical shell (see Chapter 6). Knowing the natural frequencies of the shell will also aid in analyzing the measured frequency spectra of shell motion.

#### 3.1 A Survey of Experimental Techniques

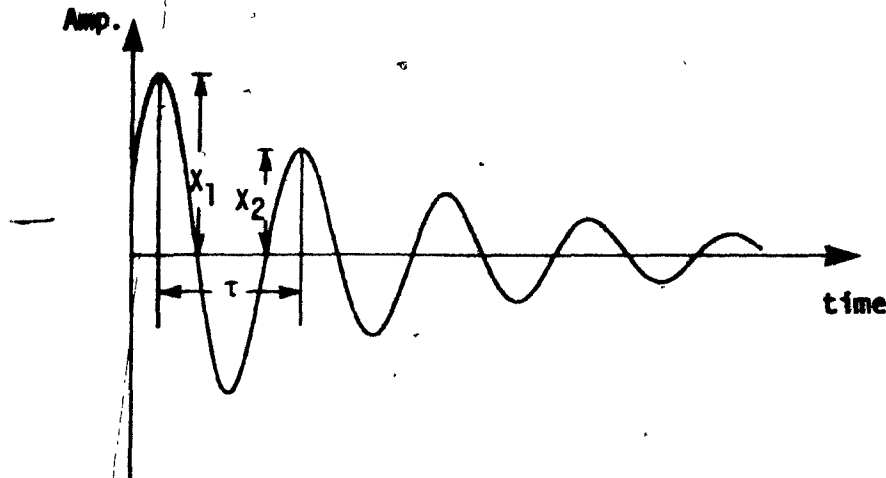
There are numerous methods for determining the natural frequencies and modal damping of a system [17-22].

The simplest experimental technique, which requires little instrumentation and is easy to perform, is the so-called *decay of free vibration method*. Ideally, the rate of decay of vibration of a structure excited by a force impulse is recorded first; then the time between peak amplitudes gives the period  $\tau$ , and the amplitude ratio gives the logarithmic decrement  $\delta$  (damping). However, this approach will only yield reasonable results for simple structures, as in the case of axial, torsional or bending motions of a bar. Moreover, only the fundamental mode of the system may be determined, and difficulties associated with beating arise if two frequencies are close together. )

---

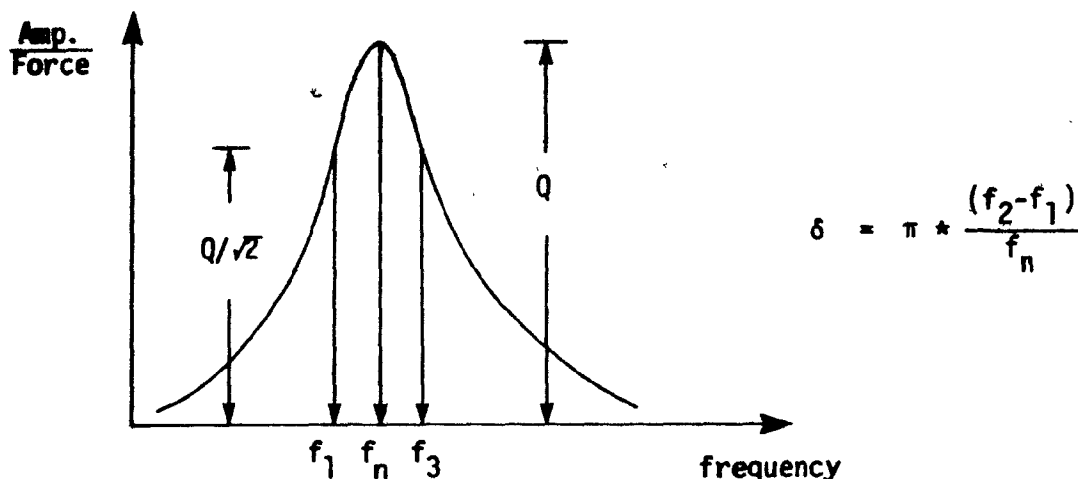
<sup>†</sup>The theory suggests that for certain modes of oscillation, the motion is aerodynamically negatively damped; instability then occurs when this negative damping is equal to the internal dissipative (positive) damping of the shell; hence the need to know the latter.





$$\delta = \ln \frac{x_1}{x_2}$$

*Resonance testing* is a more elegant method, where the structure to be studied is excited harmonically by a force, and the displacement (response) is monitored as a function of frequency. Hence, in principle, any mode of the system may be determined. The most common form of resonance testing is the *peak amplitude method*, where the natural frequency and damping are deduced from a "response curve" of total displacement amplitude (or, better yet, the ratio of response to excitation) plotted against the driving frequency. As the name suggests, the resonance is defined, very simply, to occur when the response reaches a maximum. The logarithmic decrement is given by  $\pi(f_2 - f_1)/f_n$  where  $f_1, f_2$  are the frequencies associated with the half-power ( $1/\sqrt{2}$  of the amplitude) points and  $f_n$  is the natural frequency. The advantage of this technique is that no phase information (between response and excitation) is needed. However, this phase information can, in fact, lead to enhanced accuracy. A second shortcoming of this method is that it is limited to lightly damped systems having no closely-spaced natural frequencies. Two closely-spaced natural frequencies may contribute to the amplitude at an intermediate frequency, resulting in the erroneous determination of frequency and damping of only one (pseudo) mode.



Being aware of the possible defects generated by the techniques mentioned above, it was then decided to perform the tests for the present study by the method of *Kennedy and Pancu* [20,21]. This approach is capable of providing reliable results, even when the damping is high and the frequencies are close to one another; as such, it has proven particularly suitable for shell-type structures. This is a sophisticated method which requires the driving frequency to be precisely controllable, also the frequency and phase of the excitation force, as well as the response, must be measured accurately. The method itself will be described in terms of sample results in Section 3.4.

### 3.2 Description of the Experiment

The experimental set-up is shown schematically in Figure 3.1. The shell was excited acoustically by a small loud-speaker, placed near its upper end; the excitation frequency could be precisely controlled through an oscillator. Measurement of the input force (pressure) was made *via* a microphone, and the shell vibration was monitored by the fonic sensor. Both measurements were made on the same level above the tunnel floor.

### 3.3 Testing Procedure

The natural frequencies and modal damping for the second and third modes of ovalling were measured in still air. Before the actual testing was conducted, it was necessary to ensure that the "excitation force" was stable<sup>†</sup> and sinusoidal in nature. This is essential, as the quality of the measurement depends largely on the stability of the driving frequency, and a very small variation in frequency may give rise to very large fluctuations in the response levels when measuring near a resonance. Figure 3.2 shows the power spectral density of the excitation signal registered by the microphone. It is seen that only one prominent peak was recorded, suggesting that only the fundamental forcing frequency was exciting the shell<sup>§</sup>. The frequency spectrum of the shell vibration, as shown on Figure 3.3, also contains one dominant frequency peak.

The general experimental procedure was to first monitor (on the oscilloscope) the shell response due to the acoustic excitation, while sweeping the excitation frequency through a specified frequency range; in this way a rough value of the natural frequency could be obtained. Then, the actual measurement was obtained by initially setting the forcing frequency around 10 Hz below this value and slowly increasing the frequency, up to about 10 Hz above it, concentrating more measurements in the neighbourhood of the resonance frequency. Both the excitation and response signals

---

<sup>†</sup>During the early stages of the experiment, it was discovered that both the oscillator and fonic sensor units had "drifting" problems; *i.e.*, the oscillator frequency might shift by 0.5 Hz per half hour, and a zero shift of about 50 mV (typically 2% on the set value) on the fonic sensor unit could also occur. This was overcome by allowing the instruments to warm up for a sufficiently long time (about 2 hours).

<sup>§</sup>The small circles on the peak and on the abscissa are, respectively, at the fundamental frequency and at (absent) harmonics.

were processed in the transfer function mode of the FFT dynamic signal analyzer. As it takes some time for the system to achieve a steady-state value whenever the frequency was varied, readings were taken when two consecutive sample sets (25 averages each) of the signals produced sensibly the same results.

### 3.4 Results and Discussion

The data reduction technique for the Kennedy-Pancu method is to plot the complex impedance of the system at different frequencies on an Argand diagram. Ideally, the data points for a one-degree-of-freedom system form an exact circle (see Figure 3.4). The resonant frequency lies at the absolute maximum of the circle on, or parallel to, the imaginary axis. The logarithmic decrement is then given by [22]

$$\delta = 2\pi(f_2 - f_1) / [f_0(\tan \phi_1 + \tan \phi_2)],$$

where  $f_2$ ,  $f_1$ ,  $\phi_2$  and  $\phi_1$  are defined in Figure 3.4 and  $f_0$  is the natural frequency. For a multi-degree-of-freedom system, such as the shells used in the experiments, if sufficient points are available to draw a circle in the complex impedance plane, then the modal logarithmic decrement,  $\delta_{n,m}$ , is given by

$$\delta_{n,m} = 2\pi(f_2 - f_1) / [f_{n,m}(\tan \phi_1 + \tan \phi_2)],$$

where  $f_{n,m}$  is the natural frequency associated with the  $n$ th circumferential and  $m$ th axial number. Ideally,  $\phi_1$ ,  $\phi_2$ ,  $f_1$  and  $f_2$  are the angles and

frequencies associated with half-power points, but could simply correspond to any two points on either side of the maximum.

As the shell response to the acoustic excitation is very low<sup>†</sup>, only a very sensitive instrument, such as a photonic sensor, is capable of picking up the vibration.

The circumferential mode number, corresponding to any given natural frequency, is identified with the aid of a stroboscope, with the shell excited into ovaling by the wind. Moreover, since the present experimental set-up resembles that of Suen's [10], the corresponding axial mode number of the clamped-clamped shell is based on his findings.

Results will now be presented for shells with and without a glued-on insert (see Section 2.2).

In the course of the experiment, some technical difficulties were encountered with shell A when an insert was utilized; it was observed that the glue (LiquiSilk), which was used to hold the insert into position, reacted with the shell surface. As a result, pockets of air bubbles were formed between the insert and the shell. This glue was chosen as it was readily dissolved by acetone, and the original idea was to salvage the shell after the experiment, by dissolving the glue. Because of the difficulties with the air bubbles, the experimental results for shell A were viewed with some suspicion; they will be presented in Appendix B.

The same experiment was repeated with shell B. This time epoxy glue, which has the same chemical properties as that of the shell, was used. Epoxy glue also provides a better bonding between the metal insert and the shell.

---

<sup>†</sup>The amplitude of vibration is of the order of 1 mm.

Figures 3.5 and 3.6 show the mechanical properties of shell B (without an insert). It is seen that the experimental points fall almost exactly onto the locus of a perfect circle; the effect of the other modes, has slightly displaced the origin of the modal circle away from the imaginary axis (comparing with the plot for a single mode, Figure 3.4). The natural frequencies and modal damping of the second and third modes of ovalling are respectively:  $f_{2,1} = 166.1$  Hz,  $\delta_{2,1} = 0.051$ ;  $f_{3,1} = 216.0$  Hz,  $\delta_{3,1} = 0.052$ . The repeatability of the measurements is excellent (compare Figures 3.5-3.6 and 3.7-3.8); the discrepancy for the resonant frequencies and modal damping between two different measurements, done on different days, are approximately 0.2 and 4 percent, respectively.

The effect on the Nyquist plot of having an aluminium insert glued onto the inside surface of the shell (preventing motion of about 20% of the shell surface) is shown in Figures 3.9 and 3.10. It is seen that for the  $n=2$  mode, the natural frequency increases to 209.0 Hz (an increase of approximately 26%) and modal damping increases to  $\delta_{2,1}^i = 0.053$  (an increase of 4 to 8%); while for the  $n=3$  mode,  $f_{3,1}^i = 227.7$  Hz (an increase of 5%) and  $\delta_{3,1}^i = 0.144$  (an increase of 175%). The distortion of the Nyquist plot (see Figure 3.10) to a non-circular locus may be caused by the presence of another (yet to be identified) mode. The repeatability of the  $n=2$  mode is good (compare Figures 3.11 with 3.9) whilst it is poor for the  $n=3$  mode (compare Figures 3.12 with 3.10). The poor repeatability of the  $n=3$  mode may be, because of the higher damping, the loud speaker used is incapable of providing consistent excitation for this particular mode.

Another shell, shell C, was used for the second phase of wind tunnel testing. The natural frequencies and modal damping in this case are

determined from Figures 3.13 and 3.14. For the  $n=2$  mode,  $f_{2,1} = 163.8$  Hz,  $\delta_{2,1} = 0.032$ , and for the  $n=3$  mode,  $f_{3,1} = 226.1$  Hz,  $\delta_{3,1} = 0.036$ , were obtained.

The mechanical properties of the three shells are summarized in Table 3.1. It may be seen that the present experimental set-up and procedure, using acoustic excitation, appear to be ideal for any shell-type structure with logarithmic decrement less than or equal to 0.05. For higher damping, the method is probably still good, but a more powerful loud speaker would certainly have to be used. Another advantage of the set-up is that it provides a source of "multiple-point" excitation, as compared with a single-point excitation of a mechanical exciter, where the chances of missing a vibration mode are greatly reduced.

## CHAPTER 4

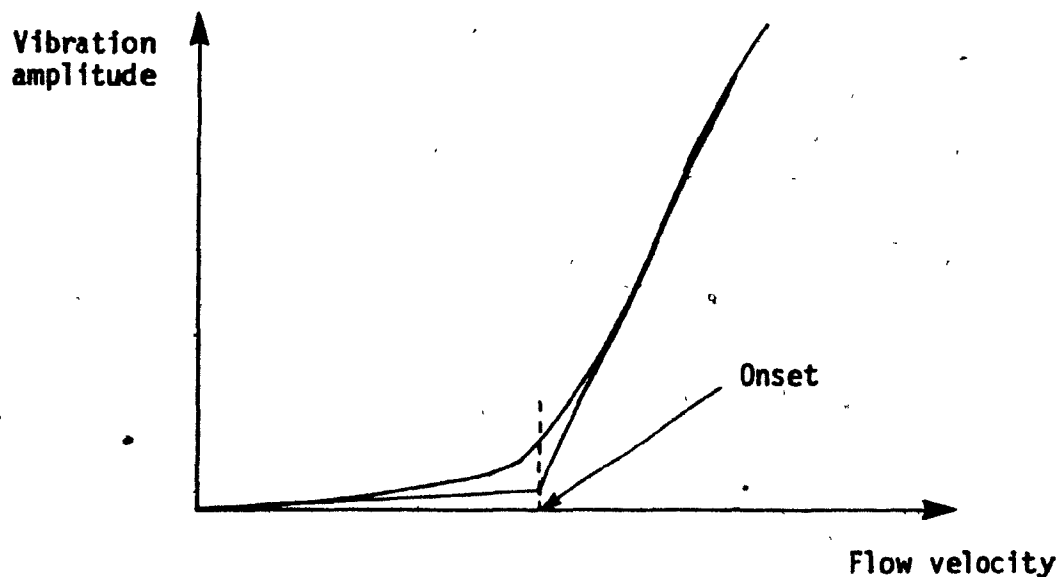
### FIRST PHASE OF WIND TUNNEL TESTING

#### 4.1 Preliminary Remarks

In this Chapter, experiments to examine the behaviour of a cylindrical shell with and without an insert are described. Before presenting the results, one of the difficulties of these experiments will be discussed, namely that of pinpointing the velocity for the threshold of ovaling. This difficulty arises because the shell response, as registered by the fonic probe, does not increase abruptly from zero at the onset of instability, as is indicated by linearized theory but, in fact, a more gradual increase in amplitude is obtained. Therefore, a "tangent method" was used to define the threshold flow velocity for the onset of ovaling. This method proceeds as follows: (a) a tangent is drawn from the curve of vibration amplitude *versus* flow velocity, at the point where the amplitude change becomes distinct; (b) to compensate for the increase in amplitude with flow due to buffeting induced by the turbulence, a second tangent is drawn at a small angle to the x-axis (flow-velocity axis); (c) the intersection of these two tangents then defines the threshold of instability; see the following sketch.

The fonic sensor used to monitor shell response was calibrated and set to operate within a predetermined range, in which it behaved in an almost linear manner; the calibration factor could then be determined from the calibration curve (Figure 4.1). Care was taken to ensure that the shell amplitudes were never large enough to cause the fonic sensor to depart from its linear range.





#### 4.2 Ovalling Results for the Insert-Less Clamped-Clamped Shell

Since the main objective of this work is to investigate the mechanism of ovalling oscillation, and since it is reasonable to presume that the same mechanism would be responsible for all modes of ovalling, the only types of ovalling to be studied here are restricted to the second and third circumferential modes.

Typically, the dynamical behaviour of a test shell with increasing wind speed is as follows. The first observed instability is in the second circumferential mode ( $n=2$ ), followed by the third circumferential mode ( $n=3$ ) - always in the first axial mode ( $m=1$ ). For the  $n=2$  mode, the shell deformation is such that the positions of maximum vibration (antinodes) are located at 45 degrees to the flow; for the  $n=3$  mode, the shell vibrates with one of its three antinodes facing upstream. An interesting feature of third mode ovalling is that it is accompanied by a loud acoustic noise and that (by visual inspection) it has a larger amplitude of vibration than the second mode.

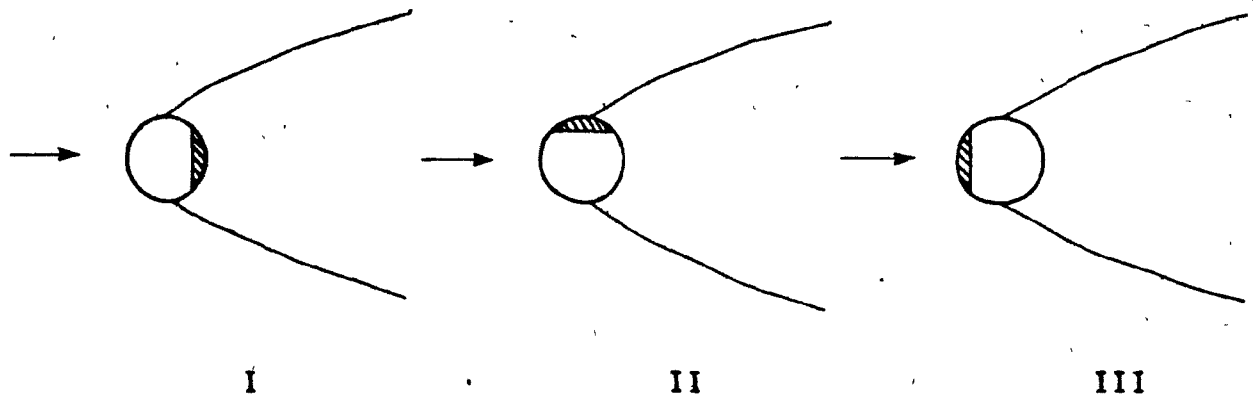
A typical experimental result, for shell B, is shown in Figure 4.2. The Strouhal number is  $\sim 0.18$  for flow velocities of less than 20 m/s, beyond which it decreases to  $\sim 0.16$ . The  $n=2$  mode ( $f_{2,1} \sim 167$  Hz) instability begins at  $U_{cr} \approx 21.2$  m/s, and at this flow velocity the ratio,  $r$ , of ovaling frequency to vortex shedding frequency  $r = 3.4-3.5$ ; the uncertainty in  $r$  arises from the corresponding difficulty in pinpointing  $U_{cr}$ . The  $n=3$  mode ( $f_{3,1} \sim 223$  Hz) was precipitated at a slightly higher wind speed of  $U_{thr} \approx 22.9$  m/s. It is noted that, beyond this flow, third and second-modes ovaling take place concurrently; it would be reasonable to suppose that, in that flow range, the third mode vibration is coupled with that of the second mode in some way.

The same experiment was repeated on another date and the result is presented in Figure 4.3. Similar results for a nominally identical shell (shell A of Table 2.1) will be given in Appendix C. Finally, the results for shells A and B are summarized in Table 4.1. The repeatability of the results for the same shell is good, as may be seen from a comparison of Figures 4.2 and 4.3, for instance. Small differences between the two nominally identical shells may arise from manufacturing discrepancies and differences in clamping.

These results confirm the conclusion arrived at previously [8-10] that, at the onset of ovaling, the ratio  $f_{n,m}/f_{vs}$  need not be an integer.

#### 4.3 Shell with an Insert

In these experiments the test model was oriented in three different ways with respect to the on-coming flow, as shown in the diagram below;



to facilitate discussion of the results for the three different configurations, they will be referred to as configurations I, II and III, respectively.

According to the theory proposed by Paidoussis *et al.* [11,12], the wake region is considered to be effectively stagnant, so that an insert in arrangement I should have little effect on ovalling, whilst in arrangements II and III it might. The purpose of these experiments, it is recalled, was to test this hypothesis.

The following observations were made with increasing wind speed. In orientation I the system was seen to be stable at all flow velocities, up to  $U = 50$  m/s! For the model orientated at configurations II and III, on the other hand, ovalling was eventually precipitated, although at a higher flow velocity than without the insert, and the familiar acoustic noise was heard when the amplitude of vibration became large. The ovalling mode shape looked like a truncated  $n=2$  mode, with a node at  $270^\circ$  for orientation II, and at  $180^\circ$  for orientation III.

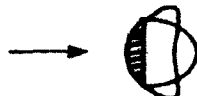


Here it should be noted that it was not too surprising that no instability was observed for the  $n=3$  mode, in none of the configurations tested, because the increase in modal damping in this mode after affixing the insert is high ( $\delta_{3,1}^i > 0.100$ ) and presumably inhibits the onset of ovalling, whilst this is not the case for the  $n=2$  mode ( $\delta_{2,1}^i \approx 0.052$ ).

It is seen (Figure 4.4) that the onset of instability for shell B with an insert, has a lower critical flow velocity,  $U_{cr}^i \approx 27.0$  m/s ( $f_{2,1}^i \sim 212$  Hz;  $r^i = 3.3-3.4$ ) at orientation II than orientation III with  $U_{cr}^i \approx 28.7$  m/s<sup>†</sup> ( $f_{2,1}^i \sim 214$  Hz;  $r^i = 3.2-3.3$ ). For both configurations II and III,  $U_{cr}^i$  is higher than that of a shell with no insert; this may be partly due to the higher mechanical damping and partly due to the higher ovalling frequencies when an insert is utilized. In any case, the effect of aerodynamic forces on a body which is partly rigid is quite different from that of a cylindrical shell. The same effect may also explain the difference in the onset of instability for a shell with an insert at configurations II and III. The results of the same experiment, repeated after the system had been dismantled and remounted on another date, are shown in Figure 4.5; once again repeatability is good.

Similar experiments were conducted also with shell A and are discussed in Appendix C. A summary of the results is given in Table 4.2. The repeatability of the results for different tests on the same shell is reasonably good.

<sup>†</sup> There is some doubt as to whether the onset of ovalling in that mode actually occurs at this flow speed ( $U_{cr}^i \approx 28.7$  m/s), as this could correspond to the onset of instability of another mode (the symmetric, as opposed to the anti-symmetric second mode) as shown below; (a change of ovalling mode shape was observed in a clamped-free shell with no insert [10,29]); alternatively, it



could simply be that the onset of instability is at a higher flow speed  $U_{cr}^i \approx 35$  m/s ( $r^i \sim 2.6-2.7$ ).

Finally, the experimental results for the second mode of ovaling (with and without an insert) are compared in Table 4.3. It may be seen that for a shell with an insert, the orientation of the model does play an important role in precipitating ovaling oscillation. An interesting feature of these results is that, at the onset of instability, the ratio  $r$  and  $r^1$  ( $f_{2,1}/f_{vs}$  and  $f_{2,1}^1/f_{vs}^1$ ) falls in the range of 3.1 to 3.5.

Here it is recalled that the original expectation was that a small insert at the back of the shell (such as the one used in these experiments) would have a small effect on ovaling and that only for larger inserts the effect would be pronounced. The results found here, however, have been contrary to these expectations and they have already permitted the tentative conclusion that wake flow does considerably aid in precipitating ovaling (or, for that matter, that it is entirely responsible for it). Partly for this reason and partly because it was believed that the addition of a larger insert would further increase the modal damping and natural frequencies of the system (such that it would be stable within the flow speed of the wind tunnel), these experiments were terminated at this stage.

#### 4.4 Wake Characteristics Without and With a Splitter Plate

Since all previous experiments with a long splitter plate [6,8-10,14]<sup>†</sup> were carried out with a narrow gap between the shell and the plate placed downstream of the shell, it could be argued that this gap may provide a communication path between the two sides in the wake of the cylinder; thus, it could be argued, some organization of the wake may take place in this way,

---

<sup>†</sup>Ovaling oscillation does occur, albeit at somewhat higher threshold flow velocities, even when periodic vortex shedding has been suppressed by a long splitter plate.

resulting in organized periodicity after all. Moreover, a more recent study [23] suggested that, although a splitter plate of length at least  $5D^{\dagger}$  ( $L/D \geq 5$ ), would inhibit the formation of regular periodic vortex shedding, nevertheless some traces of a time-varying vortex shedding frequency appear to be present still. The frequency of a periodic component,  $f'_{vs}$ , if it exists in such circumstances need not be the same as the  $f_{vs}$  without a splitter plate. Hence, if periodicity does exist, one could still have  $f_{n,m}/f'_{vs} = \text{integer}$ , overturning the conclusion reached in Section 4.2.

For this reason, a hot wire probe was systematically traversed in the base region of a rigid cylinder, to investigate the existence of periodicity of the wake, without and with a splitter plate. Figure 4.6 shows the locations of the hot wire probe.

Typical frequency spectra of the wake at a flow speed  $U = 18.0 \text{ m/s}$  ( $Re = 9.10 \times 10^4$ ) both with and without a splitter plate for some representative locations of the hot wire probe are shown in Figures 4.7-4.11.

It may be seen that in the absence of the splitter plate, the vortex shedding frequency is recognized as the dominant peak in the wake signal; for this flow velocity,  $f_{vs} = 43.8 \text{ Hz}$ , giving rise to  $S = 0.185$ . Moreover, not too surprisingly when the probe was located close to the centerline of the system (at positions 3, 17 and 23), and in the absence of a splitter plate, vortices on the other side of the wake are also sensed to some extent, giving rise to the peak at  $2f_{vs} = 87.5 \text{ Hz}$ .

However, with the splitter plate in position, hard as one tried, no periodic signal was detected in the domain of investigation. It is seen

---

<sup>†</sup>  $L$  is the length of the splitter plate and  $D$  is the diameter of the cylinder. In the experiments [6,8-10,14], the ratio of  $L/D$  is approximately 4.7.

that, in most cases (Figures 4.7-4.11), the dominant peak recorded is the 60 Hz electrical noise generated by the instrumentation. Perhaps it is worth mentioning that the diagrams in the Figures 4.7-4.11 are not plotted on the same scale, but rather on a normalized scale dictated by the largest peak, whatever its nature. In order to fully appreciate the power spectral density of the wake, the diagrams of Figure 4.11 (randomly chosen) are replotted on the same scale in Figure 4.12, showing conclusively that there is no discernible vortex shedding frequency when a splitter plate is positioned in the wake.

Hence, the conclusions arrived at previously [6,8-10,14] that a splitter plate suppresses periodic vortex shedding but not ovaling are valid. With this firmly established, the second phase of wind tunnel experimentation could then proceed.

## CHAPTER 5

### SECOND PHASE OF WIND TUNNEL TESTING

Earlier experimental findings demonstrated the importance of the wake in determining the onset of ovaling and, indeed, whether ovaling occurs or not. The important role played by the wake would further be demonstrated if it could be shown that no ovaling is possible when the wake is entirely eliminated. Hence, a specially built "wake eliminator", in the form of a wake bubble, as shown in Figure 5.1 and Figure 5.2 was used in the second phase of the experimental work. The purpose of the wake eliminator, as implied by the name, is to reduce, if not totally eliminate, the effect of the wake region.

The set-up was later modified to have some coherent flow in the back of the cylindrical shell (see Figure 5.3), by sucking air through the holes in the suction device attached to the wake eliminator. The suction was generated by a constant-rpm blower fan and the amount of suction at different wind speeds is shown in Figure 5.4. The ultimate aim of this apparatus was to create a fully potential flow around the complete circumference of the model. This experiment could then be used to further test the theory, which predicted that no ovaling would occur in an ideal flow field [12].

#### 5.1 Flow Around the Shell with Wake Eliminator

The effect of the wake eliminator on the flow field around the test shell was difficult to predict. In order to gain some basic understanding



of the flow field, the static pressure distributions of a rigid cylinder<sup>†</sup>, both with wake eliminator and suction were measured. It should be noted that these measurements were taken without "boundary layer guards"<sup>‡</sup>.

Pressure distributions for each configuration were measured at three wind speeds, giving a range of Reynolds number  $3.5 \times 10^4 < Re < 2.0 \times 10^5$ . It had been checked that the measured pressure was symmetric about the centerline of the cylinder and uniform over most of the span. In fact, this was not so when suction was applied through the wake eliminator, in which case the pressure in the base region seemed to vary along the length of the cylinder.

Pressure distributions in terms of  $C_p$  at  $U = 7.5$  m/s ( $Re = 3.80 \times 10^4$ ) for a circular cylinder, with wake eliminator, and with or without suction, are shown in Figure 5.5,  $C_p$  being defined as  $P - P_\infty / \frac{1}{2} \rho U^2$ . The pressure measurements were taken at approximately mid-span of the cylinder.

In the case of no suction, it is seen that from  $\theta = 0^\circ$  to  $40^\circ$ , the wake eliminator has little effect on the pressure distribution; nevertheless, it seems to cause earlier separation of the flow (at  $\theta = 70^\circ$ ) from the cylinder. Also, the pressure in the base region is much higher than that of a circular cylinder with no eliminator, with the pressure coefficient

---

<sup>†</sup> A rigid cylinder was used in place of a flexible shell because the instrumentation for the former was simple, and it was believed that before the onset of instability, shell motion was small and would have negligible effect on the static pressure distribution.

<sup>‡</sup> Even though the effect of boundary layer guards on base pressure measurements is profound [24], they are not employed for two main reasons. Firstly, a comparison of the pressure field between a rigid cylinder, with wake eliminator and (with wake eliminator plus) suction, should provide enough insight into the velocity field, so that the absolute magnitude of the pressure was not important. Secondly, considerable modification would have had to be made to the present set-up to accommodate the boundary layer guards.

from  $\theta = 110^\circ$  to  $180^\circ$  being almost constant at  $-0.35$ . This suggests that there may be little (if not zero) flow in the back of the cylinder.

When suction was applied from the wake eliminator (so as to attempt to simulate a coherent back flow), the pressure distribution becomes quite complicated, and is far from close to that of a fully potential flow (with  $C_p = 1 - 4 \sin^2 \theta$ ).

Increasing the wind speed to  $U = 18.0 \text{ m/s}$  ( $Re = 9.10 \times 10^4$ ) causes the pressure coefficients for a cylinder with and without a wake eliminator to become quite similar for the forward part of the cylinder (see Figure 5.6); a slightly lower base pressure ( $C_p = -0.42$ ) is recorded for the former configuration. Comparing the  $C_p$  curves of a cylinder with and without suction (always with wake eliminator), it is seen that the suction device becomes even less effective at this higher wind speed.

The pressure distributions at an even higher flow velocity,  $U = 36.0 \text{ m/s}$  ( $Re = 1.82 \times 10^5$ ), are shown in Figure 5.7. The measured  $C_p$  curves of a cylinder with wake eliminator and suction follow closer to that without suction. For the latter case, there seems to be some residual flow at the back of the cylinder.

The generation of coherent flow at the back of the cylinder when suction was applied is further complicated by the existence of variations of pressure distribution along the span, as shown in Figure 5.8. This problem had been anticipated, as there is a pressure drop along the length of the suction device which, in turn, would be expected to cause a variation of volumetric flow rate through the holes. The attempted remedy, at the design stage of the device, was to vary the size of the holes from top to bottom, with the larger holes being at the bottom. However, as may be seen from Figure 5.8, this does not seem to have been successful.

## 5.2 Wind Effects on the System

The results for the response of the shell when subjected to cross flow for the three different configurations referred to earlier will now be presented.

Shell C was used for these measurements, which had an average wall thickness 15% smaller than that of the shells used previously. It is seen (Figure 5.9) that the system becomes unstable in the second mode at a lower wind speed (as compared to shells A and B) of  $U_{cr} \approx 18.0$  m/s ( $f_{2,1} \sim 167$  Hz,  $r = 3.8-3.9$ ), while the threshold flow velocity for the onset of third-mode ovaling remains about the same, at  $U_{thr} \approx 22.7$  m/s ( $f_{3,1} \sim 234$  Hz).

Figures 5.10 and 5.11 show the behaviour of shell C with wake eliminator, with and without suction at the back of the cylindrical shell. The system is stable for both configurations.

One intriguing finding of these experiments is that flow periodicity<sup>†</sup> was detected at some wind speeds, even in the presence of an extended splitter splate ( $L/D = 6$ ). On closer examination, however, it is noticed that the calculated Strouhal numbers, based on a cylinder of 76 mm (3.0 in.) diameter, range from 0.14 to 0.15, which are much lower than the usual value for a circular cylinder ( $S = 0.18-0.19$ ). It is seen (Figure 5.12) that at the same flow velocity, the vortex shedding frequency for a cylindrical shell is higher without the wake eliminator. A reasonable explanation then emerges for this wake periodicity: that it originates from the wake eliminator, which, together with the shell, in effect acts like a bluff body of larger effective diameter, reducing the ratio of  $L/D$  and hence rendering the splitter plate ineffective in suppressing periodicity.

---

<sup>†</sup>The hot wire probe was located at 254 mm (10.0 in.) downstream and 165 mm (6.5 in.) away from the center of the cylinder.

It should be noted that the magnitude of the above-mentioned vortex shedding signal, when the wake eliminator is in place, is very small. Figure 5.13 compares the power spectral density of the wake for the three different configurations at one selected flow velocity of  $U = 15.5$  m/s. This may best be appreciated by replotting the same diagram on the same scale as shown in Figure 5.14.

The experimental evidence collected in this phase of wind tunnel testing, together with the previous results of a shell with an insert (Chapter 4), have clearly and forcefully demonstrated that the near wake flow plays a crucial role, insofar as the stability of the system is concerned.

## CHAPTER 6

### FLUTTER ANALYSIS OF A CLAMPED-CLAMPED SHELL

The theory formulated by Suen [10,12] to study the stability of a thin elastic cylindrical shell clamped at both ends, provides remarkable qualitative agreement with experimental observations; nevertheless, the quantitative performance of the theory is poor. It should be remarked here, in view of the findings of the previous two Chapters, that in Suen's analysis, the flow field within the wake is assumed to be zero - i.e. the wake effect on the stability of the system has been ignored.

The goal of the present study is to improve the quantitative aspect of the original theory [10,12] - i.e. to obtain a better prediction of threshold flow velocities of ovaling. The theory will be modified in a manner proposed by Paidoussis [25]. Firstly, the change in radial flow velocity, due to shell displacement, will be allowed for in the fluid-solid boundary condition. Secondly, the variation of the base pressure in the wake, induced by shell deformation, will be incorporated into the theory.

The flow field around the cylindrical shell is assumed to be quasi-irrotational. The wake is separated from the outer flow by a dividing streamline. Within the wake, a constant flow velocity is assumed to exist (in a time-averaged sense), the magnitude of which is dictated by the base-pressure in the wake. It is further assumed that the flow field is comprised of the superposition of the mean flow and the perturbation flow field induced by shell vibration. Further, it is assumed that the positions where the mean flow separates from the body surface are unaffected by shell motions, which are considered to be small.

The method of analysis is briefly as follows. Firstly, the time-varying flow field associated with shell vibration at a typical cross section is determined, and then, utilizing strip theory aerodynamics, the resultant pressure fluctuations on the shell are calculated; if these pressure fluctuations are such as to attenuate or amplify the initial vibration, then stability or instability, respectively, is indicated.

### 6.1 Equations of Motion

The shell is treated as purely elastic, homogeneous, isotropic and thin, and its motions are described by displacements  $u$ ,  $v$  and  $w$  of the middle surface of the shell from its initial position in the cylindrical coordinate system  $x$ ,  $\theta$  and  $r$  (Figure 6.1).

The equations of motion of the shell are taken as given by Flügge [26], i.e.,

$$a^2 \frac{\partial^2 u}{\partial x^2} + \frac{1-\nu}{2} \frac{\partial^2 u}{\partial \theta^2} + a \frac{1+\nu}{2} \frac{\partial^2 v}{\partial x \partial \theta} + a \nu \frac{\partial w}{\partial x} + \kappa \left\{ \frac{1-\nu}{2} \frac{\partial^2 u}{\partial \theta^2} - a^3 \frac{\partial^3 w}{\partial x^3} + \frac{1-\nu}{2} a \frac{\partial^3 w}{\partial x \partial \theta^2} \right\} = \gamma \frac{\partial^2 u}{\partial t^2}, \quad (6.1)$$

$$a \frac{1+\nu}{2} \frac{\partial^2 u}{\partial x \partial \theta} + \frac{\partial^2 v}{\partial \theta^2} + a^2 \frac{1-\nu}{2} \frac{\partial^2 v}{\partial x^2} + \frac{\partial w}{\partial \theta} + \kappa \left\{ \frac{3}{2} a^2 (1-\nu) \frac{\partial^2 v}{\partial x^2} - \frac{3-\nu}{2} a^2 \frac{\partial^3 w}{\partial x^2 \partial \theta} \right\} = \gamma \frac{\partial^2 v}{\partial t^2}, \quad (6.2)$$

$$\begin{aligned}
av \frac{\partial u}{\partial x} + \frac{\partial v}{\partial \theta} + w + \kappa \left\{ a \frac{1-\nu}{2} \frac{\partial^3 u}{\partial x \partial \theta^2} - a^3 \frac{\partial^3 u}{\partial x^3} - \frac{3-\nu}{2} a^2 \frac{\partial^3 v}{\partial x^2 \partial \theta} + a^4 \frac{\partial^4 w}{\partial x^4} \right. \\
\left. + 2a^2 \frac{\partial^4 w}{\partial x^2 \partial \theta^2} + \frac{\partial^4 w}{\partial \theta^4} + 2 \frac{\partial^2 w}{\partial \theta^2} + w \right\} = -\gamma \left\{ \frac{\partial^2 w}{\partial t^2} - \frac{q_r}{\rho_s h} \right\}, \quad (6.3)
\end{aligned}$$

where  $\kappa = h^2/12a^2$ ,  $\gamma = \rho_s a^2(1-\nu^2)/E$  and  $q_r = p_i - p_e$ ,  $p_i$  and  $p_e$  being, respectively, the internal and external pressure on the shell surface,  $h$  and  $a$  the shell wall-thickness and radius, respectively,  $\rho_s$  the shell density and  $E$  the modulus of elasticity;  $\nu$  is Poisson's ratio.

These equations are linear, and, thus,  $q_r$  may be separated into two components -  $\bar{q}_r(\theta)$ , which is due to the static loading of the mean flow, and  $q_r^*(x, \theta, t)$ , which is due to the perturbation associated with the deformation with components  $u^*(x, \theta, t)$ ,  $v^*(x, \theta, t)$  and  $w^*(x, \theta, t)$ . Considering the effect of static loading,  $\bar{q}_r$ , on the dynamics of the system to be negligible, equations (6.1) to (6.3) may be viewed as relationships among  $u^*$ ,  $v^*$ ,  $w^*$  and  $q_r^*$ .

## 6.2 The Fluid Pressure on the Shell

Assuming the induced flow in the  $x$ -direction to be small, a two-dimensional velocity potential may be defined as

$$V_r = \frac{\partial \Phi}{\partial r}, \quad V_\theta = \frac{1}{r} \frac{\partial \Phi}{\partial \theta} \quad \text{and} \quad V_x = 0, \quad (6.4)$$

where  $V_r$ ,  $V_\theta$  and  $V_x$  are, respectively, the radial, tangential and axial

flow velocities; (the last of the three relationships above makes the use of strip theory aerodynamics possible).

Furthermore, because of the linearity of the velocity potential,  $\phi$  can be represented by a superposition of the mean flow potential  $\phi_0(r,\theta)^{\dagger}$  and the perturbation flow potential  $\phi^*(r,\theta,t)$ , so that

$$\phi(x,r,\theta,t) = \phi_0(r,\theta) + \phi^*(r,\theta,t) , \quad (6.5)$$

where the latter is entirely associated with shell motions.

Using the condition of impermeability of a stationary shell, the mean surface velocities in the radial and tangential directions are

$$\left. \frac{\partial \phi_0}{\partial r} \right|_{r=a} = 0 , \quad \frac{1}{a} \left. \frac{\partial \phi_0}{\partial \theta} \right|_{r=a} = U f(\theta) , \quad (6.6)$$

where  $U$  is the free stream velocity and  $f(\theta)$  may be determined empirically from the pressure distribution around a circular cylinder.

Unlike previous analysis [10,12], the effect of changes in the velocity field as a result of the instantaneous radial displacement, described by

$$r = a + w^*(\theta,t) ,$$

---

<sup>†</sup> Here it is realized, of course, that the true mean flow is not derivable from a potential, as it is viscous; nevertheless, it is found convenient to suppose the existence of  $\phi_0$ , which will eventually yield the empirically determined mean pressure on the shell surface from the front stagnation point to the separation points.



are taken into account when calculating the surface velocities; thus,

$$\begin{aligned}
 v_r|_{r=a+w^*} &\approx v_r|_{r=a} + \left. \frac{\partial v_r}{\partial r} \right|_{r=a} w^* \\
 &\approx \left. \frac{\partial \phi^*}{\partial r} \right|_{r=a} + \left. \frac{\partial^2 \phi_0}{\partial r^2} \right|_{r=a} w^*
 \end{aligned} \tag{6.7}$$

and

$$\begin{aligned}
 v_\theta|_{r=a+w^*} &\approx v_\theta|_{r=a} + \left. \frac{\partial v_\theta}{\partial r} \right|_{r=a} w^* \\
 &\approx Uf(\theta) + \frac{1}{a} \left. \frac{\partial \phi^*}{\partial \theta} \right|_{r=a} + \frac{1}{a} \left. \frac{\partial^2 \phi_0}{\partial r \partial \theta} \right|_{r=a} w^* - \frac{1}{a^2} \left. \frac{\partial \phi_0}{\partial \theta} \right|_{r=a} w^*.
 \end{aligned} \tag{6.8}$$

Therefore, the total velocity is given by

$$\begin{aligned}
 v^2 &= v_r^2 + v_\theta^2 + v_x^2 \\
 &\approx U^2 f^2(\theta) + 2 \frac{Uf(\theta)}{a} \left. \frac{\partial \phi^*}{\partial \theta} \right|_{r=a} + 2 \frac{Uf(\theta)}{a} \left. \frac{\partial^2 \phi_0}{\partial r \partial \theta} \right|_{r=a} w^* - 2 \frac{Uf(\theta)}{a^2} \left. \frac{\partial \phi_0}{\partial \theta} \right|_{r=a} w^*,
 \end{aligned} \tag{6.9}$$

with higher order terms being neglected.

The Bernoulli equation for unsteady flow may be written as

$$\frac{p}{\rho} + \frac{1}{2} \underline{v}^2 + \frac{\partial \phi}{\partial t} - (\underline{v} + \underline{\omega} \times \underline{r}) \cdot \underline{\nabla} \phi = \frac{p_0}{\rho}, \quad (6.10)$$

where the term  $(\underline{v} + \underline{\omega} \times \underline{r}) \cdot \underline{\nabla} \phi$  arises from the non-stationary fluid-solid boundary condition (Appendix D). As the fluid is assumed to be irrotational,  $\underline{\omega} = 0$  and  $\underline{v} = \frac{\partial w^*}{\partial t} \underline{e}_r + \frac{\partial v^*}{\partial t} \underline{e}_\theta$ . Thus, utilizing the above expression for the velocity, the surface pressure becomes

$$p = p_0 - \rho \left( \frac{\partial \phi^*}{\partial t} + \frac{1}{2} U^2 f^2(\theta) + \frac{U f(\theta)}{a} \frac{\partial \phi^*}{\partial \theta} + \frac{U f(\theta)}{a} \frac{\partial^2 \phi_0}{\partial r \partial \theta} w^* - \frac{U f(\theta)}{a^2} \frac{\partial \phi_0}{\partial \theta} w^* - U f(\theta) \frac{\partial v^*}{\partial t} \right) \Big|_{r=a}. \quad (6.11)$$

### 6.3 Boundary Condition

The perturbation potential may be related to shell displacement by the boundary relationship

$$v_r \Big|_{r=a+w^*} = \frac{Dw^*}{Dt},$$

where  $D/Dt$  denotes the convective derivative; comparing this with equation (6.7) gives

$$\frac{\partial \phi^*}{\partial r} \Big|_{r=a} + \frac{\partial^2 \phi_0}{\partial r^2} \Big|_{r=a} w^* = \frac{\partial w^*}{\partial t} + U f(\theta) \frac{1}{a} \frac{\partial w^*}{\partial \theta},$$

where second-order terms,  $V_r|_{r=a} \frac{\partial w^*}{\partial r}$ ,  $\partial V_r / \partial r|_{r=a} w^* \frac{\partial w^*}{\partial r}$ ,  $\frac{1}{a} \frac{\partial \phi^*}{\partial \theta}|_{r=a} \frac{\partial w^*}{\partial \theta}$  and  $\frac{1}{a} \partial V_\theta / \partial r|_{r=a} w^* \frac{\partial w^*}{\partial \theta}$  have been neglected; the above equation may be rearranged as

$$\frac{\partial \phi^*}{\partial r}|_{r=a} = \frac{\partial w^*}{\partial t} + \frac{U f(\theta)}{a} \frac{\partial w^*}{\partial \theta} - \frac{\partial^2 \phi_0}{\partial r^2}|_{r=a} w^* . \quad (6.12)$$

#### 6.4 Determination of the Velocity Potential

Using Roshko's measurements [27],  $f(\theta)$  which defines the mean surface flow velocity on the shell, may be represented by the polynomial

$$f(\theta) = -1.6073|\theta| + 0.5700|\theta|^2 - 0.9394|\theta|^3 + 0.1714|\theta|^4 \text{ for } 0 \leq |\theta| \leq \theta_s , \quad (6.13)$$

and, in an attempt to incorporate the correct wake pressure into the stability analysis (as explained below),

$$f(\theta) = -f(\theta_s) \text{ for } |\theta| > \theta_s . \quad (6.14)$$

Thus, to obtain a constant base pressure in the wake,  $f(\theta)$  is set to  $-f(\theta_s)$  in the back (downstream side) of the shell. This formulation effectively suggests that there is a quasi-coherent reverse flow on the surface of the shell in the wake region. Of course, physically there is no evidence to suggest that this is so. This formulation has however been introduced here for the following reason: if it is assumed that  $f(\theta)=0$

in the wake (as was previously done [10,12]), then the mean pressure there is wrong; whilst, if  $f(\theta) = -f(\theta_s)$  is assumed, the mean pressure is correct, at the expense of a doubtful assumption regarding surface flow velocity in the wake. In what follows, calculations will be made with both of these partially incorrect assumptions and the results compared to the experimental stability data.

It may be shown [9,11] that for harmonic shell motions with an antinode facing the free stream, the perturbation velocity potential, which must satisfy the Laplace equation, has external and internal components of the form

$$\phi_e^* = e^{i\omega t} \sum_{\lambda=0}^{\infty} D(\lambda) r^{-\lambda} \cos \lambda \theta, \quad (6.15)$$

$$\phi_i^* = e^{i\omega t} \sum_{\lambda=0}^{\infty} E(\lambda) r^{\lambda} \cos \lambda \theta. \quad (6.16)$$

Using a simplified solution, where circumferential coupling between modes is considered to be inconsequential (where it had been shown in reference [12] there is little loss in accuracy), the shell displacements may be expressed as

$$u^* = e^{i\omega t} \sum_{n=1}^{\infty} A_n \cos n\theta \psi_n',$$

$$v^* = e^{i\omega t} \sum_{n=1}^{\infty} B_n \sin n\theta \psi_n, \quad (6.17)$$

$$w^* = e^{i\omega t} \sum_{m=1}^{\infty} C_m \cos n\theta \psi_m, \quad (6.17)$$

where  $\psi_m(x)$  are comparison functions for the axial mode shape of the shell; the prime denotes differentiation with respect to  $x$ .

To solve for  $\phi_e^*$ , which is the velocity potential outside the shell, the mean-flow velocity potential  $\phi_0$  has to be determined first; as a first approximation, *solely for evaluating terms in equations (6.11) and (6.12) involving  $\phi_0$* , an idealized fully potential flow is assumed, in the absence of measurements for the velocity gradients in the real (viscous) flow field<sup>†</sup>.

Then  $\phi_0$  may be written as

$$\phi_0 = -U(r \cos\theta + \frac{a^2}{r} \cos\theta), \quad (6.18)$$

for  $|\theta| \leq 1.484$  rad ( $85^\circ$ ), which is the point of separation, and  $\phi_0 = 0$  for  $1.484$  rad  $< |\theta| \leq \pi$ .

Substituting equations (6.15), (6.17) and (6.18) into (6.12) gives

$$\begin{aligned} - \sum_{\lambda=0}^{\infty} \lambda D(\lambda) a^{-\lambda-1} \cos\lambda\theta &= \sum_{m=1}^{\infty} C_m \{ i\omega \cos n\theta - \frac{Un}{a} f(\theta) \sin n\theta \\ &+ \frac{2U}{a} \cos\theta \cos n\theta \} \psi_m, \end{aligned} \quad (6.19)$$

<sup>†</sup>This is a first approximation. If the addition of these terms produces interesting results, then a more refined evaluation of them would be indicated.

multiplying both sides by  $\cos j\theta$  and integrating from 0 to  $\pi$ , noting that

$$\int_0^{\pi} \cos \lambda \theta \cos j \theta d\theta = \frac{\pi}{2} \quad \text{if } \lambda = j,$$

$$= 0 \quad \text{if } \lambda \neq j,$$

and that the integration for the last term on the right hand side of equation (6.19) is only applicable from 0 to  $\theta_s$ , yields

$$D(j) = \left(\frac{a^{j+1}}{j}\right) \sum_{m=1}^{\infty} C_m \left\{ -i\omega \delta_{nj} + \frac{2}{\pi} \frac{U_n}{a} \int_0^{\pi} f(\theta) \sin n\theta \cos j\theta d\theta \right. \\ \left. - \frac{2}{\pi} \frac{2U}{a} \int_0^{\theta_s} \cos \theta \cos n\theta \cos j\theta d\theta \right\} \psi_m$$

for  $j = 1, 2, 3, \dots$ , where  $\delta$  is the Kronecker delta. Defining

$$F(n, j) = \int_0^{\pi} f(\theta) \sin n\theta \cos j\theta d\theta$$

$$= \int_0^{\theta_s} f(\theta) \sin n\theta \cos j\theta d\theta - \int_{\theta_s}^{\pi} f(\theta_s) \sin n\theta \cos j\theta d\theta, \quad (6.20)$$

where equation (6.14) has been utilized, the foregoing expression may then be rewritten as



$$D(j) = \left(\frac{a^{j+1}}{j}\right) \sum_{m=1}^{\infty} C_m \left\{ -i\omega \delta_{nj} + 2 \frac{Un}{\pi a} F(n, j) - \frac{U}{\pi a} \left[ \frac{\sin(1+n+j)\theta_s}{1+n+j} + \frac{\sin(1+n-j)\theta_s}{1+n-j} + \frac{\sin(1-n+j)\theta_s}{1-n+j} + \frac{\sin(1-n-j)\theta_s}{1-n-j} \right] \right\} \psi_m. \quad (6.21)$$

In a similar manner, inside the shell, where there is no flowing fluid, the constant  $E(j)$  is given by

$$E(j) = \left(\frac{a^{1-j}}{j}\right) \sum_{m=1}^{\infty} i\omega C_m \delta_{nj} \psi_m. \quad (6.22)$$

Finally,  $\phi_e^*$  and  $\phi_i^*$  may be expressed as

$$\phi_e^* = e^{i\omega t} \left[ D(0) + \sum_{j=1}^{\infty} D(j) r^{-j} \cos j\theta \right], \quad (6.23)$$

$$\phi_i^* = e^{i\omega t} \left[ E(0) + \sum_{j=1}^{\infty} E(j) r^j \cos j\theta \right], \quad (6.24)$$

where  $D(0)$  and  $E(0)$  are arbitrary constants, since only the derivative of  $\phi^*$  is specified at the boundary (see equation (6.12)).

## 6.5 Pressure Fluctuations

The pressure fluctuations on the shell outer surface are conveniently specified separately in two distinct regions:  $p_e^*$  associated with the

flow ahead of the separation point, and  $p_e^*$  associated with the flow after the separation point (in the wake). From equation (6.11) the pressure fluctuation ahead of separation is given by

$$p_e^* = -\rho \left[ \frac{\partial \phi_e^*}{\partial t} + \frac{Uf(\theta)}{a} \frac{\partial \phi_e^*}{\partial \theta} + \frac{Uf(\theta)}{a} \frac{\partial^2 \phi_0}{\partial r \partial \theta} w^* - \frac{Uf(\theta)}{a^2} \frac{\partial \phi_0}{\partial \theta} w^* - Uf(\theta) \frac{\partial v^*}{\partial t} \right] \Big|_{r=a}$$

$$\text{for } 0 \leq |\theta| \leq \theta_s.$$

where the static components have been filtered out.

Applying now equations (6.23) in conjunction with (6.21), the above equation gives

$$\begin{aligned} p_e^* = & -\rho e^{i\omega t} \sum_{j=1}^{\infty} \left\{ \frac{a \cos j\theta}{j} \sum_{n=1}^{\infty} C_n \left[ \omega^2 \delta_{nj} + 2 \frac{U\omega i}{\pi a} n F(n, j) \right. \right. \\ & - \frac{U\omega i}{\pi a} \left( \frac{\sin(1+n+j)\theta_s}{1+n+j} + \frac{\sin(1+n-j)\theta_s}{1+n-j} + \frac{\sin(1-n+j)\theta_s}{1-n+j} + \frac{\sin(1-n-j)\theta_s}{1-n-j} \right) \Big] \psi_n \\ & - \sin j\theta Uf(\theta) \sum_{n=1}^{\infty} C_n \left[ -i\omega \delta_{nj} + 2 \frac{U}{\pi a} n F(n, j) - \frac{U}{\pi a} \left( \frac{\sin(1+n+j)\theta_s}{1+n+j} \right. \right. \\ & + \frac{\sin(1+n-j)\theta_s}{1+n-j} + \frac{\sin(1-n+j)\theta_s}{1-n+j} + \frac{\sin(1-n-j)\theta_s}{1-n-j} \Big) \Big] \psi_n - 2 \frac{U^2}{a} f(\theta) \sin \theta \sum_{n=1}^{\infty} C_n \cos n\theta \psi_n \\ & \left. - Uf(\theta) \sum_{n=1}^{\infty} B_n [i\omega \sin n\theta] \psi_n \right\} - \rho e^{i\omega t} i\omega D(0), \end{aligned} \quad (6.25)$$



where the term  $\left. \frac{\partial^2 \phi_0}{\partial r \partial \theta} \right|_{r=a} = 0$  in accordance with the assumption that  $\phi_0$  is approximately given by equation (6.18).

Within the wake region, it is presumed that shell motions would cause variations of flow pattern around the body, and consequently changes in base pressure. Hence, equation (6.10) may be written as

$$\frac{p}{\rho} + \frac{1}{2} v^2 + \frac{\partial \phi}{\partial t} - (\underline{v} + \underline{\omega} \times \underline{r}) \cdot \underline{\nabla} \phi = \frac{1}{\rho} \left[ p_b + \frac{\partial p_b}{\partial \left( \frac{w^*}{a} \right)} \left( \frac{w^*}{a} \right) e^{-i\psi} \right],$$

where the term  $\partial p_b / \partial (w^*/a) (w^*/a) e^{-i\psi}$  has been introduced to account for the changes in base pressure, which are here taken to lag behind the shell displacements, as suggested by experimental evidence. The measurements of changes in base pressure and of the phase lag  $\psi$ , will be presented in Chapter 7 and Appendix E, respectively.

To simplify the analysis, the base pressure variations and  $\psi$  are assumed to be independent of  $\theta$  within the wake, and the calculation is based on the values measured at  $\theta = 180^\circ$ . The measured base pressure coefficient may then be approximated by a first order polynomial, as shown in Figures 6.2 and 6.3 for the  $n=2$  and  $n=3$  modes of ovaling with an anti-node facing the free stream, at  $Re = 3.80 \times 10^4$ . Hence,

$$C_{p_b} = \frac{p_b - p_\infty}{\frac{1}{2} \rho U^2} = H \frac{w^*}{a} + H_0,$$

where  $H_0$  and  $H$  are constants; thus,

$$\frac{\partial p_b}{\partial \left(\frac{w^*}{a}\right)} = \frac{H}{Z} \rho U^2 .$$

Substituting into the pressure expression as before, but with  $\phi_0 = 0$  and  $\theta_s$  replacing  $\theta$ , yields

$$\begin{aligned} p_e^* &= -\rho \left[ \frac{\partial \phi_e^*}{\partial t} - \frac{U f(\theta_s)}{a} \frac{\partial \phi_e^*}{\partial \theta} + U f(\theta_s) \frac{\partial V^*}{\partial t} \right] \Big|_{r=a} + \frac{H}{Z} \rho U^2 \left( \frac{w^*}{a} \right) e^{-i\psi} \\ &= -\rho e^{i\omega t} \sum_{j=1}^{\infty} \left\{ \frac{a \cos j\theta}{j} \sum_{n=1}^{\infty} C_n \left[ \omega^2 \delta_{nj} + 2 \frac{U\omega i}{\pi a} n F(n,j) \right. \right. \\ &\quad \left. \left. - \frac{U\omega i}{a} \left( \frac{\sin(1+n+j)\theta_s}{1+n+j} + \frac{\sin(1+n-j)\theta_s}{1+n-j} + \frac{\sin(1-n+j)\theta_s}{1-n+j} + \frac{\sin(1-n-j)\theta_s}{1-n-j} \right) \right] \psi_n \right. \\ &\quad \left. + \sin j\theta U f(\theta_s) \sum_{n=1}^{\infty} C_n \left[ -i\omega \delta_{nj} + 2 \frac{U}{\pi a} n F(n,j) - \frac{U}{\pi a} \left( \frac{\sin(1+n+j)\theta_s}{1+n+j} \right. \right. \right. \\ &\quad \left. \left. + \frac{\sin(1+n-j)\theta_s}{1+n-j} + \frac{\sin(1-n+j)\theta_s}{1-n+j} + \frac{\sin(1-n-j)\theta_s}{1-n-j} \right) \right] \psi_n \right. \\ &\quad \left. + U f(\theta_s) \sum_{n=1}^{\infty} B_n [i\omega \sin n\theta] \psi_n - \frac{HU^2}{2a} e^{-i\psi} \sum_{n=1}^{\infty} C_n \cos n\theta \psi_n \right\} \\ &= \rho e^{i\omega t} i\omega D(0) \quad \text{for } |\theta| > \theta_s . \end{aligned} \tag{6.26}$$

Equations (6.25) and (6.26) may be combined into a more general form

$$\begin{aligned}
p_e^* = & - \rho e^{i\omega t} \sum_{n=1}^{\infty} \left\{ C_n \left\{ \frac{\omega^2 a \cos n\theta}{n} + 2 \frac{U\omega}{\pi} \left[ n \sum_{j=1}^{\infty} \frac{\cos j\theta}{j} F(n,j) \right. \right. \right. \\
& - \frac{1}{2} \left( \sum_{j=1}^{\infty} \frac{\cos j\theta}{j} \left( \frac{\sin(1+n+j)\theta_s}{1+n+j} + \frac{\sin(1+n-j)\theta_s}{1+n-j} + \frac{\sin(1-n+j)\theta_s}{1-n+j} + \frac{\sin(1-n-j)\theta_s}{1-n-j} \right) \right) \right\} \\
& - U f(\theta) \delta_1 \left\{ i\omega \sin n\theta [B_n - C_n] + 2 \frac{U}{\pi a} C_n \left[ n \sum_{j=1}^{\infty} F(n,j) \sin j\theta \right. \right. \\
& - \frac{1}{2} \left( \sum_{j=1}^{\infty} \sin j\theta \left( \frac{\sin(1+n+j)\theta_s}{1+n+j} + \frac{\sin(1+n-j)\theta_s}{1+n-j} + \frac{\sin(1-n+j)\theta_s}{1-n+j} + \frac{\sin(1-n-j)\theta_s}{1-n-j} \right) \right) \right\} \\
& - 2 \frac{U^2}{a} C_n f(\theta) \sin\theta \cos n\theta \delta_2 - \frac{H U^2}{2a} e^{-i\psi} C_n \cos n\theta \delta_3 \left. \right\} \psi_n \\
& - \rho e^{i\omega t} i\omega D(0) , \tag{6.27}
\end{aligned}$$

where  $f(\theta) \delta_1 = f(\theta)$  ,  $\delta_2 = 1$  and  $\delta_3 = 0$  if  $0 \leq |\theta| \leq \theta_s$  ,

$f(\theta) \delta_1 = -f(\theta_s)$  ,  $\delta_2 = 0$  and  $\delta_3 = 1$  if  $|\theta| > \theta_s$  .

Proceeding in a similar manner, gives

$$p_i^* = - \rho e^{i\omega t} \sum_{n=1}^{\infty} \left\{ -C_n \frac{\omega^2 a \cos n\theta}{n} \right\} \psi_n - \rho e^{i\omega t} i\omega E(0) . \tag{6.28}$$

Hence, the aerodynamic term  $q_r^* = p_i^* - p_e^*$  becomes

$$\begin{aligned}
q_r^* = & \rho e^{i\omega t} \sum_{n=1}^{\infty} \left\{ C_n \left[ 2 \frac{\omega^2 a \cos n\theta}{n} + 2 \frac{U\omega i}{\pi} \left[ n \sum_{j=1}^{\infty} \frac{\cos j\theta}{j} F(n,j) \right. \right. \right. \\
& - \left. \left. \left. \frac{1}{2} \left( \sum_{j=1}^{\infty} \frac{\cos j\theta}{j} \left( \frac{\sin(1+n+j)\theta_s}{1+n+j} + \frac{\sin(1+n-j)\theta_s}{1+n-j} + \frac{\sin(1-n+j)\theta_s}{1-n+j} + \frac{\sin(1-n-j)\theta_s}{1-n-j} \right) \right) \right] \right\} \\
& - U f(\theta) \delta_1 \left\{ i\omega \sin n\theta [B_n - C_n] + 2 \frac{U}{\pi a} C_n \left[ n \sum_{j=1}^{\infty} F(n,j) \sin j\theta \right. \right. \\
& - \left. \left. \frac{1}{2} \left( \sum_{j=1}^{\infty} \sin j\theta \left( \frac{\sin(1+n+j)\theta_s}{1+n+j} + \frac{\sin(1+n-j)\theta_s}{1+n-j} + \frac{\sin(1-n+j)\theta_s}{1-n+j} + \frac{\sin(1-n-j)\theta_s}{1-n-j} \right) \right) \right] \right\} \\
& - 2 \frac{U^2}{a} C_n f(\theta) \sin\theta \cos n\theta \delta_2 - \frac{H U^2}{2a} e^{-i\psi} C_n \cos n\theta \delta_3 \} \psi_n \\
& + \rho e^{i\omega t} i\omega \{D(0) - E(0)\} .
\end{aligned} \tag{6.29}$$

## 6.6 Solution of the Equations

Substituting equations (6.17) and (6.29) into the shell equations yields the following set of equations:

$$\begin{aligned}
\sum_{n=1}^{\infty} \left\{ (a^2 \psi_n'' - \frac{1}{2} n^2 (1-\nu)(1+\kappa) \psi_n') \cos n\theta A_n + \left( \frac{1}{2} a n (1+\nu) \psi_n' \right) \cos n\theta B_n \right. \\
+ (a \nu \psi_n' - a^3 \kappa \psi_n'' - \frac{1}{2} a n^2 \kappa (1-\nu) \psi_n') \cos n\theta C_n \\
\left. + \gamma \omega^2 \psi_n' \cos n\theta A_n \right\} = 0 ,
\end{aligned} \tag{6.30}$$

$$\begin{aligned}
& \sum_{n=1}^{\infty} \left\{ \left( -\frac{1}{2} a n(1+\nu) \psi_n'' \right) \sin n\theta A_n + \left( -n^2 \psi_n'' + \frac{1}{2} a^2 (1+3\kappa)(1-\nu) \psi_n'' \right) \sin n\theta B_n \right. \\
& + \left( -n \psi_n'' + \frac{1}{2} a^2 n \kappa (3-\nu) \psi_n'' \right) \sin n\theta C_n \\
& \left. + \gamma \omega^2 \psi_n \sin n\theta B_n' \right\} = 0, \quad (6.31)
\end{aligned}$$

$$\begin{aligned}
& \sum_{n=1}^{\infty} \left\{ \left( -a\nu \psi_n'' + \frac{1}{2} a n^2 \kappa (1-\nu) \psi_n'' + a^3 \kappa \psi_n^{iv} \right) \cos n\theta A_n \right. \\
& + \left( -n \psi_n'' + \frac{1}{2} a^2 n \kappa (3-\nu) \psi_n'' \right) \cos n\theta B_n \\
& + \left\{ -\psi_n - a^4 \kappa \psi_n^{iv} + 2a^2 n^2 \kappa \psi_n'' - (n^2-1)^2 \kappa \psi_n \right\} \cos n\theta C_n + \gamma \omega^2 \psi_n \cos n\theta C_n \\
& + \frac{\rho \gamma}{\rho_s h} \left\{ 2 \frac{\omega^2 a \cos n\theta}{n} + 2 \frac{U \omega i}{\pi} \left[ n \sum_{j=1}^{\infty} \frac{\cos j\theta}{j} F(n,j) - \frac{1}{2} \left( \sum_{j=1}^{\infty} \frac{\cos j\theta}{j} \right. \right. \right. \\
& \left. \left. \left. + \left( \frac{\sin(1+n+j)\theta_s}{1+n+j} + \frac{\sin(1+n-j)\theta_s}{1+n-j} + \frac{\sin(1-n+j)\theta_s}{1-n+j} + \frac{\sin(1-n-j)\theta_s}{1-n-j} \right) \right] \right\} C_n \\
& - U f(\theta) \delta_1 \{ i \omega \sin n\theta [B_n - C_n] + 2 \frac{U}{\pi a} C_n \left[ n \sum_{j=1}^{\infty} F(n,j) \sin j\theta \right. \\
& \left. - \frac{1}{2} \left( \sum_{j=1}^{\infty} \sin j\theta \left( \frac{\sin(1+n+j)\theta_s}{1+n+j} + \frac{\sin(1+n-j)\theta_s}{1+n-j} + \frac{\sin(1-n+j)\theta_s}{1-n+j} + \frac{\sin(1-n-j)\theta_s}{1-n-j} \right) \right] \right\} \\
& - 2 \frac{U^2}{a} C_n f(\theta) \sin\theta \cos n\theta \delta_2 - \frac{H U^2}{2a} e^{-i\psi} C_n \cos n\theta \delta_3 \} \psi_n \}
\end{aligned}$$

continued

$$+ \frac{\rho_Y}{\rho_s h} \omega_1 \{D(0) - E(0)\} = 0. \quad (6.32)$$

Using a variant of Galerkin's method, equations (6.30) and (6.32) are multiplied by  $\cos n\theta$  and (6.31) by  $\sin n\theta$  and integrated from 0 to  $\pi$ . Next, equation (6.30) is multiplied by  $\psi_k'$  and equations (6.31) and (6.32) by  $\psi_k$ , and then integrated from 0 to  $L$ , yielding

$$\sum_{n=1}^M \left\{ \{a^2 g_{km} - \frac{1}{2} n^2 (1-\nu)(1+\kappa) f_{km} + \gamma \omega^2 f_{km}\} A_m + \{\frac{1}{2} a n (1+\nu) f_{km}\} B_m \right. \\ \left. + \{a \nu f_{km} - a^3 \kappa g_{km} - \frac{1}{2} a n^2 \kappa (1-\nu) f_{km}\} C_m \right\} = 0, \quad (6.33)$$

$$\sum_{n=1}^M \left\{ \{-\frac{1}{2} a n (1+\nu) c_{km}\} A_m + \{-n^2 a_{km} + \frac{1}{2} a^2 (1+3\kappa)(1-\nu) c_{km} + \gamma \omega^2 a_{km}\} B_m \right. \\ \left. + \{-n a_{km} + \frac{1}{2} a^2 n \kappa (3-\nu) c_{km}\} C_m \right\} = 0, \quad (6.34)$$

$$\sum_{n=1}^M \left\{ \{-a \nu c_{km} + \frac{1}{2} a n^2 \kappa (1-\nu) c_{km} + a^3 \kappa e_{km}\} A_m + \{-n a_{km} + \frac{1}{2} a^2 n \kappa (3-\nu) c_{km}\} B_m \right. \\ \left. + \{-a_{km} - a^4 \kappa e_{km} + 2 a^2 n^2 \kappa c_{km} - (n^2-1)^2 \kappa a_{km} + \gamma \omega^2 a_{km} + \frac{\rho_Y}{\rho_s h} \frac{2\omega^2 a}{n} a_{km}\} C_m \right. \\ \left. + \frac{\rho_Y}{\rho_s h} \frac{2U}{\pi} \omega_1 \left\{ [F(n,n) - \frac{1}{2} \left( \frac{\sin(1+2n)\theta_s}{n(1+2n)} + 2 \frac{\sin \theta_s}{n} + \frac{\sin(1-2n)\theta_s}{n(1-2n)} \right)] a_{km} C_m \right. \right.$$

continued

$$\begin{aligned}
& + F(n,n) a_{km} [C_m - B_m] \} - \frac{\rho \gamma}{\rho_s h} \left( \frac{4U^2}{\pi^2 a} \right) \left\{ n \sum_{j=1}^{\infty} F(n,j) F(j,n) \right. \\
& - \frac{1}{2} \left( \sum_{j=1}^{\infty} \left( \frac{\sin(1+n+j)\theta_s}{1+n+j} + \frac{\sin(1+n-j)\theta_s}{1+n-j} + \frac{\sin(1-n+j)\theta_s}{1-n+j} + \frac{\sin(1-n-j)\theta_s}{1-n-j} \right) F(j,n) \right) \\
& \left. + \pi F(1,n,n) + \frac{\pi}{8} \operatorname{He}^{-i\psi} [\pi - \theta_s - \frac{1}{2n} \sin 2n\theta_s] \right\} a_{km} C_m \} = 0, \quad (6.35)
\end{aligned}$$

where

$$F(j,n) = \int_0^{\theta_s} f(\theta) \sin j\theta \cos n\theta \, d\theta - \int_{\theta_s}^{\pi} f(\theta_s) \sin j\theta \cos n\theta \, d\theta,$$

$$F(1,n,n) = \int_0^{\theta_s} f(\theta) \sin\theta \cos n\theta \cos n\theta \, d\theta,$$

$$a_{km} = \int_0^L \psi_k \psi_m \, dx = L \delta_{km},$$

$$c_{km} = \int_0^L \psi_k \psi_m^* \, dx,$$

$$e_{km} = \int_0^L \psi_k \psi_m^{iv} \, dx,$$

$$f_{km} = \int_0^L \psi_k' \psi_m' \, dx,$$

$$g_{km} = \int_0^L \psi_k' \psi_m^{**} \, dx;$$

the analytical expressions for the above integrals,  $a_{km}$  to  $g_{km}$ , may be found in reference [28]. The summation over  $m$  is truncated at  $M$ .

For convenience, let now

$$C_1^i = 2 \frac{\rho a}{n} ,$$

$$C_2^i = 4 \frac{\rho U}{\pi} F(n, n) ,$$

$$C_3^i = 4 \frac{\rho U^2}{\pi a} n \sum_{j=1}^{\infty} F(n, j) F(j, n) ,$$

$$C_4^i = \frac{\rho U}{\pi} \left[ \frac{\sin(1+2n)\theta_s}{n(1+2n)} + 2 \frac{\sin \theta_s}{n} + \frac{\sin(1-2n)\theta_s}{n(1-2n)} \right] ,$$

$$C_5^i = 2 \frac{\rho U^2}{\pi a} \sum_{j=1}^{\infty} \left[ \frac{\sin(1+n+j)\theta_s}{1+n+j} + \frac{\sin(1+n-j)\theta_s}{1+n-j} + \frac{\sin(1-n+j)\theta_s}{1-n+j} + \frac{\sin(1-n-j)\theta_s}{1-n-j} \right] F(j, n) ,$$

$$C_6^i = 4 \frac{\rho U^2}{\pi a} F(1, n, n) ,$$

$$C_7^i = \frac{\rho U^2}{2\pi a} e^{-i\psi} \left[ \pi - \theta_s - \frac{1}{2n} \sin 2n\theta_s \right] .$$

Then, the equations of motion (6.33)-(6.35) may be written in the following matrix form:



$$-\omega^2 \begin{bmatrix} -\gamma f_{km} & 0 & 0 \\ 0 & -\gamma a_{km} & 0 \\ 0 & 0 & -\gamma a_{km} - \frac{\gamma}{\rho_s h} C_1' a_{km} \end{bmatrix} \begin{bmatrix} A_m \\ B_m \\ C_m \end{bmatrix} +$$

$$i\omega \begin{bmatrix} 0 & 0 & 0 \\ 0 & 0 & 0 \\ 0 & -\frac{\gamma}{\rho_s h} \frac{C_2'}{2} a_{km} & \frac{\gamma}{\rho_s h} [C_2' - C_4'] a_{km} \end{bmatrix} \begin{bmatrix} A_m \\ B_m \\ C_m \end{bmatrix} +$$

$$\begin{bmatrix} (a^2 g_{km} - \frac{1}{2} n^2 (1-\nu)(1+\kappa) f_{km}) & (\frac{1}{2} a n (1+\nu) f_{km}) & (a \nu f_{km} - a^3 \kappa g_{km} - \frac{1}{2} a n^2 \kappa (1-\nu) f_{km}) \\ (-\frac{1}{2} a n (1+\nu) c_{km}) & (-n^2 a_{km} + \frac{1}{2} a^2 (1+3\kappa)(1-\nu) c_{km}) & (-n a_{km} + \frac{1}{2} a^2 n \kappa (3-\nu) c_{km}) \\ (-a \nu c_{km} + \frac{1}{2} a n^2 \kappa (1-\nu) c_{km} + a^3 \kappa e_{km}) & (-n a_{km} + \frac{1}{2} a^2 n \kappa (3-\nu) c_{km}) & (-a_{km} - a^4 \kappa e_{km} + 2a^2 n^2 \kappa c_{km} - (n^2 - 1)^2 \kappa a_{km} - \frac{\gamma}{\rho_s h} [C_3' - C_5' + C_6' + C_7'] a_{km}) \end{bmatrix} \begin{bmatrix} A_m \\ B_m \\ C_m \end{bmatrix}$$

= (0)

(6.36)

or

$$-\omega^2 [M](q) + i\omega [C](q) + [K](q) = (0) . \quad (6.37)$$

To obtain a solution, let

$$\{y\} = \{q\}e^{i\omega t};$$

then,

$$\{\dot{y}\} = i\omega\{q\}e^{i\omega t} \quad \text{and} \quad \{\ddot{y}\} = -\omega^2\{q\}e^{i\omega t}.$$

Substituting the above into (6.37) gives

$$[M]\{\ddot{y}\} + [C]\{\dot{y}\} + [K]\{y\} = \{0\}. \quad (6.38)$$

Defining the square partitioned matrices and partitioned vector as

$$[A] = \begin{bmatrix} [0] & [M] \\ [M] & [C] \end{bmatrix}, \quad [B] = \begin{bmatrix} -[M] & [0] \\ [0] & [K] \end{bmatrix} \quad \text{and} \quad \{z\} = \begin{Bmatrix} \{\dot{y}\} \\ \{y\} \end{Bmatrix},$$

equation (6.38) may then be written as

$$[A]\{\dot{z}\} + [B]\{z\} = \{0\}. \quad (6.39)$$

To solve this equation, let

$$\{z\} = \{z_0\}e^{\lambda t}, \quad (6.40)$$

where

$$\lambda = i\omega.$$

Applying now equation (6.40) into (6.39) yields

$$\lambda [A]\{z_0\} + [B]\{z_0\} = \{0\} ,$$

or

$$- [B]\{z_0\} = \lambda [A]\{z_0\} ,$$

which is of a standard eigenvalue form and may be solved numerically.

Perhaps it should be mentioned that the specific expressions shown above pertain to the case of ovaling with an antinode facing the free stream. The present theory may easily be modified, however, as outlined in Appendix F, to obtain equivalent expressions for the case of a node facing the free stream.

A listing of the computer programs to perform the foregoing numerical calculations is given in Appendix G.

## 6.7 Theoretical Results

The following results are computed with the series of equations (6.17) truncated at  $m=1$  ( $M=1$ )<sup>†</sup> and the parameters (as listed in Table 6.1) used in the computations are close to those corresponding to the experiments<sup>§</sup>.

Since a number of modifications have been introduced in this theory, *vis-à-vis* its original form [10,12], the effect of each new term on the stability of the system will be studied.

---

<sup>†</sup>It has been verified [12] that there is little loss in accuracy by truncating the series at  $M=1$ , i.e., a much simplified (uncoupled) solution.

<sup>§</sup>There are small variations in parameters for the various shells used in the experiments.

Case 0: original analysis [10,12] with no modification

Figures 6.4 and 6.5 show the results of the  $n=2$  and  $n=3$  modes of ovaling, vibrating, respectively, with an antinode and a node facing the free stream. For convenience, an instability threshold zone is also defined and plotted on the same graph; it is based on the measured (Chapter 3) natural frequency,  $\text{Re}(f)$ , and logarithmic decrement,  $\delta$ , of shells A and B, and may be related to  $\text{Im}(f)$  as

$$\text{Im}(f) = \frac{1}{2\pi} \delta \text{Re}(f) ,$$

where  $\text{Re}(f)$  and  $\text{Im}(f)$  are, respectively, the real and imaginary parts of the complex frequency.

As internal dissipation (material damping) has not been included in the theoretical model, the eigenfrequencies of the shell are wholly real at  $U = 0$ . For  $U > 0$ , the eigenfrequencies become complex. It is seen that second-mode oscillation is associated with negative aerodynamic damping, i.e.  $\text{Im}(f) < 0$  - if a node faces the free stream. On the other hand, when an antinode faces the free stream, the motion is aerodynamically positively damped. The opposite is true for the  $n=3$  mode ovaling.

With increasing flow velocity, the vibration frequencies, i.e.  $\text{Re}(f)$ , remain almost constant, indicating little effect from the "aerodynamic stiffness" terms. The system would eventually become unstable, at sufficiently high flow velocity, when the negative aerodynamic damping exceeds the positive dissipative modal damping of the shell (i.e. the computed  $\text{Im}(f)$  for certain  $U$  crosses the instability threshold zone).

As was stated at the outset, the original theory provides poor quantitative agreement with experimental data. In its original form, the theory predicts the threshold flow velocities of second and third mode<sup>†</sup> of ovaling at  $U$  that are very much greater than 28 m/s, whereas the experimental threshold flow velocities for the  $n=2$  and  $n=3$  modes of ovaling are approximately 21.5 m/s and 23.5 m/s, respectively (see Table 4.1).

Case 1: Effect of moving boundary condition in unsteady Bernoulli equation

The non-stationary fluid-solid boundary condition at the shell surface will give rise to an additional term,  $(\underline{v} + \underline{\omega} \times \underline{r}) \cdot \underline{\nabla} \Phi$ , in equation (6.10). As shown in Figures 6.6 and 6.7, the addition of this term, slightly increases aerodynamic damping, as compared with Case 0 - more for the  $n=2$  mode of vibration. However, agreement is only slightly improved by this refinement to the theory.

Case 2: Effect of imposing a coherent reverse flow in the wake region

As explained in Section 6.4, a quasi-coherent reverse flow is imposed on the shell surface in the wake region, so as to obtain a correct mean pressure in the wake. The complex frequencies  $f_{2,1}$  and  $f_{3,1}$  for an antinode and a node facing the free stream are plotted in Figures 6.8 and 6.9. Comparing with Case 0 (Figures 6.4 and 6.5), it may be seen that

---

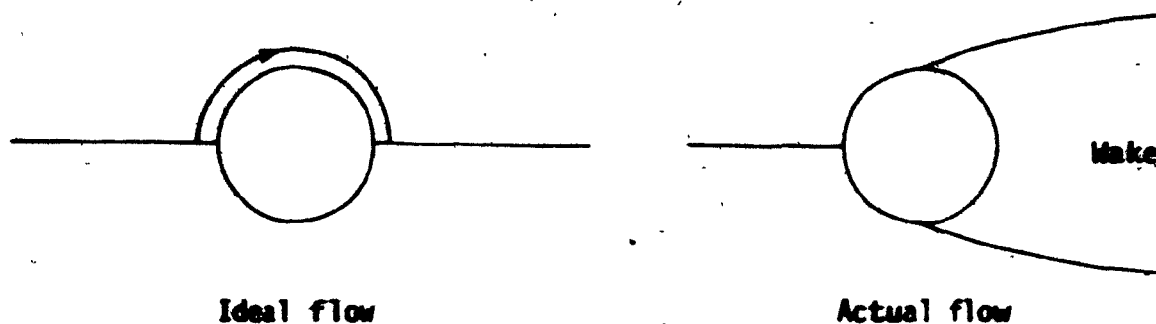
<sup>†</sup>If, for these flow velocities, the negative aerodynamic damping were in the experimental instability zone, then perfect agreement with theory would have been obtained.

the aerodynamic damping of the  $n=3$  mode is more than tripled; on the other hand, the aerodynamic damping of the  $n=2$  mode has marginally been decreased.

Case 3: Effect of applying the boundary condition at  $r = a+w^*$

As shown in equation (6.11), additional terms  $\frac{Uf(\theta)}{a} (\partial^2 \phi_0 / \partial r^2 \partial \theta) \Big|_{r=a} w^*$  and  $\frac{Uf(\theta)}{a^2} (\partial \phi_0 / \partial \theta) \Big|_{r=a} w^*$ , arise from applying the boundary condition at  $r = a+w^*$ , in the derivation of the pressure expression. There is also an extra term,  $(\partial^2 \phi_0 / \partial r^2) \Big|_{r=a} w^*$  (in equation (6.12)), in relating the perturbation potential to shell displacement.

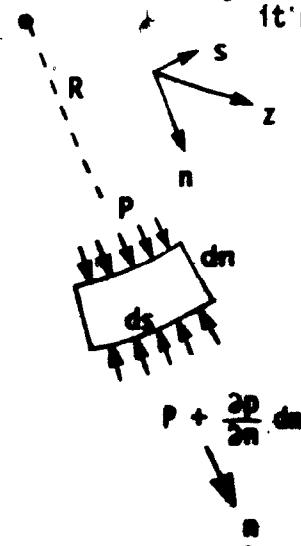
Complex frequency plots of  $f_{2,1}$  and  $f_{3,1}$  with an antinode and a node facing the free stream, with  $\phi_0$  approximated by a fully potential flow function (equation (6.18)), are shown in Figures 6.10 and 6.11. The effect is very strong: the originally unstable modes,  $n=2$  with a node and  $n=3$  with an antinode facing the free stream have now been stabilized. Presuming that this modification to the theory is indeed correct, then the fault likely lies with the use of the potential function,  $\phi_0$ ; using  $\phi_0$  possibly tends to overestimate the effect of applying the boundary condition at  $r = a+w^*$ . Perhaps, this is not too surprising, if one compares the flow pattern of an inviscid ideal flow around a circular cylinder with that of the actual flow. In a real flow there is a growth of boundary layer thickness along the circumference of the cylinder and flow separation from the surface; hence, the flow ahead of separation would be more like that of a flow over an elongated bluff body, and consequently the fluid would follow a path with less curvature than that prescribed by an ideal flow. The greater the curvature of the



fluid flow, the greater will be the pressure gradient<sup>†</sup> in the normal direction of the flow, and consequently a larger velocity in the normal direction too. Thus, the idealized potential function  $\phi_0$ , would tend to overestimate the fluid flow in the normal direction. The pressure coefficient,  $C_p$ , on a circular cylinder of potential flow and that of Roshko's experimental results are compared in Figure 6.12. It is seen that the agreement between the ideal and actual flow is only good up to  $\theta = 20^\circ$ , whilst for the purposes of this analysis, it is used for up to  $\theta = \theta_s$ .

In view of the poor agreement with experiment, on the one hand, and the strength of this effect, on the other, a better representation of  $\phi_0$  must be sought. The proper and most accurate method to proceed would

<sup>†</sup>For an elementary fluid element flowing in a curvature path of radius  $R$ , it may be shown that



$$\frac{\partial p}{\partial n} = \frac{\rho U^2}{R}$$

be to actually measure the flow field in the wind tunnel by means of hot wire anemometers. However, an easier approach would be to construct the function  $\phi_0$ , using an electrical analogue method.

#### Case 4: Effect of base pressure variations due to shell deformation

The term associated with variations in base pressure induced by shell vibration may be found in Section 6.5. The measured base pressure coefficient as a function of  $(w^*/a)$  at  $\theta = 180^\circ$ , for the  $n=2$  and  $n=3$  modes of ovalling with an antinode facing the free stream, are shown respectively in Figures 6.2 and 6.3. For ovalling with a node facing the free stream, since the displacement at  $\theta = 180^\circ$  is zero, the base pressure coefficient is based on  $\theta = 175^\circ$  for the  $n=2$  mode (Figure 6.13) and  $\theta = 170^\circ$  for the  $n=3$  mode (Figure 6.14). The phase lag  $\psi$  was measured experimentally (Appendix E); it is  $40^\circ$  for the  $n=2$  mode vibrating with a node and  $270^\circ$  for the  $n=3$  mode vibrating with an antinode facing the free stream.

The results are presented in Figures 6.15 and 6.16. It may be seen that the base pressure variations play a dominant role on the stability of the system. In its present form, the threshold flow velocities for ovalling are slightly more than 28 m/s for the  $n=3$  mode (antinode facing the free stream) and 26 m/s for the  $n=2$  mode (node facing the free stream). Thus, inclusion of this effect improves agreement between theory and experiment.

#### Case 5: Combination of all the foregoing effects

Figures 6.17 and 6.18 show the combined effects of Cases 2-4 on



system stability. For vibration with an antinode facing the free stream, the  $n=2$  mode is stable, while the  $n=3$  mode becomes unstable at approximately  $U = 25$  m/s. For vibration with a node facing the free stream, the  $n=2$  mode is associated with positive aerodynamic damping at low flow velocity ( $U < 6$  m/s) and it becomes negative as  $U$  increases beyond 8 m/s; in this case, the  $n=3$  mode is stable.

As suggested in the discussion of Case 3, the approximation of  $\phi_0$  by inviscid ideal flow would overestimate the effect of applying the boundary condition at  $r = a + w^*$ . It is then of interest, to ignore this effect (Case 3) - i.e. to apply the boundary condition at  $r=a$  instead, and investigate the combination of the other effects on the improved theory.

Case 6: Combination of all the effects, but with the boundary condition applied at  $r=a$

The results are shown in Figures 6.19 and 6.20. The threshold flow velocities for the two unstable modes are approximately 19 m/s for the  $n=3$  mode and 24 m/s for the  $n=2$  mode, which are not far off the experimental threshold flow velocities of approximately 21.5 m/s for the  $n=2$  mode and 23.5 m/s for the  $n=3$  mode.

Finally, a quantitative comparison is summarized in Table 6.2, in which the negative aerodynamic damping  $-\delta_{ad}$  at the (experimental) threshold of flutter is compared to the modal damping  $\delta_{md}$ ; according to the theory, the two should be equal. It is seen that, the theoretical and experimental overlying frequencies are reasonably close.

## CHAPTER 7

### ENERGY INPUT TO THE SHELL

#### 7.1 Preliminary Remarks

According to the experimental evidence presented in Chapter 4 and Chapter 5, vortex shedding is not the cause of ovaling oscillation. Hence, an alternative physical explanation must be sought for the underlying mechanism of the above mentioned intriguing phenomenon. It has been shown analytically that the cylindrical shell may become unstable due to the negative aerodynamic damping (arising from interaction of shell motion and the mean flow) exceeding the mechanical damping. So, a plausible mechanism for ovaling oscillation may be an aeroelastic oscillatory type of instability, where the oscillation is initiated and sustained by aerodynamic forces induced by the elastic shell itself. Consequently, if at a certain wind speed, the mode and frequency of oscillation of the system are such that energy can be absorbed from the free stream by the cylindrical shell, and if the energy absorbed is larger than that dissipated by structural damping, the amplitude of vibration will increase and the system will become unstable. This, indeed, has been the underlying philosophy of the original theoretical model of references [10,12], which has been refined in Chapter 6. However, in what follows, a more direct approach will be taken to assess the energy balance, and thus define the threshold of instability.

Ideally, the dynamic pressure around the shell vibrating in  $n^{\text{th}}$  circumferential mode should be measured and the work done by the aerodynamic

forces then computed for one complete cycle of oscillation. If this work done is positive, then there will eventually be an instability.

However, it is an extremely difficult, if not impossible, task to obtain the fluctuating pressure on a vibrating thin cylindrical shell without causing some change to the shell mode shape. Thus, before initiating an extensive program to measure these dynamic pressures, a preliminary set of experiments was done to investigate the feasibility of such measurements. A commercially available miniature piezoresistive pressure transducer (Endevco, model 8515) was selected for making these measurements. This transducer is of a flat-pack design with dimensions of 0.500" x 0.200" x 0.035" (12.7 mm x 5.10 mm x 0.90 mm) and weighs only 0.3 g. It was selected because of its small size and weight and also because it may be flush-mounted on the shell surface. However, before purchasing the transducer, a piece of metal with the same dimensions and weight was bonded onto the shell surface, and wires attached as would be the case for the real pressure transducer. The shell was then tested dynamically in the wind tunnel. Although the ovaling frequencies and the critical flow velocities at which the shell became unstable remain approximately the same as for a shell without the "simulated" transducer, the observed ovaling mode shape was severely distorted by its presence. As a result of these preliminary tests, it was decided to postpone the dynamic pressure measurements until a better technique could be found.

An alternative but not so elegant method for the energy calculations is to undertake quasi-static measurements. In doing this, it is implicitly assumed that the aerodynamic characteristics of the shell at different stationary deformations, in the correct mode of ovaling (with a particular

fixed orientation with respect to the on-coming flow), are equal, at any instant of time, to the actual instantaneous values of a shell vibrating harmonically, taking correct account of the resultant velocity vector. Thus, the need to measure the dynamic pressures is removed.

## 7.2 The Energy Expression

Consider a small element of length  $\delta s$  along the circumference of the shell, subtending an angle  $\delta\theta$  at the center. For small amplitude vibration,  $w^* \ll a$ , one may write

$$\delta s = (a + w^*)\delta\theta, \quad (7.1)$$

where  $a$  is the shell radius, and  $w^*$  is the radial displacement of the middle surface of the shell, positive in the outward direction.

The instantaneous pressure force per unit length,  $F$ , acting on the element at any instant of time may then be approximated by

$$F = [p_i(\theta, t) - p_e(\theta, t)](a + w^*)\delta\theta e^{-i\psi}, \quad (7.2)$$

where  $p_i(\theta, t)$  and  $p_e(\theta, t)$  are, respectively, the internal and external pressures acting on the shell, and  $\psi$  is the phase lag of the induced pressure ( $p_i - p_e$ ) to shell deformation. In general the angle  $\psi$  depends on the non-dimensional ("reduced") ovalling frequency,  $f_0 d/U$ , and the Reynolds number; here,  $\psi$  will be approximated more simply in the manner discussed in Appendix E.

The total energy, per unit length, transferred to the shell during a cycle of oscillation is given by

$$\begin{aligned}
 W &= \int F \, d\mathbf{r}^* \\
 &= \int_0^{2\pi/\omega_0} \int_0^{2\pi} \operatorname{Re}[F] \operatorname{Re}\left[\frac{\partial \mathbf{r}^*}{\partial t}\right] d\theta \, dt \\
 &= \int_0^{2\pi/\omega_0} \int_0^{2\pi} \operatorname{Re}[(p_i - p_e)(a + i\omega^*)e^{-i\psi}] \operatorname{Re}\left[\frac{\partial \mathbf{r}^*}{\partial t}\right] d\theta \, dt, \quad (7.3)
 \end{aligned}$$

where the physical quantities are represented by the real parts of the complex numbers.

In order to pinpoint the critical flow velocity for the onset of instability, the (positive) energy dissipated by the shell has to be calculated. The system will then become unstable if the energy absorbed from the free stream is larger than that dissipated by structural damping.

Since the experiments are conducted in air, it is reasonable to assume that external (fluid) damping is insignificant compared with internal (modal) damping. Thus, to estimate the dissipation energy, a hysteretic damping model is assumed, with the damping force (per unit length) give by

$$F_d = \frac{b}{\omega_0} \frac{\partial \mathbf{r}^*}{\partial t}. \quad (7.4)$$

where  $b$  is the hysteretic damping coefficient, and  $\omega_0$  is the ovaling

frequency in rad/S.

For harmonic motion, the hysteretic damping coefficient may conveniently be modelled by an *equivalent viscoelastic damping coefficient* [30] which results in the same energy being dissipated per cycle; the relation is

$$C_{eq} = \frac{b}{\omega_0}, \quad (7.5)$$

and consequently the damping force may be rewritten as

$$\begin{aligned} F_d &= C_{eq} \frac{\partial w}{\partial t} \\ &= 2 m \xi \omega_0 \frac{\partial w}{\partial t}, \end{aligned} \quad (7.6)$$

where  $m$  is the modal mass per unit length, and  $\xi$  is the non-dimensional damping ratio.

For a lightly damped system, the logarithmic decrement,  $\delta$ , may be related to  $\xi$  as

$$\delta = 2\pi\xi;$$

substituting into equation (7.6) yields

$$F_d = m \frac{\delta}{\pi} \omega_0 \frac{\partial w}{\partial t}. \quad (7.7)$$

Ignoring the added (virtual) mass of the fluid, the energy per unit length dissipated per cycle may be written as

$$\begin{aligned}
 W_d &= \int \operatorname{Re}[F_d] \operatorname{Re}[dw^*] \\
 &= \int_0^{2\pi/\omega_0} \int_0^{2\pi} \operatorname{Re}[\rho_s a h \frac{\delta}{\pi} \omega_0 \frac{\partial w^*}{\partial t}] \operatorname{Re}[\frac{\partial w^*}{\partial t}] d\theta dt, \quad (7.8)
 \end{aligned}$$

where  $\rho_s$ ,  $a$  and  $h$  are defined in the nomenclature.

### 7.3 Static Pressure Measurements

Special experiments were conducted, the purpose of which was to measure the static pressure around cylindrical models with cross-sectional shapes corresponding to shapes of a flexible shell undergoing second and third mode of ovaling, "frozen" at one instant of time. It should be noted that only "pure circumferential" modes of vibration of the shell were modelled (*i.e.* corresponding to infinitely long shells) and no attempt was made to model the axial deformation of the shell.

#### 7.3.1 Brief description of the experimental set-up

Five different models were used in the experiments. One was a circular cylinder of 76.2 mm (3.00 in.) diameter and 292.1 mm (11.50 in.) long; this was used for reference, to compare with the results of the deformed "circular" shapes.

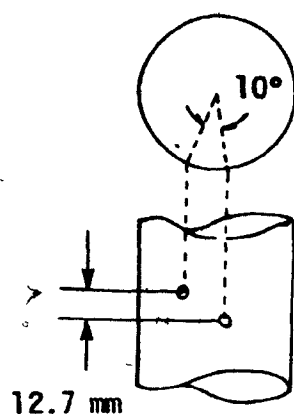
To simulate the second mode of ovaling at different instants of

time, two elliptical rigid models of different sizes were constructed. Both models represented deformed shapes of a circular cylinder of 76.2 mm (3.00 in.) diameter. The geometry or surface of the ellipse may be described by the equation  $R = \sqrt{(a^2 \times b^2) / (a^2 \sin^2 \theta + b^2 \cos^2 \theta)}$ , where  $R$  is the radius from the center;  $a$  and  $b$  are, respectively, the semi-major and semi-minor axis of the ellipse. The two test models had dimensions of  $a = 39.9$  mm (1.57 in.),  $b = 36.3$  mm (1.43 in.) and  $a = 41.2$  mm (1.62 in.),  $b = 35.1$  mm (1.38 in.); the deformation of these mode shapes from the equilibrium (round) form is as shown in Figure 7.1 - which corresponds to a maximum "frozen" amplitude of ovaling ( $w^*$ ) of 1.80 mm (0.07 in.) for the first model and 3.10 mm (0.12 in.) for the second. To achieve high precision in the manufacture of the model, it was made by an N.C. machine in twelve identical pieces, each 25.4 mm (1.00 in.) long; then all twelve pieces were stacked to a final assembled length of 304.8 mm (12.00 in.).

For the two models representing the third mode of ovaling, the surface of the deformed cylinder (see Figure 7.2) was generated by the equation  $R = 1.46 * (1 + P \cos 3\theta) / (1 + P)$ , where the radius  $R$  is in inches and  $P$  is a parameter corresponding to the maximum radial deformation from an undeformed circular cylinder. One model had the dimensions corresponding to  $P = 0.075$  (with a maximum  $w^*$  of 2.54 mm (0.10 in.)) and an undeformed circular cylinder of diameter 69.1 mm (2.72 in.), while the other corresponded to  $P = 0.100$  (with a maximum  $w^*$  of 3.30 mm (0.13 in.)) and an equivalent undeformed circle of diameter 67.6 mm (2.66 in.). This time the model was constructed from twenty-three identical pieces of 12.7 mm (0.50 in.) long, and these were then stacked to a final assembled length of 292.1 mm (11.50 in.).



All four models were equipped with 19 pressure taps, spiralling equally at 10 degree intervals around one half of the circumference and



12.7 mm (0.50 in.) apart, in the axial direction. Precautions were taken to ensure that the pressure taps were perpendicular to the outer surface of the model, such that static pressure of the flow field around the model would be correctly measured. This was one of the reasons for positioning the pressure taps spirally along the length of the model.

The test rig was mounted between two "boundary-layer guards" in the wind tunnel test section, as shown diagrammatically in Figure 7.3. These end plates serve two purposes: (i) their main function is to ensure that the boundary layers at the base and top of the model are thin (much thinner than the wind-tunnel wall boundary layers), hence eliminating the effects of boundary layer thickness on the base pressure [24]; (ii) because of the short length of the test model, the plates also serve to render the flow over the model and in the wake more nearly two dimensional. The plate design was based on the optimum (most effective) plate size suggested by Stansby [24]. Positioned between the plates and the tunnel

walls were cylinders of 76.2 mm (3.00 in.) diameter to provide nearly equal blockage for the flow throughout the working section.

The pressure distribution around the model was measured at  $Re = 3.80 \times 10^4$ <sup>†</sup> ( $U = 7.5$  m/s) and  $Re = 1.18 \times 10^5$  ( $U = 23.5$  m/s)<sup>‡</sup>. The second of these velocities corresponds, very closely, to the velocity at which a typical shell becomes unstable. However, by measuring the pressure distribution at the lower velocity, the effect of Reynolds number could be checked.

### 7.3.2 Pressure coefficient of various models

The effectiveness of the boundary layer guards was verified first; this is discussed in Appendix H. Next, the results obtained in the experiments will be presented and discussed.

In Figure 7.4 are shown the quasi-static pressures around the circumference, in terms of pressure coefficients, for the second mode shape, orientated in such a way as to yield information for ovaling with an antinode facing the free stream. The pressure coefficients around a circular cylinder are also plotted on the same graph for reference. The pressure distributions around the same models at a higher  $Re$  are shown in Figure 7.5.

Figures 7.6 and 7.7 show  $C_p$  vs  $\theta$  for the more highly deformed n<sub>2</sub> mode model, at  $U = 7.5$  m/s and  $U = 23.5$  m/s, respectively. Finally, in order to appreciate the effect of mode-shape deformation (static

<sup>†</sup> Under ambient conditions in the wind tunnel, wind speed  $U$  may be converted to  $Re$  as  $Re = 5.04 \times 10^3 \times U$ .

<sup>‡</sup> The higher flow speed of 23.5 m/s ( $Re = 1.18 \times 10^5$ ) may lie in the transition range of Reynolds number. The sub-critical range of Reynolds number is normally between 300 and  $2 \times 10^5$ .

"amplitude") on the pressure distribution, the data of Figures 7.4-7.7 are replotted in Figures 7.8 and 7.9 for  $U = 7.5$  m/s and  $U = 23.5$  m/s, respectively.

It is interesting to compare the data of the present study with the experiments of Modi [31], which involve two elliptical models of eccentricity  $e \equiv \sqrt{1 - (b^2/a^2)}$  = 0.60 and 0.80 - as compared to the present experiments, where  $e = 0.42$  and  $0.52$ . The results for  $\alpha = 0^\circ$  are plotted in Figure 7.10, where  $\alpha$  is the angle between the major axis and the free stream. It is seen that, in general, the base pressure increases as  $e$  increases. The peculiar behaviour of the measured  $C_p$ , from  $\theta = 60^\circ$  to  $100^\circ$  at the higher Reynolds number in the present study (see Figure 7.11) may be a direct result of the Reynolds number approaching the critical regime.

Figures 7.12 and 7.13 compare the  $C_p$  of the present study at  $U = 7.5$  m/s ( $Re = 3.80 \times 10^4$ ) and  $U = 23.5$  m/s ( $Re = 1.18 \times 10^5$ ) for  $\alpha = 90^\circ$  with those of Modi's. Unlike the case of  $\alpha = 0^\circ$ , the base pressure here decreases as  $e$  increases.

The pressure distributions around the test models with  $\theta = 45^\circ$  are shown in Figures 7.14-7.17. These orientations would give information useful for ovaling with a nose facing the free stream. At the lower  $Re$ , it may be seen (Figures 7.14 and 7.16) that the  $C_p$  curve for the inclined elliptical cylinders resembles that of a circular cylinder, whereas, at higher  $Re$  (Figures 7.15 and 7.17), the  $C_p$  in the wake of the circular cylinder is lower than that of the elliptical models.

Finally, to demonstrate more fully the effects of the "deformation amplitude" and  $Re$  on the pressure distributions, the data of Figures 7.14-7.17 are replotted in Figure 7.18.

The same set of measurements as described above were repeated for the  $n=3$  mode models. In Figures 7.19-7.22 the static pressure distributions around the two different  $n=3$  mode models with an antinode facing the wind, at two different  $Re$ , are presented and compared with the pressure distribution around a circular cylinder. It may be seen that when the "nose" of the deformed cylinder (antinode) is facing the free stream, the  $C_p$  is slightly higher than that of a circular cylinder in the wake region. The reverse trend is observed when the model was rotated by  $180^\circ$  so that the flat portion of the surface faces the wind.

The data of Figures 7.19-7.22 are replotted in Figures 7.23 and 7.24 to more fully demonstrate the effect of deformation on the pressure distribution, at  $Re = 3.80 \times 10^4$  ( $U = 7.5$  m/s) and  $Re = 1.18 \times 10^5$  ( $U = 23.5$  m/s), respectively.

The quasi-static pressure distributions for the  $n=3$  mode models with a node facing the wind (*i.e.* with the "nose" of the model tilted at  $30^\circ$  with respect to the on-coming flow) are plotted in Figures 7.25-7.28.

Again, to see more clearly the effects of deformation and  $Re$  on  $C_p$ , the data of Figures 7.25-7.28 are replotted in Figure 7.29.

#### 7.4 Computation of Work Done by the Fluid Flow

The expression for the energy flux per unit length, from the flow field to the shell, as given by equation (7.3), has the form

$$W = \int_0^{2\pi/\omega_0} \int_0^{2\pi} \text{Re}[(p_i - p_e)(a + w^*)e^{-i\psi}] \text{Re}\left[\frac{\partial w^*}{\partial t}\right] d\theta dt. \quad (7.3)$$

Assuming that the pressure fluctuation inside the shell is negligible and is approximately equal to  $p_{atm}$ , the atmospheric pressure, which may be further approximated by  $p_0^+$ , the front stagnation pressure, then

$$\begin{aligned}
 p_i(\theta, t) - p_e(\theta, t) &= p_i(\theta, \frac{w^*}{a}) - p_e(\theta, \frac{w^*}{a}) \\
 &= p_{atm} - p_e(\theta, \frac{w^*}{a}) \\
 &= p_0 - p_e(\theta, \frac{w^*}{a}) \\
 &= (p_0 - p_\infty) - (p_e(\theta, \frac{w^*}{a}) - p_\infty) \\
 &= \frac{1}{2}\rho U^2 (1 - C_p(\theta, \frac{w^*}{a})) , \quad (7.9)
 \end{aligned}$$

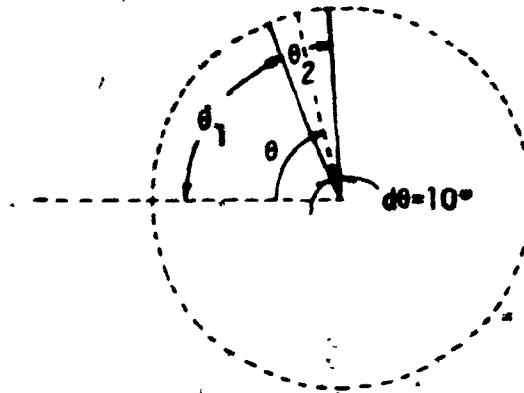
where  $(p_0 - p_\infty)/\frac{1}{2}\rho U^2 = 1$ , and  $C_p(\theta, \frac{w^*}{a})$  is the static pressure coefficient, measured experimentally as described in Section 7.3.

Ideally, with  $p_i - p_e$  expressed as a function of  $\theta$  and  $w^*/a$  and  $\psi$  as a function of  $\theta$ , the energy input into the system in one cycle of oscillation may, thence, be obtained by integrating equation (7.3).

However, as a first approximation,  $p_i - p_e$  will only be expressed as a function of  $w^*/a$  at each angular position,  $\theta$ , and the energy for a small segment  $(a + w^*)d\theta$  then computed. Within each segment, all the parameters are assumed to be constant. The total energy will then be the

---

<sup>†</sup>This is applicable for a suction type wind tunnel. It is found experimentally that there is an average of 6% difference between  $p_{atm}$  and  $p_0$ . The difference arises from a drop in pressure as the air passes through the screens.



sum of all the energy values calculated for the individual segments.

As already mentioned in the previous Chapter, the measured  $C_p$  may be approximated by a first-order polynomial as

$$C_p = H \frac{w^*}{a} + H_0,$$

and thence

$$p_i - p_e = \frac{1}{2} \rho U^2 (1 - H \frac{w^*}{a} - H_0). \quad (7.10)$$

For a shell (of infinite length) performing ovaling oscillations with an antinode facing the flow velocity vector,  $w^*$  may be expanded in the series form

$$\begin{aligned} w^* &= e^{i\omega_0 t} \sum_{\ell=0}^{\infty} B_{\ell} \cos^2(2\ell+1)n\theta \\ &= e^{i\omega_0 t} B_0 \cos n\theta, \end{aligned} \quad (7.11)$$

where it had been determined that the modal shapes are adequately described by the leading term in the above series [11].

Now, substitution of (7.10) and (7.11) into (7.3) yields the energy expression for a small segment subtending an angle  $\theta_2 - \theta_1$ , at the center, i.e. at  $\theta = (\theta_1 + \theta_2)/2$ . Thus, the energy expression becomes

$$\begin{aligned}
 W_{\theta_2 - \theta_1} &= \int_0^{2\pi/\omega_0} \int_{\theta_1}^{\theta_2} \operatorname{Re} \left[ \frac{1}{2} \rho U^2 \left( 1 - H \frac{w^*}{a} - H_0 \right) (a + w^*) e^{-i\psi} \right] \operatorname{Re} \left[ \frac{\partial w^*}{\partial t} \right] d\theta dt \\
 &= \frac{1}{2} \rho U^2 \int_0^{2\pi/\omega_0} \int_{\theta_1}^{\theta_2} \operatorname{Re} \left\{ \left[ (1 - H_0) a - H \frac{w^*{}^2}{a} + (1 - H - H_0) w^* \right] e^{-i\psi} \right\} \operatorname{Re} \left[ \frac{\partial w^*}{\partial t} \right] d\theta dt \\
 &= \frac{1}{2} \rho U^2 \int_0^{2\pi/\omega_0} \int_{\theta_1}^{\theta_2} \left[ (1 - H_0) a \cos \psi - \frac{H}{a} B_0^2 \cos^2 n\theta \cos(2\omega_0 t - \psi) \right. \\
 &\quad \left. + (1 - H - H_0) B_0 \cos n\theta \cos(\omega_0 t - \psi) \right] * \\
 &\quad [-\omega_0 B_0 \cos n\theta \sin \omega_0 t] d\theta dt \\
 &= -\frac{1}{4} B_0^2 (1 - H - H_0) \rho U^2 \pi \sin \psi [(\theta_2 - \theta_1) + \frac{1}{2n} (\sin 2n\theta_2 - \sin 2n\theta_1)] ,
 \end{aligned}$$

(7.12)

where the properties of all the parameters will be evaluated at  $\theta$ .

Proceeding in an analogous manner, the equivalent expressions for oscillations with a node facing the free stream are given by

$$w^* = e^{i\omega_0 t} B_0 \sin n\theta, \quad (7.13)$$

$$W_{\theta_2-\theta_1} = -\frac{1}{2} B_0^2 (1-H-H_0) \rho U^2 \pi \sin \psi \left[ (\theta_2 - \theta_1) - \frac{1}{2n} (\sin 2n\theta_2 - \sin 2n\theta_1) \right]. \quad (7.14)$$

## 7.5 Results

Since experimental evidence suggests that the  $n=2$  and  $n=3$  circumferential modes occur with a node and an antinode, respectively, facing the free stream; and since the phase measured in the wake region also pertains to these same orientations, the work done by the fluid for only these cases will be calculated.

The following calculations were based on the measured quasi-static  $C_p$  at  $Re = 3.8 \times 10^4$  ( $U = 7.5$  m/s)<sup>†</sup>. Typical results of  $C_p$  as a function of  $(w^*/a)$  may be found in Figures 6.2 and 6.3. The phase lag  $\psi$  (Appendix E) and the coefficients of the first degree polynomial ( $C_p = Hw^*/a + H_0$ ) are tabulated, in intervals of  $10^\circ$  from  $\theta = 5^\circ$  to  $175^\circ$ , in Tables 7.1 and 7.2, for the  $n=2$  and  $n=3$  modes of ovaling, respectively.

The energy extracted from the free stream for the two different modes of oscillation, as a function of flow velocity, is presented in Figures 7.30 and 7.31.

As was stated at the outset (*vide* Section 7.2), the system will become unstable if the energy absorbed from the free stream is larger than dissipated by structural damping. Using equation (7.8), the (positive)

---

<sup>†</sup> As shown in Section 7.3, the measurements at the higher Reynolds number,  $Re = 1.18 \times 10^5$  ( $U = 23.5$  m/s), seem to be unreliable.



energy dissipated by the shell (per unit length) is given by

$$W_d = \int_0^{2\pi/\omega_0} \int_0^{2\pi} \operatorname{Re}[\rho_s a h \frac{\delta}{\pi} \omega_0 \frac{\partial w^*}{\partial t}] \operatorname{Re}[\frac{\partial w^*}{\partial t}] d\theta dt, \quad (7.8)$$

$$= \rho_s a h \frac{\delta}{\pi} \omega_0 \int_0^{2\pi/\omega_0} \int_0^{2\pi} \operatorname{Re}[\frac{\partial w^*}{\partial t}] \operatorname{Re}[\frac{\partial w^*}{\partial t}] d\theta dt,$$

$$= B_0^2 \rho_s a h \delta \pi \omega_0^2. \quad (7.15)$$

Using the parameters listed in Tables 3.1 (for shells A and B) and 6.1, the following are obtained. For the  $n=2$  mode, assuming an ovalling frequency of 167 Hz,  $W_d = 3973 B_0^2$  to  $4404 B_0^2$  J/m; and for the  $n=3$  mode, with an ovalling frequency of 230 Hz,  $W_d = 7353 B_0^2$  to  $8682 B_0^2$  J/m. The uncertainty in  $W_d$  arises from the corresponding uncertainty in the measured value of  $\delta$  and differences between shells A and B.

Referring now to Figures 7.30 and 7.31, it is seen that, according to this analysis, ovalling would first develop in the second mode of the shell  $U_{thr} \approx 22.0$  m/s, followed by ovalling in the third mode at  $U_{thr} \approx 35.0$  m/s. The theoretical  $U_{thr}$  for the  $n=2$  mode is relatively close to the experimental value of 21.5 m/s. However, this theory overestimates  $U_{thr}$  for the  $n=3$  mode by a factor of 1.5 (here it must be recalled that this theoretical model is for a two-dimensional (infinite length) shell, whereas the experiments were with finite length shells).

As described in Chapter 4, the experimental observations suggest that the system will first become unstable in the second mode. At a higher

flow velocity, third-mode ovaling develops, and it is noted that, beyond this flow, third and second mode ovaling takes place concurrently. Here, an additional possible reason for the discrepancy in the value of  $U_{thr}$  for the  $n=3$  mode is that coupling between the two circumferential modes has been neglected in the present analysis - presuming that an exchange of energy may actually take place between the two different modes of ovaling.

Finally, the amount of energy transferred from the flow field into the system, ahead of flow separation and in the wake region, is compared in Tables 7.3. It is seen that more than half of the energy is fed into the system through the wake region. This finding is consistent with the experimental observations, previously made in this thesis, that the wake region plays a very important role in the development of ovaling oscillation.

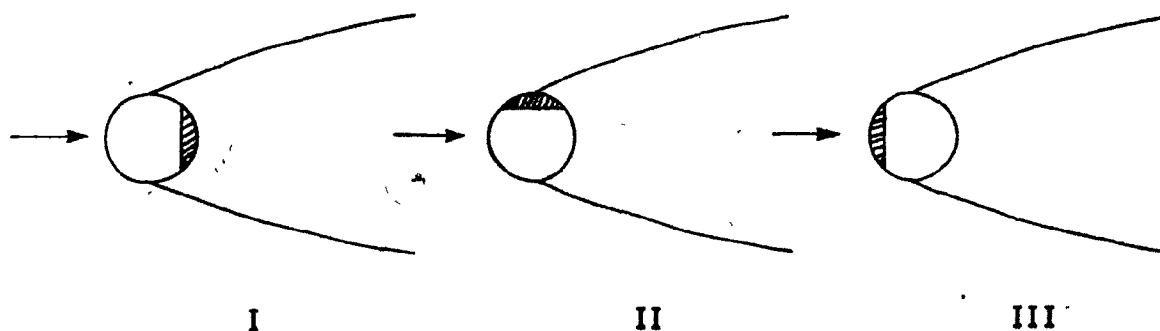
## CHAPTER 8

### DISCUSSION AND CONCLUSION

#### 8.1 On Vortex Shedding as the Excitation Mechanism for Ovaling

The experimental evidence of this work, suggests that periodic vortex shedding neither initiates nor sustains ovaling oscillation. Nevertheless, in many cases [29], the occurrence of an integral value for the ratio,  $r$ , of ovaling to vortex shedding frequency at the onset of instability remains to be explained.

Perhaps further insight into the role of vortex shedding may be gained by examining the power spectral density of the shell for the experiments with an insert. It should be noted that, despite the existence of wake periodicity, the system is stable for configuration I and unstable for both configurations II and III. The onset of instability for



configurations II and III is approximately at 27.0 m/s and 29.0 m/s, respectively. Figures 8.1 to 8.3 compare the power spectral density plots of the three configurations at flow speeds of approximately 21.5 m/s,

29.0 m/s and 37.5 m/s.

At a flow velocity *below the onset of instability* ( $U = 21.5$  m/s), the shell is seen (Figure 8.1) to respond to vortex shedding excitation. Other components of shell response are at 211 Hz and 305 Hz, and arise from buffeting excitation of the turbulent flow. The former frequency is associated with  $f_{2,1}^i$  and the latter is suspected to be  $f_{1,1}^i$  - the first beam like mode of the shell. On closer examination, the magnitude of vibration, for configurations II and III, at  $f_{2,1}^i$  is bigger than that for configuration I. This points to the importance of near-wake effects on the stability of the system.

At a flow velocity *beyond the point of instability* for configuration II, it is seen ( $U = 29.0$  m/s; Figure 8.2) that the second mode, at  $f_{2,1}^i$ , has become the dominant oscillation, and a change in scale of the ordinate should be noticed. At yet higher flow velocity ( $U = 37.5$  m/s; Figure 8.3), *beyond the point of instability* for configuration III,  $f_{2,1}^i$  is the dominant frequency of oscillation for both configuration II and configuration III - whereas for configuration I, the shell remains stable, mainly responding to vortex shedding excitation.

It is then interesting to study the behaviour of the shell in configuration I, at a yet higher flow velocity, where the ratio  $r$  is close to 2. Figure 8.4 shows the shell response at  $U = 41.4$  m/s, 45.6 m/s and 48.2 m/s for which  $r = 2.2$ , 2.0 and 1.9, respectively. It is seen that even though the periodic force from vortex shedding is capable of exciting the shell at twice the vortex shedding frequency, the system remains stable<sup>†</sup>.

<sup>†</sup> When the system becomes unstable, the ovalling frequency, as recorded on the PSD diagram, is well defined by a sharp and narrow peak, as shown in Figures 8.2 and 8.3.

The inability of periodic vortex shedding to act as a source of excitation is further supported by a study of a clamped-clamped shell without an insert at high wind speed. Owing to a restriction in the range of tunnel wind speed, the ratio  $r$  for only the second mode of ovaling will be studied ( $f_{2,1} \approx 171$  Hz,  $f_{vs} \approx SU/D$  with  $S \approx 0.18$ ).

The shell behaviour at  $U = 32.0$  m/s,  $36.9$  m/s and  $38.7$  m/s, corresponding to  $r \approx 2.5$ ,  $2.1$  and  $2.0$  are given in Figure 8.5. Figure 8.6 gives the shell response, at yet higher flow velocity of  $U = 40.5$  m/s,  $41.9$  m/s and  $43.4$  m/s which corresponds to  $r \approx 1.9$ ,  $1.8$  and  $1.8$ , respectively. It may be seen that the magnitude of vibration for the  $n=2$  mode, does not increase even when the ovaling frequency is twice the vortex shedding frequency, *i.e.*, at  $r \approx 2.0$ . As a matter of fact, the vibration magnitude decreases somewhat at the higher flow velocity.

The above findings then seem to favour the second hypothesis proposed by Paidoussis [29]. If at  $U = U_{cr}$  the value of  $r$  that would pertain "naturally" at the onset of ovaling is close to an integral value, then the onset of ovaling may organize the wake and control periodicity sub-harmonically so as to impose  $r = \text{integer}$ .

## 8.2 In Search of a New Cause

Having disproved periodic vortex shedding as the underlying mechanism of ovaling oscillation, clearly another plausible mechanism, the true cause of ovaling, must be found.

The weight of evidence collected from this work, as well as evidence reported in reference [6], clearly demonstrates the importance of wake flow

in the occurrence of ovaling. Based on this, a hypothesis will be proposed to explain this intriguing phenomenon.

The main-stream turbulence would excite initial small amplitude vibration of the shell. When the flow velocity increases, the cavity (separation bubble), originally closed, opens up and instantaneous "alleyways" [32] of fluid are formed which penetrate the cavity. The stability of the system would then depend mainly on the interaction of shell motion and the reverse flow in the alleyways. Hence, if a certain mode and frequency of oscillation of the shell are such that energy can be extracted from the wake flow, and if this absorbed energy is larger than that dissipated by structural damping, the amplitude of vibration will increase and the system then become unstable. Obviously, however, this interaction is complex; e.g., the work of Chapter 6 clearly indicates the importance of phase lag between wake flow and pressure, on the one hand, and shell vibration, on the other.

### 8.3 Conclusion

A number of experiments were conducted, with clamped-clamped shells in different experimental set-ups. The new technique of using acoustic excitation in resonance testing (to determine natural frequencies and modal damping) proved to be very successful for shell-type structures of low modal damping. The characteristics of the shells in cross flow were found to be very similar to those reported previously, that is the cylinder undergoes ovaling oscillation at, or close to, one of its natural frequencies. The second and third modes of ovaling occur, respectively, with a node

and an antinode facing the free stream vector. At the onset of ovaling, the ratio  $r = f_o/f_{vs}$  is approximately equal to 3.4-3.5 for the  $n=2$  mode; and 4.0-4.3 for the  $n=3$  mode.

The experiments to investigate systematically wake periodicity behind a rigid cylinder, with or without a splitter plate, shows that, even with a small gap between the cylinder and the splitter plate, no periodic vortex shedding exists in the domain of investigation.

Finally, the experiments on a cylindrical shell with an insert and an insert-less shell with a "wake-eliminator" demonstrate the importance of the wake flow on the stability of the system.

A refined theory has been developed to model the aeroelastic instability of a clamped-clamped cylindrical shell in cross flow. The theory takes into account the non-stationary boundary condition of a vibrating shell, and within the wake, a constant reverse flow velocity is imposed such as to obtain a constant mean base pressure; further, it is also assumed that there is a variation of base pressure associated with shell deformation.

As discussed in Chapter 6 (Case 3), the major weakness of the theoretical model is associated with the utilization of the function  $\phi_o$ , which assumes an idealized potential flow in the forward part of the cylinder (in order to calculate some of the terms in the analysis). This tends to exaggerate the effect of the changes in radial velocity caused by shell vibration on the stability of the system. In view of the importance of this effect, a new function  $\phi_o$  must be obtained, either by an electrical-analogue or by actually measuring the flow field experimentally.

Ignoring the undesirable effect mentioned above (as was done in

Case 6 of Chapter 6), the theory provides good qualitative and quantitative agreement with experiment. It predicts flutter in the  $n=2$  (even) and  $n=3$  (odd) modes occurring with a node and an antinode, respectively, facing the free stream, except that the sequence in which ovaling occurs is reversed in comparison with experimental observations. The theory (Cases 2 and 4 of Chapter 6) also indicates the importance of the wake region in determining the stability of the system, which is consistent with the experimental findings.

In view of the above findings, it is perhaps worthwhile to venture into a full-scale study of the near wake flow of a circular cylinder. In order to fully understand and model the recirculating flow, some comprehensive flow visualization experiments should be undertaken. Ideally, the surface pressure distribution on an oscillating thin shell should also be measured. The above-mentioned experiments would be rather difficult to perform. However, if an attempt is made, the theory may be further refined with the new experimental findings.

Finally, it has been demonstrated (for certain orientations of the ovaling oscillations) that the system is capable of extracting energy from the flow field (Chapter 7). The thresholds of instability are reasonably well predicted by the energy method. Even though the expressions for this analysis are rather simple, the calculations have to be supplemented by experimental data. Firstly, the quasi-static pressure distributions for ovaling oscillations have to be measured. Secondly, the phase relation between the induced pressure and shell displacement has to be calculated and measured, respectively, ahead of flow separation and in the wake region. Although, gathering this information has been rather



labourious and tedious, the interesting results obtained have made the effort worthwhile.

# REFERENCES

1. W.L. Dickey and G.B. Woodruff (1956), The vibration of steel stacks, *Trans. ASCE*, 121, pp 1054-1070.
2. E.A. Dockstader, W.F. Swiger and E. Ireland (1956), Resonant vibration of steel stacks, *Trans ASCE*, 121, pp 1088-1112.
3. D.J. Johns and R.J. Allwood (1968), Wind induced ovaling oscillations of circular cylindrical shell structure such as chimneys, *Symposium on Wind Effects on Buildings and Structures*, Loughborough University of Technology, paper No. 28.
4. C.B. Sharma and D.J. Johns (1970), Wind-induced oscillations of circular cylindrical shells: an experimental investigation, *Loughborough University of Technology*, Report TT 7001.
5. D.J. Johns and C.B. Sharma (1974), On the mechanism of wind excited ovaling vibrations of thin circular cylindrical shells, in *Flow-Induced Structural Vibrations*, ed. E. Naudascher; Berlin: Springer-Verlag, pp 650-662.
6. M.P. Paidoussis and C. Helleur (1979), On ovaling oscillations of cylindrical shells in cross-flow, *J. of Sound and Vibration*, 63, pp 527-542.
7. A. Roshko (1955), On the wake and drag of bluff bodies, *J. Aero. Sciences*, 22, pp 124-132.
8. K.M. Aaron (1979), Cross-flow induced breathing oscillations of clamped/free thin cylindrical shells, B.Eng. (Hons) Thesis, Department of Mechanical Engineering, McGill University.
9. D.T.-M. Wong (1980), Flutter of thin shells in cross flow, M.Eng. Thesis, Department of Mechanical Engineering, McGill University.
10. H.-C. Suen (1980), Ovaling vibration of cylindrical shells in cross flow, M.Eng. Thesis, Department of Mechanical Engineering, McGill University.
11. M.P. Paidoussis and D.T.-M. Wong (1982), Flutter of thin cylindrical shells in cross flow, *J. of Fluid Mechanics*, 115, pp 411-426.

12. M.P. Paidoussis, S.J. Price and H.-C. Suen (1982), An analytical model for ovaling oscillation of clamped-clamped cylindrical shells in cross flow, *J. of Sound and Vibration*, 83, pp 555-572.
13. R. King, M.J. Prosser and D.J. Johns (1973), On vortex excitation of model piles in water, *J. of Sound and Vibration*, 29, pp 169-188.
14. S.-Y. Ang (1981), Ovaling oscillation of a clamped-clamped shell in cross flow, B.Eng. (Hons) Thesis, Department of Mechanical Engineering, McGill University.
15. I. Wygnanski and B.G. Newman (1961), General description and calibration of the McGill 3 ft. x 2 ft. low speed wind tunnel, Mechanical Engineering Research Lab., Aero. Section, Report Ae 4, McGill University.
16. E.C. Maskell (1965), A theory of the blockage effects on bluff bodies and stalled wings in a closed wind tunnel, *Aero. Research Council*, R. and M. 3400, London. H.M.S.O.
17. R.E.D. Bishop and G.M. Gladwell (1963), An investigation into the theory of resonance testing, *Royal Society of London Philosophical Transactions*, 255, Ser. A, pp 241-280.
18. C.W. Bert (1973), Material damping. an introductory review of mathematical models, measures and experimental techniques, *J. of Sound and Vibration*, 29, pp 129-153.
19. J.W. Pendered and R.E.D. Bishop (1963), A critical introduction to some industrial resonance testing techniques, *J. of Mech. Eng. Science*, 5, pp 345-367.
20. J.D. Ray, C.W. Bert and D.M. Egle (1969), The application of the Kennedy-Pancu method to experimental vibration studies of complex shell structures, *Shock and Vibration Bulletin*, 39, pp 107-115.
21. C.C. Kennedy and C.D.P. Pancu (1947), Use of vectors in vibration measurement and analysis, *J. Aero. Sciences*, 14, pp 603-625.
22. D.J. Ewins (1977), Measurement and application of mechanical impedance data, *Environmental Sciences Research Unit*, 3, Chapter 16, Cranfield Institute of Technology.
23. C.J. Apelt and G.S. West (1975), The effects of wake splitter plates on bluff-body flow in the range  $10^4 < R < 5 \times 10^4$ . Part 2, *J. of Fluid Mechanics*, 71, pp 145-160.

24. P.K. Stansby (1974), The effects of end plates on the base pressure coefficient of a circular cylinder, *Aero. J.*, 78, pp 36-37.
25. M.P. Paidoussis (1982), A new attempt at a more general analysis of the ovalling problem, part (i) and (ii), unpublished.
26. W. Flügge (1967), Stresses in shells, New York: Springer-Verlag.
27. A. Roshko (1954), A new hodograph for free streamline theory, *NACA*, T.N. 3168.
28. R.D. Blevins (1979), Formulas for natural frequency and mode shape, New York: Van Nostrand Reinhold Co. (Appendix C).
29. M.P. Paidoussis, S.J. Price and H.-C. Suen (1982), Ovalling oscillations of cantilevered and clamped-clamped cylindrical shells in cross flow: an experimental study, *J. Sound and Vibration*, 83, pp 533-553.
30. R.E.D. Bishop and D.C. Johnson (1960), The mechanics of vibration, Cambridge University Press, pp 407-493.
31. V.J. Modi and E. Wiland (1970), Unsteady aerodynamics of stationary elliptic cylinders in subcritical flow, *AIAA J.*, 8, pp 1814-1821.
32. A.E. Perry, M.S. Chong and T.T. Lim (1982), The vortex-shedding process behind two-dimensional bluff bodies, *J. of Fluid Mechanics*, 116, pp 77-90.

**Table 2.1:** Dimensions of the Testing Shells in Inches; (1 in. = 25.4 mm).

Shell	A	B	C
Diameter	3.00	3.00	3.00
Thickness around top circumference	0.0195	0.0185	0.0160
	0.0190	0.0190	0.0160
	0.0195	0.020	0.0165
Thickness around bottom circumference	0.0195	0.020	0.0160
	0.0190	0.020	0.0170
	0.0190	0.020	0.0170
Average shell thickness	0.0193	0.0195	0.0165
Original length of shell	23.00	23.00	23.00
Height of clamping position above tunnel floor	1.50	1.50	1.25
Height of clamping position below tunnel roof	1.50	1.50	1.75
Effective length of shell	21.00	21.00	21.00

**Table 3.1:** Summary of Natural Frequencies and Modal Damping for Shells A, B and C With and Without an Insert.

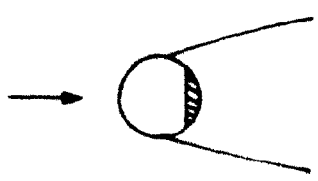
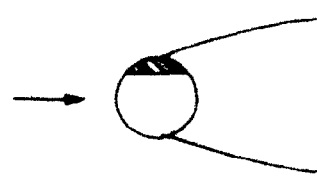
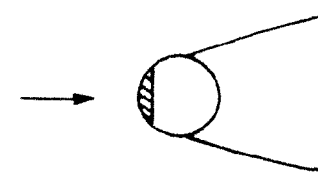
MODEL (SHELL)	n = 2				n = 3			
	f (Hz)		$\delta$		f (Hz)		$\delta$	
	1 <sup>st</sup> TRIAL	2 <sup>nd</sup> TRIAL	1 <sup>st</sup> TRIAL	2 <sup>nd</sup> TRIAL	1 <sup>st</sup> TRIAL	2 <sup>nd</sup> TRIAL	1 <sup>st</sup> TRIAL	2 <sup>nd</sup> TRIAL
A	171.0	171.2	0.047	0.046	232.1	232.3	0.046	0.046
A with insert	218.7	219.4	0.058	0.057	235.7	237.2	0.113	0.134
B	166.1	165.8	0.051	0.049	216.0	215.6	0.052	0.053
B with insert	209.0	208.8	0.053	0.058	227.7	227.1	0.144	0.108
C	163.8	-	0.032	-	226.1	-	0.036	-

**Table 4.1: Threshold Flow Velocities of Two Nominally Identical 76.2 mm Diameter Clamped-Clamped Shells.**

Shell	$\theta^\dagger$ (deg.)	Mode: $(n,m) = (2,1)$			Mode: $(n,m) = (3,1)$		
		$U_{cr}$ (m/s)	$f_{n,m}$ (Hz)	$f_{n,m}/f_{vs}$ (-)	$U_{cr}$ (m/s)	$f_{n,m}$ (Hz)	$f_{n,m}/f_{vs}$ (-)
A	315	21.7	173	3.4 - 3.5	24.4	236	4.1 - 4.2
A	340	21.6	174	3.4 - 3.5	24.4	238	4.1 - 4.2
B	315	21.2	167	3.4 - 3.5	22.9	223	4.0 - 4.1
B	300	21.2	168	3.4 - 3.5	22.9	227	4.2 - 4.3

$^\dagger \theta$  indicates the angular position of the photonic sensor, measured clockwise from the front stagnation point at a height  $h = 89$  mm (3.5 in.);  $h$  is measured from the lower clamping position (see Figure 2.3).

Table 4.2: Threshold Flow Velocities for Shells A and B With an Insert.

Shell	Orientation of the Model													
														
	$\theta$ (deg.)	$U_{cr}$ (m/s)	$f_{2,1}^i$ (Hz)	$f_{2,1}^i/f_{vs}$ (-)	$\theta$ (deg.)	$U_{cr}$ (m/s)	$f_{2,1}^i$ (Hz)	$f_{2,1}^i/f_{vs}$ (-)	$\theta$ (deg.)	$U_{cr}$ (m/s)	$f_{2,1}^i$ (Hz)	$f_{2,1}^i/f_{vs}$ (-)	$U_{cr}^{\dagger}$ (m/s)	$f_{2,1}^i/f_{vs}$ (-)
A	0	Stable			-	-	-	-	145	30.8	225	3.2 - 3.3	-	-
	315				-	-	-	-	145	31.8	227	3.1 - 3.2	-	-
	325				-	-	-	-	-	-	-	-	-	-
	325				-	-	-	-	-	-	-	-	-	-
	330				-	-	-	-	-	-	-	-	-	-
B	315				225	27.0	212	3.4 - 3.5	135	28.7	214	3.2 - 3.3	35.0	2.6 - 2.7
	315				225	26.7	216	3.4 - 3.5	135	27.8	216	3.2 - 3.3	33.4	2.7 - 2.8

<sup>†</sup> This second critical flow velocity could correspond to a change of ovaling mode (from an antisymmetric to a symmetric one); see footnote of Section 4.3.



Table 4.3: A Summary of the Results of Tables 4.2 and 4.3.

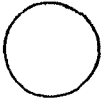
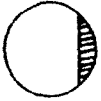
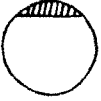
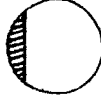
Model (Shell)				
$f_{2,1}$ (Hz)	173-174 167-168	Stable	- 212-216	225-227 214-216
$f_{2,1}/f_{vs}$ (-)	3.4-3.5 3.4-3.5		- 3.4-3.5	3.1-3.3 3.2-3.3
$U_{cr}$ (m/s)	21.6-21.7 21.2-21.2		- 26.7-27.0	30.8-31.8 27.8-28.7

Table 6.1: The Shell and Fluid Parameters Used in Theoretical Calculations.

(a) Shell dimensions

mean radius	$a = 38.1 \text{ mm (1.50 in.)}$
mean thickness	$h = 0.508 \text{ mm (0.020 in.)}$
overall length	$= 0.584 \text{ m (23.00 in.)}$
effective length	$L = 0.533 \text{ m (21.00 in.)}$

$$\kappa = \frac{h^2}{12a^2} = 1.48 \times 10^{-5}$$

(b) Material properties of the shell

density $\rho_s$	$= 1.29 \times 10^3 \text{ kg/m}^3$
Young's modulus $E$	$= 0.28 \times 10^{10} \text{ N/m}^2$
Poisson's ratio $\nu$	$= 0.4$

$$\gamma = \rho_s a^2 \frac{(1-\nu)^2}{E} = 5.62 \times 10^{-10} \text{ sec}^2$$

(c) Density of air

At 20°C and 1 atmospheric pressure

$$\rho_{\text{air}} = 1.204 \text{ kg/m}^3$$

**Table 6.2: Theory and Experiment Compared in Terms of Predicted and Measured Owalling Frequencies; Negative Aerodynamic Damping  $-\delta_{ad}$  and Modal Damping  $\delta_{n,m}$ , at the Measured Critical-Flow Velocities.**

Case	n = 2				n = 3			
	Expt (Hz)	Theory (Hz)	$\delta_{2,1}$ (expt)	$-\delta_{ad}$ (theory)	Expt (Hz)	Theory (Hz)	$\delta_{3,1}$ (expt)	$-\delta_{ad}$ (theory)
0	167- 174	165	0.046- 0.051	0.021	223- 238	206	0.046- 0.053	0.011
1		165		0.027		206		0.013
2		164		0.020		202		0.037
3		166		Positive damping		207		Positive damping
4		166		0.043		207		0.032
5		166		0.011		203		0.056
6		165		0.042		202		0.070

**Table 7.1:** Summary of the Phase Lag and  $C_p = Hw^*/a+H_0$  for the  $n=2$  Mode Vibrating With a Node Facing the Free Stream.

Angular position $\theta$		Phase						Polynomial $C_p = Hw^*/a+H_0$		
		U=5 m/s	U=10 m/s	U=15 m/s	U=20 m/s	U=25 m/s	U=30 m/s	H	$H_0$	$1-H-H_0$
C A L C U L A T E D	5	165	151	138	127	118	110	2.408600	0.947070	-2.355670
	15	166	154	143	134	127	121	2.210300	0.800840	-2.011140
	25	170	162	155	151	148	146	1.211600	0.496170	-0.707770
	35	176	174	172	171	171	171	-0.220290	0.027876	1.192414
	45	185	189	190	190	190	189	-2.436800	-0.497190	3.933990
	55	196	205	208	208	207	205	-3.037800	-1.019400	5.057200
	65	210	223	228	228	227	225	-1.252600	-1.930100	4.182700
	75	230	249	257	262	266	268	-0.042934	-1.214200	2.257134
	85	262	280	291	300	397	313	5.232000	-1.140600	-3.091400
† E S T.	95	276	289	307	307	300	300	0.865420	-1.116700	1.251280
	105	266	290	278	278	282	282	0.510740	-1.126100	1.615360
	115	255	255	258	258	258	258	0.276180	-1.138700	1.862520
M E A S U R E D	125	240	240	240	240	240	240	-0.156550	-1.163600	2.320150
	135	228	228	228	228	228	228	-0.369860	-1.211100	2.580960
	145	215	215	215	215	215	215	-0.427900	-1.228200	2.656100
	155	210	210	210	210	210	210	-0.616450	-1.277400	2.893850
	165	204	204	204	204	204	204	-0.048939	-1.323500	2.372439
	175	160	160	160	160	160	160	2.110500	-1.344000	0.233500

† Estimated as a smooth progression from the last set of calculated values to the first set of the measured ones.

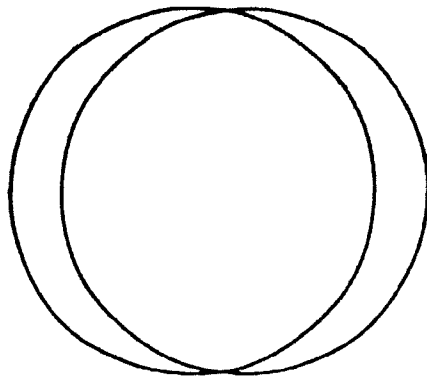
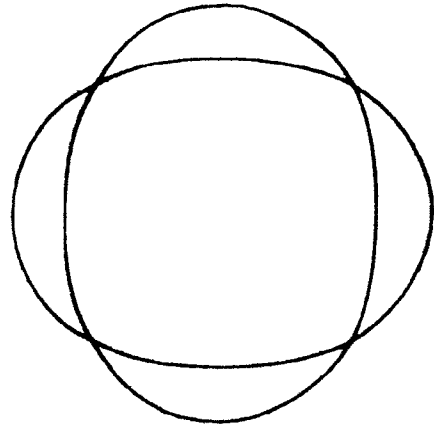
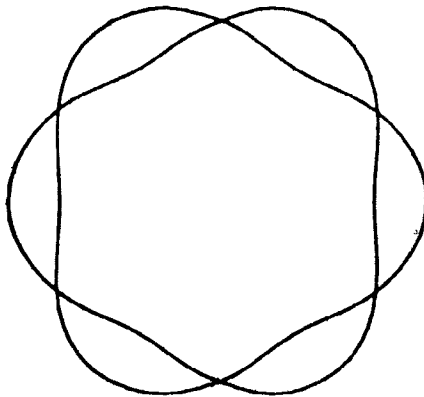
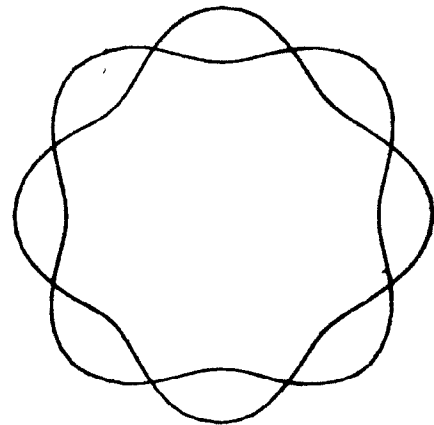
**Table 7.2 :** Summary of the Phase Lag and  $C_p = Hw^*/a+H_0$  for the  $n=3$  Mode Vibrating With an Antinode Facing the Free Stream.

Angular position $\theta$		Phase						Polynomial $C_p = Hw^*/a+H_0$		
		U=5 m/s	U=10 m/s	U=15 m/s	U=20 m/s	U=25 m/s	U=30 m/s	H	$H_0$	1-H- $H_0$
C A L C U L A T E D	5	193	205	214	222	228	233	-0.196350	0.928000	0.268350
	15	205	222	231	237	239	241	-1.898000	0.740400	2.157600
	25	241	252	255	256	256	256	-9.472400	0.478800	9.993600
	35	295	285	282	281	281	282	8.570100	0.144000	-7.714100
	45	328	314	309	398	309	311	-1.363600	-0.367000	2.730600
	55	350	345	344	344	346	347	-5.202000	-0.933800	7.135800
	65	9	13	14	13	12	10	-2.762200	-1.034000	4.795200
	75	31	45	50	51	50	48	-2.027100	-1.183800	4.210900
	85	74	96	109	119	127	133	-0.427630	-1.243400	2.671030
† E S T.	95	135	148	160	160	170	170	2.157800	-1.212000	0.054200
	105	200	200	198	198	204	204	1.590200	-1.186400	0.596200
	115	227	227	227	227	227	227	1.356900	-1.191600	0.834700
M E A S U R E D	125	205	205	205	205	205	205	1.324600	-1.216200	0.891600
	135	164	164	164	164	164	164	1.654600	-1.254400	0.599800
	145	125	125	125	125	125	125	4.350800	-1.302200	-2.048600
	155	180	180	180	180	180	180	-4.808000	-1.356600	7.164600
	165	278	278	278	278	278	278	-2.222600	-1.410400	4.633000
	175	269	269	269	269	269	269	-2.146200	-1.453600	4.599800

† Estimated (see footnote of Table 7.1).

**Table 7.3:** Comparison of the Amount of Energy Transferred from the Flow Field into the System, to the Portions of the Shells Ahead of Flow Separation and in the Wake Region.

Modes	Flow Velocity (m/s)	Energy Extracted from Free Stream					
		Before Separation		Wake Region		Total Energy	
		0-90° ( $B_0^2$ J/m)	% (-)	90°-180° ( $B_0^2$ J/m)	% (-)	0-180° ( $B_0^2$ J/m)	% (-)
n=2	5	54	30	125	70	179	100
	10	320	39	500	61	820	100
	15	805	42	1128	58	1933	100
	20	1457	42	2005	58	3462	100
	25	2269	42	3128	58	5397	100
	30	3144	41	4504	59	7648	100
n=3	5	9	7	125	93	134	100
	10	64	11	499	89	563	100
	15	167	13	1121	87	1288	100
	20	344	15	1994	85	2338	100
	25	504	14	3128	86	3632	100
	30	789	15	4504	85	5293	100

 $n = 1$  $n = 2$  $n = 3$  $n = 4$ 

**Figure 1.1:** Various circumferential mode shapes of breathing oscillation of cylindrical shells.

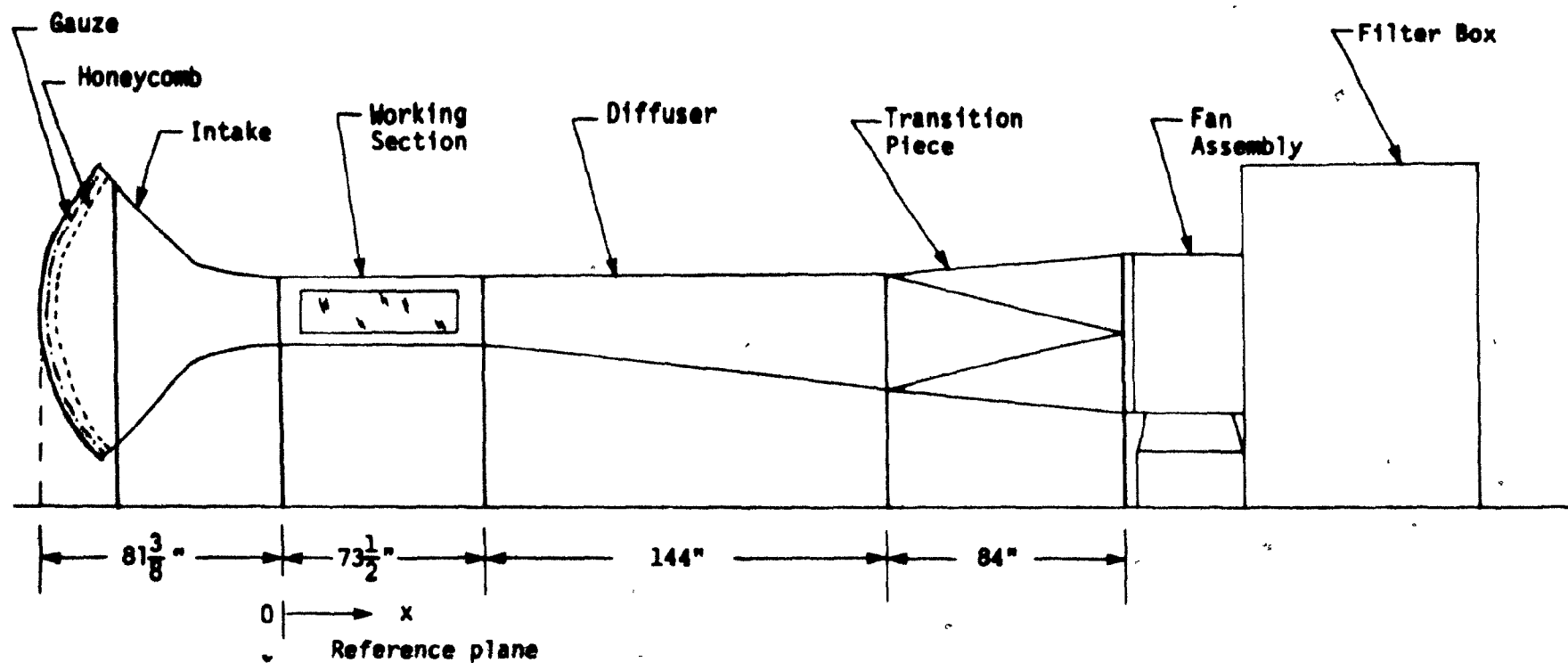
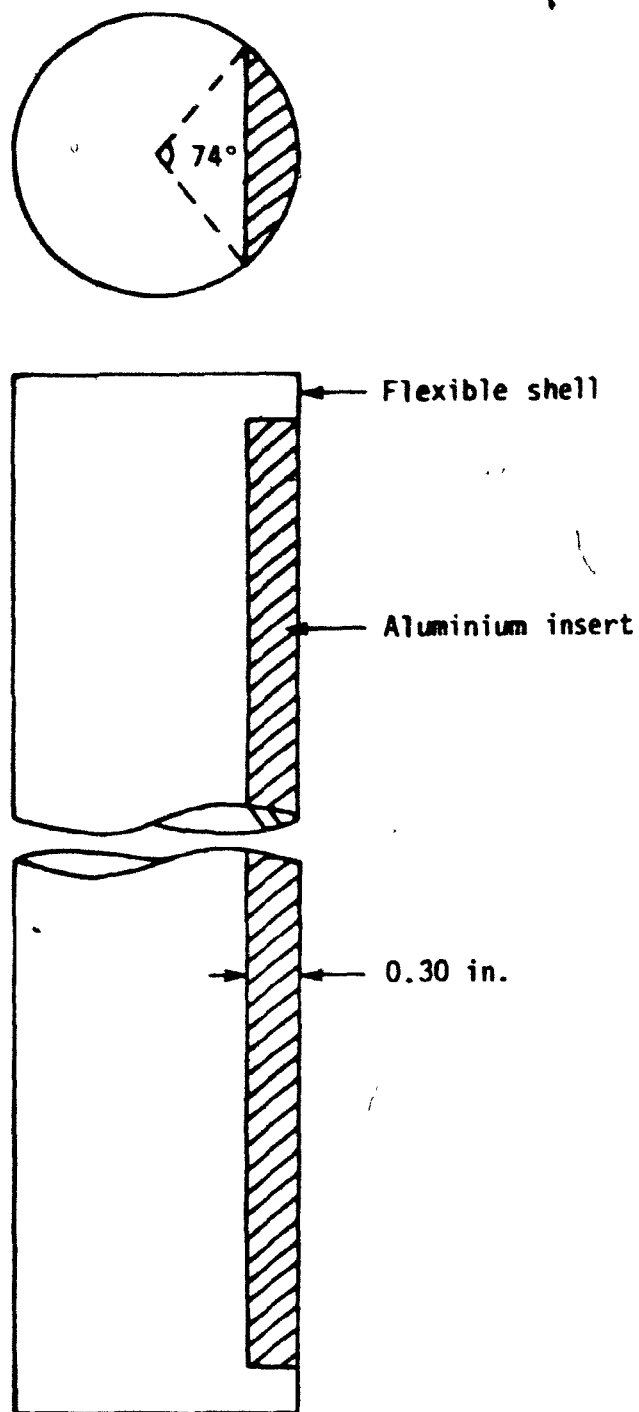
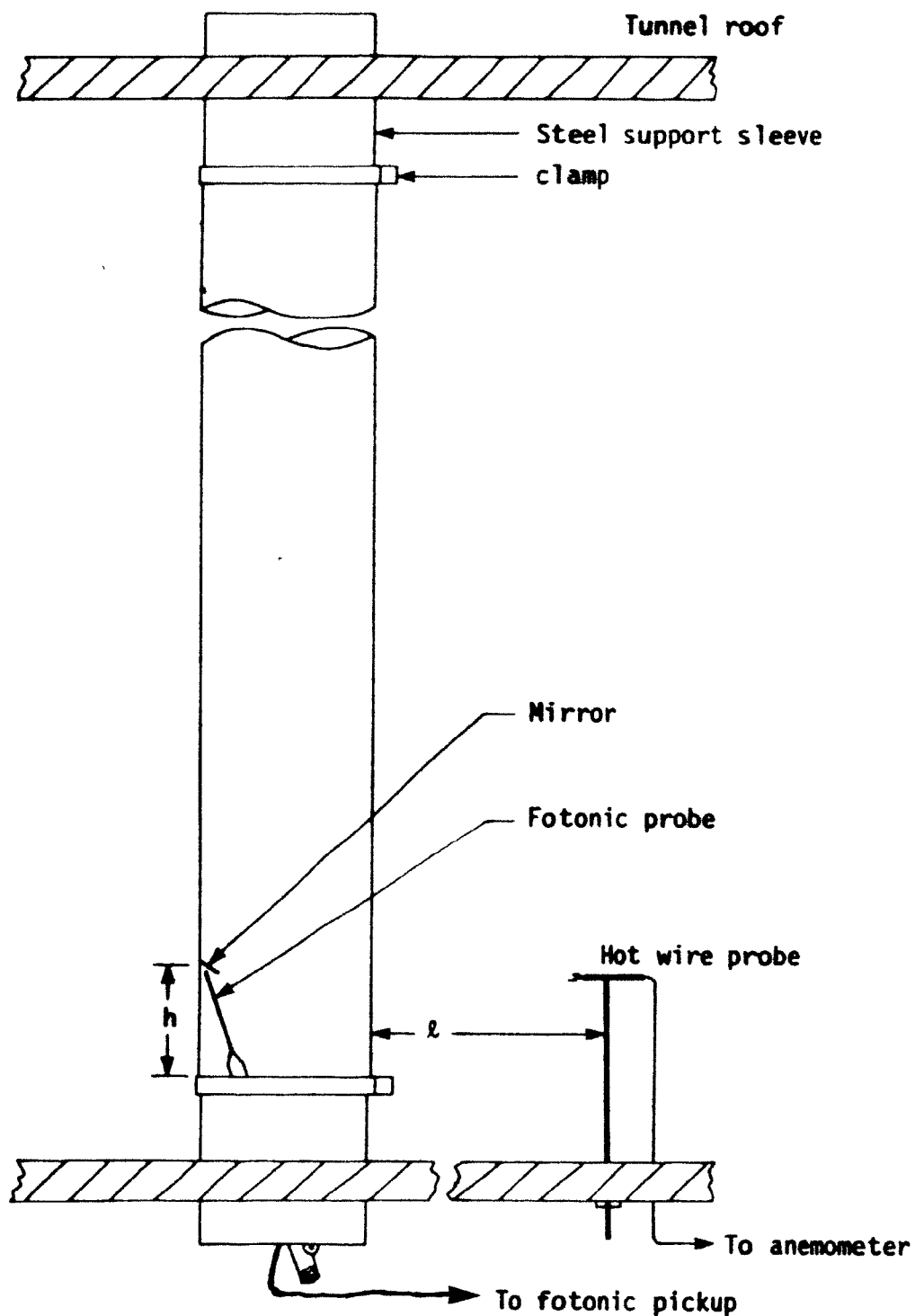


Figure 2.1: Side view of wind tunnel.





**Figure 2.2:** Top and side view of the cylindrical shell with an aluminium insert.



\* **Figure 2.3:** Side view of the cylindrical shell in position in the wind tunnel test section; typically  $\ell = 254 \text{ mm}$  (10.0 in.).

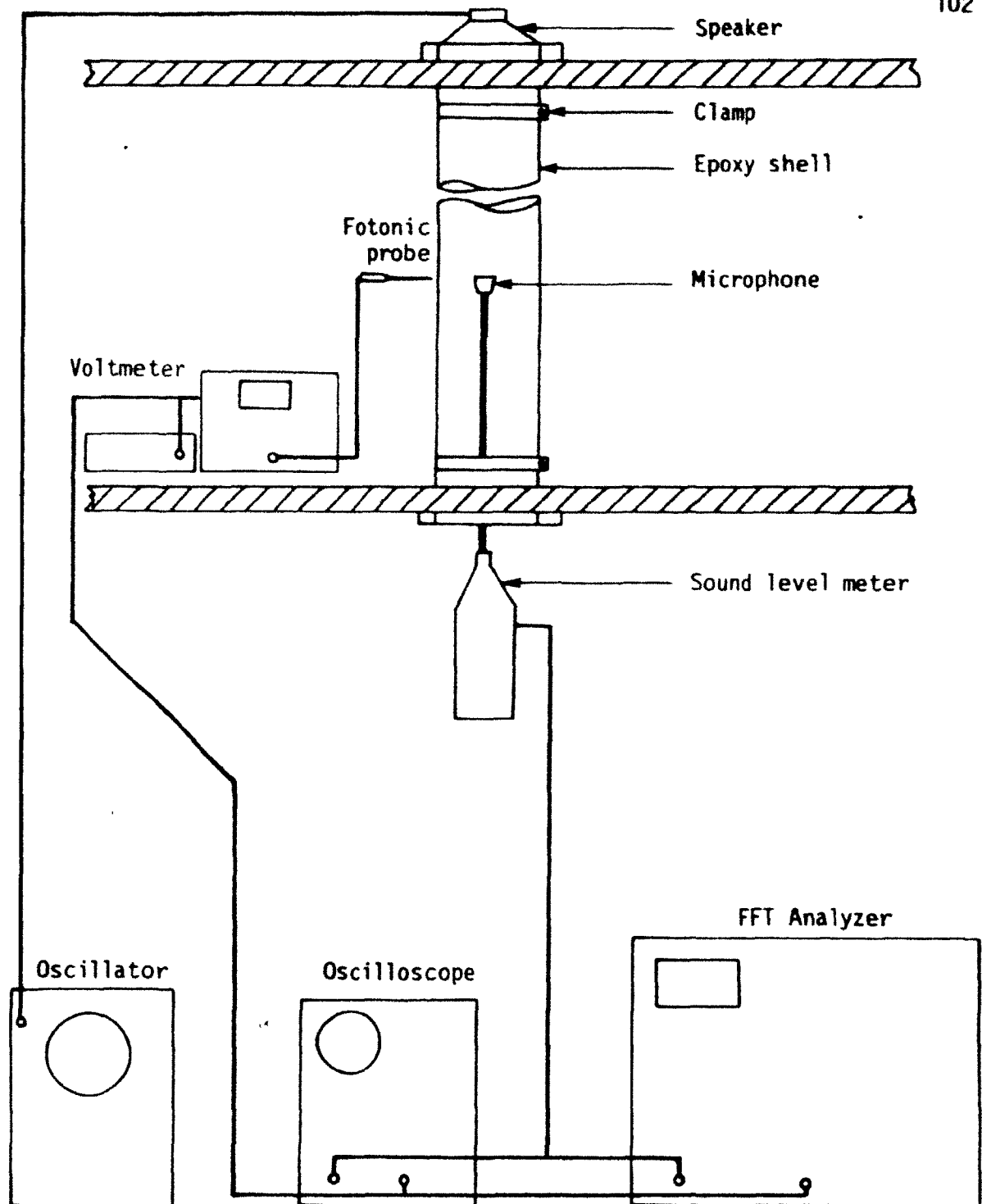


**Figure 3.1:** Schematic of the experiment to determine the natural frequency and damping of a clamped-clamped shell.

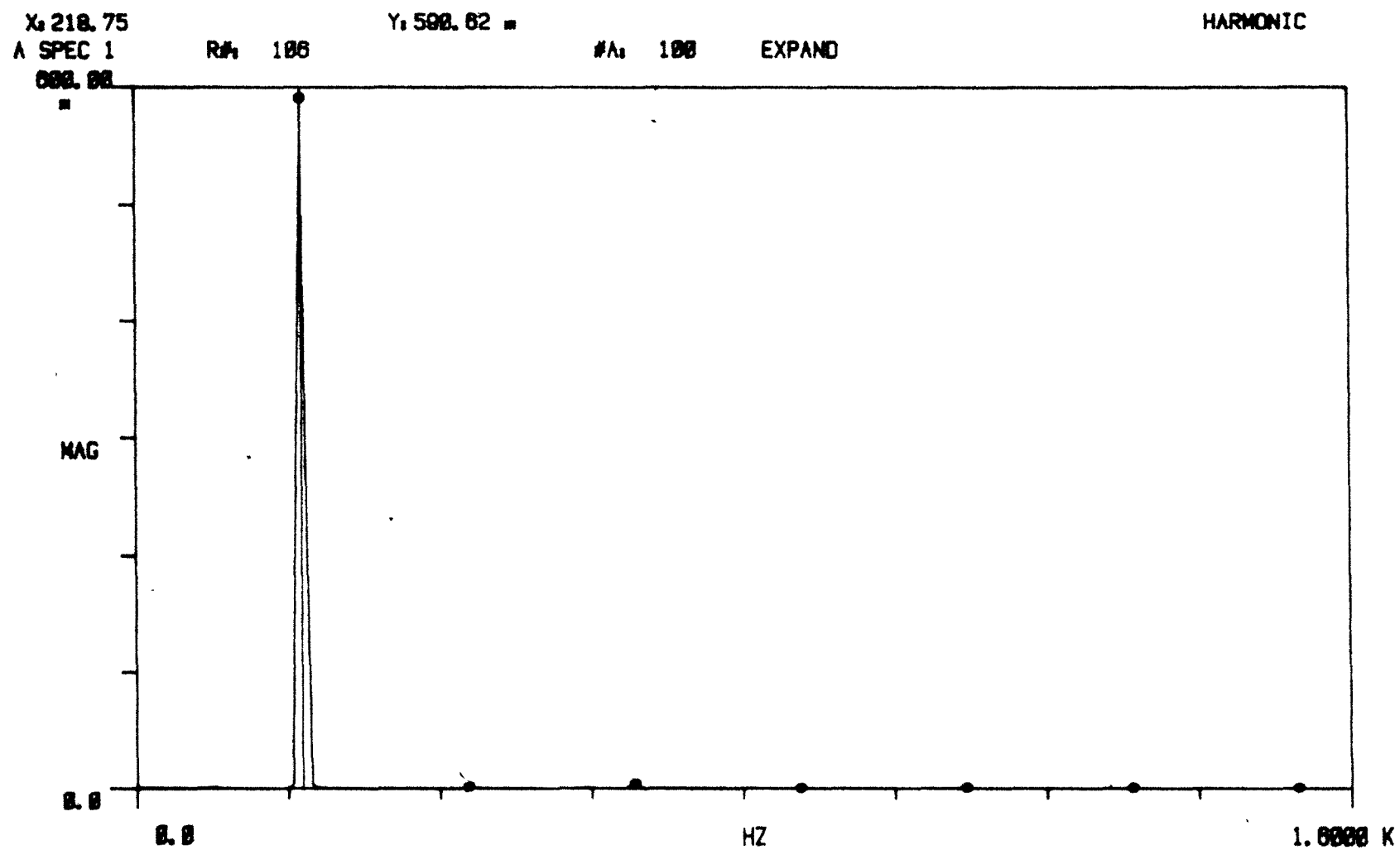


Figure 3.2: Frequency spectrum of the acoustic excitation monitored by the sound level meter.

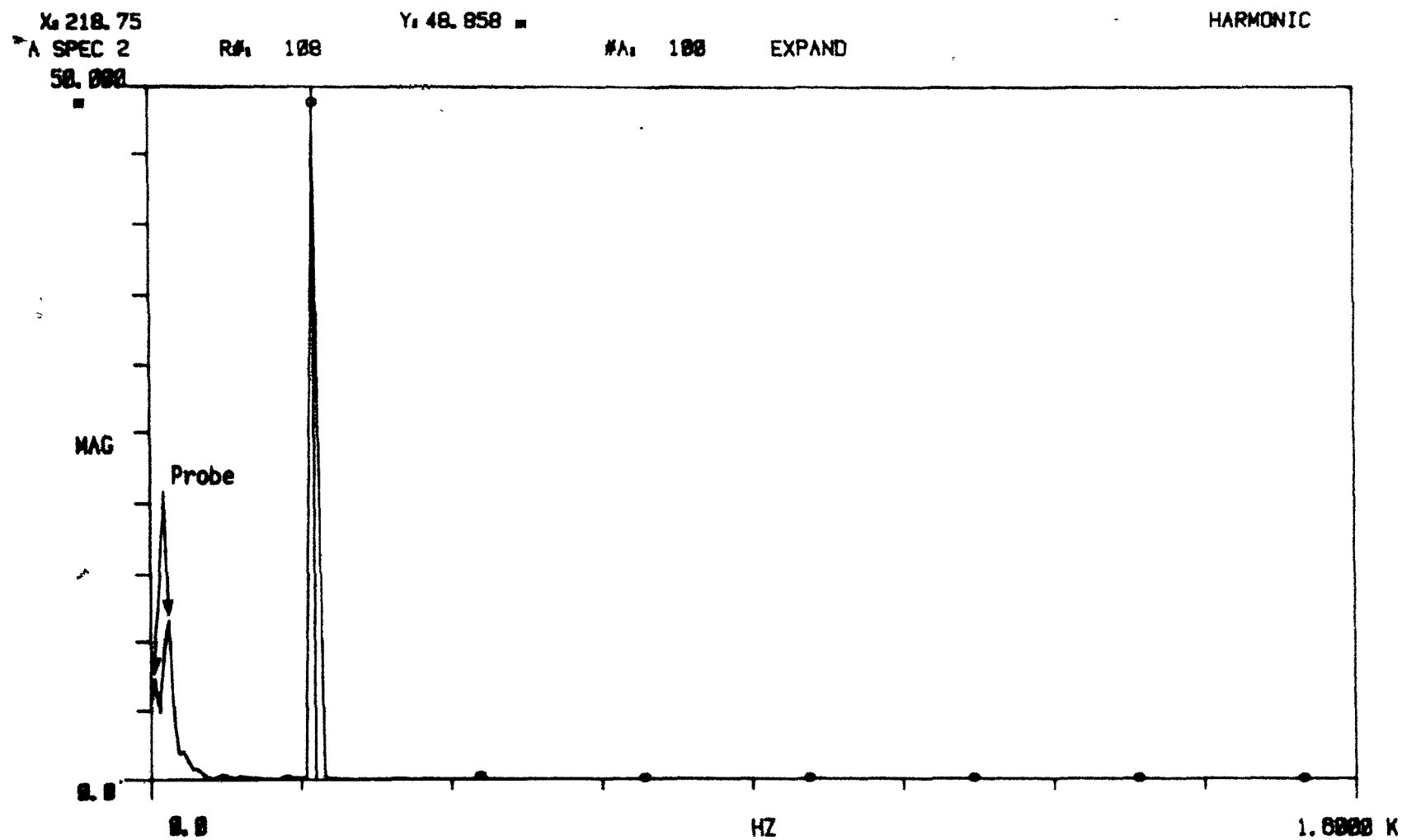
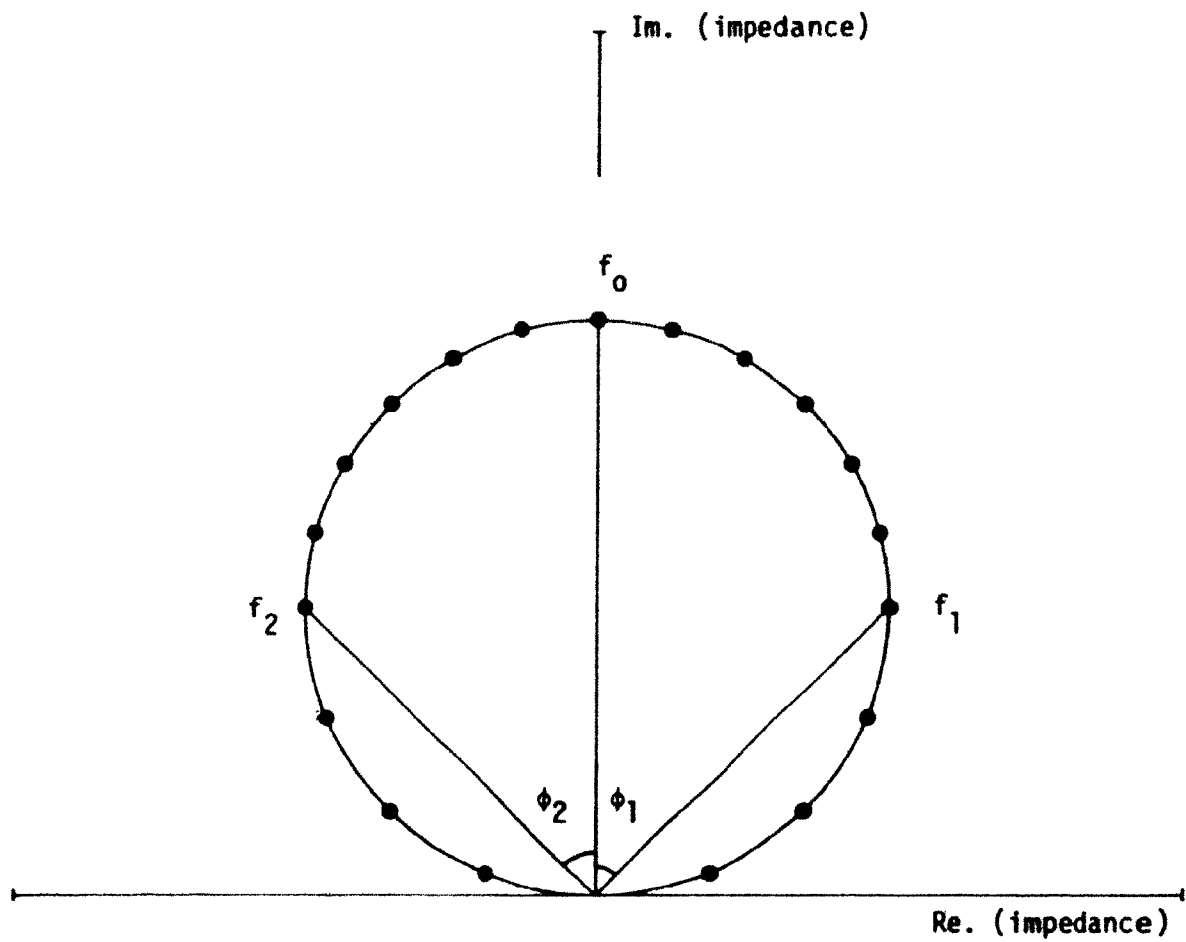
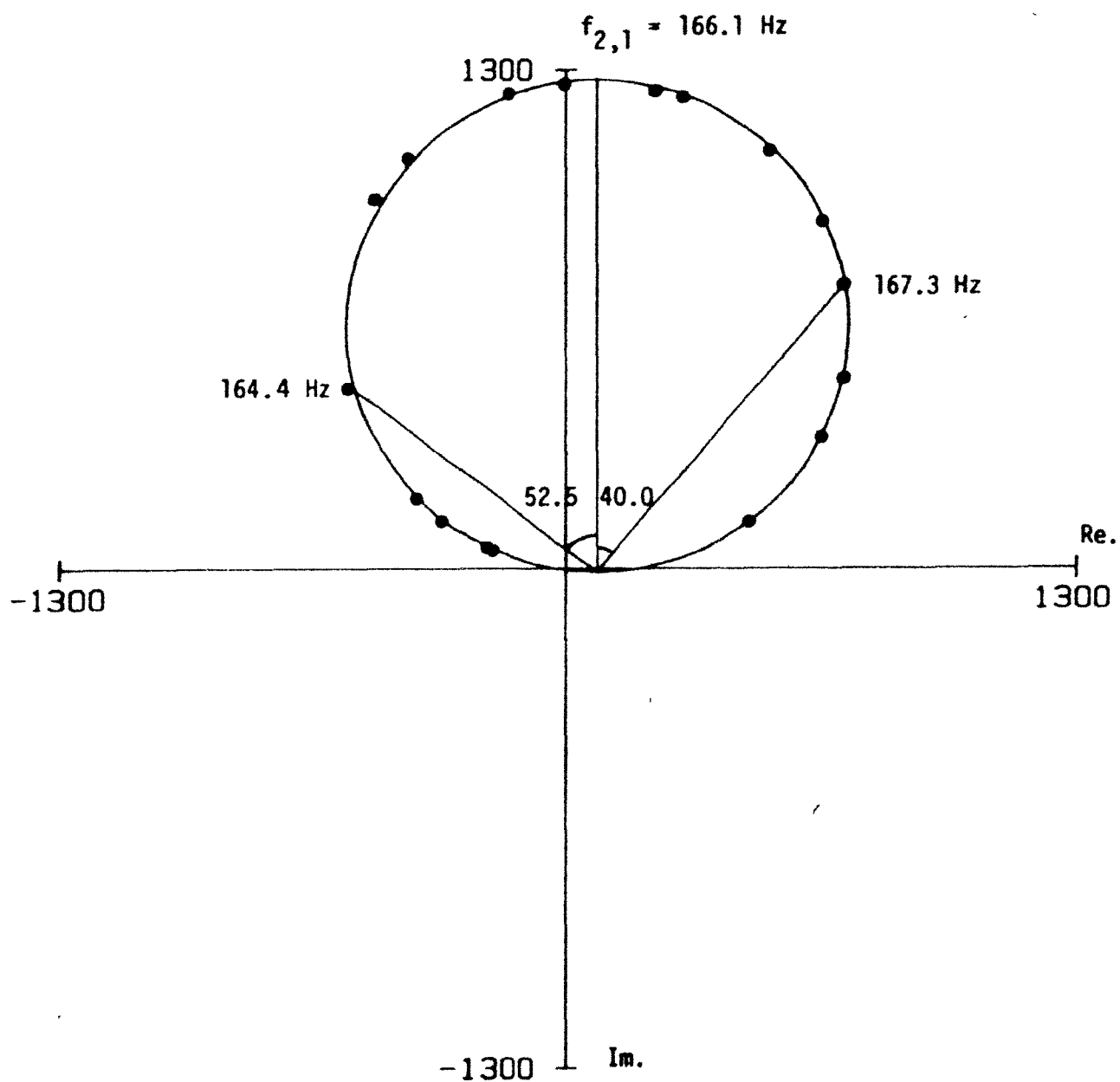


Figure 3.3: Frequency spectrum of the shell vibration monitored by the fotonic sensor.



**Figure 3.4:** Ideal Nyquist plot for a one-degree-of-freedom system. The logarithmic decrement  $\delta$  is determined by the relationship  $\delta = 2\pi(f_2 - f_1) / [f_0(\tan \phi_1 + \tan \phi_2)]$ .



**Figure 3.5:** Nyquist plot for shell B without an insert: (2,1)-mode;  
 $f_{2,1} = 166.1$  Hz,  $\delta_{2,1} = 0.051$ .

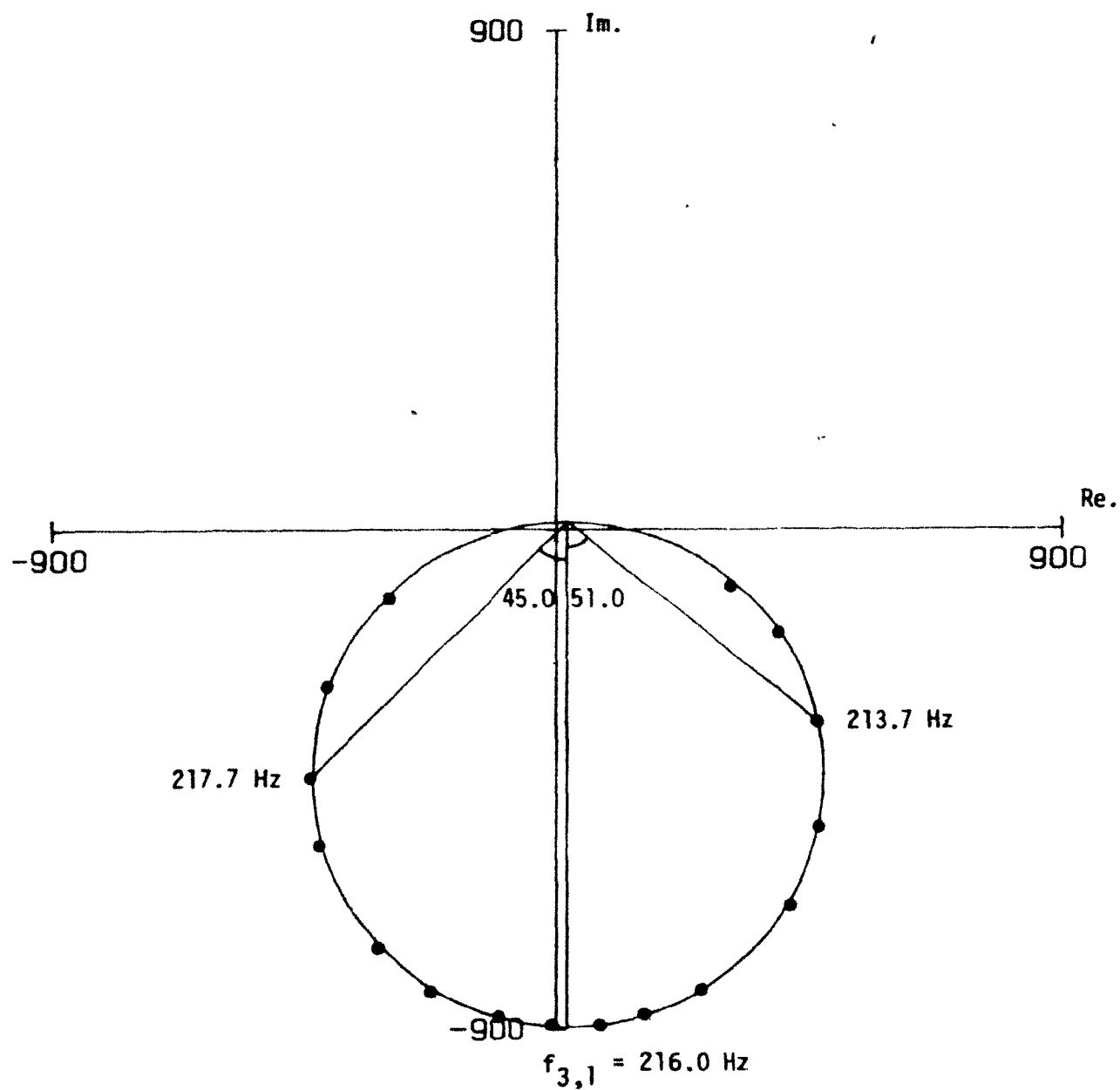


**Figure 3.6:** Nyquist plot for shell B without an insert: (3,1)-mode;  
 $f_{3,1} = 216.0 \text{ Hz}$ ,  $\delta_{3,1} = 0.052$ .



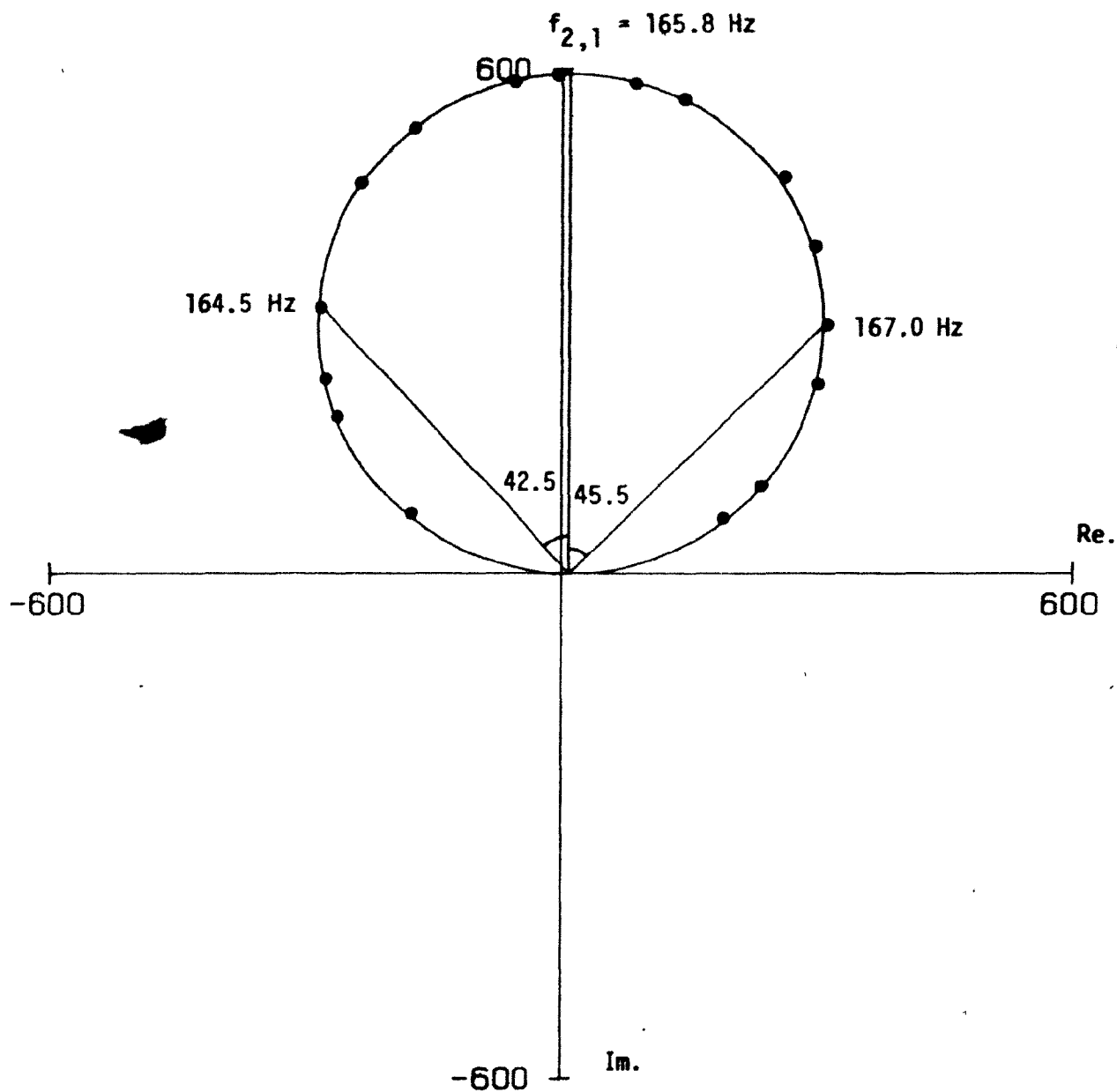
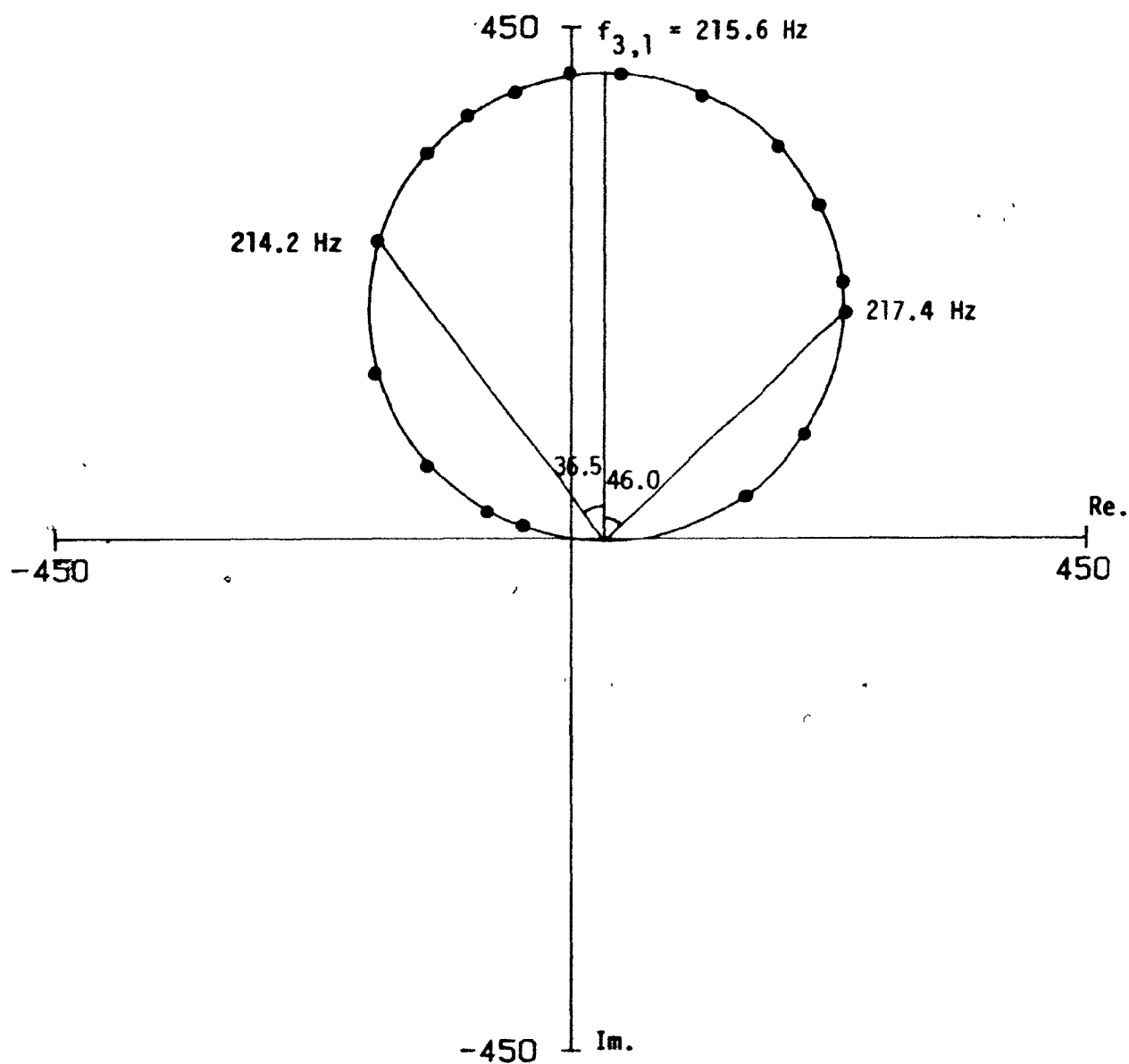
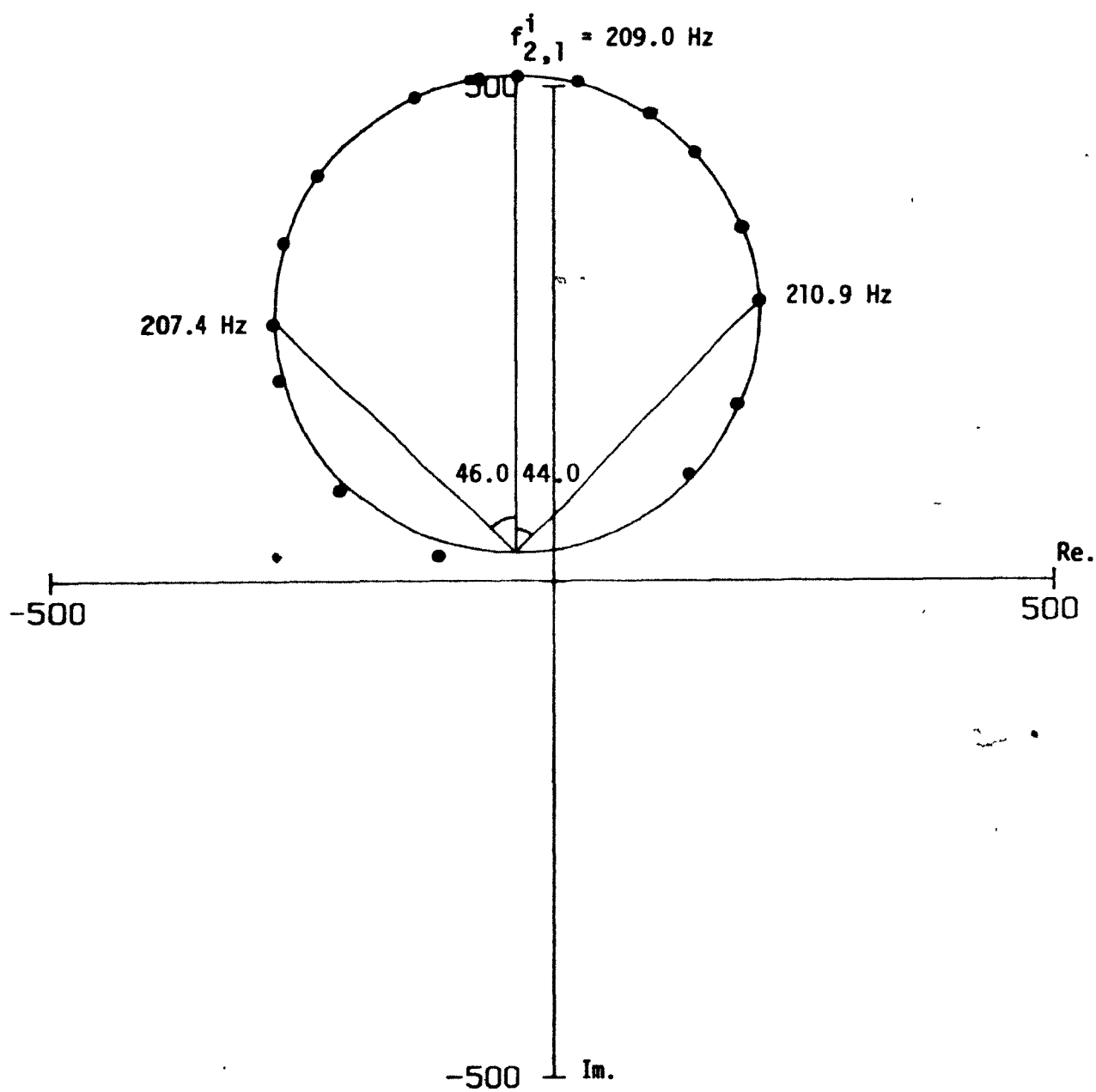


Figure 3.7: Nyquist plot for shell B without an insert: (2,1)-mode;  
 $f_{2,1} = 165.8 \text{ Hz}$ ,  $\delta_{2,1} = 0.049$  - second set of measurements.



**Figure 3.8:** Nyquist plot for shell B without an insert: (3,1)-mode;  
 $f_{3,1} = 215.6 \text{ Hz}$ ,  $\delta_{3,1} = 0.053$  - second set of measurements.



**Figure 3.9:** Nyquist plot for shell B with an insert: (2,1)-mode;  
 $f_{2,1}^1 = 209.0 \text{ Hz}$ ,  $\delta_{2,1}^1 = 0.053$ .

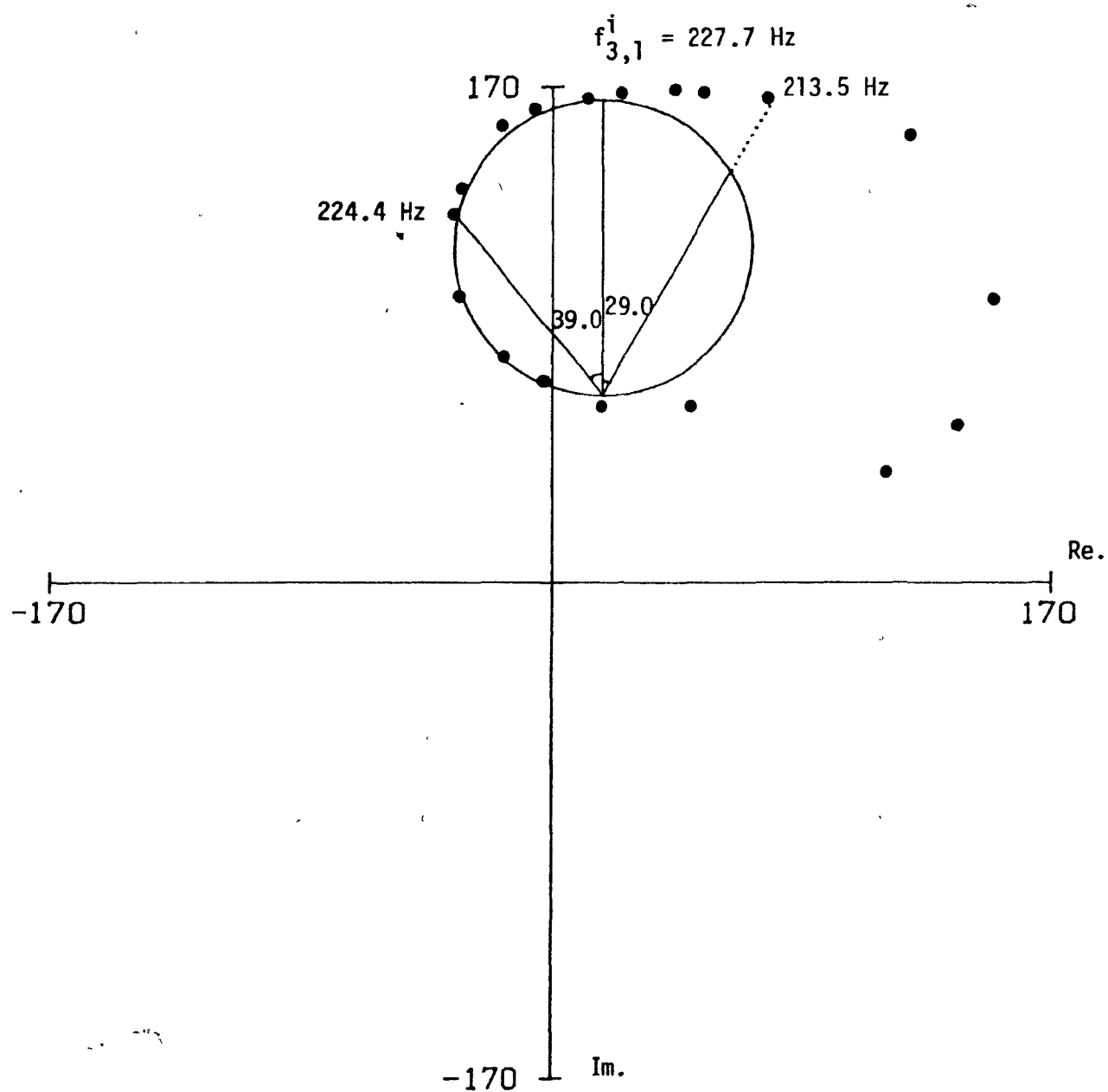


Figure 3.10: Nyquist plot for shell B with an insert: (3,1)-mode;  
 $f_{3,1}^i = 227.7 \text{ Hz}$ ,  $\delta_{3,1}^i = 0.144$ .

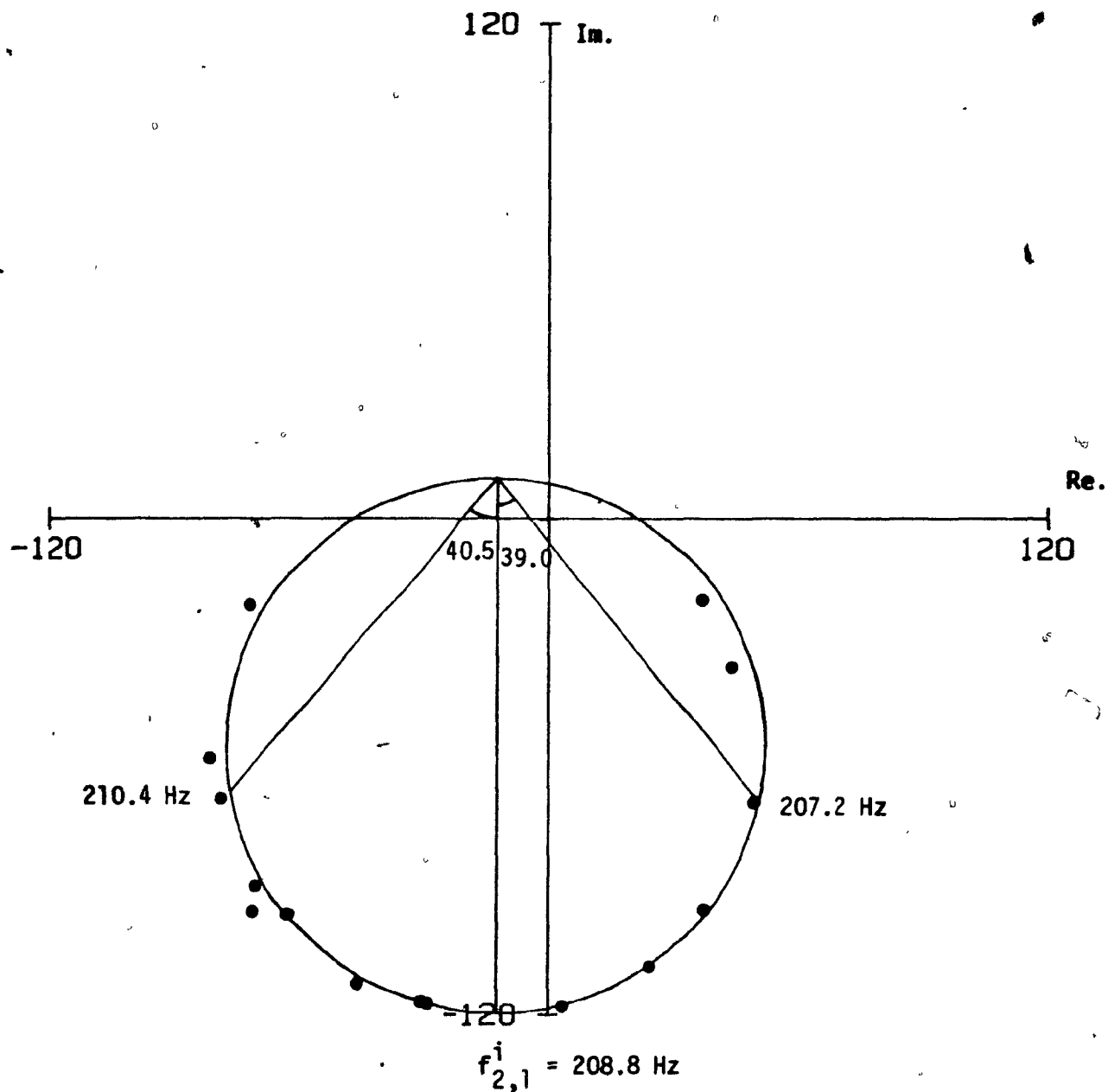
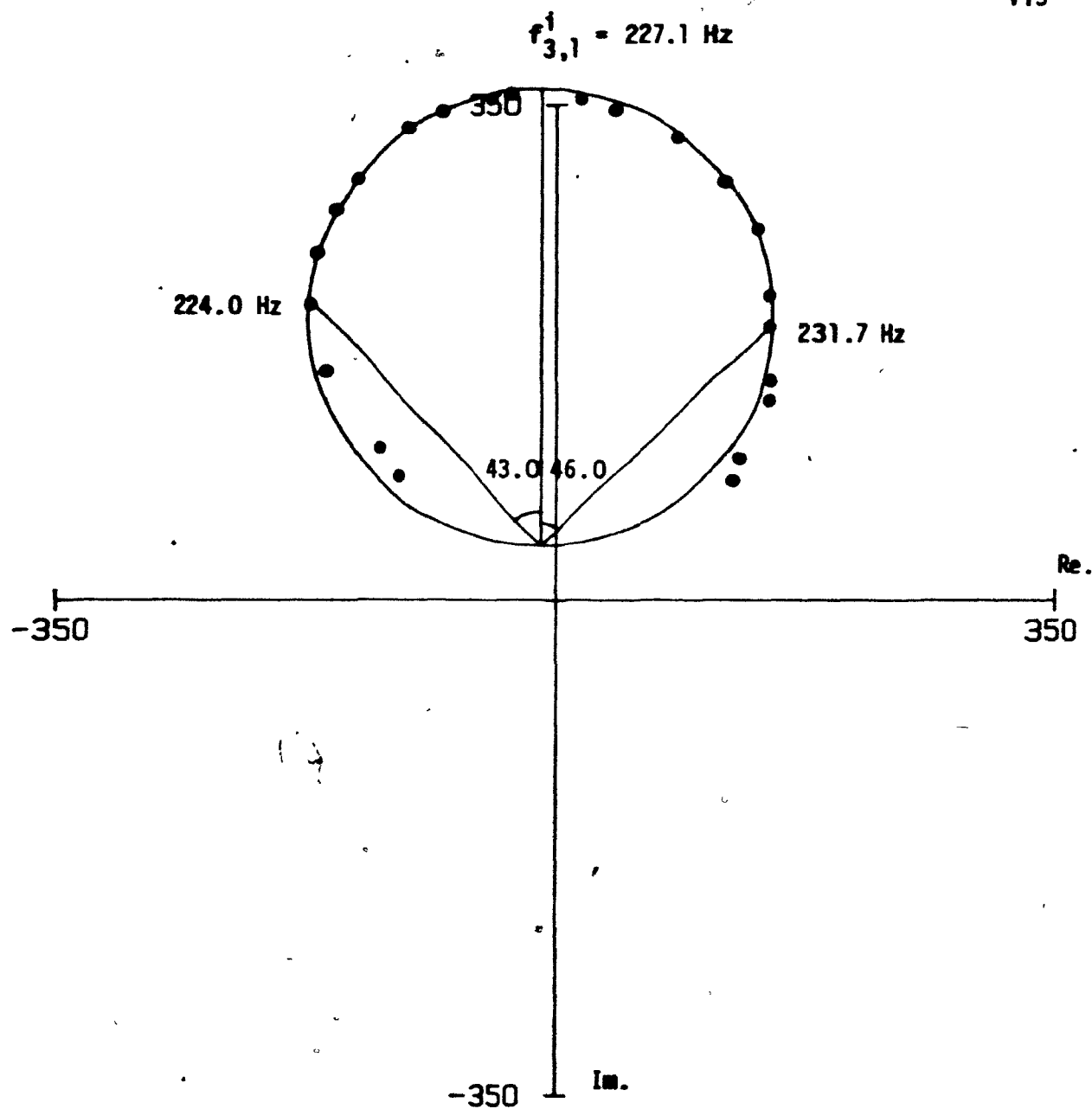
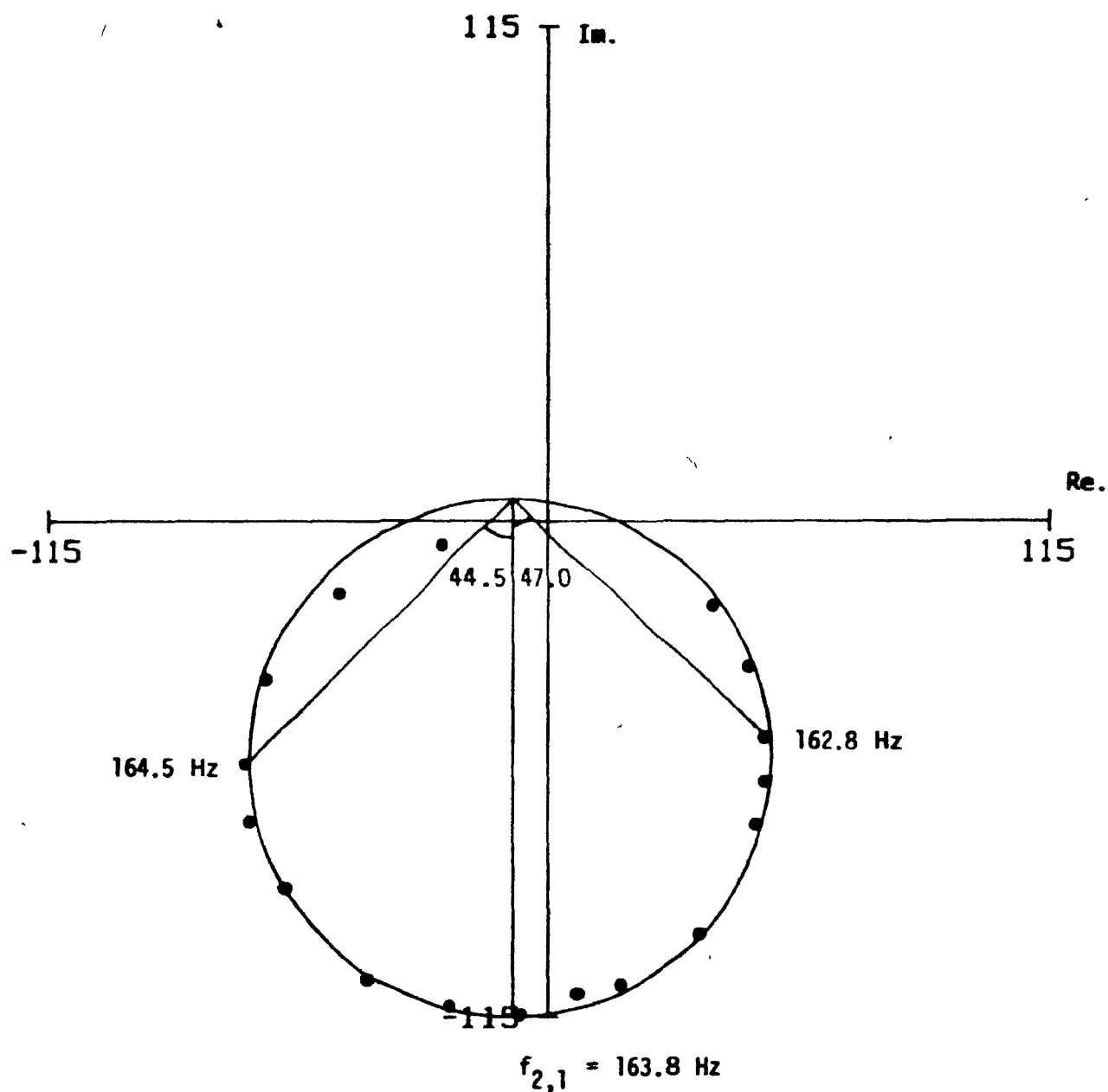


Figure 3.11: Nyquist plot for shell B with an insert: (2,1)-mode;  
 $f_{2,1}^i = 208.8 \text{ Hz}$ ,  $\delta_{2,1}^i = 0.058$  - second set of measurements.



**Figure 3.12:** Nyquist plot for shell B with an insert: (3,1)-mode;  
 $f_{3,1}^i = 227.1 \text{ Hz}$ ,  $\delta_{3,1}^i \rightarrow 0.108$  - second set of measurements.



**Figure 3.13:** Nyquist plot for shell C without an insert: (2,1)-mode;  
 $f_{2,1} = 163.8 \text{ Hz}$ ,  $\delta_{3,1} = 0.032$ .

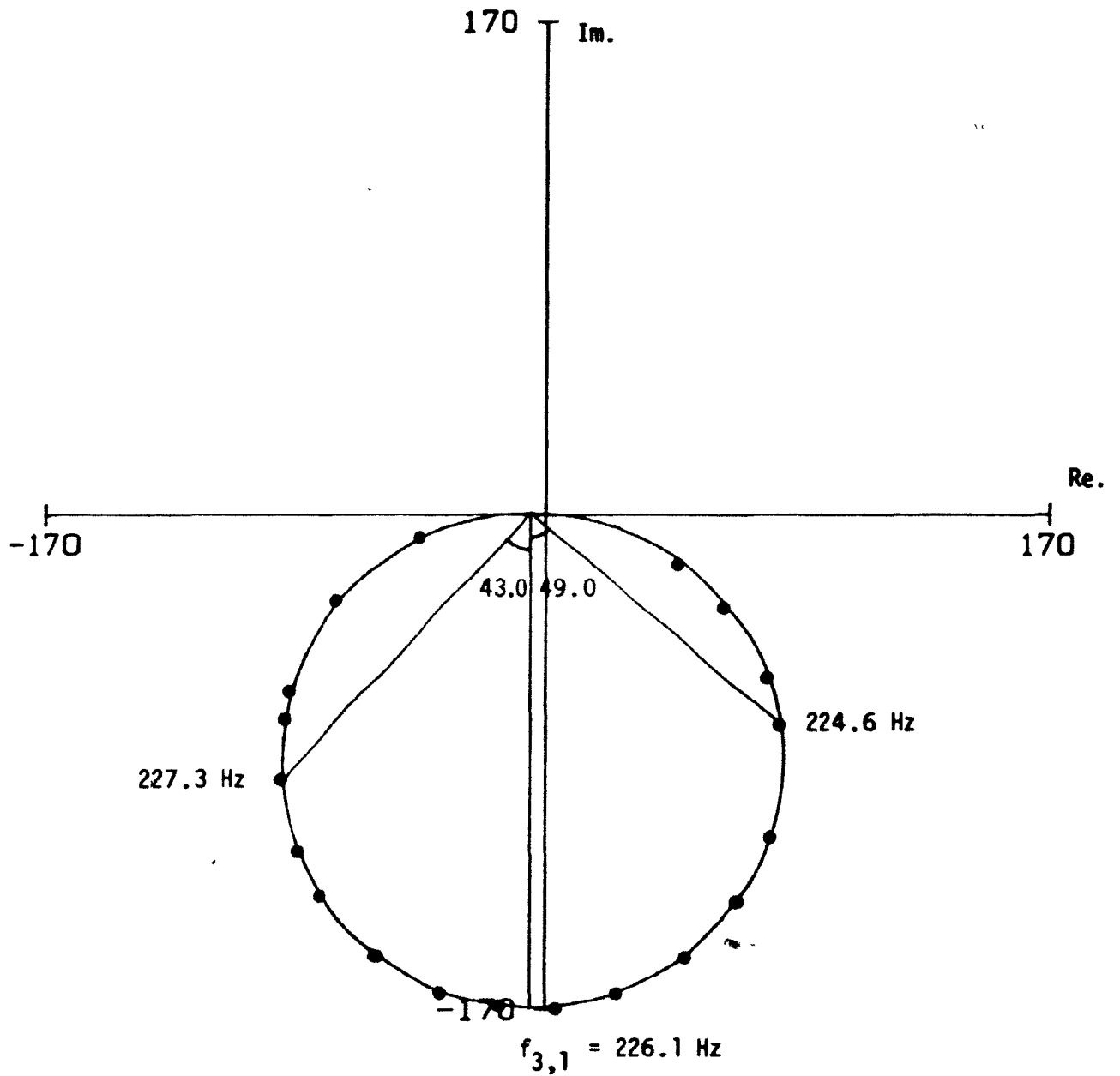


**Figure 3.14:** Nyquist plot for shell C without an insert: (3,1)-mode;  
 $f_{3,1} = 226.1 \text{ Hz}$ ,  $\delta_{3,1} = 0.036$ .



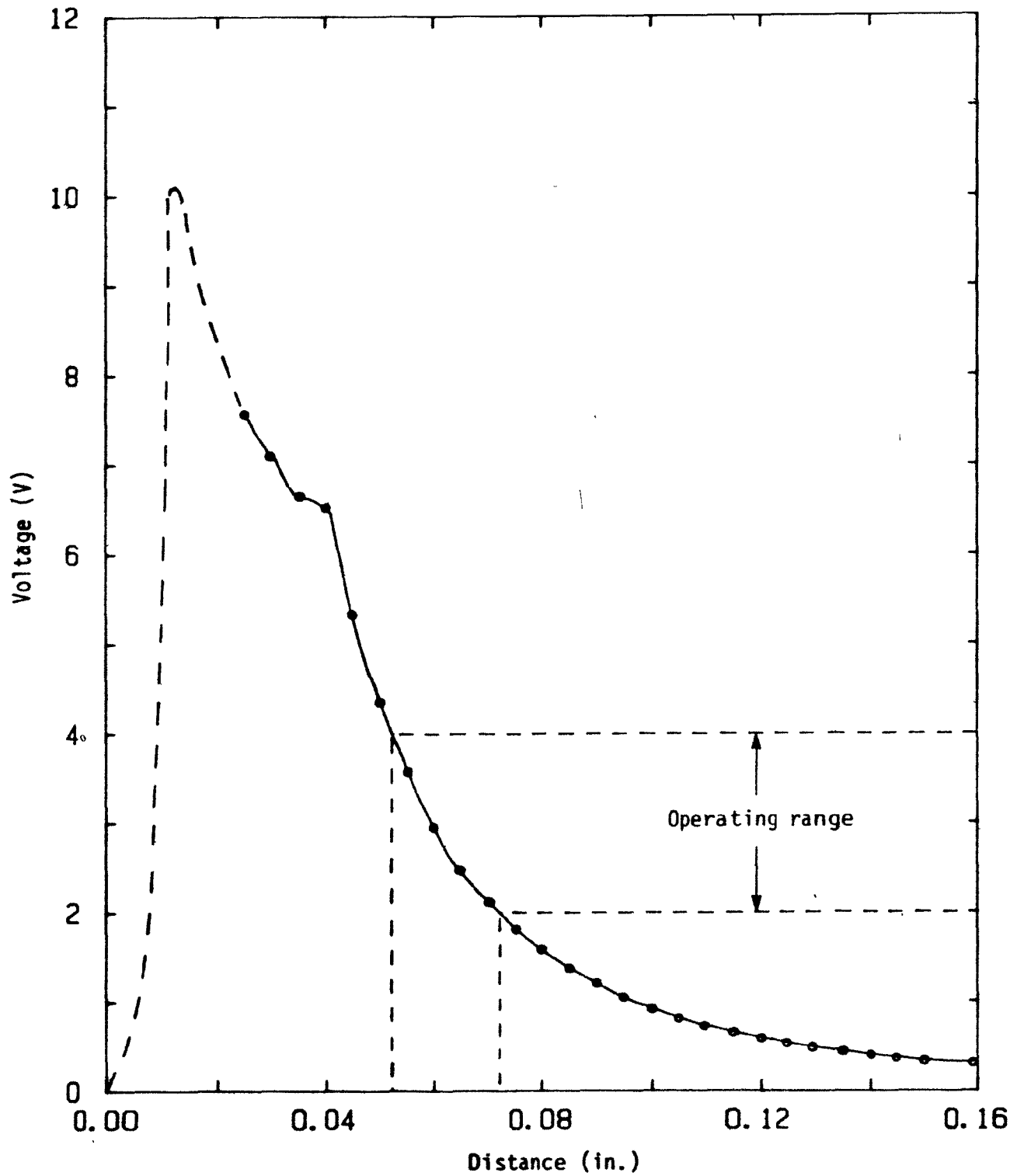


**Figure 4.1:** Typical calibration curve of photonic sensor.

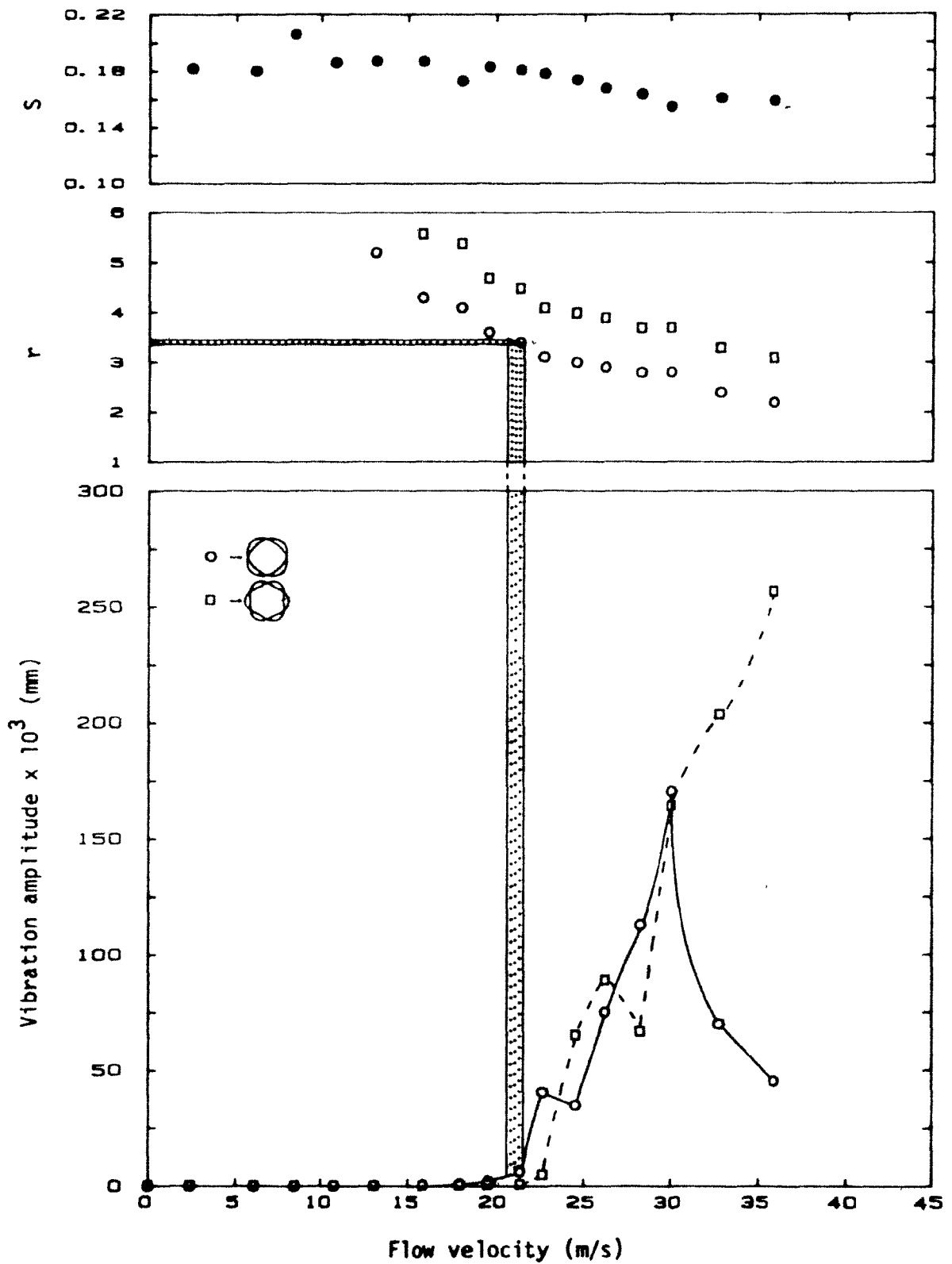
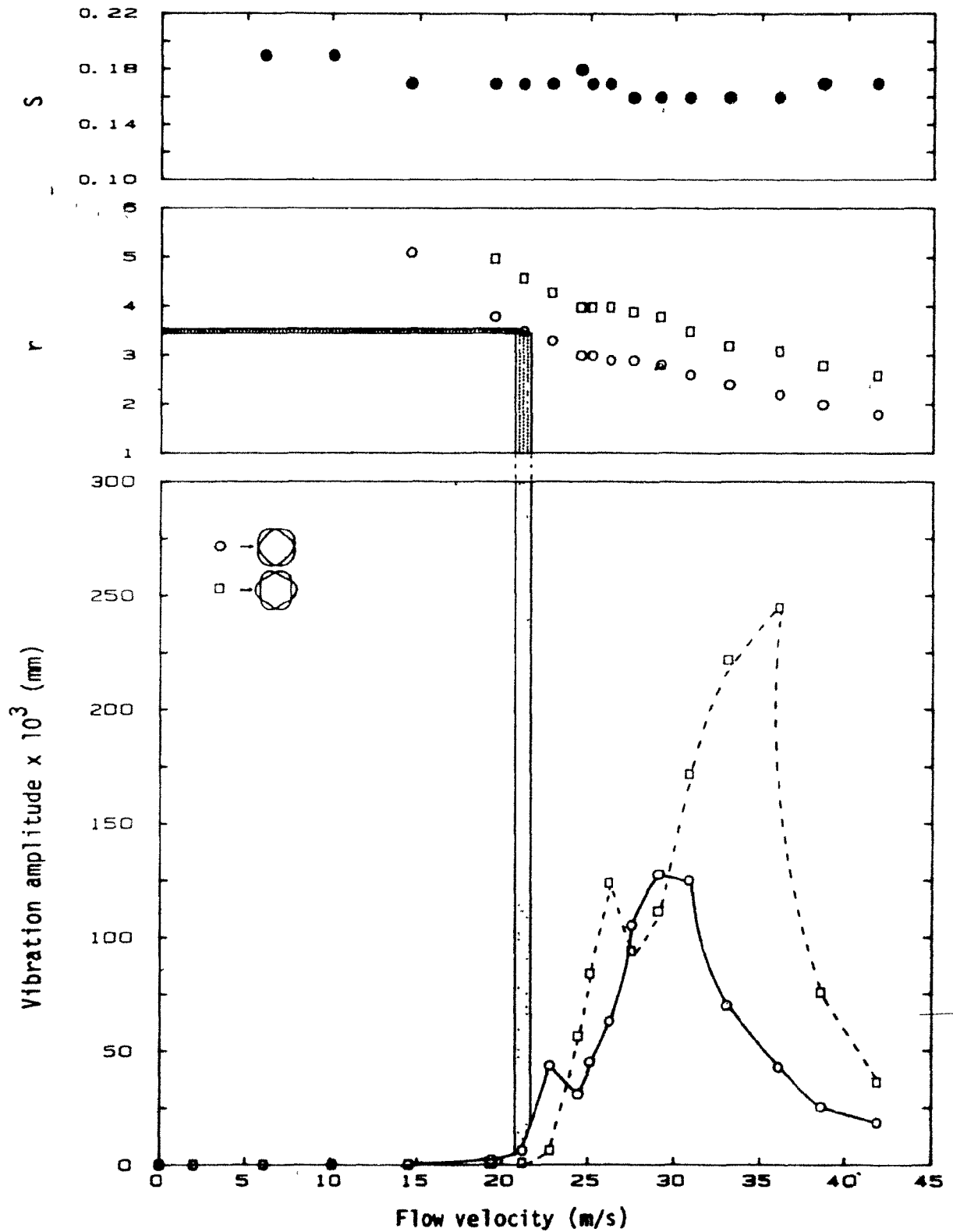
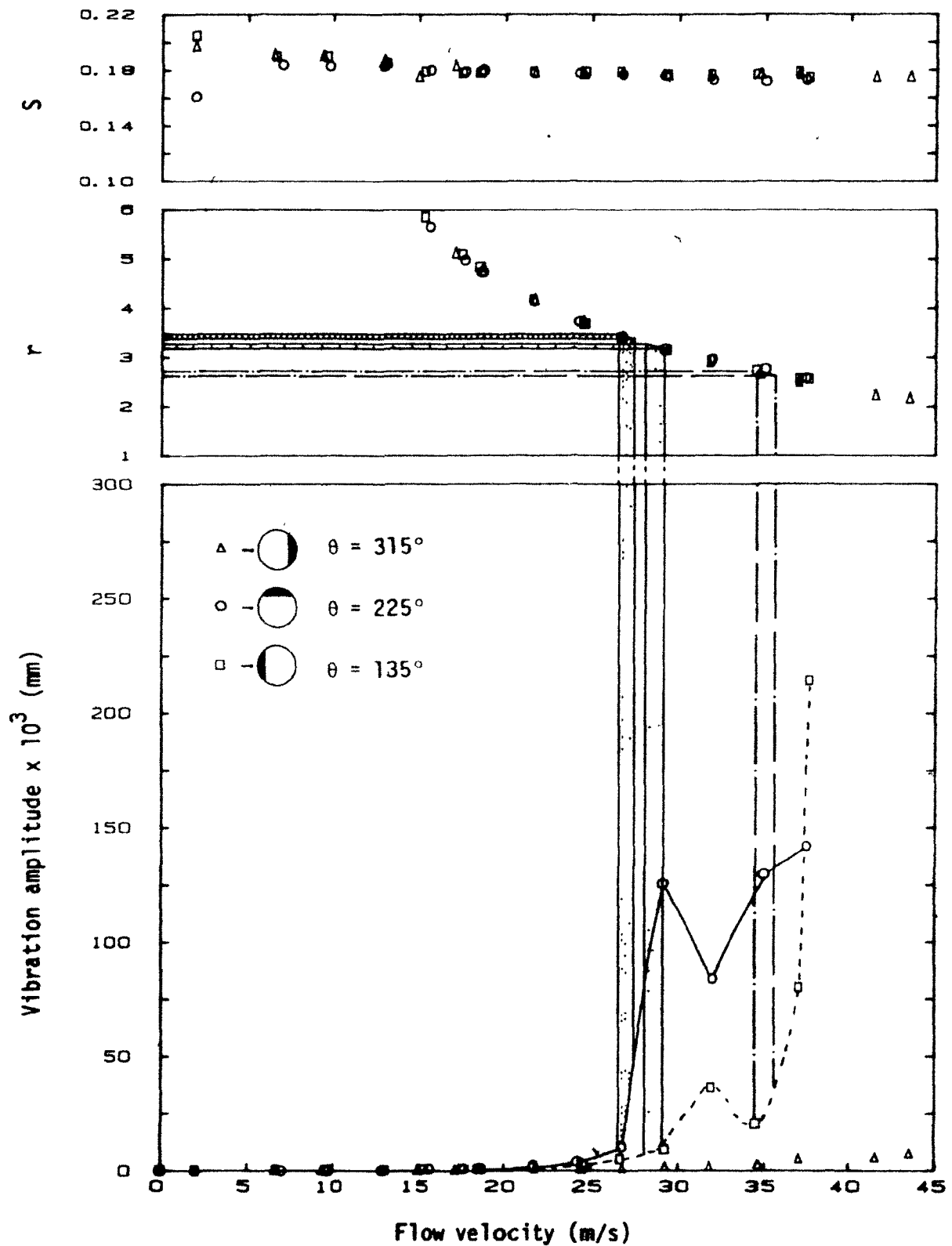


Figure 4.2: Measured vibration amplitude [at  $\theta = 315^\circ$ ,  $h = 89$  mm (3.5 in.)], wake flow periodicity in terms of Strouhal number  $S$ , and  $r = f_{n,m}/f_{vs}$  for a clamped-clamped shell (shell B) in cross flow.



**Figure 4.3:** Measured vibration amplitude [at  $\theta = 300^\circ$ ,  $h = 89$  mm (3.5 in.)], wake flow periodicity in terms of Strouhal number  $S$ , and  $r = f_{n,m}/f_{vs}$  for a clamped-clamped shell (shell B) in cross flow - repetition of test of Figure 4.2.



**Figure 4.4:** Measured vibration amplitude [at  $h = 89$  mm (3.5 in.) for  $n=2$  mode], wake flow periodicity in terms of Strouhal number  $S$ , and  $r = f_{n,m}/f_{vs}$  for shell B with an insert.  $\theta$  gives the angular position of photonic sensor ( $\theta = 0$  corresponds to the front stagnation point).

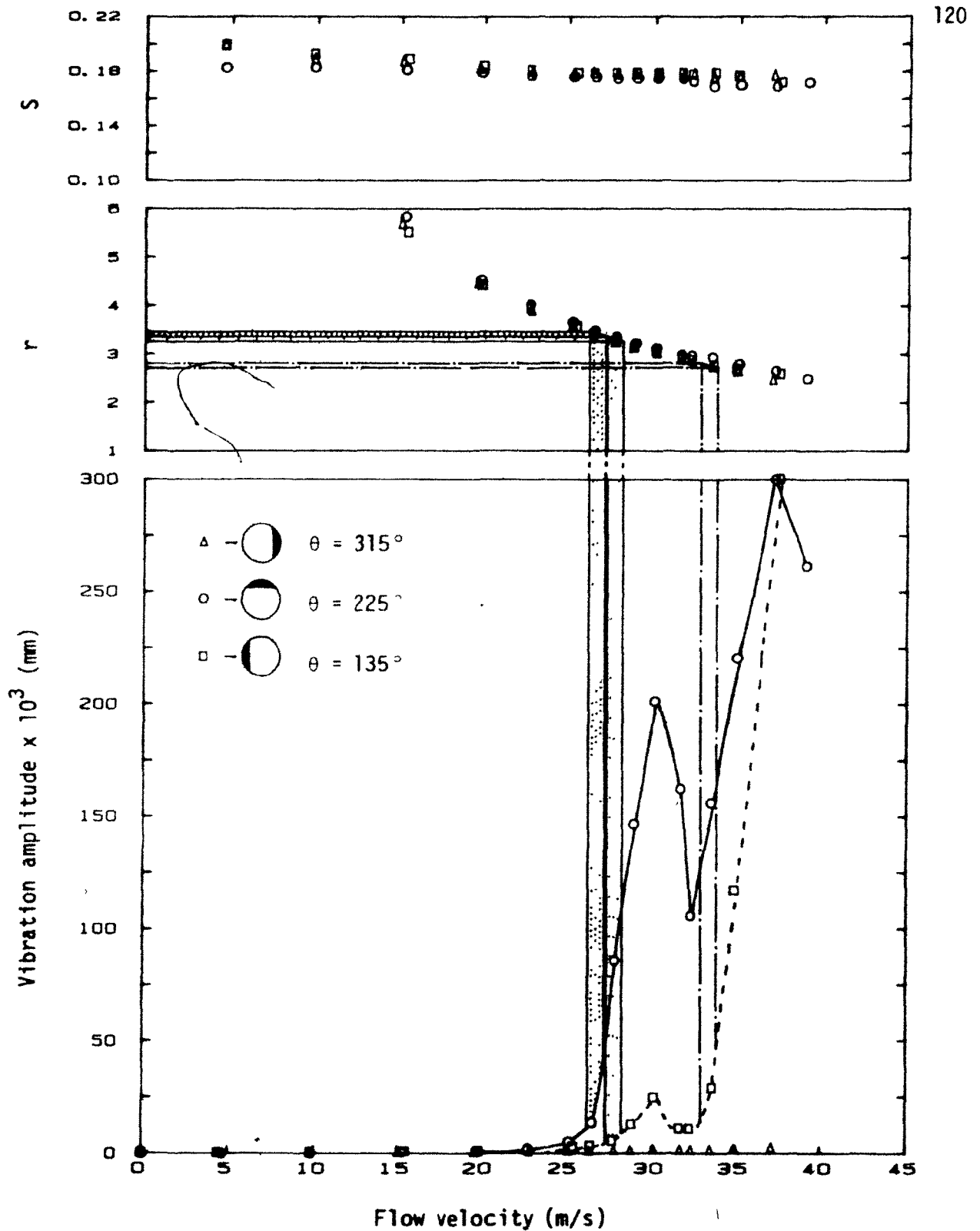


**Figure 4.5:** Measured vibration amplitude [at  $h = 89$  mm (3.5 in.) for  $n=2$  mode], wake flow periodicity in terms of Strouhal number  $S$ , and  $r = f_{n,p}/f_{vs}$  for shell B with an insert.  $\theta$  gives the angular position of photonic sensor - repetition of test of Figure 4.4.

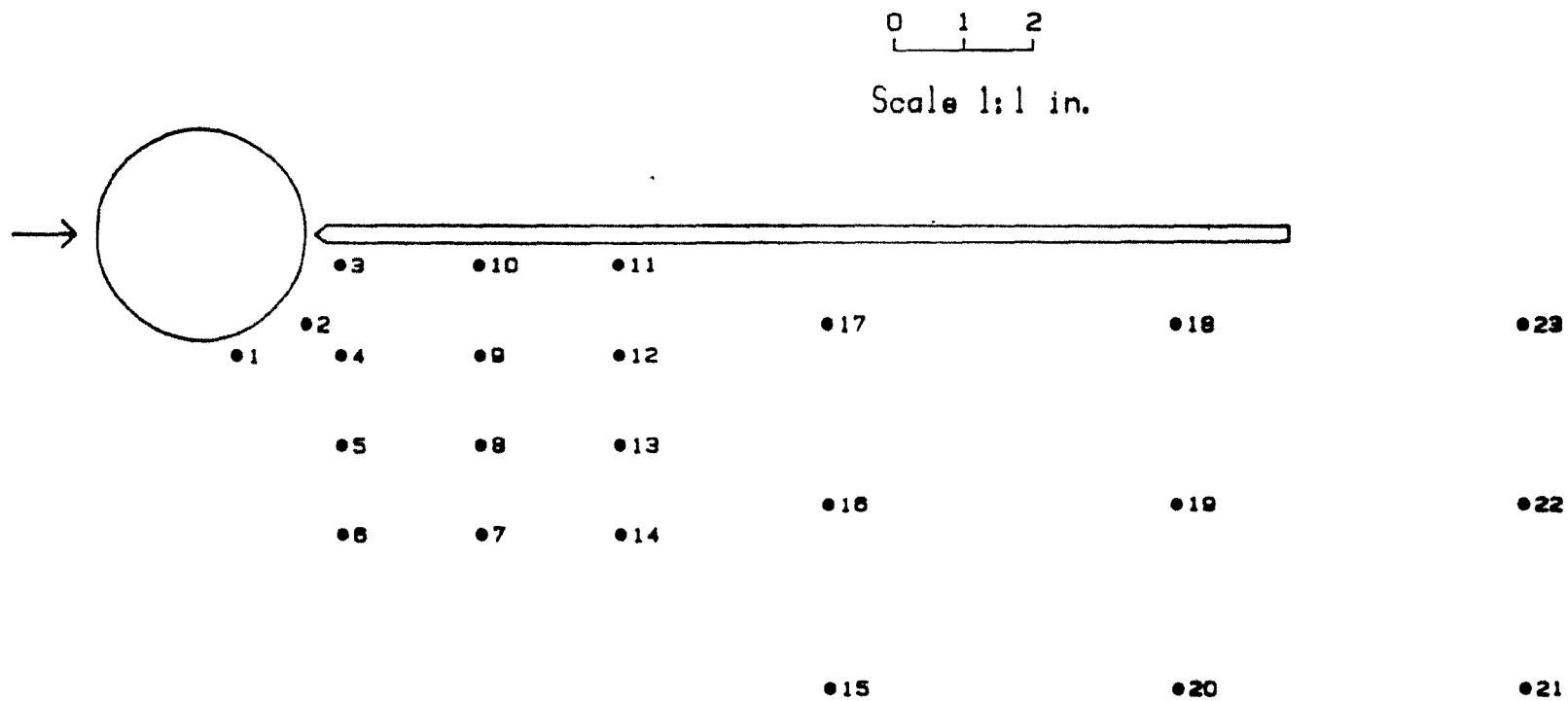
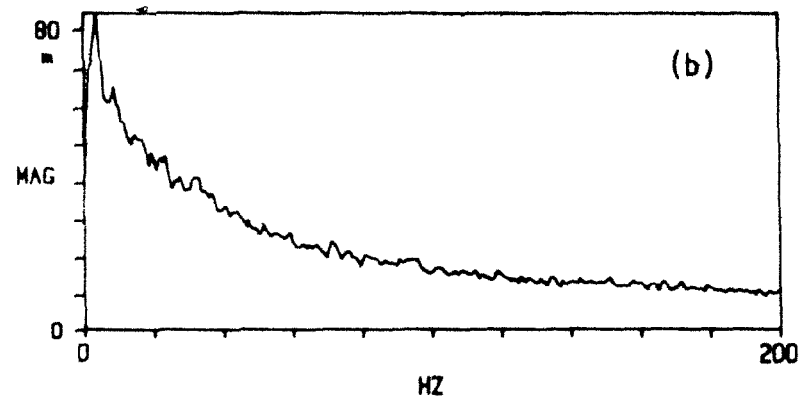
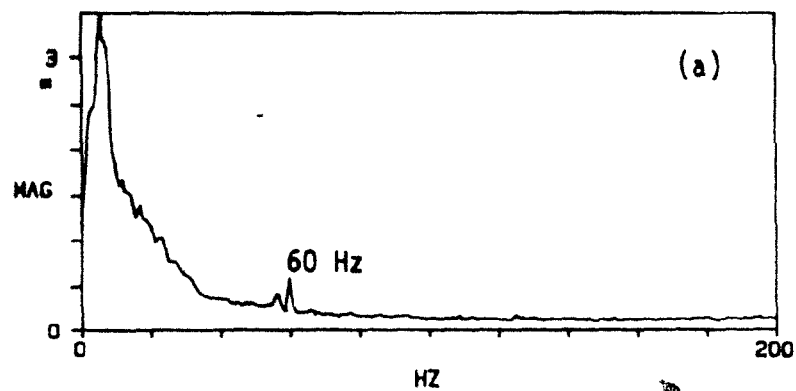
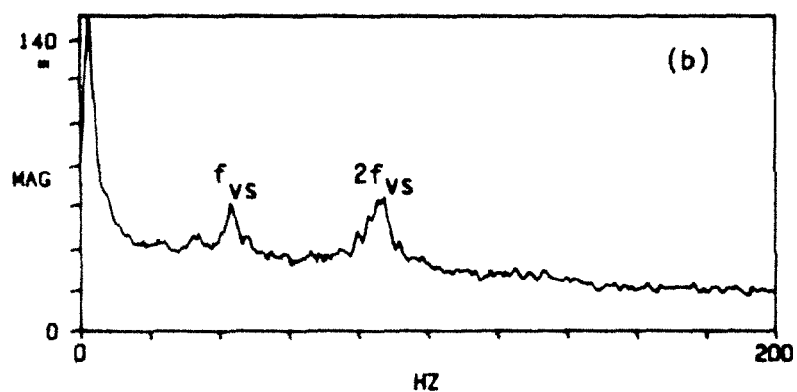
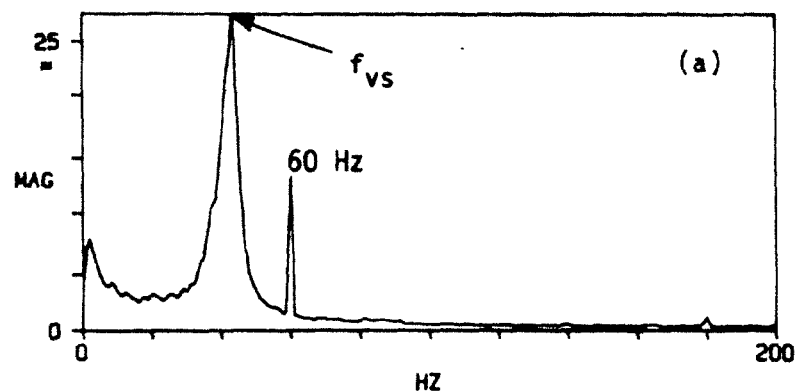


Figure 4.6: Various locations of the hot wire probe to investigate periodicity in the wake.



**Figure 4.7:** Frequency spectra of the wake at  $U = 18.0$  m/s ( $Re = 9.1 \times 10^4$ ) without (top) and with (bottom) a splitter plate. (a) At position 1; (b) at position 3 (see Figure 4.6).

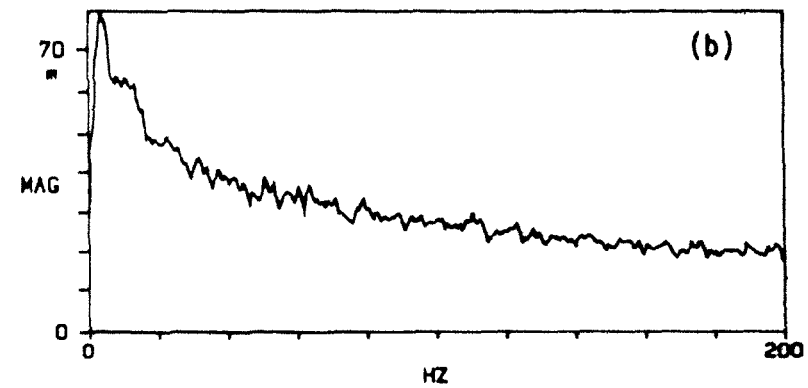
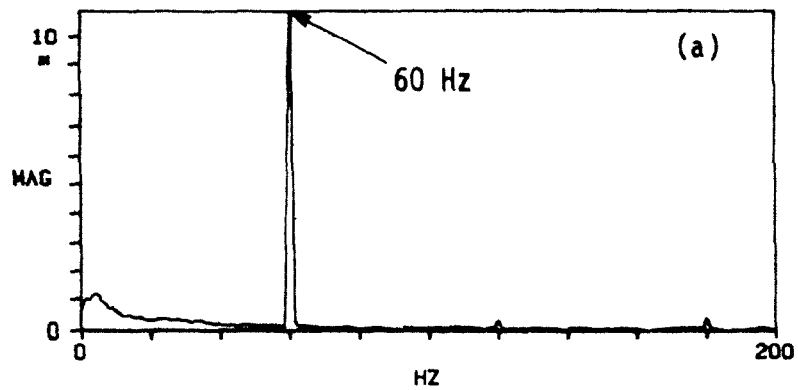
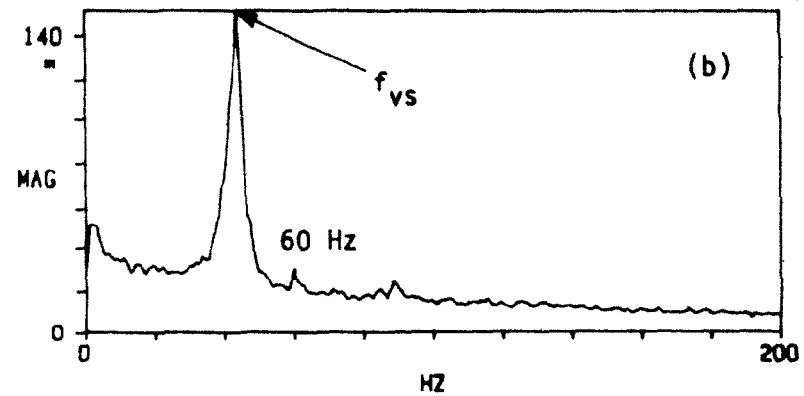
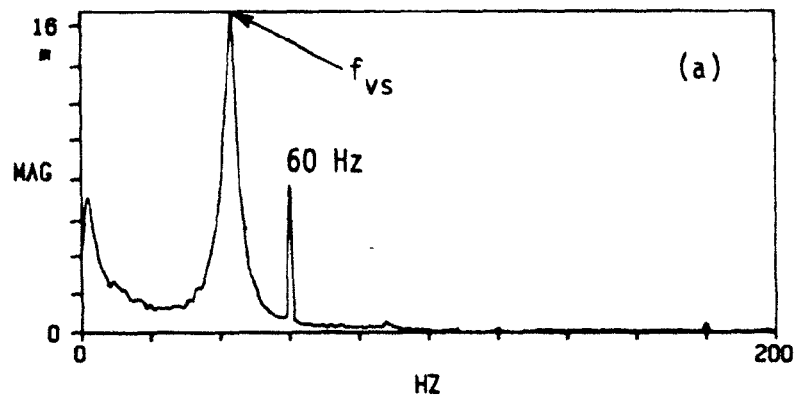
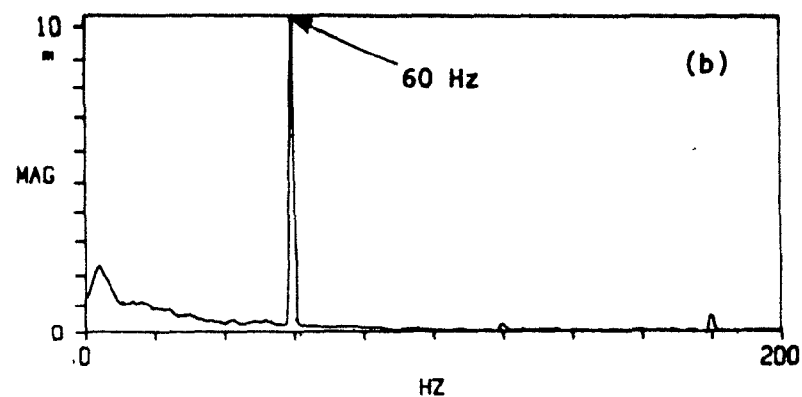
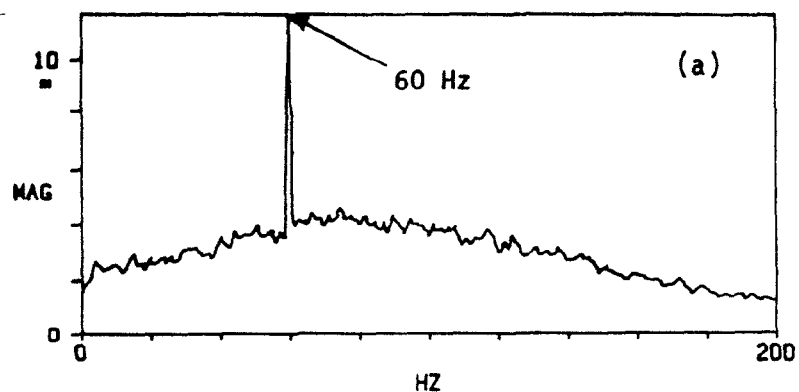
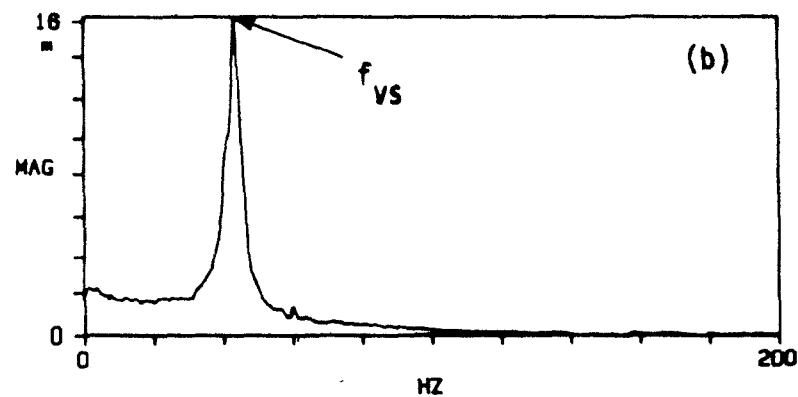
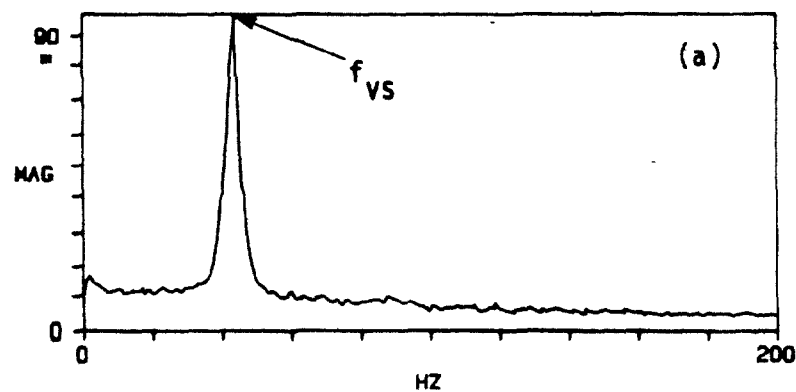
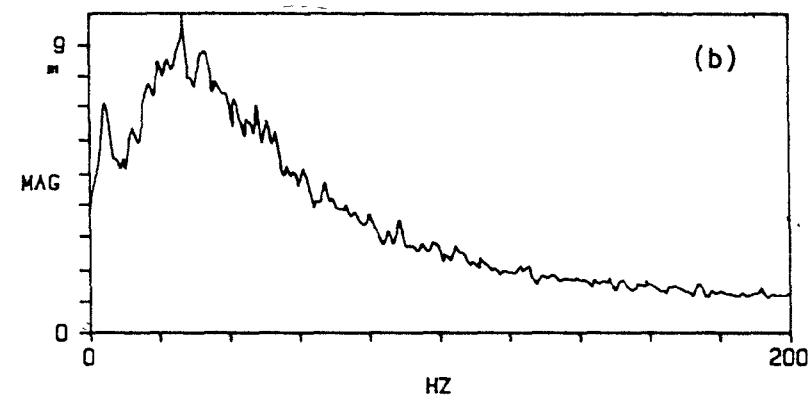
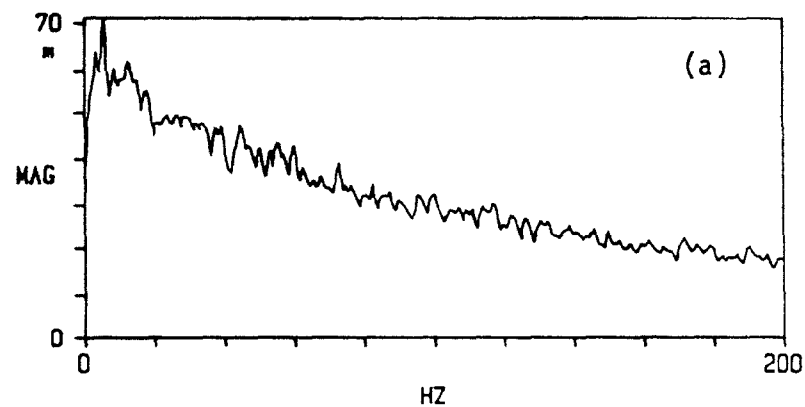
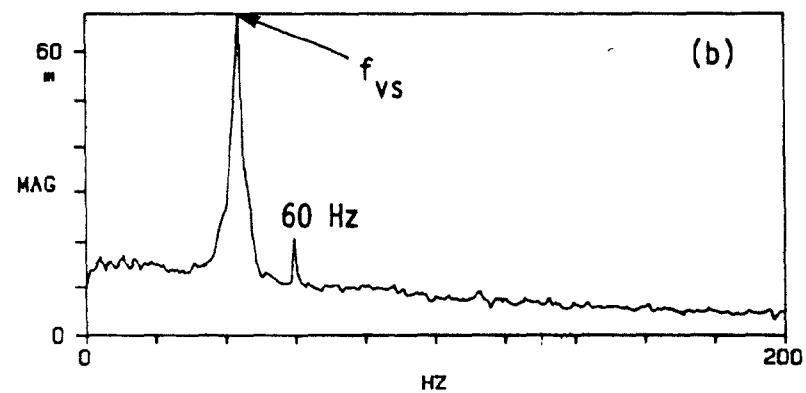
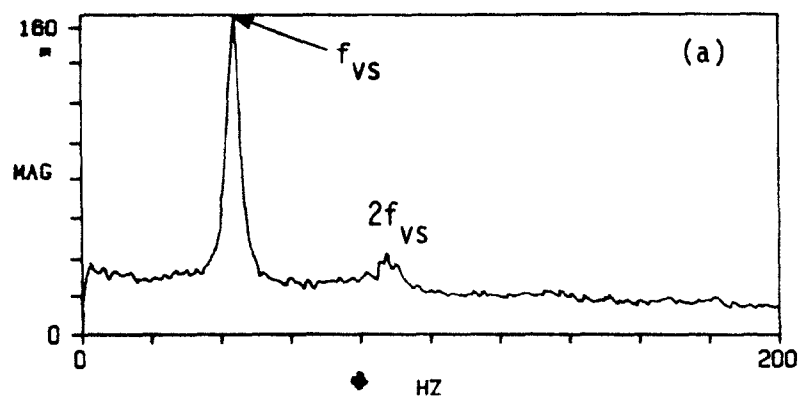


Figure 4.8: Frequency spectra of the wake at  $U = 18.0$  m/s ( $Re = 9.1 \times 10^4$ ) without (top) and with (bottom) a splitter plate. (a) At position 6; (b) at position 9 (see Figure 4.6).





**Figure 4.9:** Frequency spectra of the wake at  $U = 18.0$  m/s ( $Re = 9.1 \times 10^4$ ) without (top) and with (bottom) a splitter plate. (a) At position 13; (b) at position 15 (see Figure 4.6).



**Figure 4.10:** Frequency spectra of the wake at  $U = 18.0$  m/s ( $Re = 9.1 \times 10^4$ ) without (top) and with (bottom) a splitter plate. (a) At position 17; (b) at position 19 (see Figure 4.6).

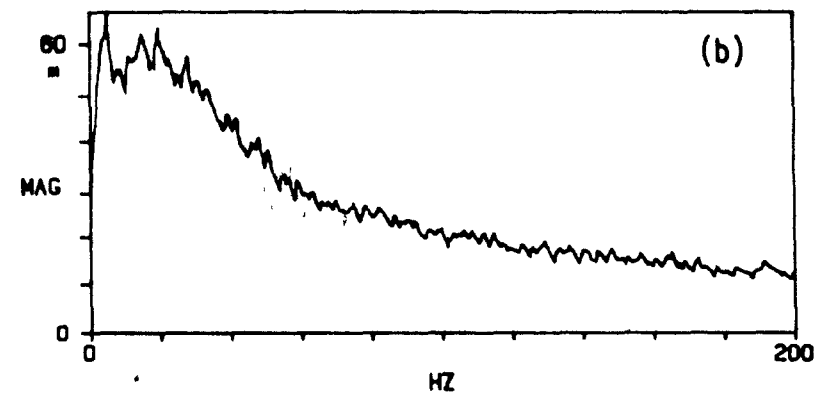
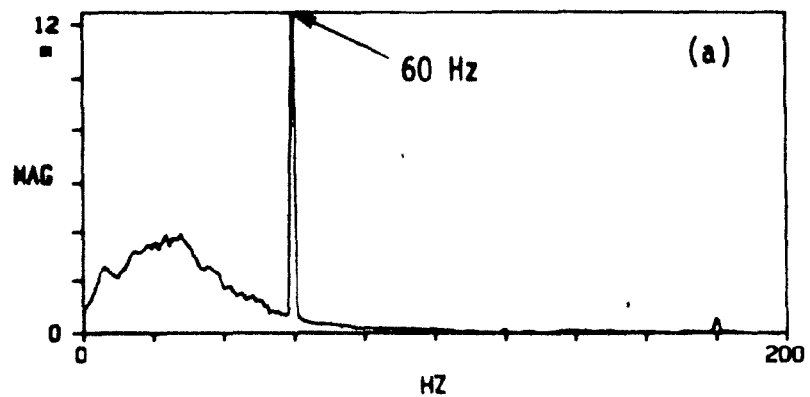
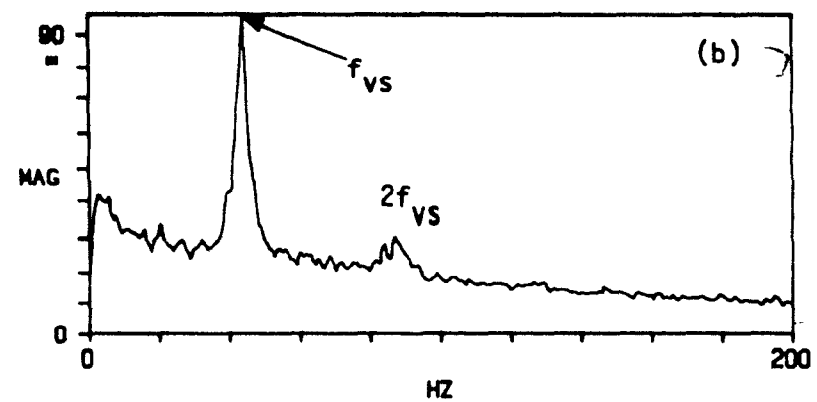
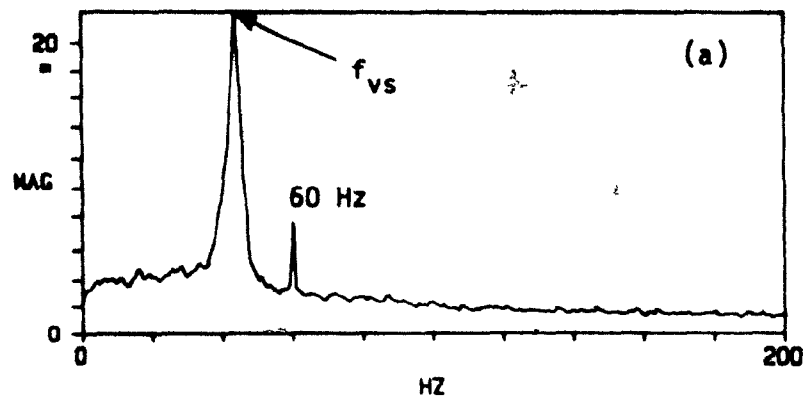


**Figure 4.11:** Frequency spectra of the wake at  $U = 18.0$  m/s ( $Re = 9.1 \times 10^4$ ) without (top) and with (bottom) a splitter plate. (a) At position 21; (b) at position 23 (see Figure 4.6).

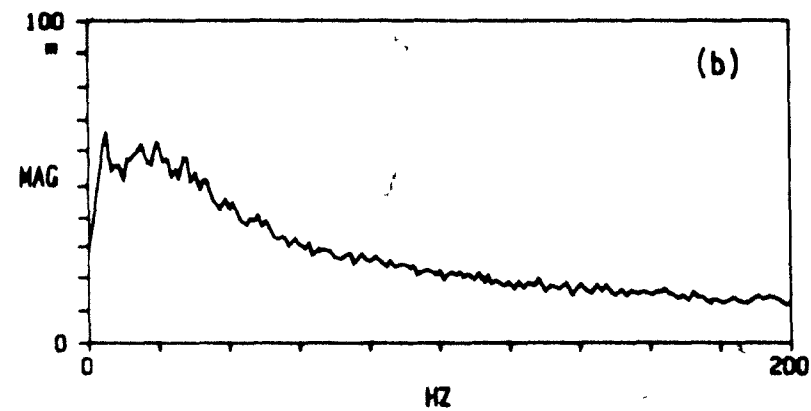
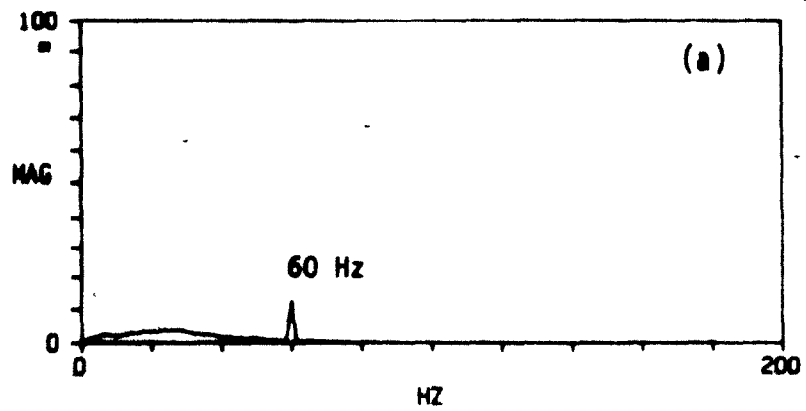
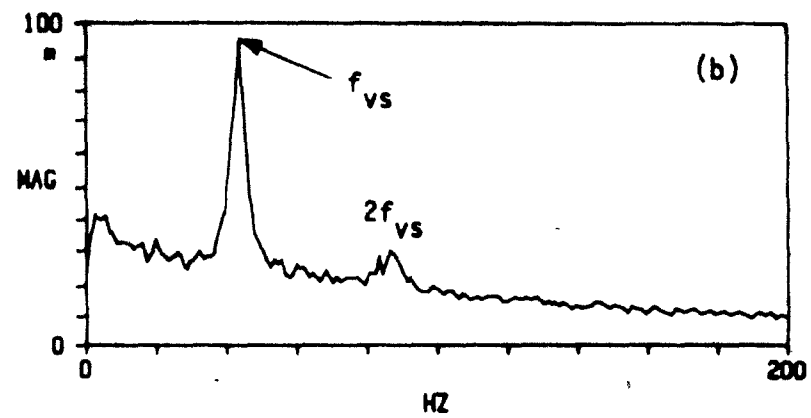
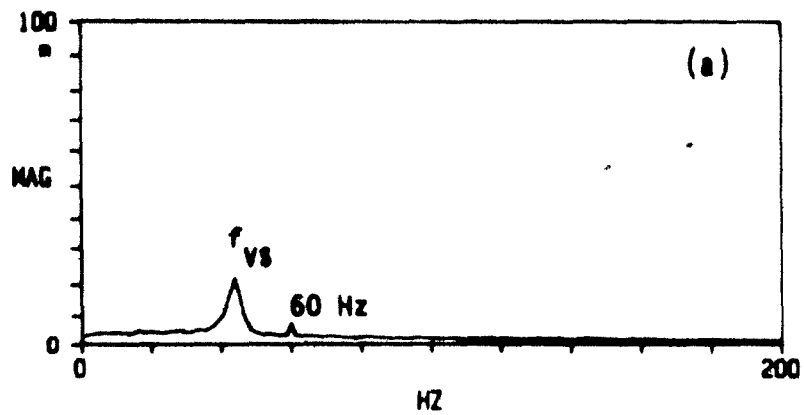
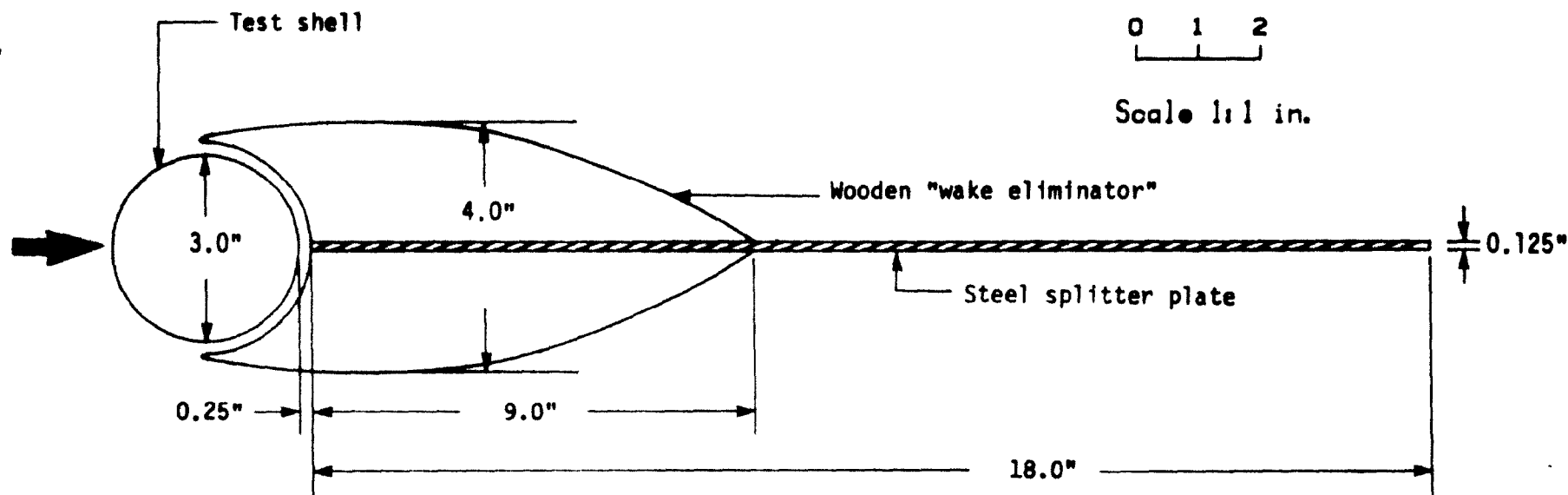
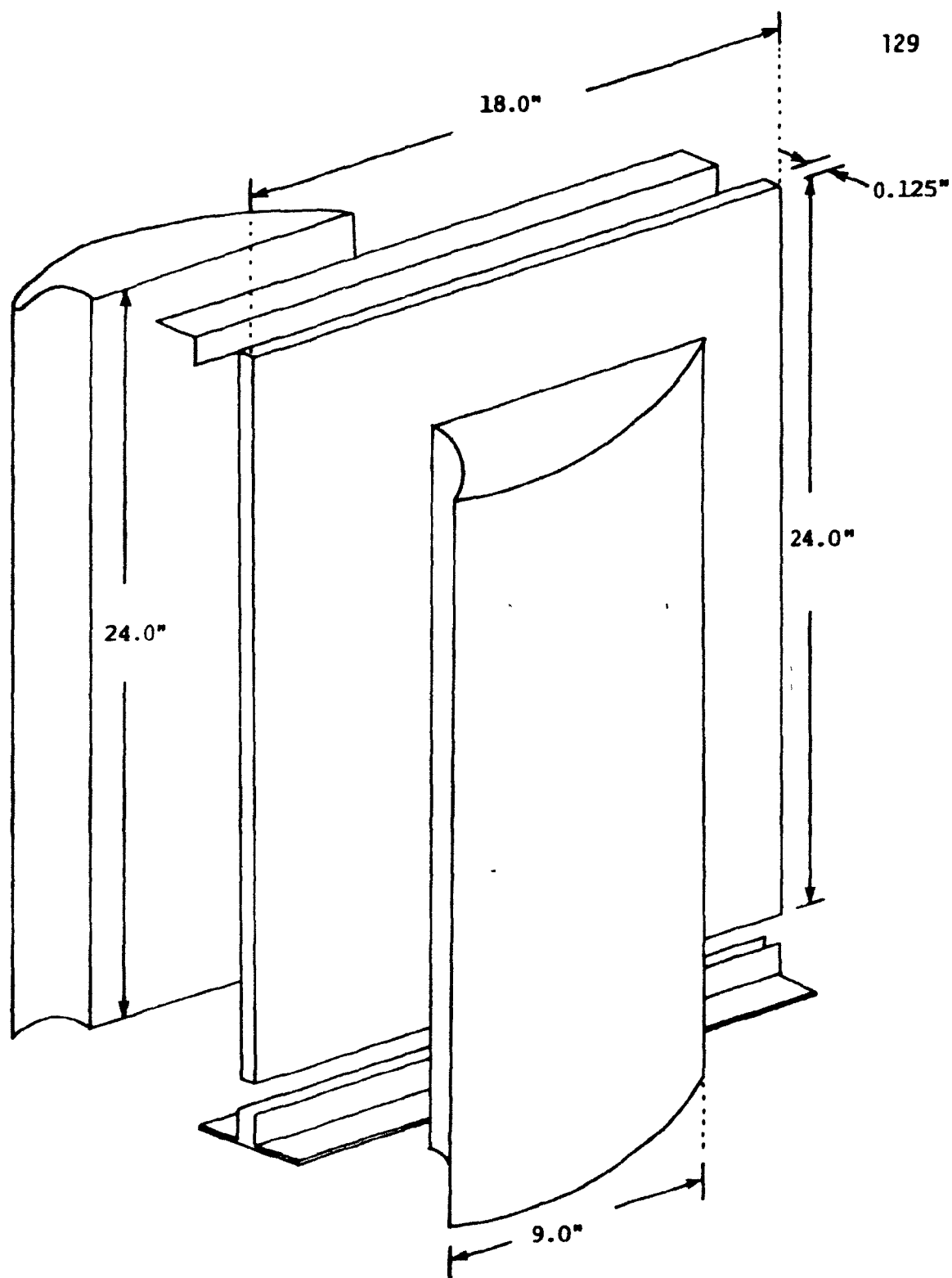


Figure 4.12: The frequency spectra of Figure 4.11 replotted on the same scale.



**Figure 5.1:** Top view of the cylindrical shell with wake eliminator and extended splitter plate in position in the wind tunnel test section. (All dimensions are in inches; 1 in. = 25.4 mm).



**Figure 5.2:** Exploded view of the wake eliminator without the suction device.

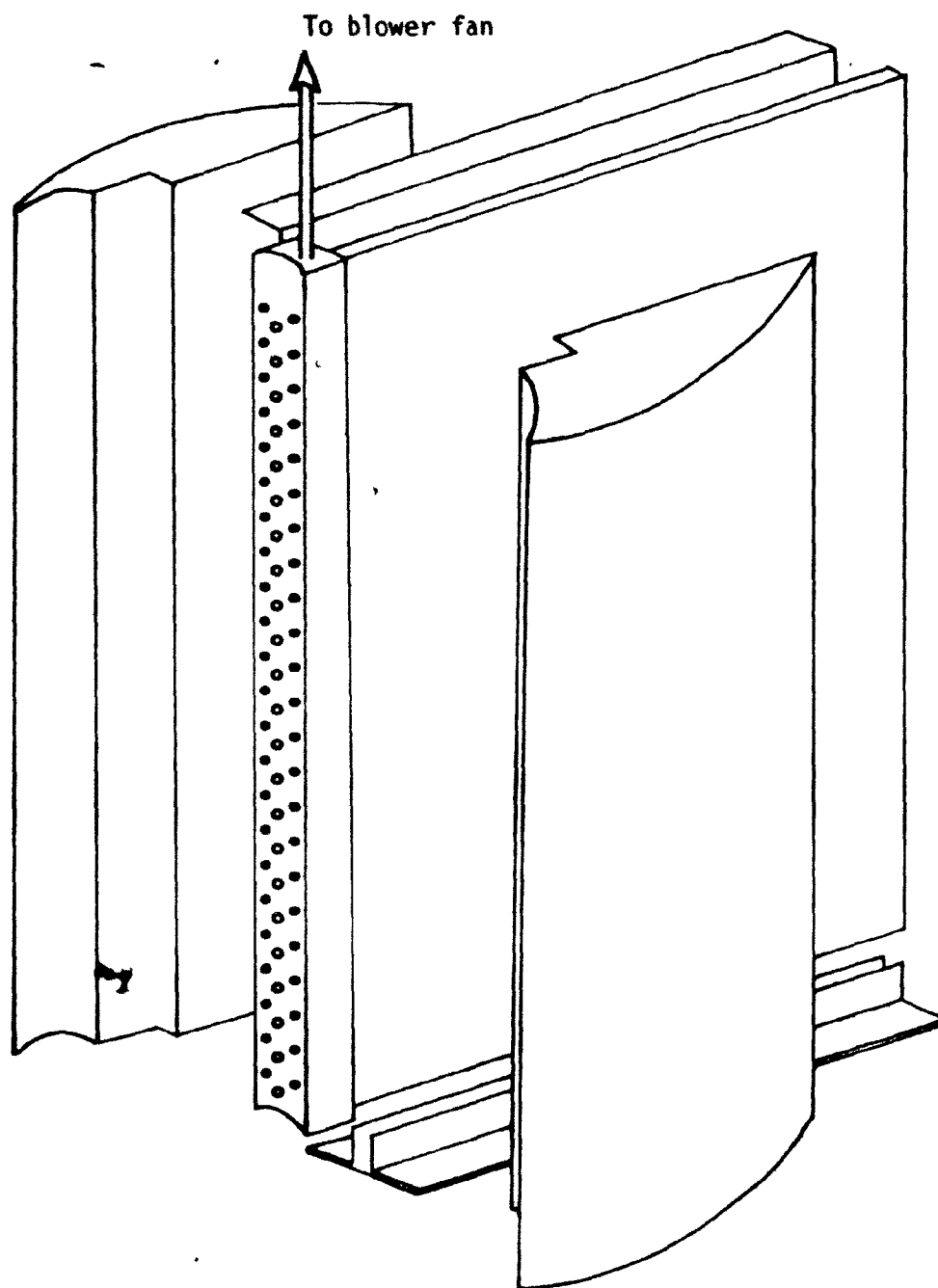


**Figure 5.3:** Exploded view of the wake eliminator, with the suction device, used in an attempt to create a coherent back flow.

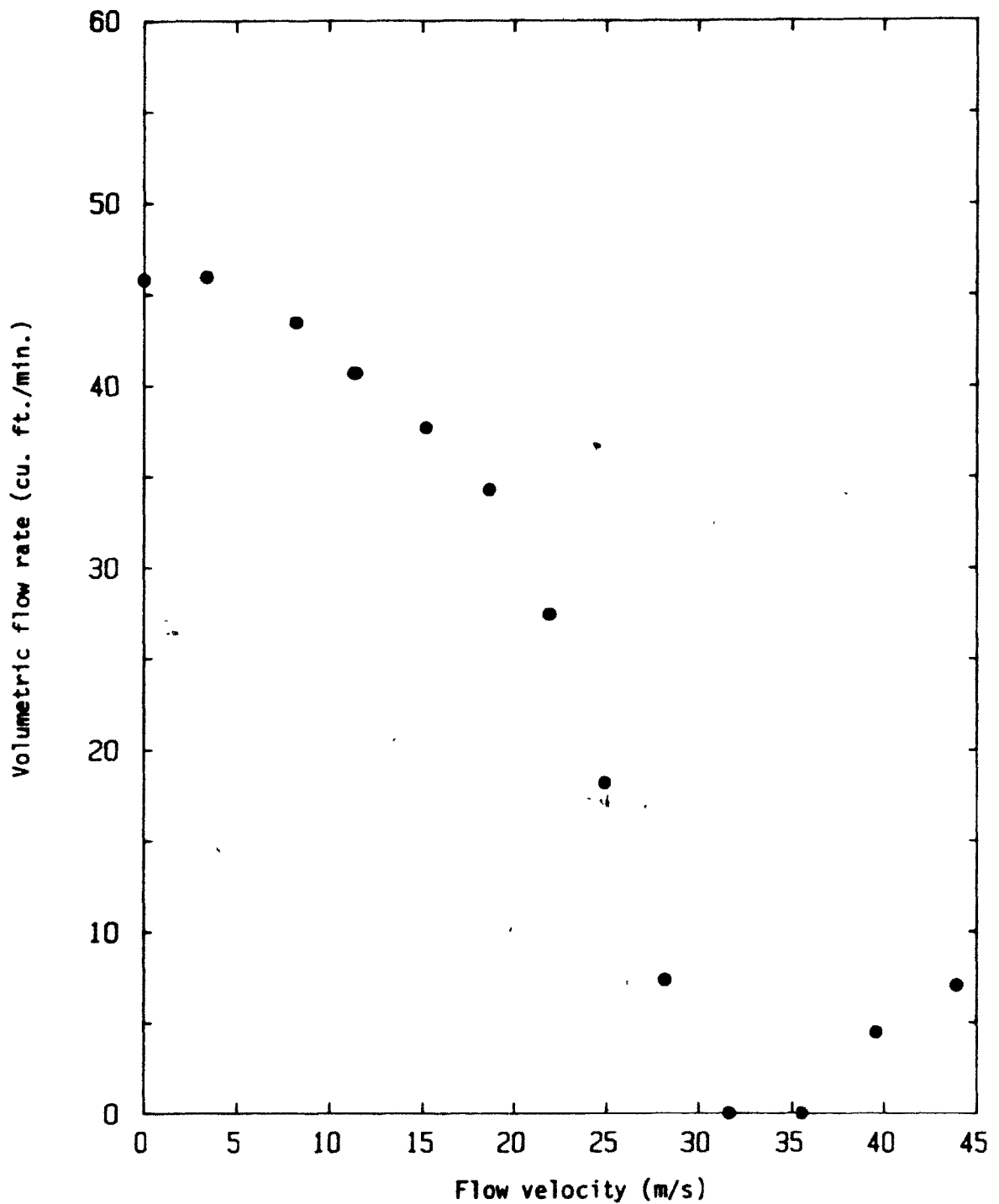


**Figure 5.4:** Volumetric flow rate through the suction device *versus* flow velocity in the tunnel (1 cu. ft. = 0.03 m<sup>3</sup>).



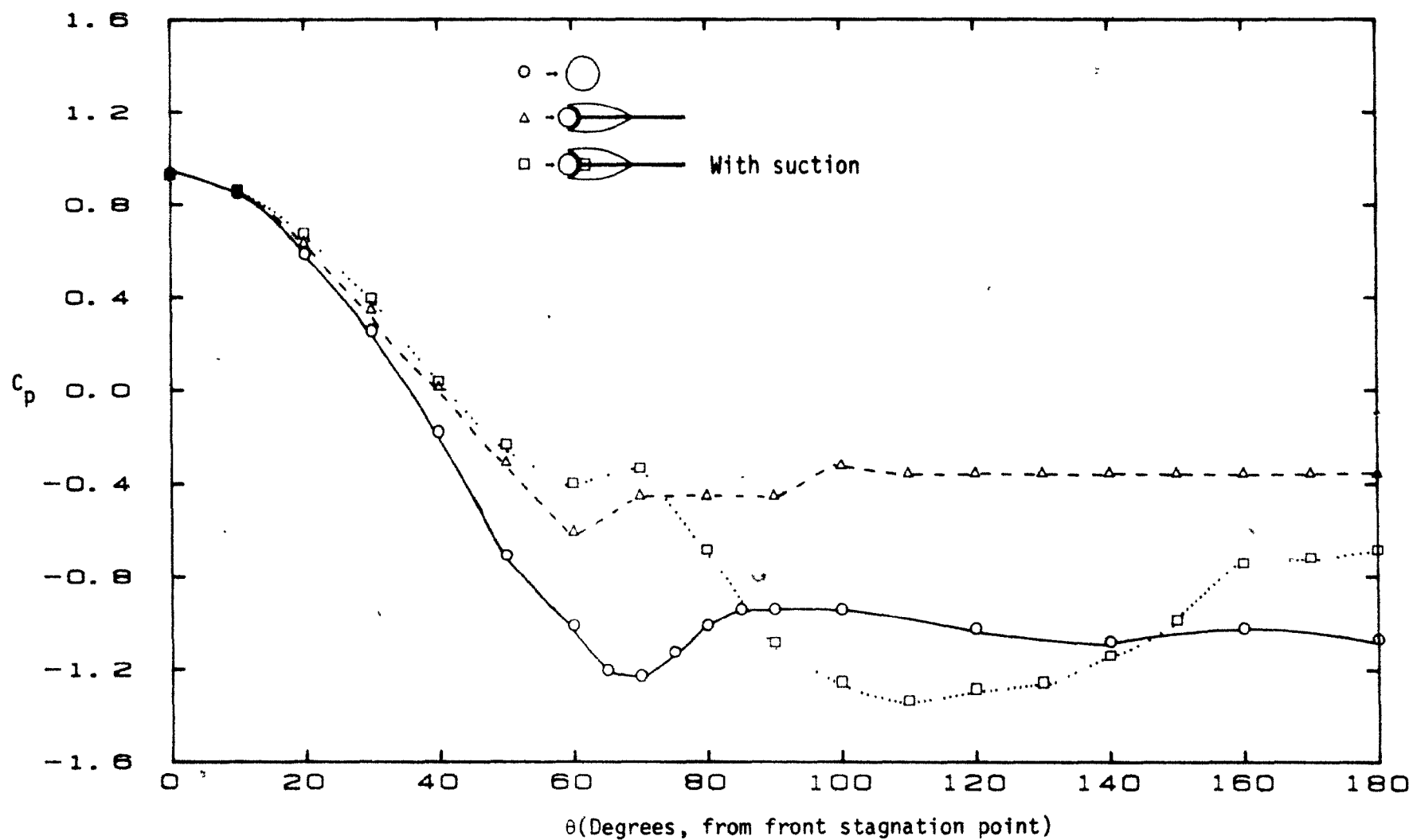


**Figure 5.5:** Pressure distribution around a circular cylinder, with and without wake eliminator and suction, at mid-span of the cylinder for  $U = 7.5$  m/s ( $Re = 3.80 \times 10^4$ ).

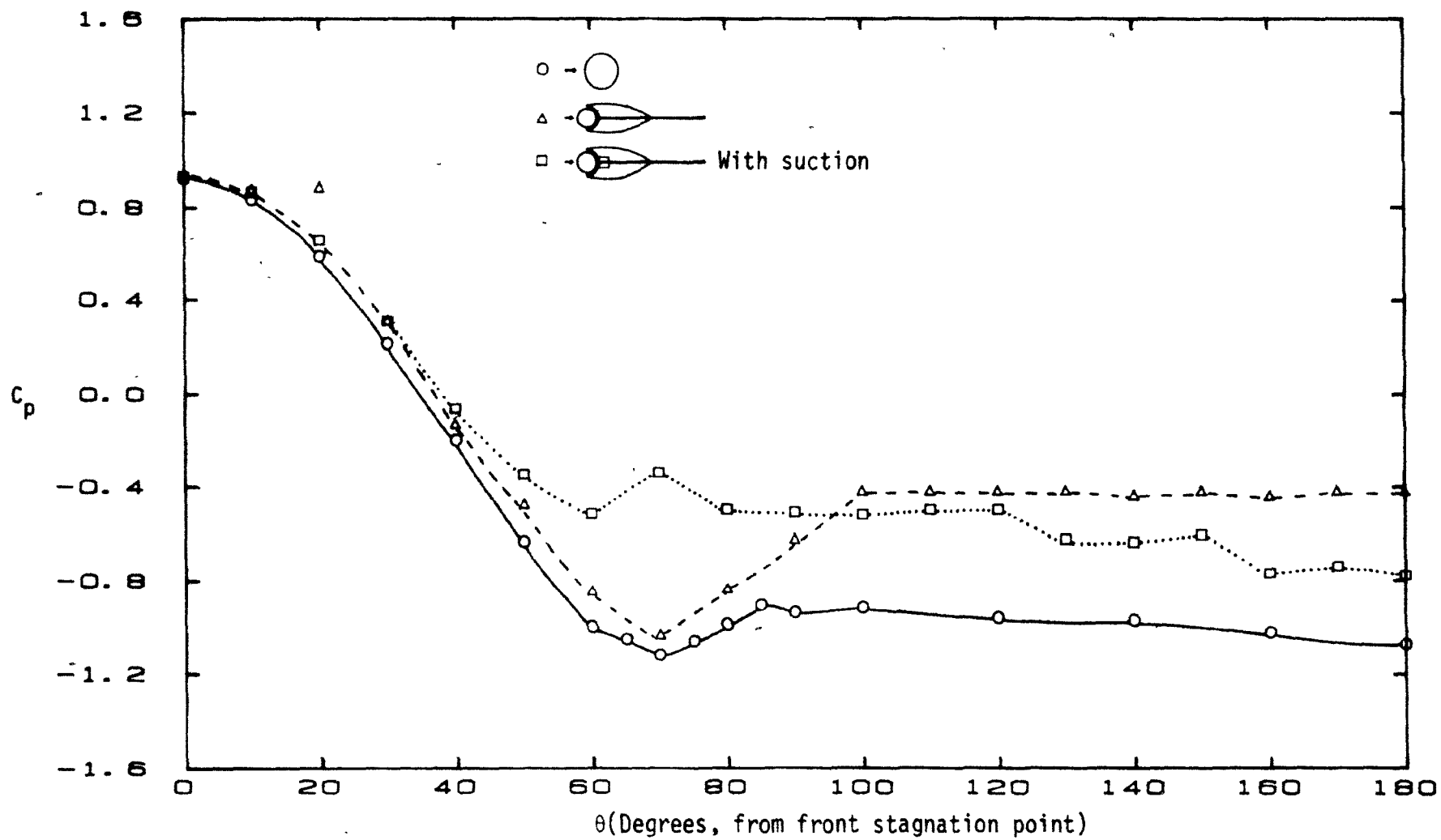


**Figure 5.6:** Pressure distribution around a circular cylinder, with and without wake eliminator and suction, at mid-span of the cylinder, for  $U = 18.0$  m/s ( $Re = 9.0 \times 10^4$ ).

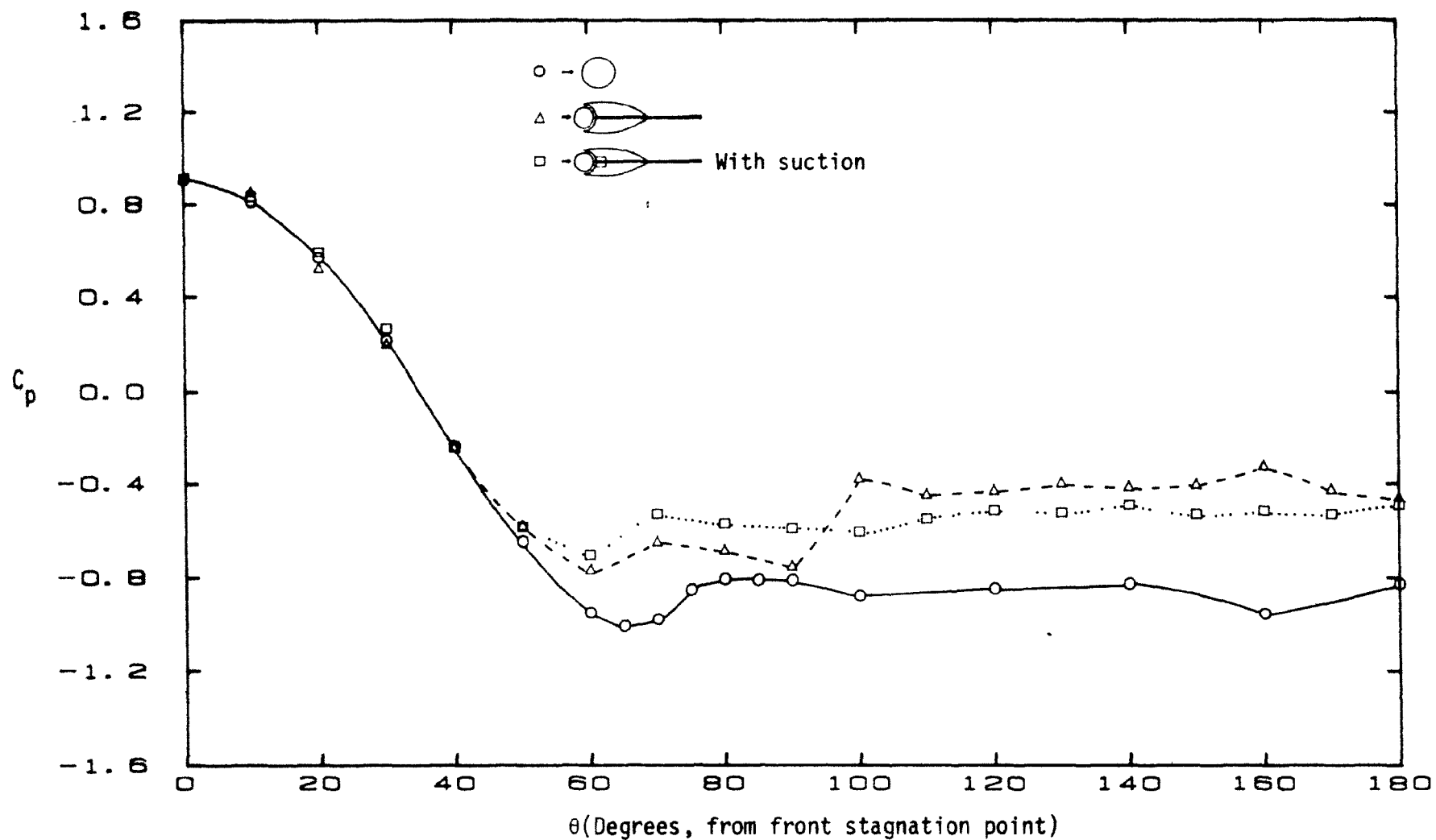


**Figure 5.7:** Pressure distribution around a circular cylinder, with and without wake eliminator and suction, at mid-span of the cylinder, for  $U = 36.0$  m/s ( $Re = 1.82 \times 10^5$ ).

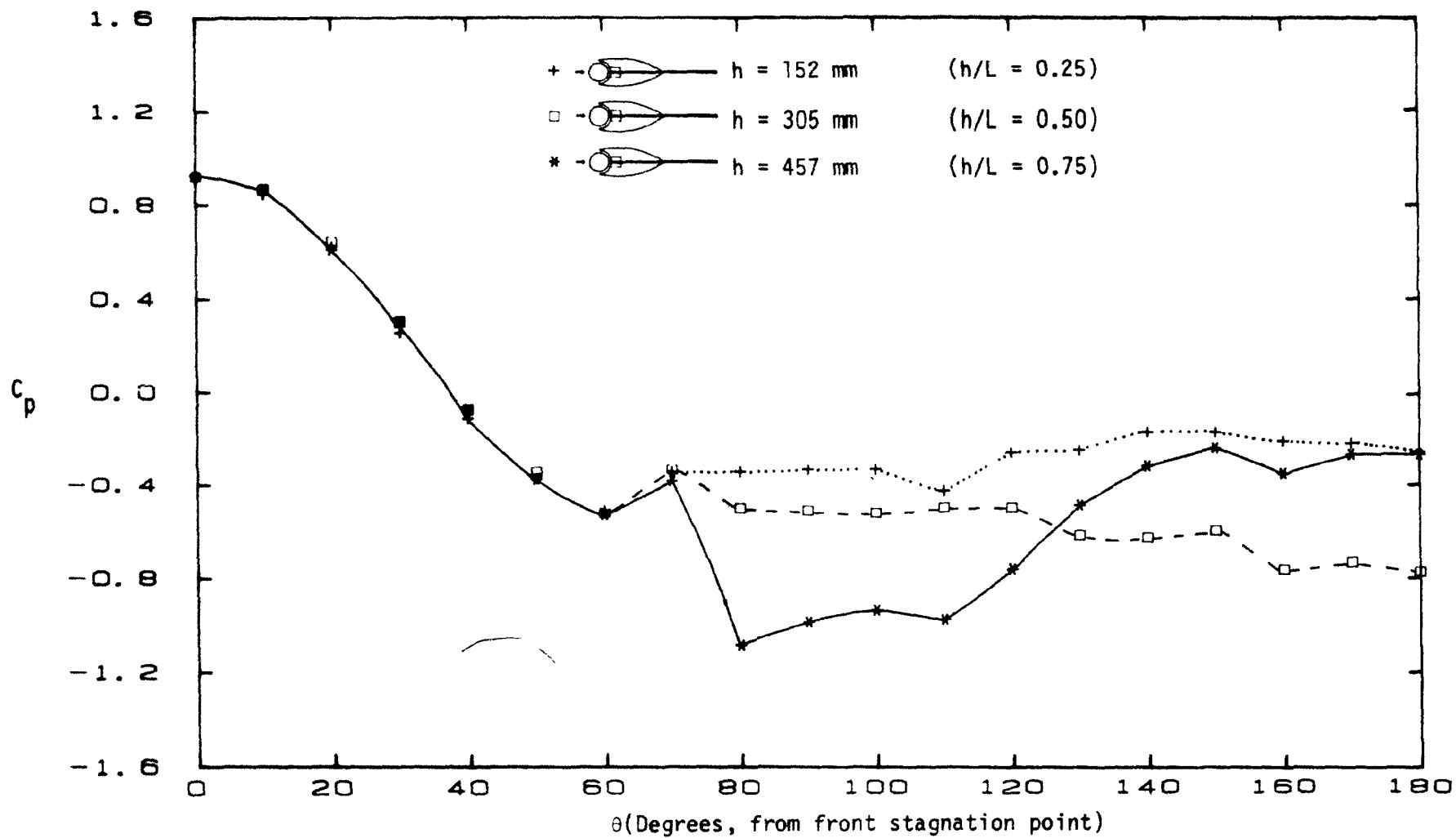


**Figure 5.8:** Comparison of the pressure distribution around a circular cylinder with wake eliminator and suction, at different heights,  $h$ , along the span of the cylinder;  $U = 18.0 \text{ m/s}$  ( $Re = 9.10 \times 10^4$ );  $h$  is measured from the tunnel floor upwards.

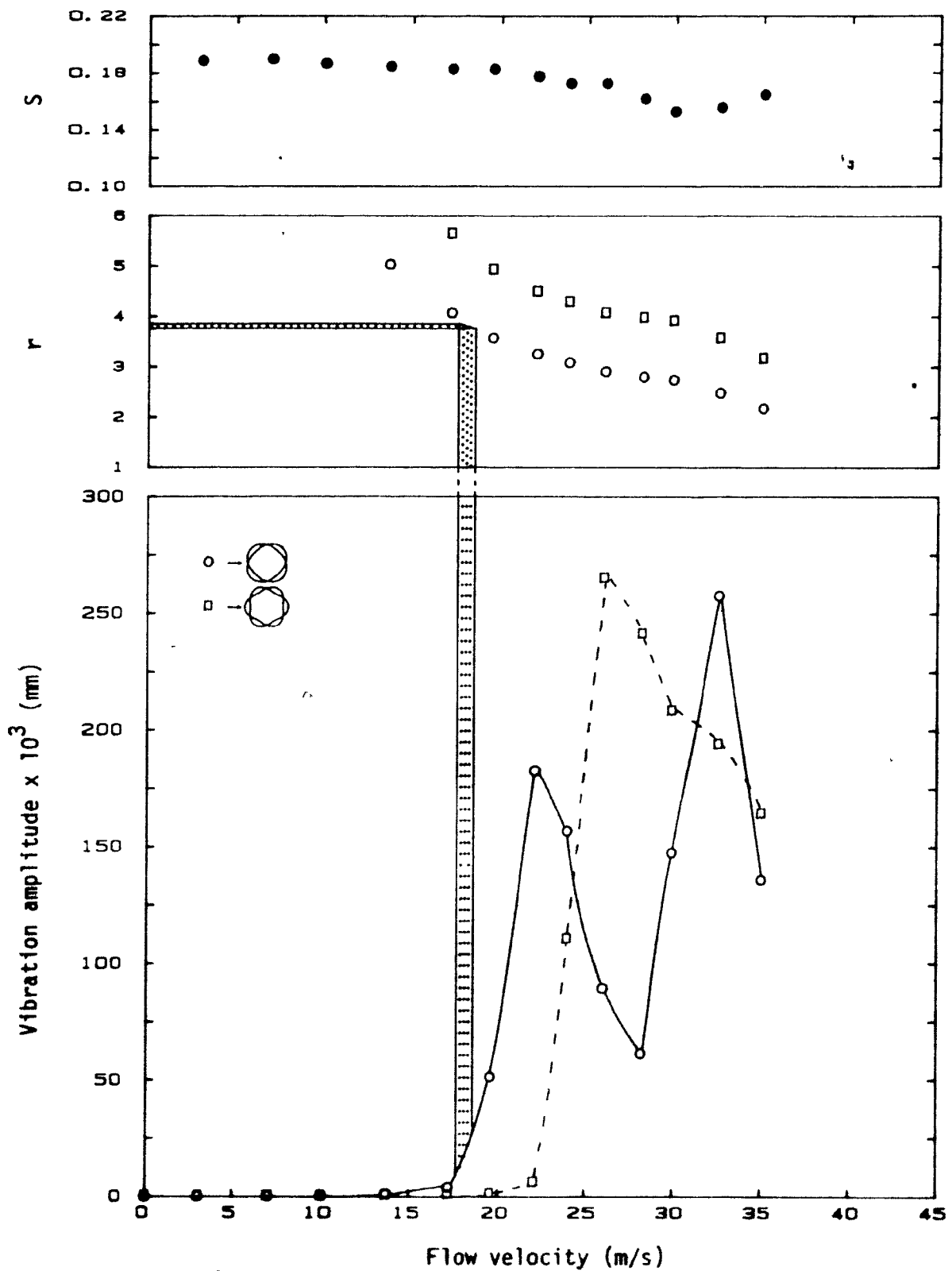


**Figure 5.9:** Measured vibration amplitude [at  $\theta = 315^\circ$ ,  $h = 94$  mm (3.7 in.)], wake flow periodicity in terms of Strouhal number  $S$ , and  $r = f_{n,m}/f_{vs}$  for a clamped-clamped shell (shell C) in cross flow.

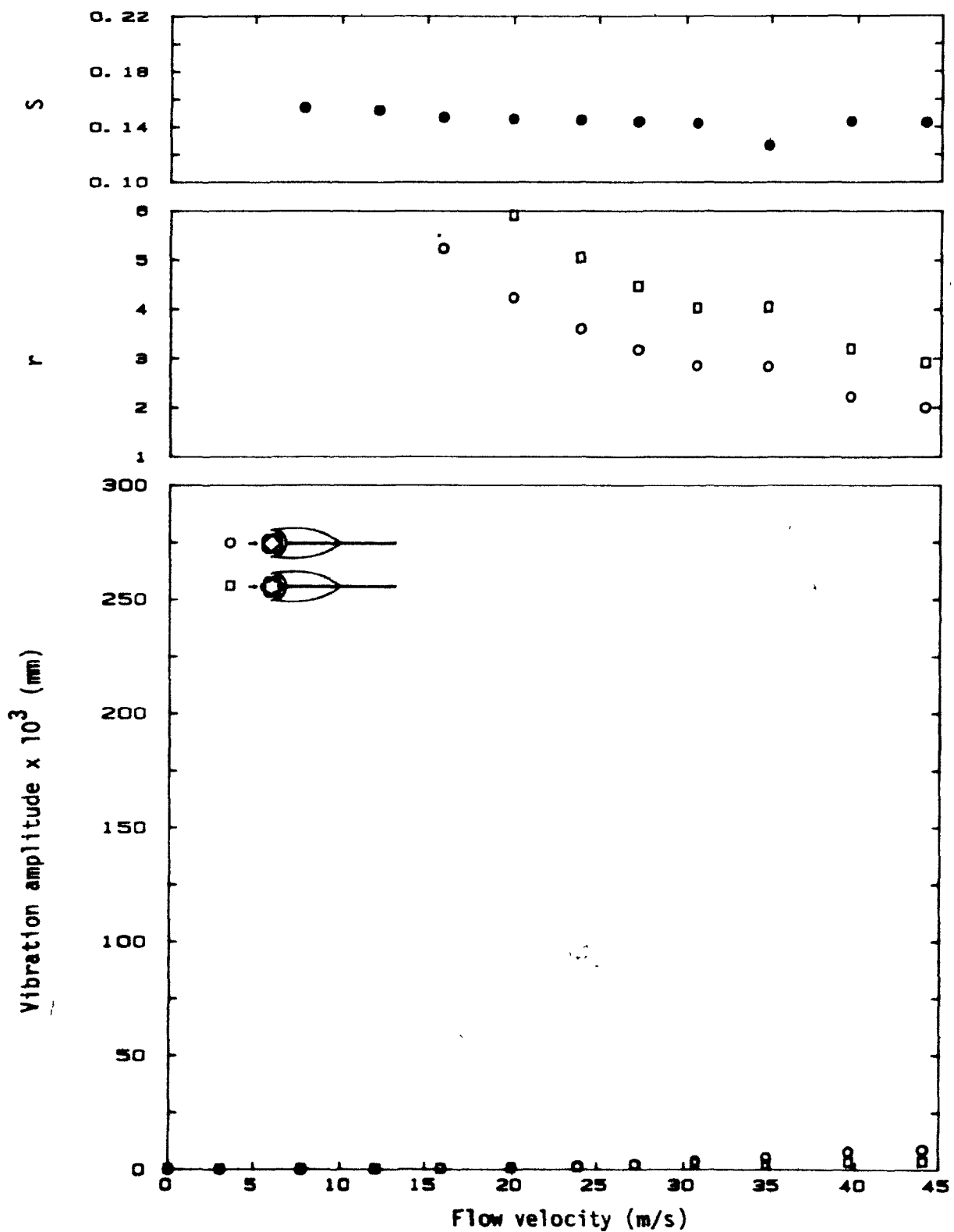


**Figure 5.10:** Measured vibration amplitude [at  $\theta = 315^\circ$ ,  $h = 94$  mm (3.7 in.)], wake flow periodicity in terms of Strouhal number  $S$ , and  $r = f_{n,m}/f_{vs}$  for a clamped-clamped shell (shell C) with wake eliminator in position.

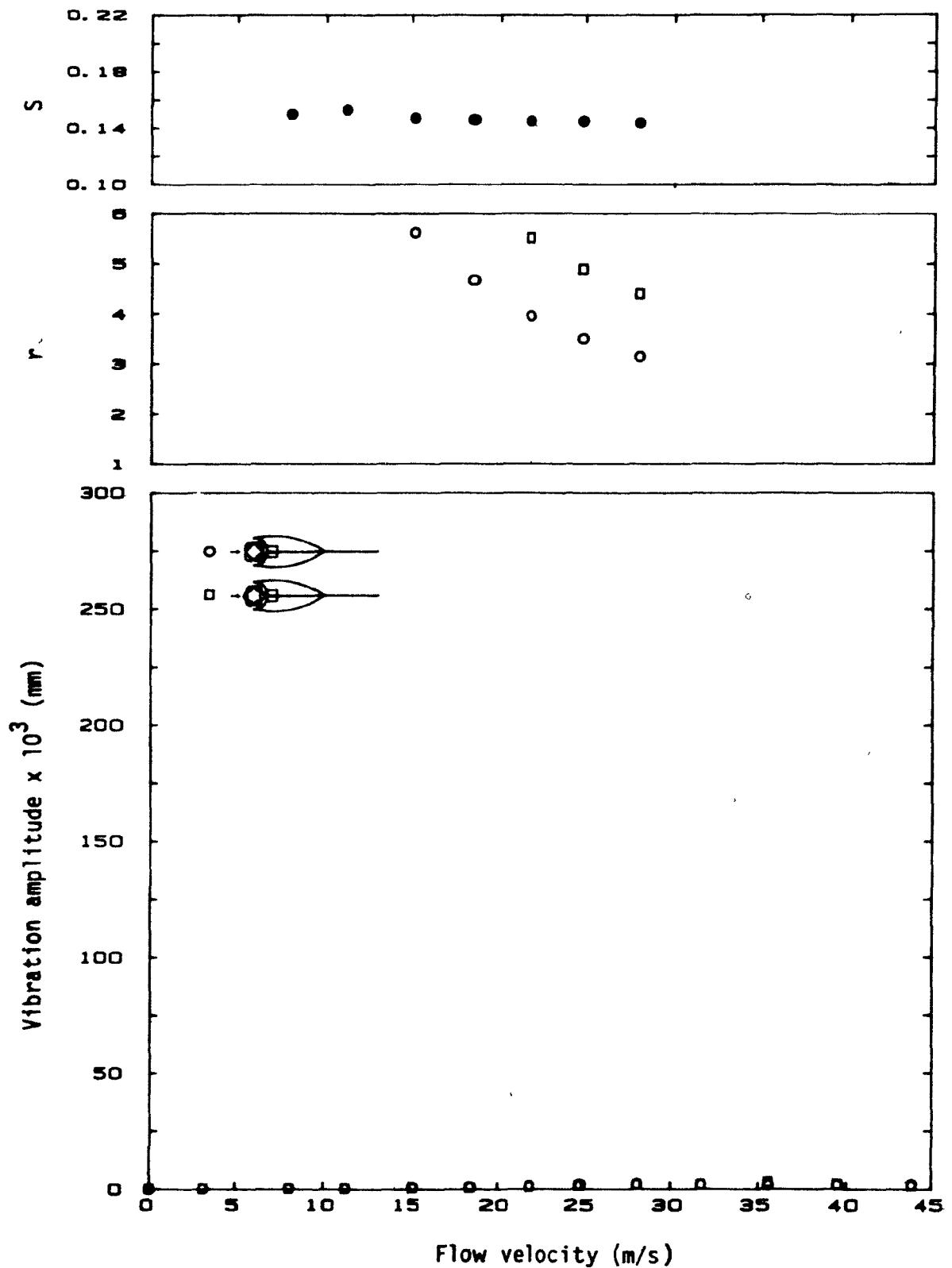


**Figure 5.11:** Measured vibration amplitude [at  $\theta = 315^\circ$ ,  $h = 94$  mm (3.7 in.)], wake flow periodicity in terms of Strouhal number  $S$ , and  $r = f_{n,m}/f_{VS}$  for a clamped-clamped shell (shell C) with wake eliminator and suction.

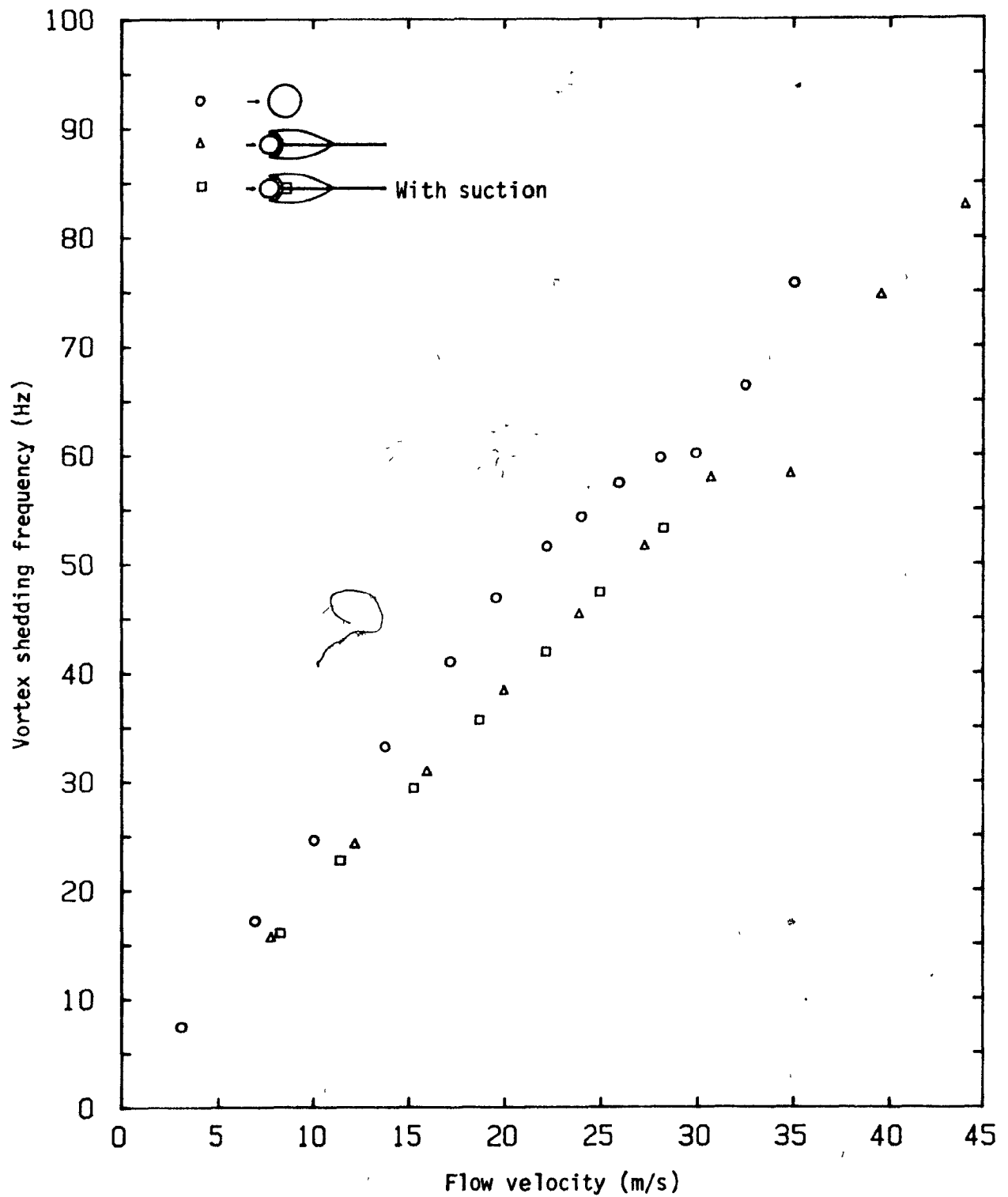


**Figure 5.12:** The wake flow periodicity of a clamped-clamped shell, without and with wake eliminator and suction.



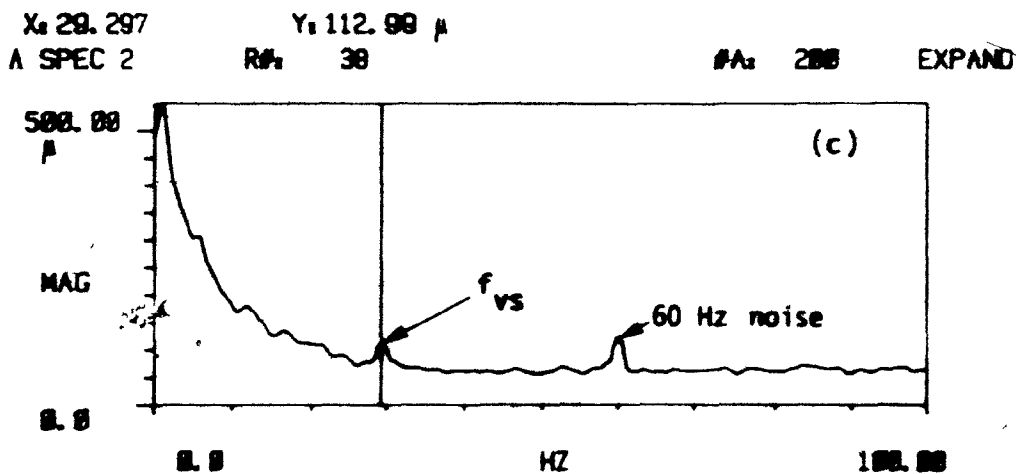
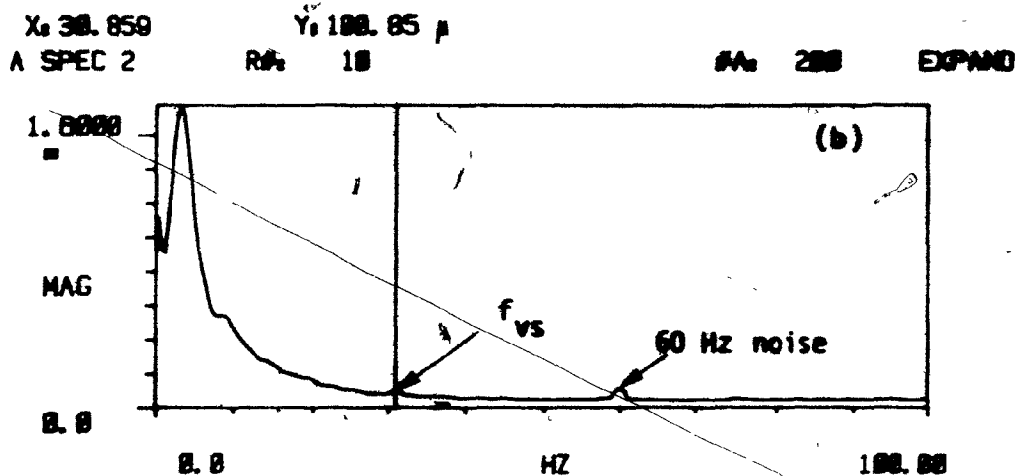
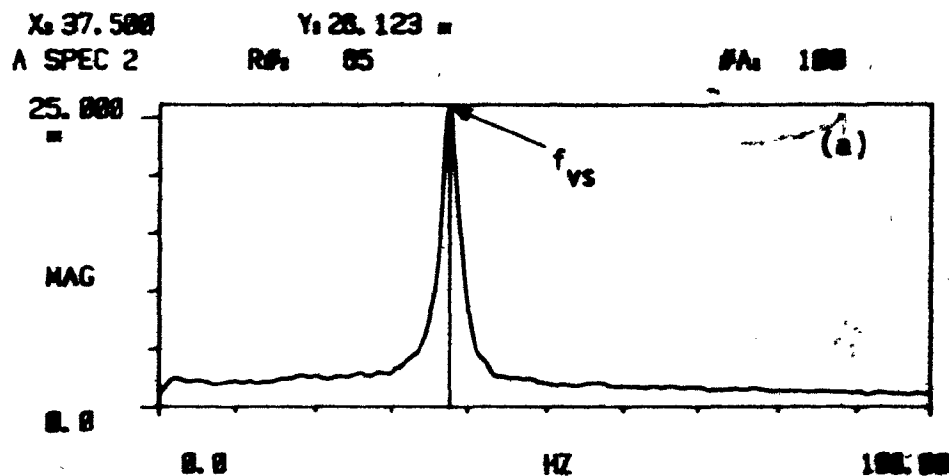


**Figure 5.13:** Frequency spectra of the wake at a flow velocity of approximately 15.5 m/s. (a) Shell without wake eliminator, (b) with wake eliminator and (c) with wake eliminator and suction.

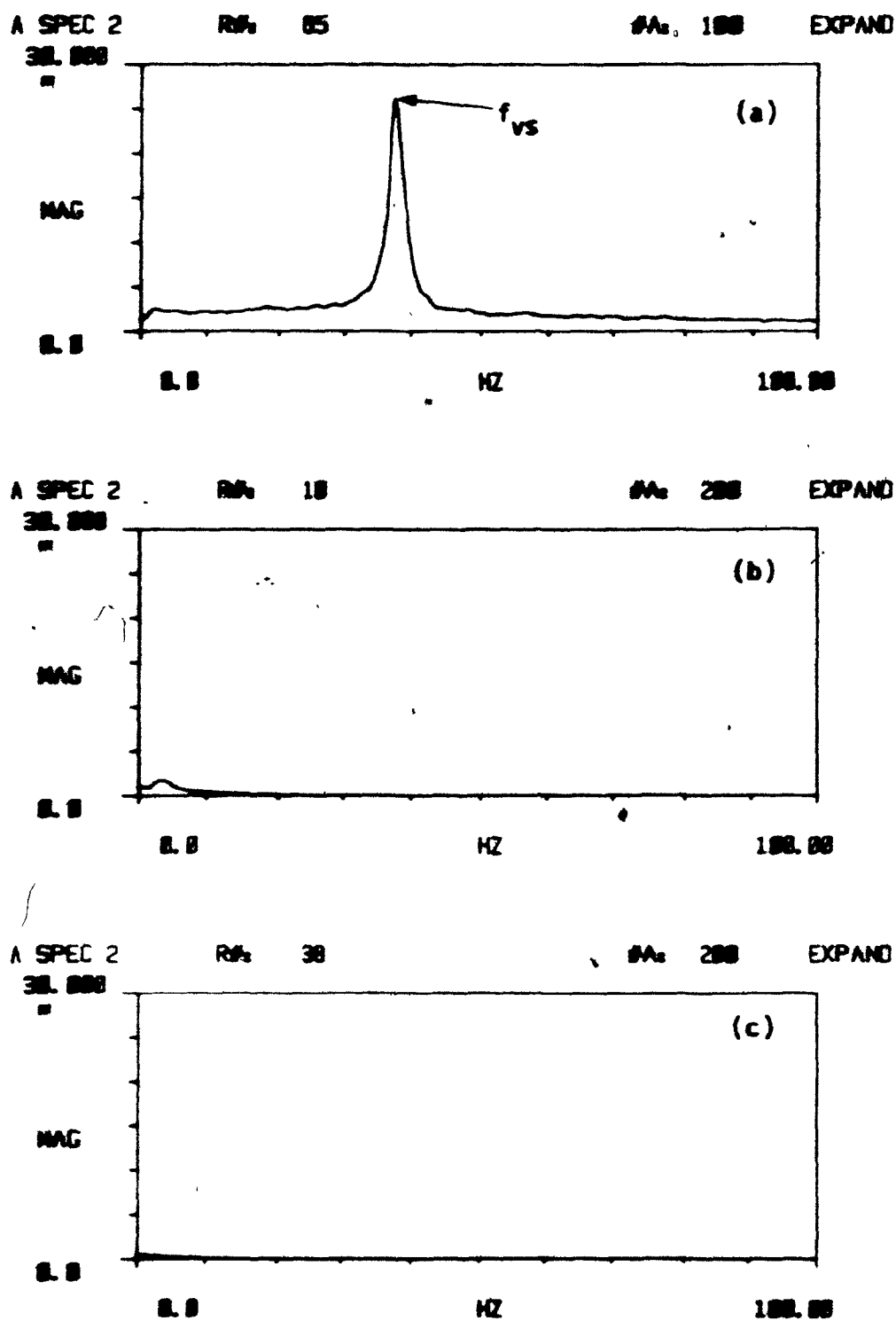


**Figure 5.14:** The frequency spectra of Figure 5.12 plotted on the same scale.

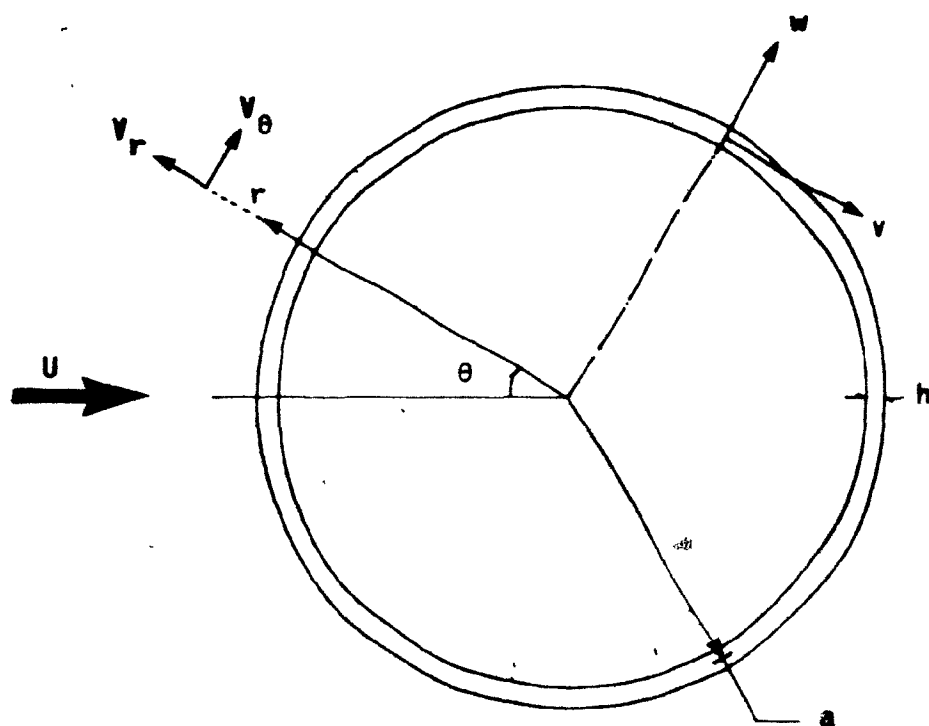


**Figure 6.1:** Definition diagram for various quantities used in the theoretical model.

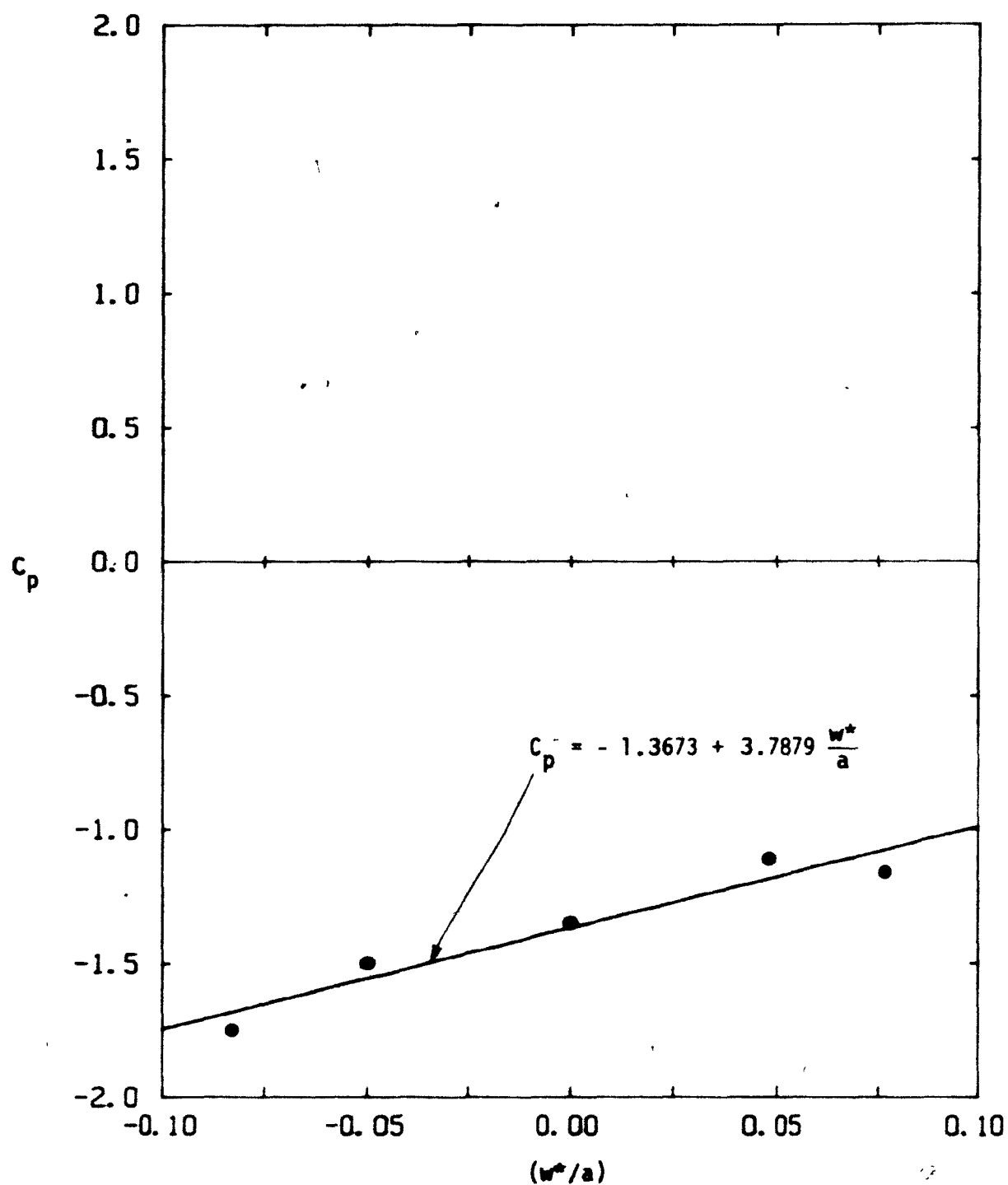


**Figure 6.2:** The quasi-static pressure variations in the wake,  $C_p$  vs  $(w^*/a)$  at  $\theta = 180^\circ$ , for the  $n=2$  mode shape with an antinode facing the free stream at  $Re = 3.80 \times 10^4$  ( $U = 7.5$  m/s).

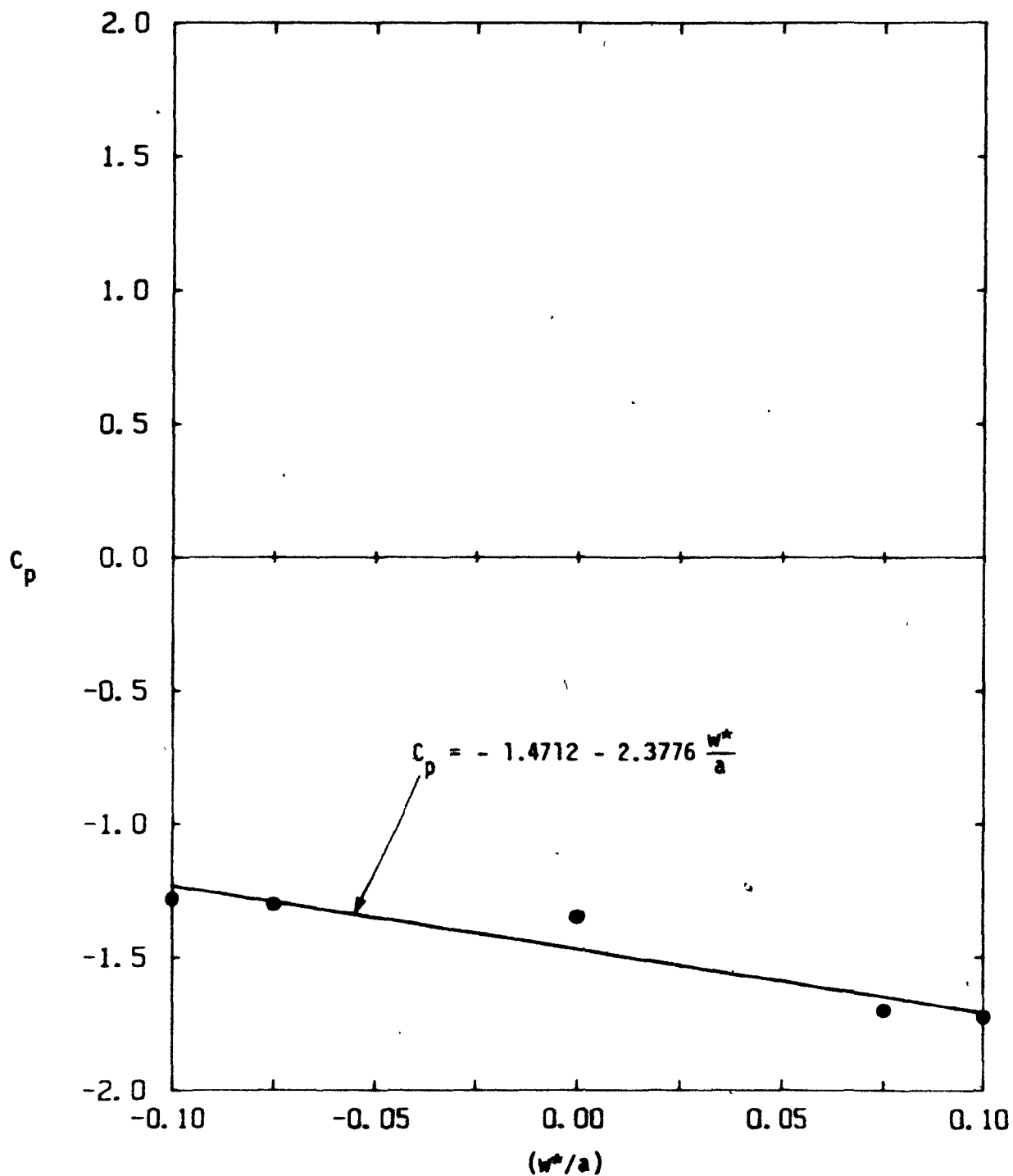


**Figure 6.3:** The quasi-static pressure variations in the wake,  $C_p$  vs  $(w^*/a)$  at  $\theta = 180^\circ$ , for the  $n=3$  mode shape with an antinode facing the free stream at  $Re = 3.80 \times 10^4$  ( $U = 7.5$  m/s).

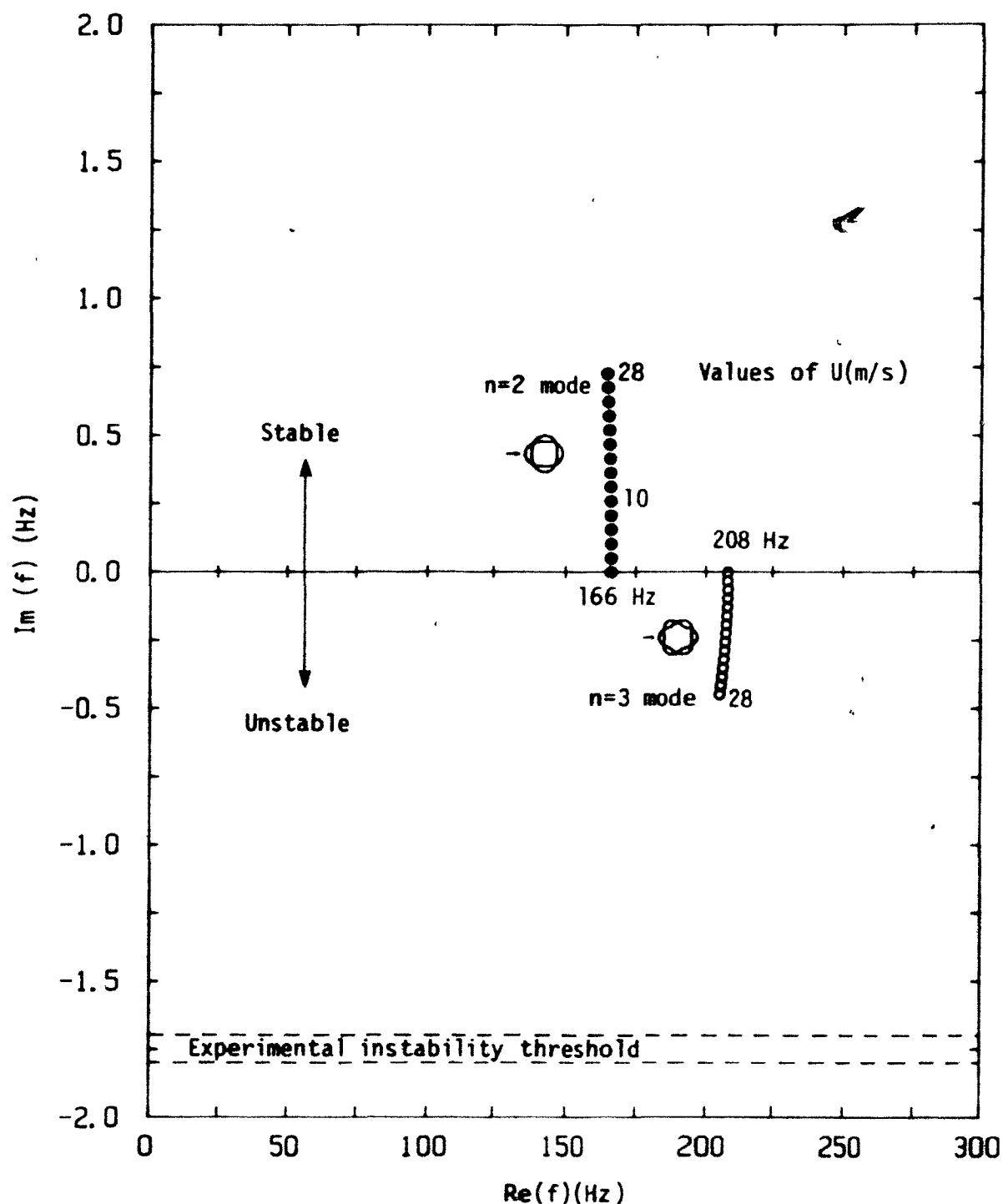


**Figure 6.4:** Argand diagram of the complex frequencies  $f_{2,1}$  and  $f_{3,1}$  of a clamped-clamped cylindrical shell, with an antinode facing the free stream, as functions of the flow velocity  $U$ , for Case 0 (original theory); circles correspond to solutions at equal steps in  $U$  of 2 m/s, from 0 to 28 m/s.

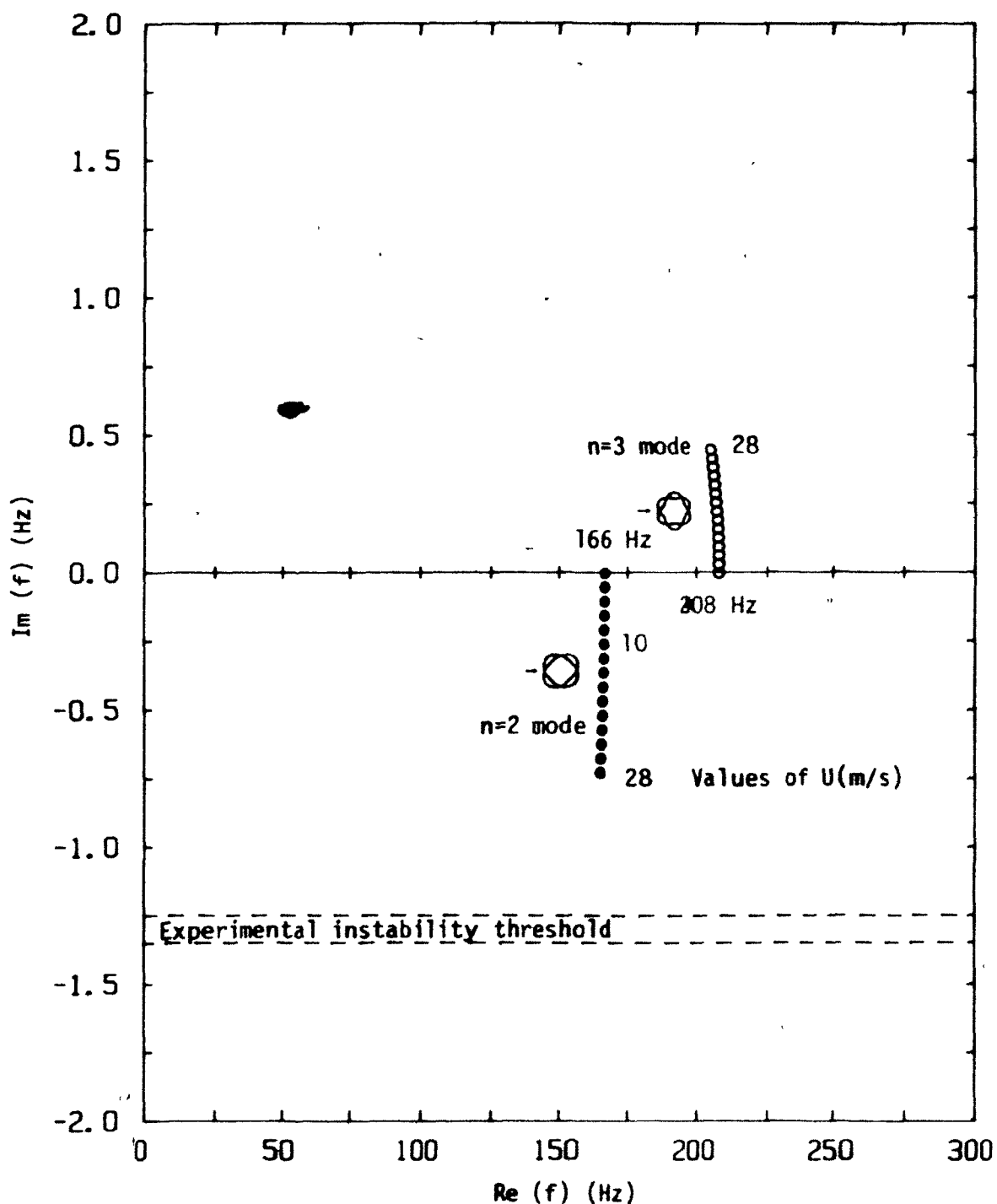


**Figure 6.5:** Argand diagram of the complex frequencies  $f_{2,1}$  and  $f_{3,1}$  of a clamped-clamped cylindrical shell, with a node facing the free stream, as functions of the flow velocity  $U$ , for Case 0 (original theory); circles correspond to solutions at equal steps in  $U$  of 2 m/s, from 0 to 28 m/s.

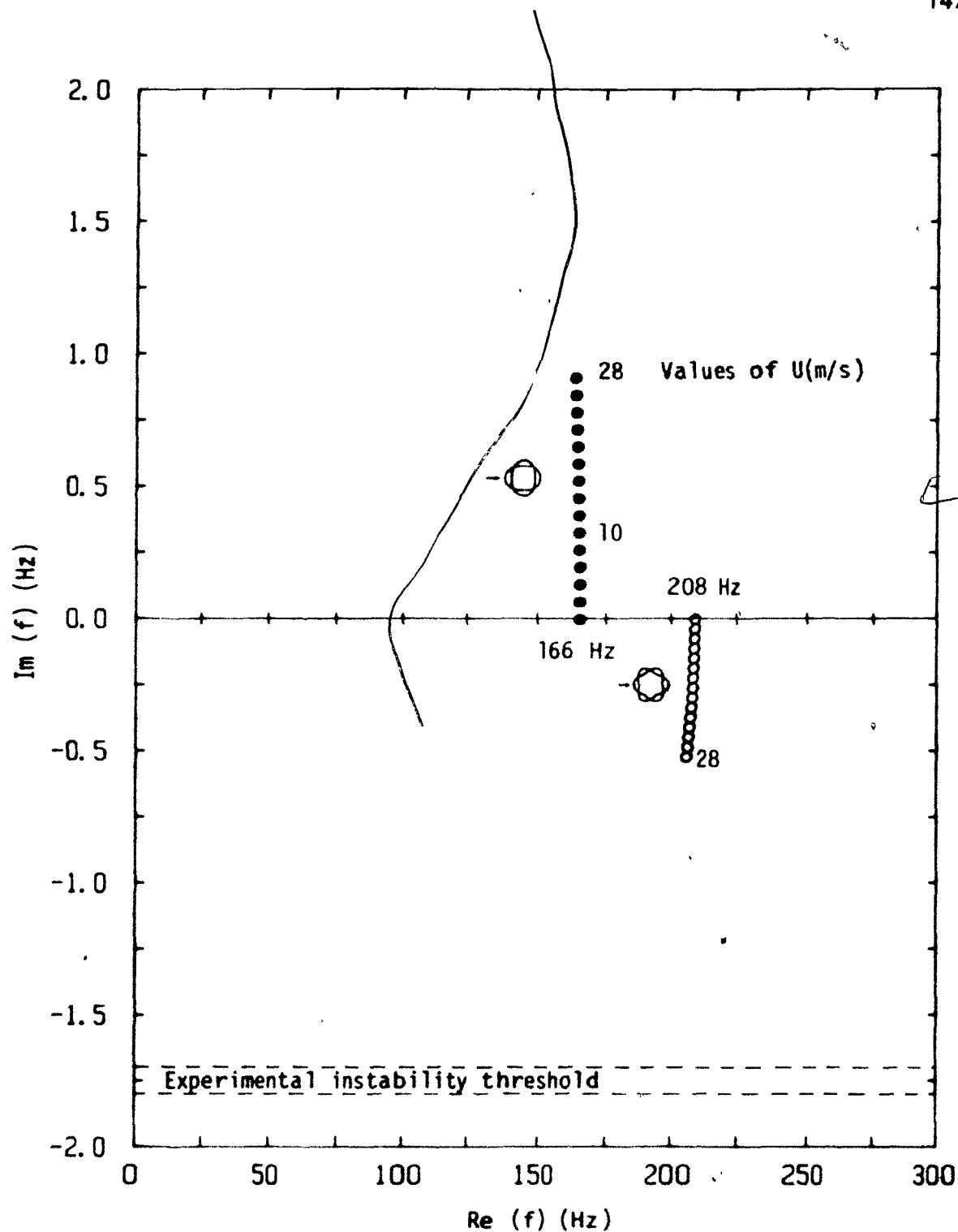


**Figure 6.6:** Argand diagram of the complex frequencies  $f_{2,1}$  and  $f_{3,1}$  of a clamped-clamped cylindrical shell, with an antinode facing the free stream, as functions of the flow velocity  $U$ , for Case 1 (effect of moving boundary condition).



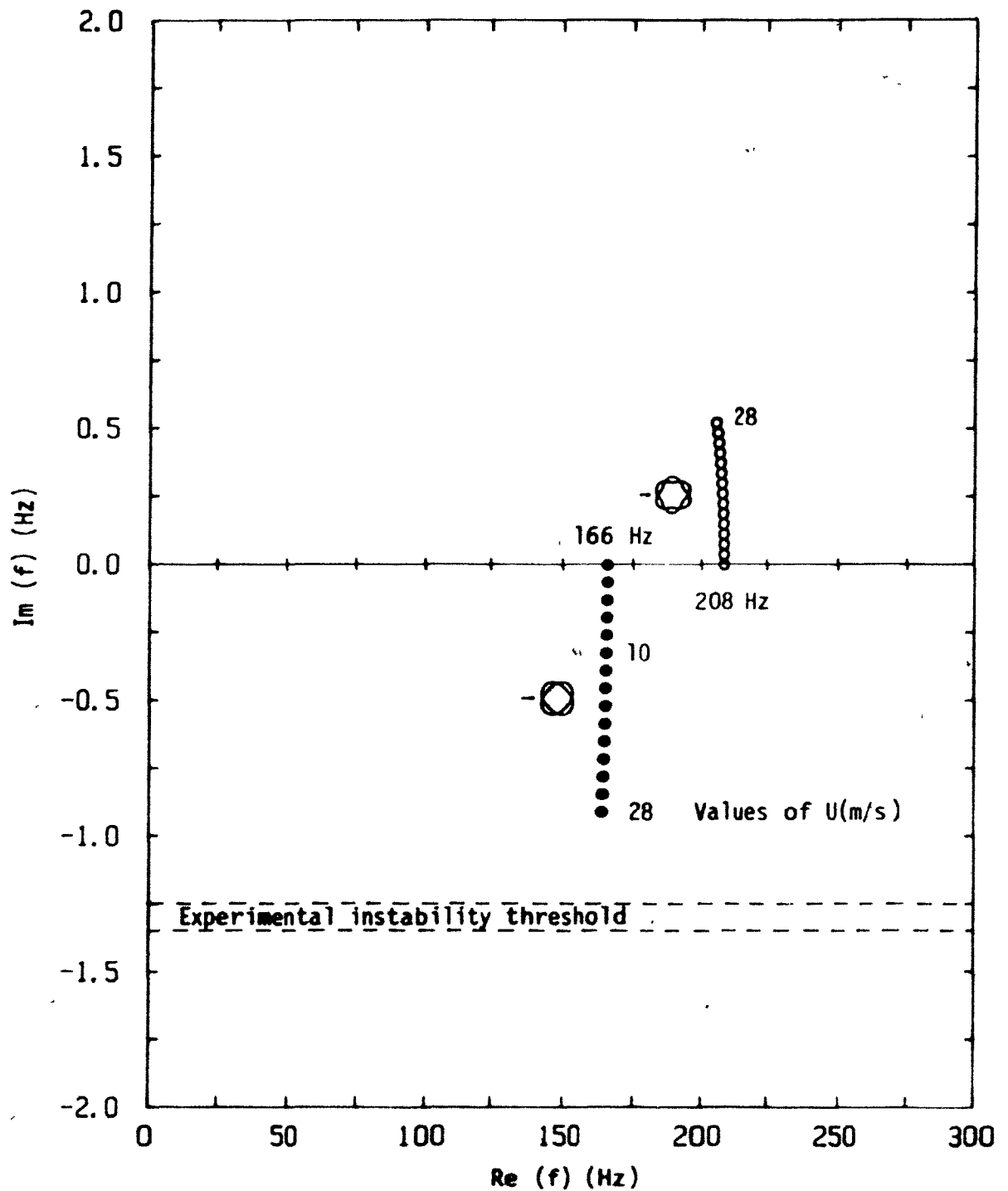


**Figure 6.7:** Argand diagram of the complex frequencies  $f_{2,1}$  and  $f_{3,1}$  of a clamped-clamped cylindrical shell, with a node facing the free stream, as functions of the flow velocity  $U$ , for Case 1 (effect of moving boundary condition).

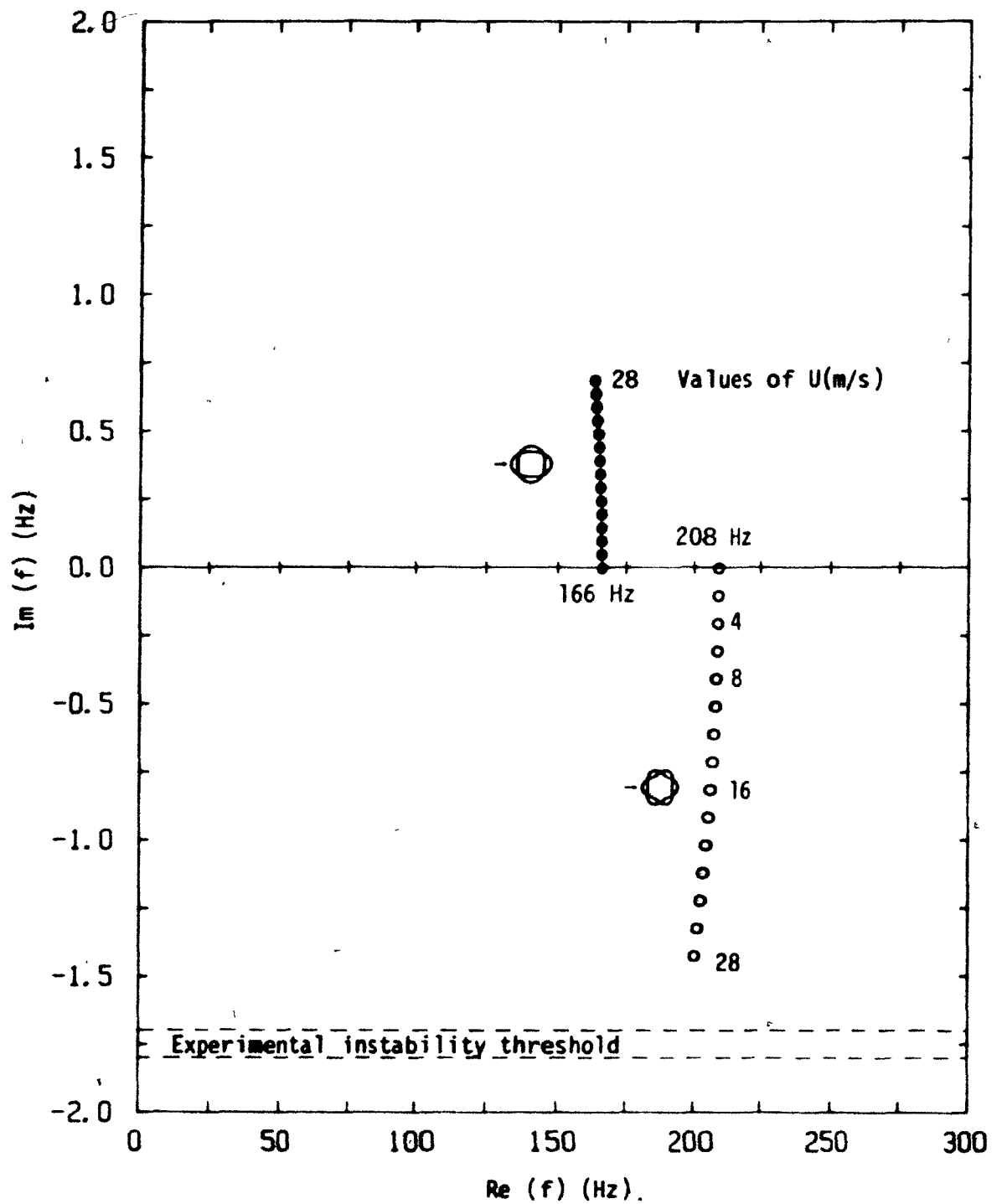


**Figure 6.8:** Argand diagram of the complex frequencies  $f_{2,1}$  and  $f_{3,1}$  of a clamped-clamped cylindrical shell, with an antinode facing the free stream, as functions of the flow velocity, for Case 2 (coherent reverse flow in the wake).

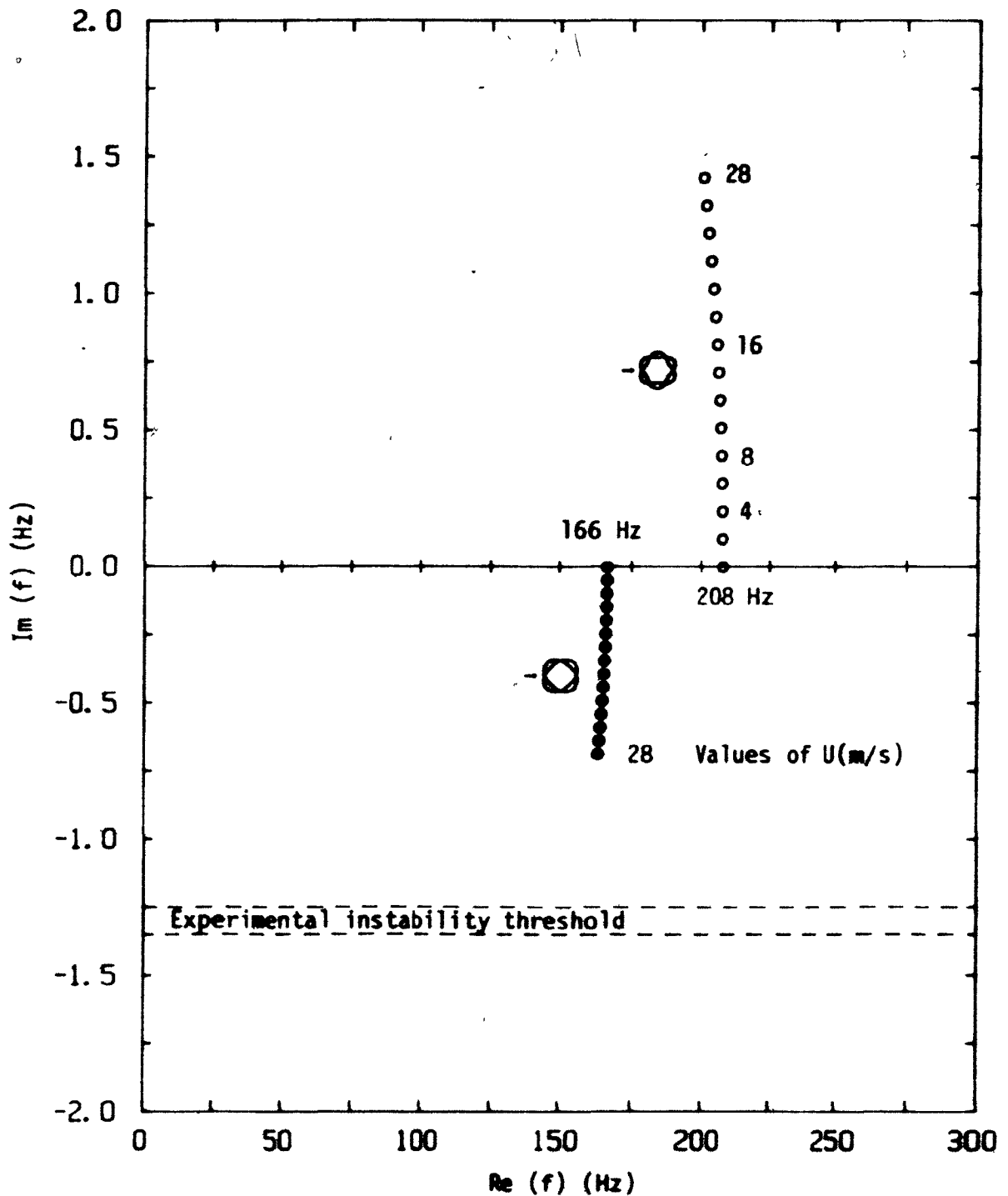


**Figure 6.9:** Argand diagram of the complex frequencies  $f_{2,1}$  and  $f_{3,1}$  of a clamped-clamped cylindrical shell, with a node facing the free stream, as functions of the flow velocity  $U$ , for Case 2 (coherent reverse flow in the wake).

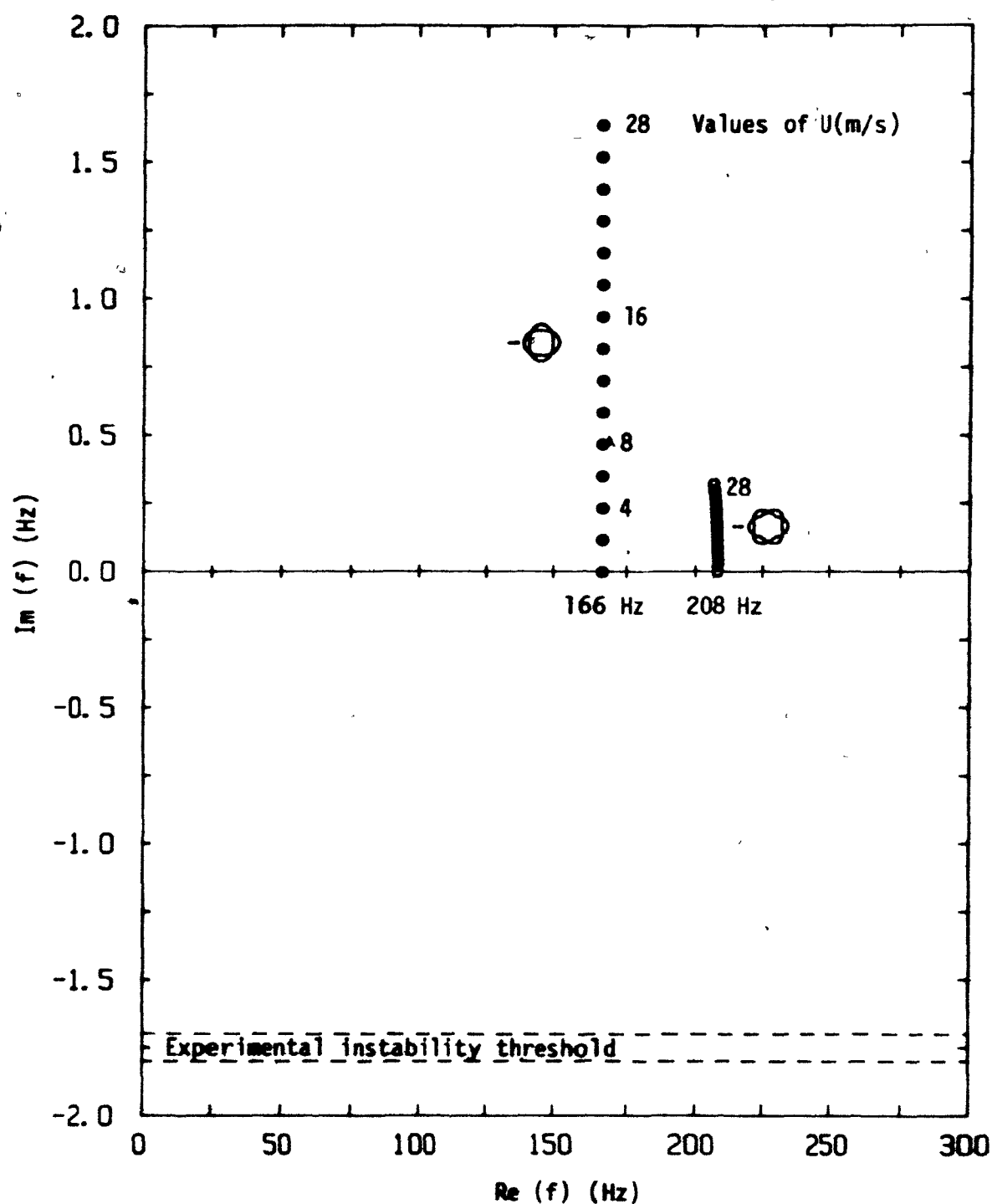


**Figure 6.10:** Argand diagram of the complex frequencies  $f_{2,1}$  and  $f_{3,1}$  of a clamped-clamped cylindrical shell, with an antinode facing the free stream, as functions of the flow velocity  $U$ , for Case 3 (with boundary condition applied at  $r = a + w^*$ ).

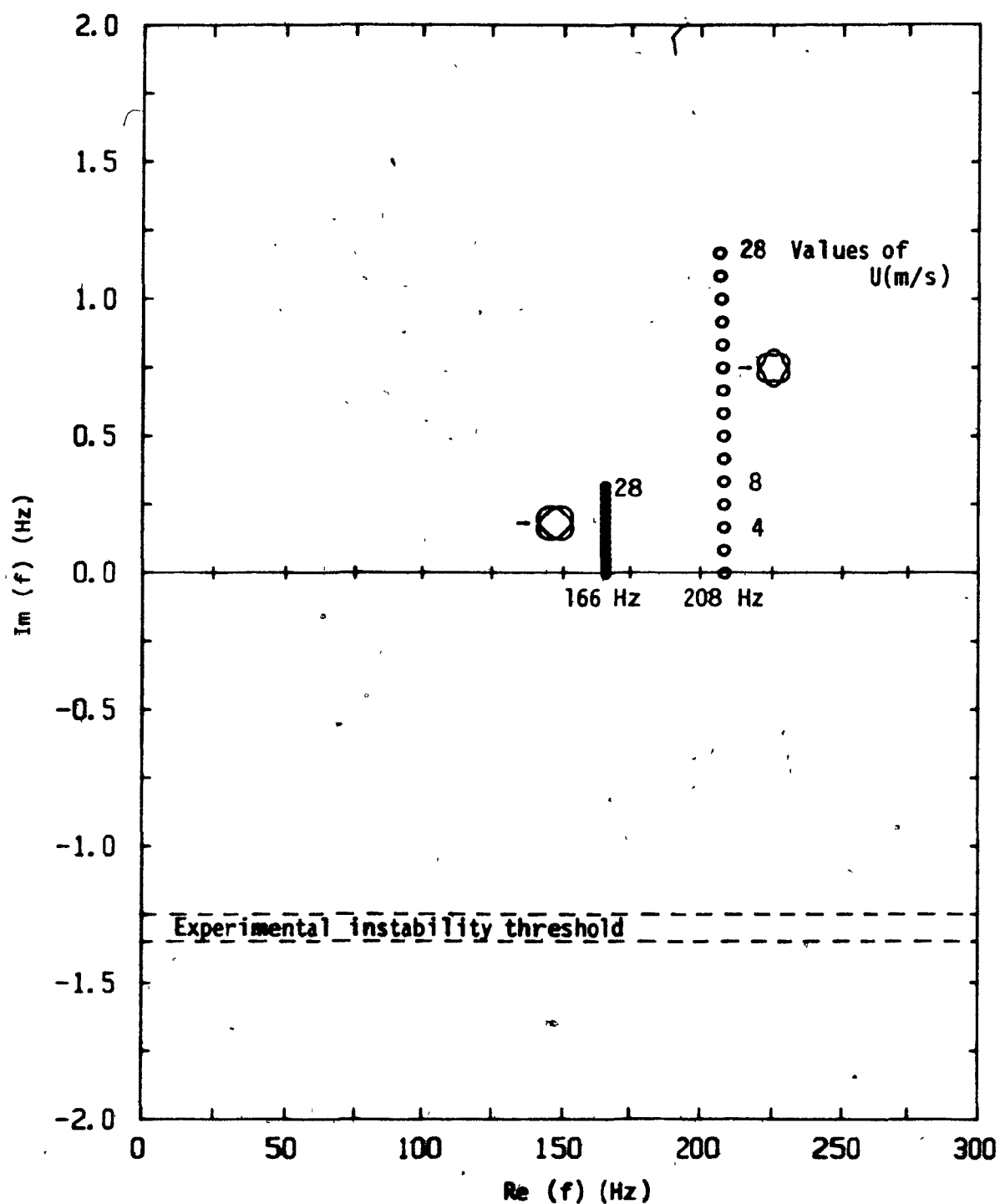


**Figure 6.11:** Argand diagram of the complex frequencies  $f_{2,1}$  and  $f_{3,1}$  of a clamped-clamped cylindrical shell, with a node facing the free stream, as functions of the flow velocities  $U$ , for Case 3 (with boundary condition applied at  $r = a + w^*$ ).

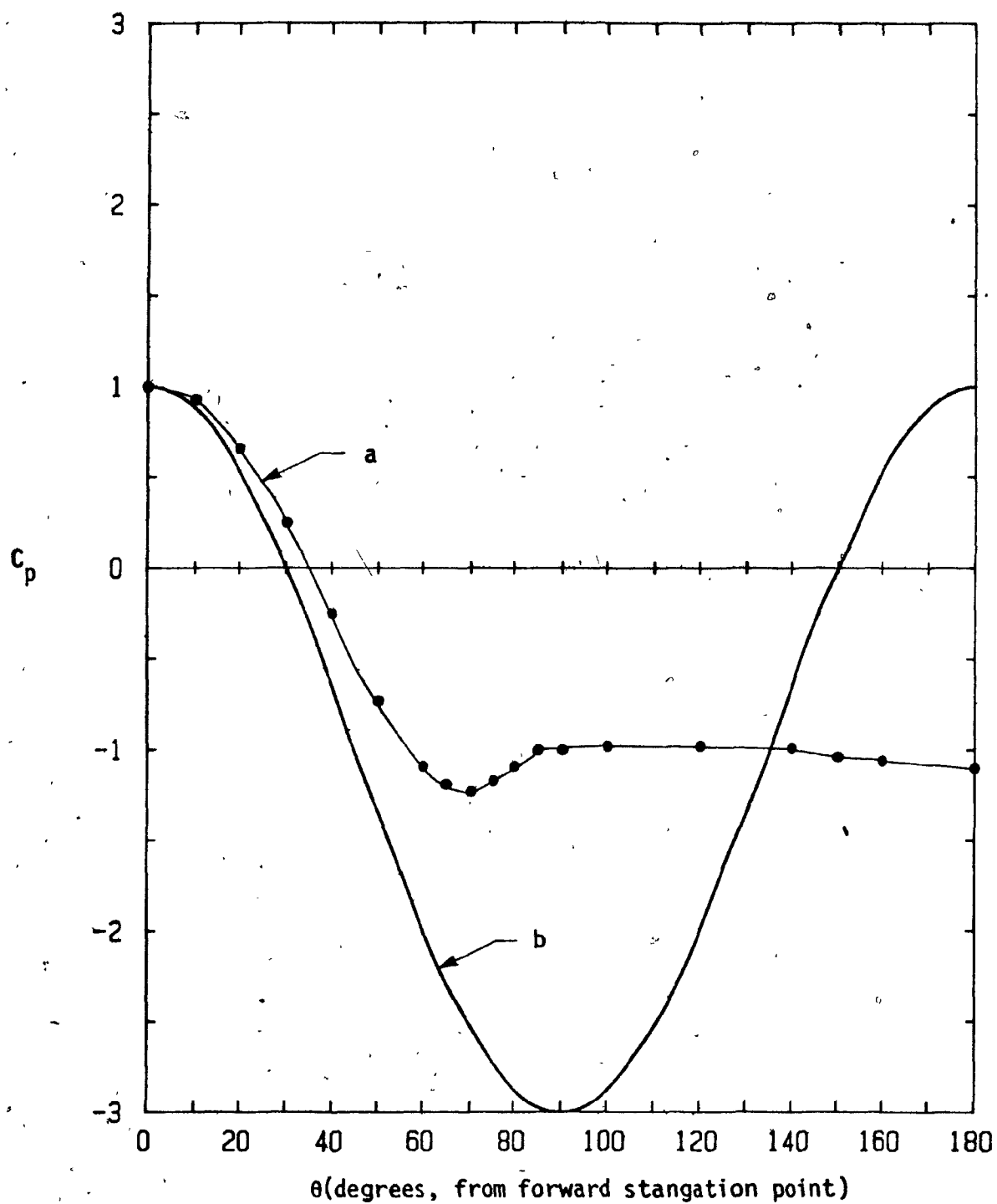


**Figure 6.12:** The pressure coefficient of a circular cylinder. Curve a is based on Roshko's experimental data. Curve b corresponds to  $C_p = 1 - 4 \sin^2 \theta$  which is given by inviscid flow theory.

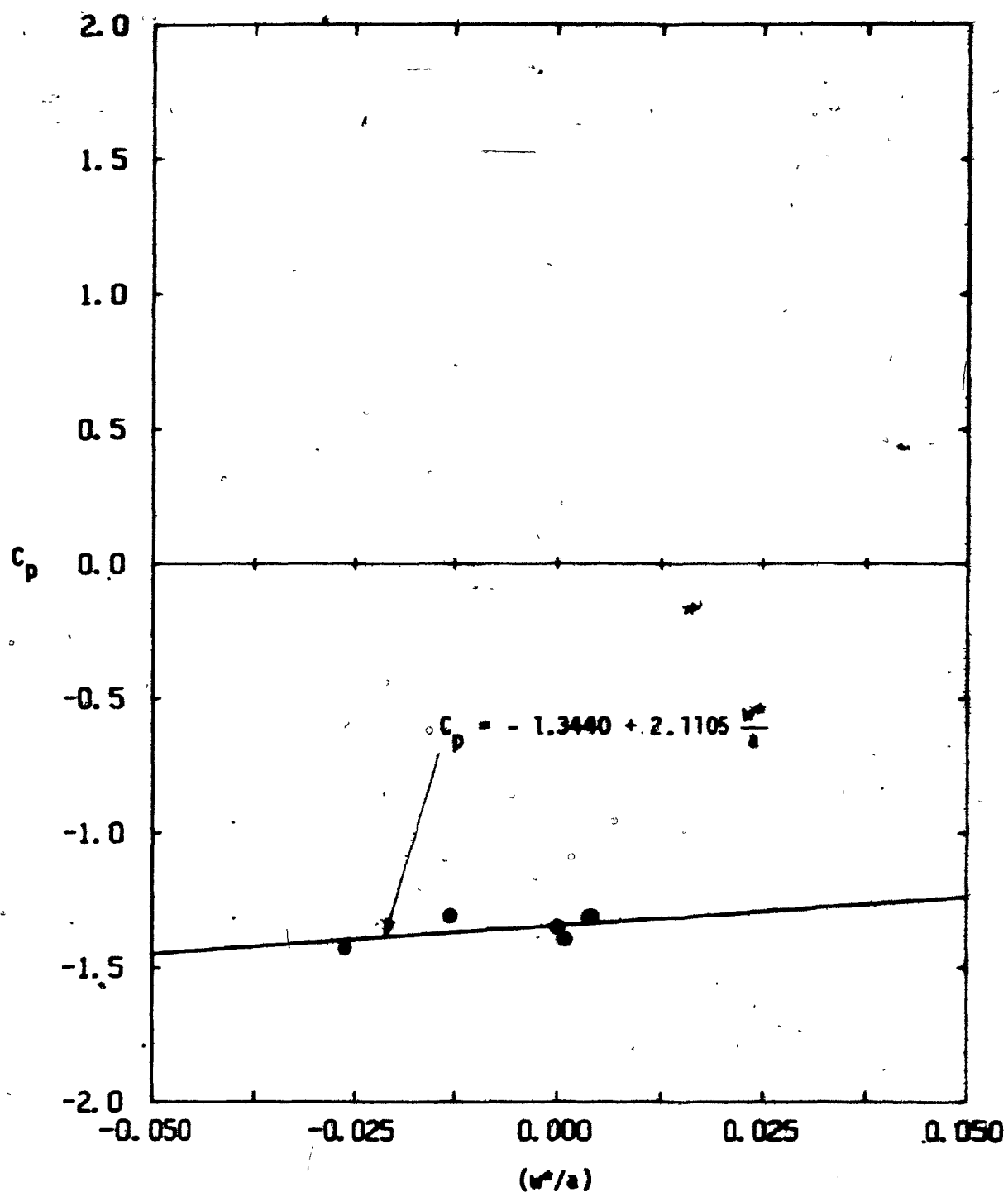


**Figure 6.13:** The quasi-static pressure variations in the wake,  $C_p$ , vs  $(w^2/a)$  at  $\theta = 175^\circ$ , for the  $n=2$  mode shape with a node facing the free stream at  $Re = 3.80 \times 10^4$  ( $U = 7.5$  m/s).

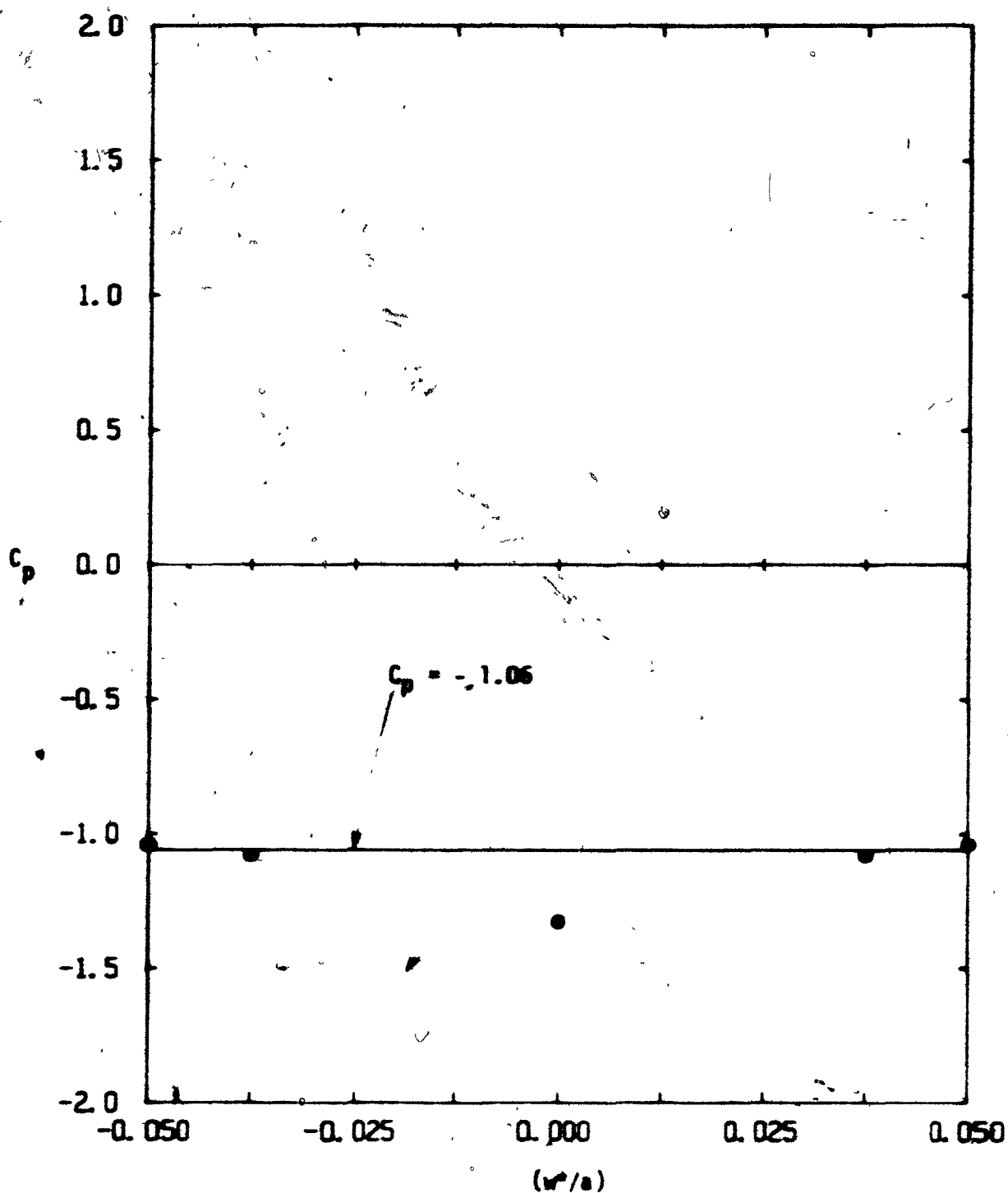


**Figure 6.14:** The quasi-static pressure variations in the wake,  $C_p$  vs  $(w/a)$  at  $\theta = 170^\circ$ , for the  $n=3$  mode shape with a node facing the free stream at  $Re = 3.80 \times 10^4$  ( $U = 7.5$  m/s).



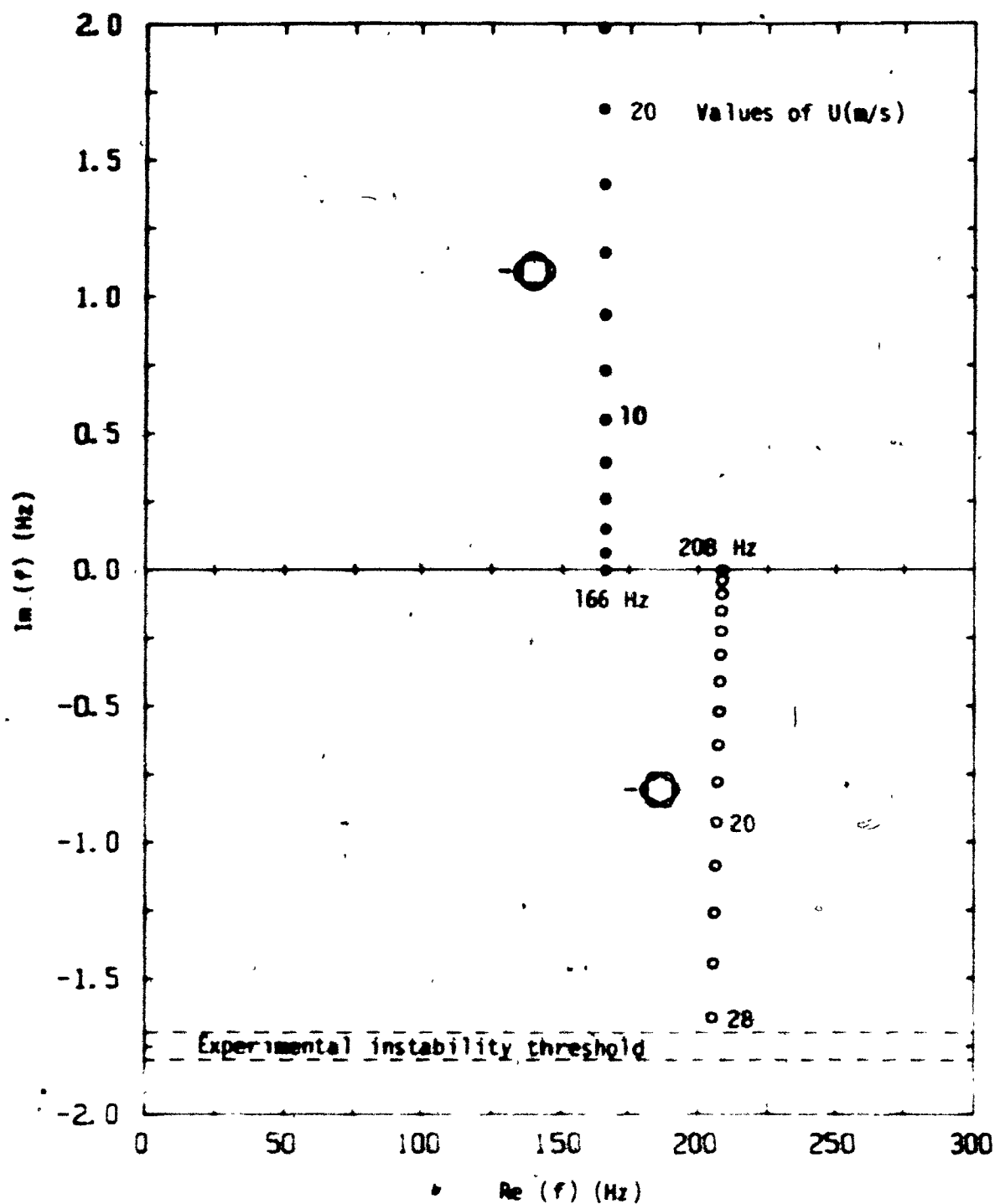
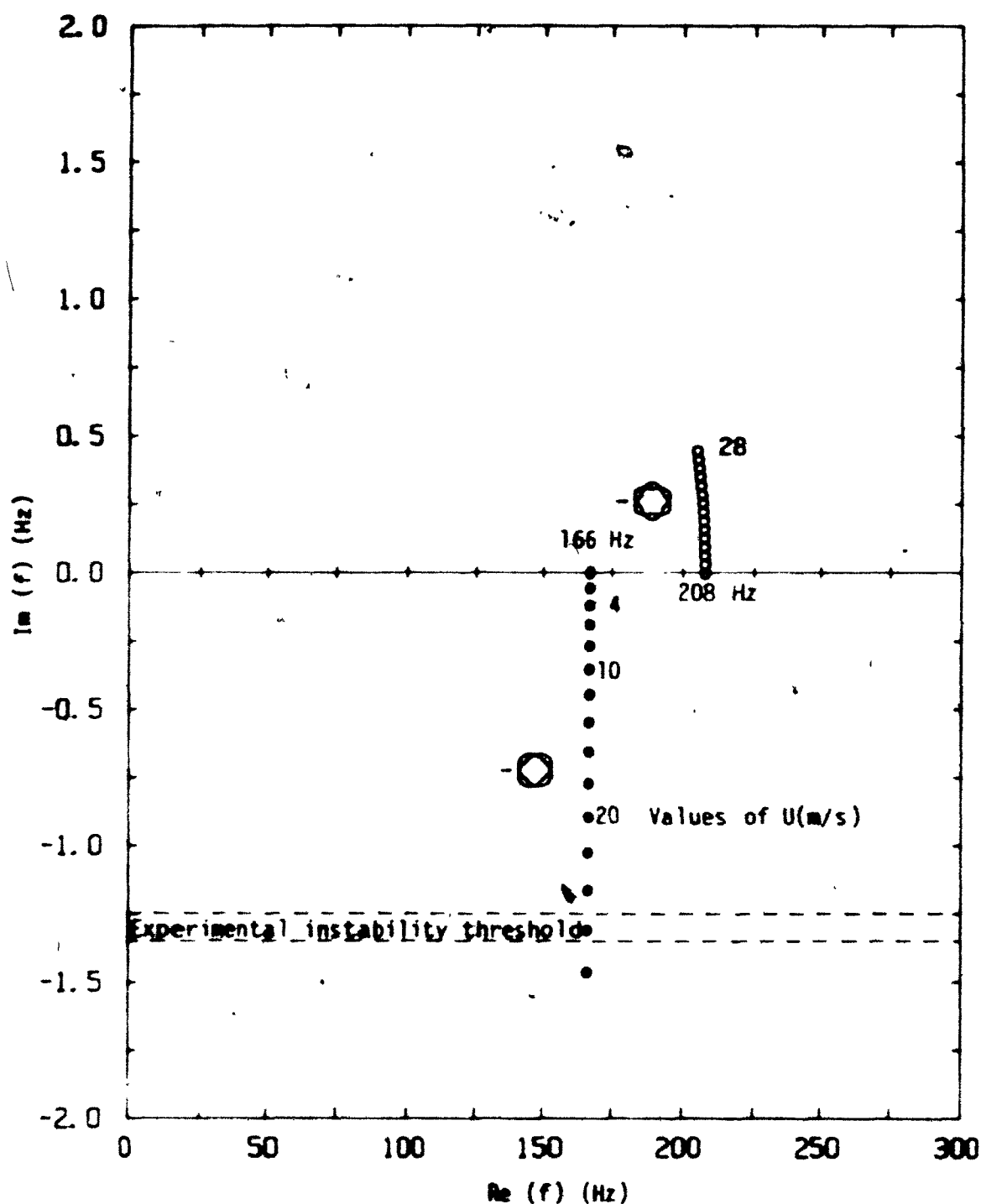
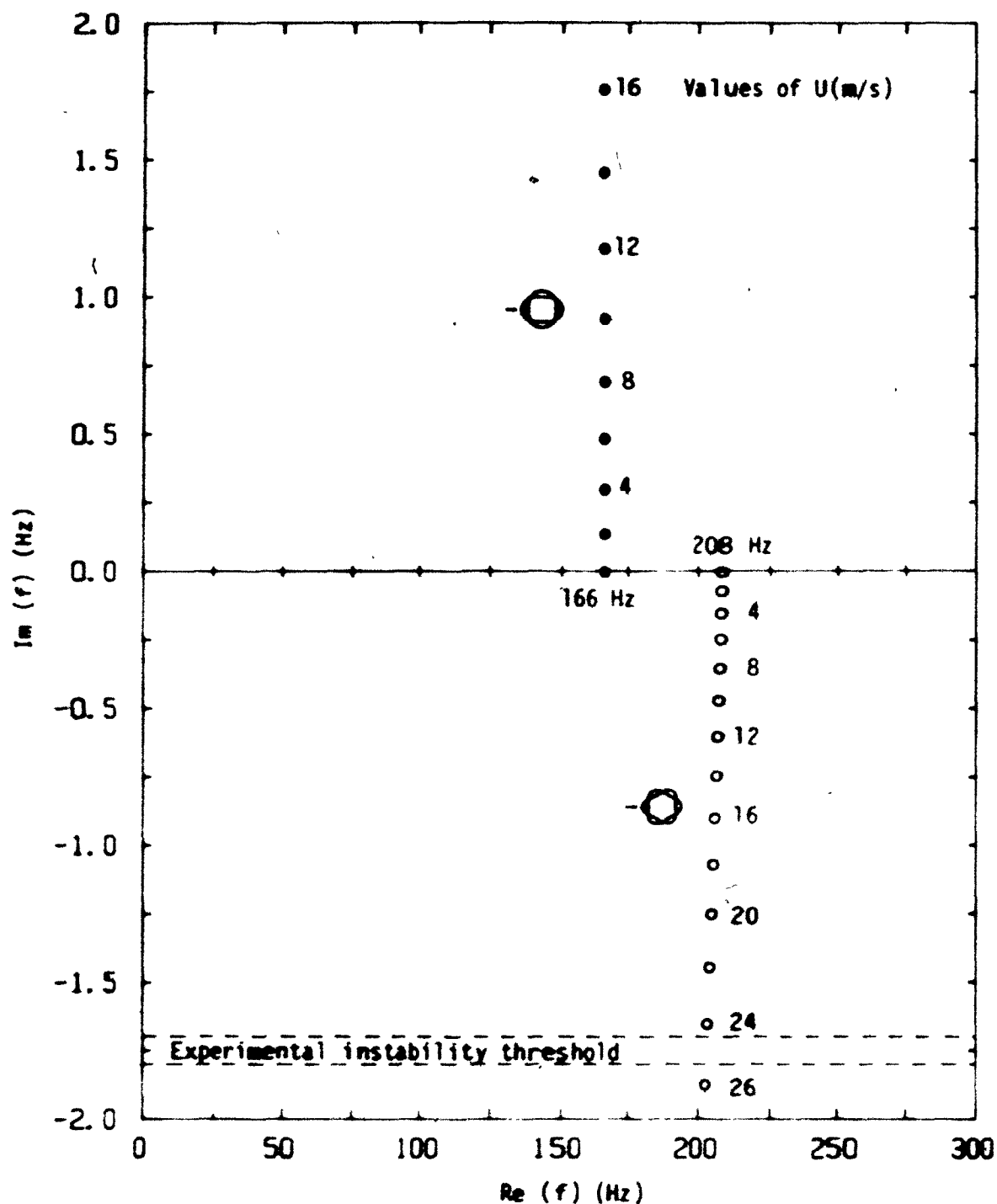


Figure 6.15: Argand diagram of the complex frequencies  $f_{2,1}$  and  $f_{3,1}$  of a clamped-clamped cylindrical shell, with an antinode facing the free stream, as functions of flow velocity  $U$ , for Case 4 (effect of base pressure variations).



**Figure 6.16:** Argand diagram of the complex frequencies  $f_{2,1}$  and  $f_{3,1}$  of a clamped-clamped cylindrical shell, with a node facing the free stream, as functions of the flow velocity  $U$ , for Case 4 (effect of base pressure variations).



**Figure 6.17:** Argand diagram of the complex frequencies  $f_{2,1}$  and  $f_{3,1}$  of a clamped-clamped cylindrical shell, with an antinode facing the free stream, as functions of flow velocity  $U$ , for Case 5 (combinations of all the foregoing effects).

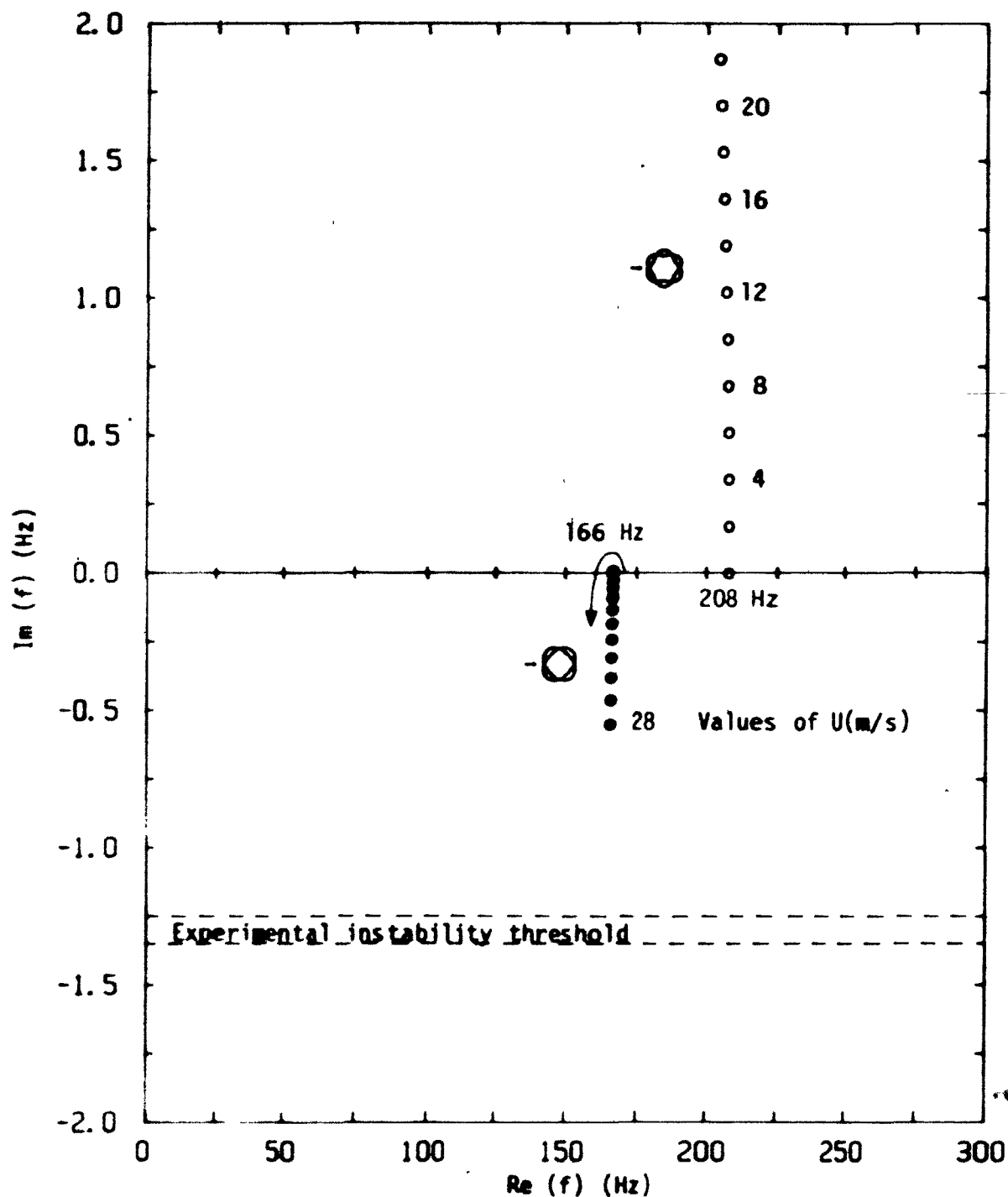


**Figure 6.18:** Argand diagram of the complex frequencies  $f_{2,1}$  and  $f_{3,1}$  of a clamped-clamped cylindrical shell, with a node facing the free stream, as functions of flow velocity  $U$ , for Case 5 (combination of all the foregoing effects).

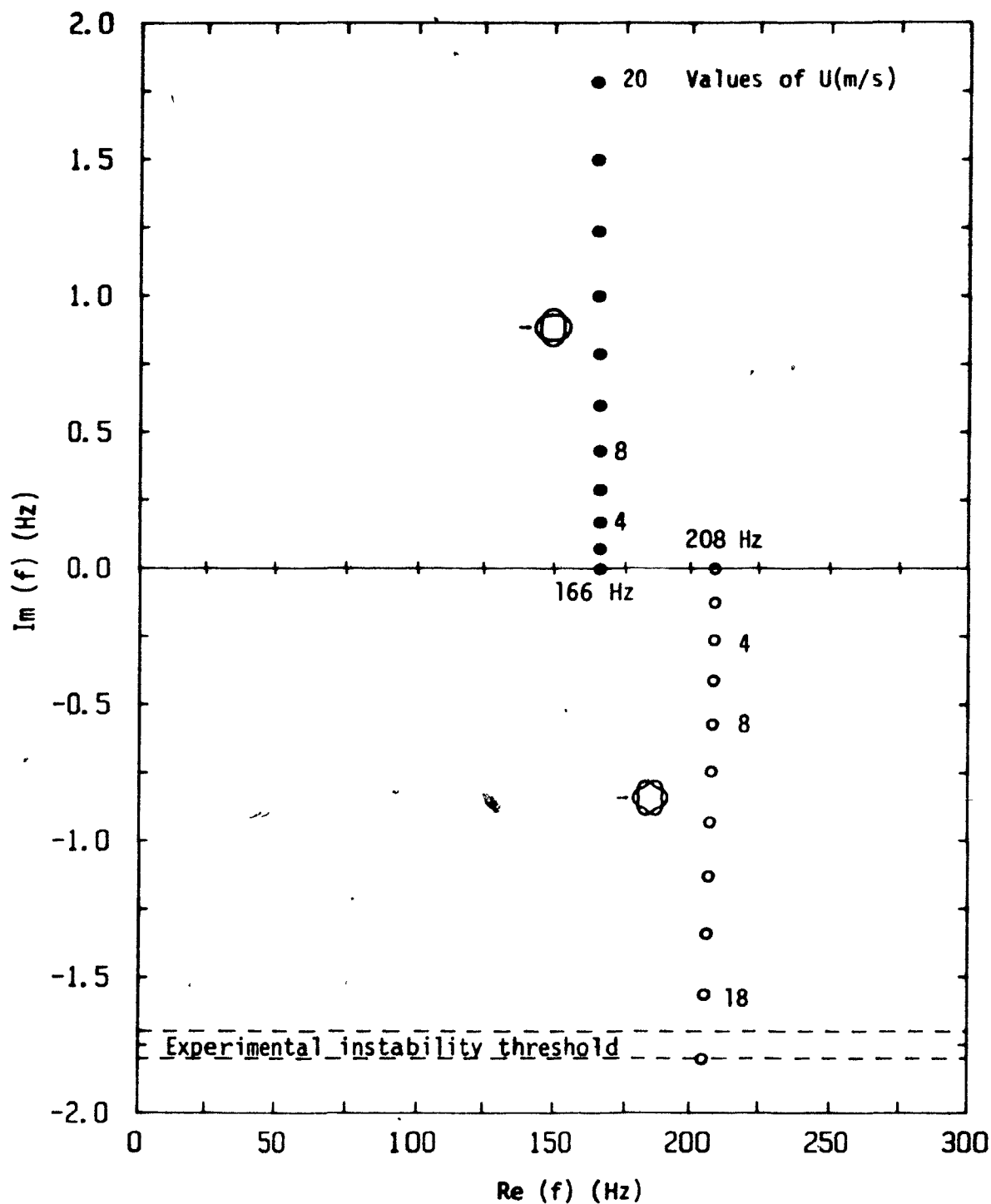


**Figure 6.19:** Argand diagram of the complex frequencies  $f_{2,1}$  and  $f_{3,1}$  of a clamped-clamped cylindrical shell, with an antinode facing the free stream, as functions of flow velocity  $U$ , for Case 6 (all combined effects, but with boundary condition applied at  $r = a$ ).

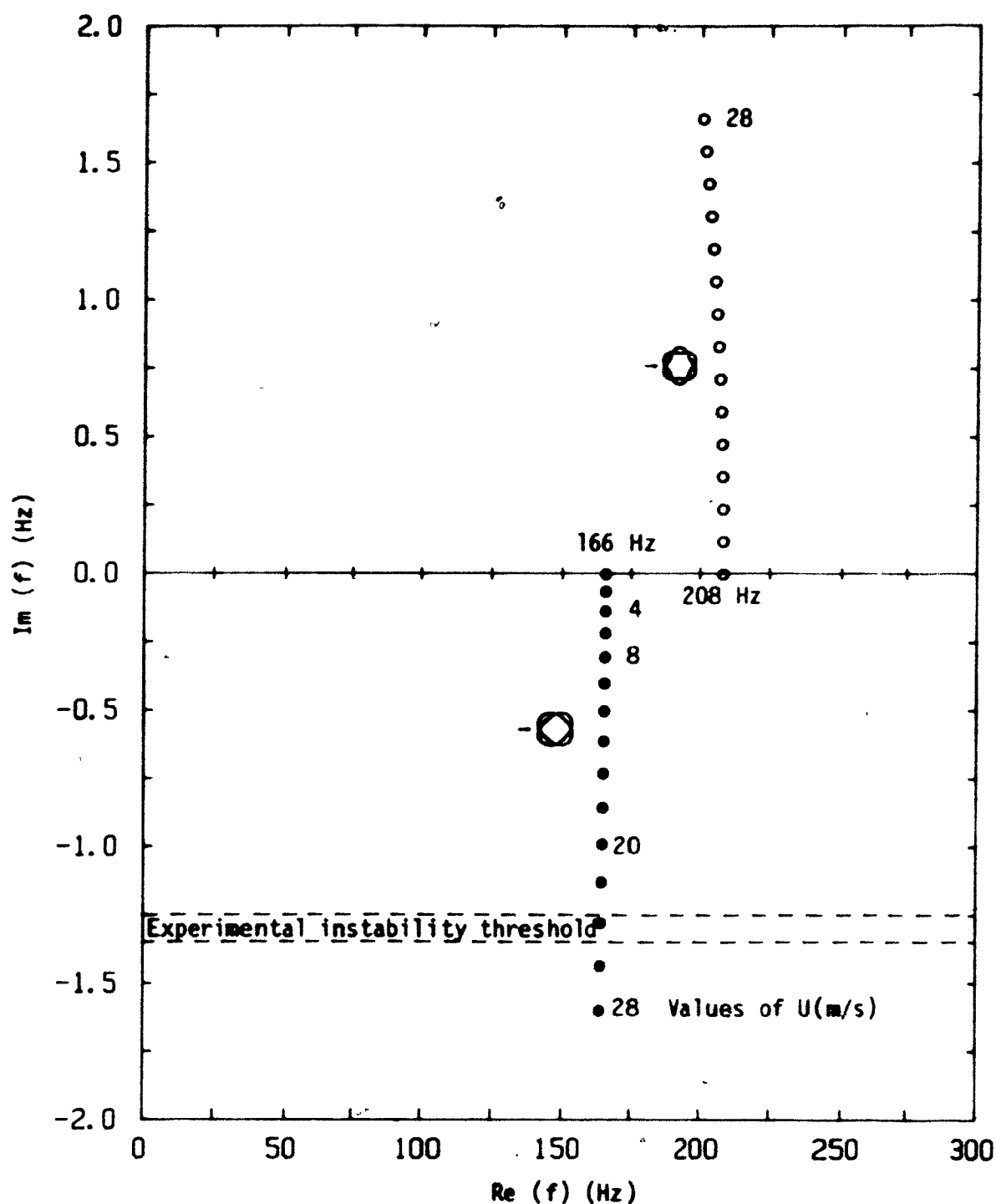


**Figure 6.20:** Argand diagram of the complex frequencies  $f_{2,1}$  and  $f_{3,1}$  of a clamped-clamped cylindrical shell, with a node facing the free stream, as functions of flow velocity  $U$ , for Case 6 (all combined effects, but with boundary condition applied at  $r = a$ ).

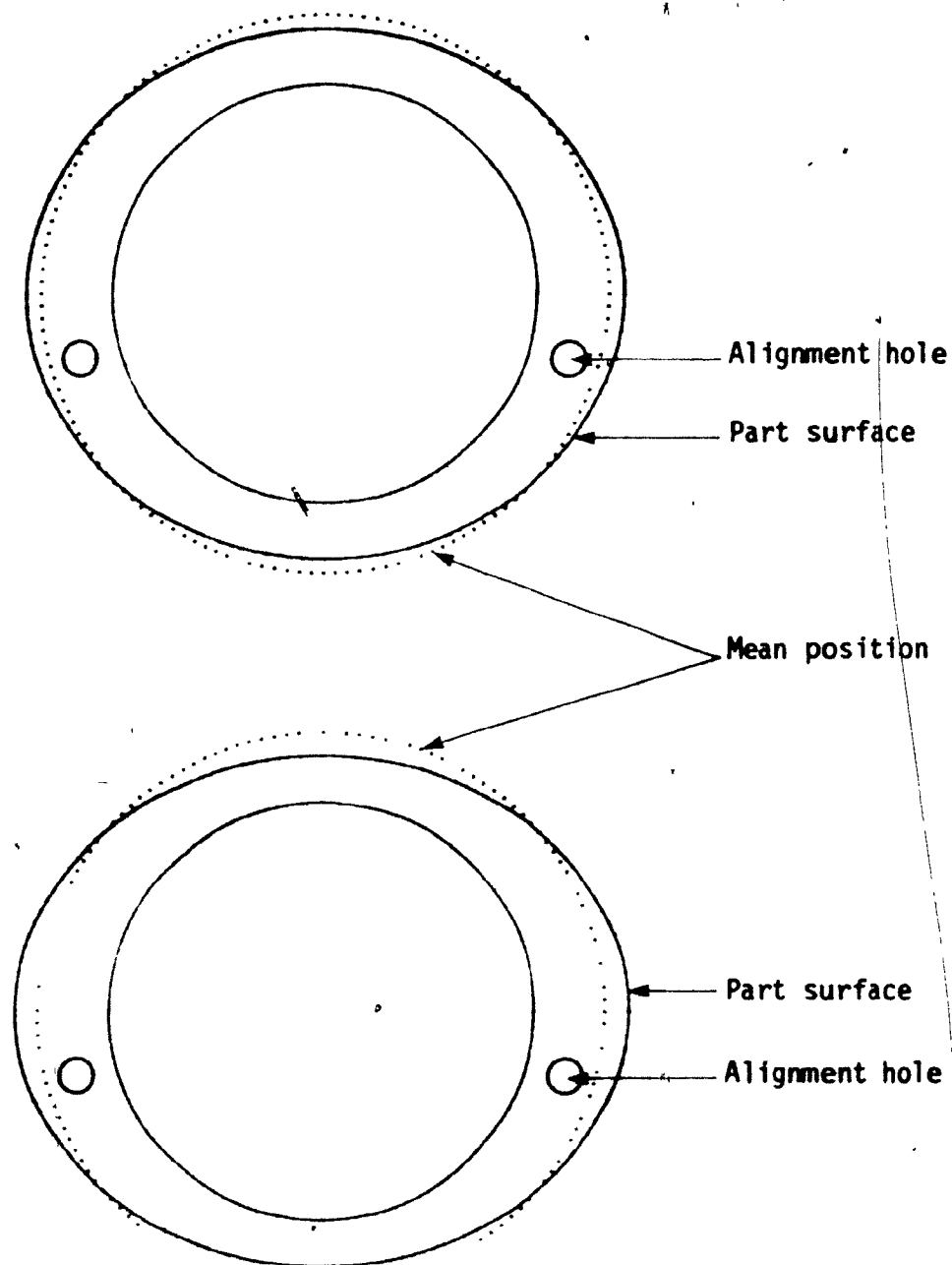


**Figure 7.1:** Cross-sectional view for the  $n=2$  mode model. The surface is described by  $R = \sqrt{(a^2 + b^2) / (a^2 \sin^2 \theta + b^2 \cos^2 \theta)}$ , where  $R = R(\theta)$  is the radius of curvature;  $a$  and  $b$  are respectively the semi-major and semi-minor axis of the ellipse. Top:  $a = 1.57$ ,  $b = 1.43$ ; bottom:  $a = 1.62$ ,  $b = 1.38$ .

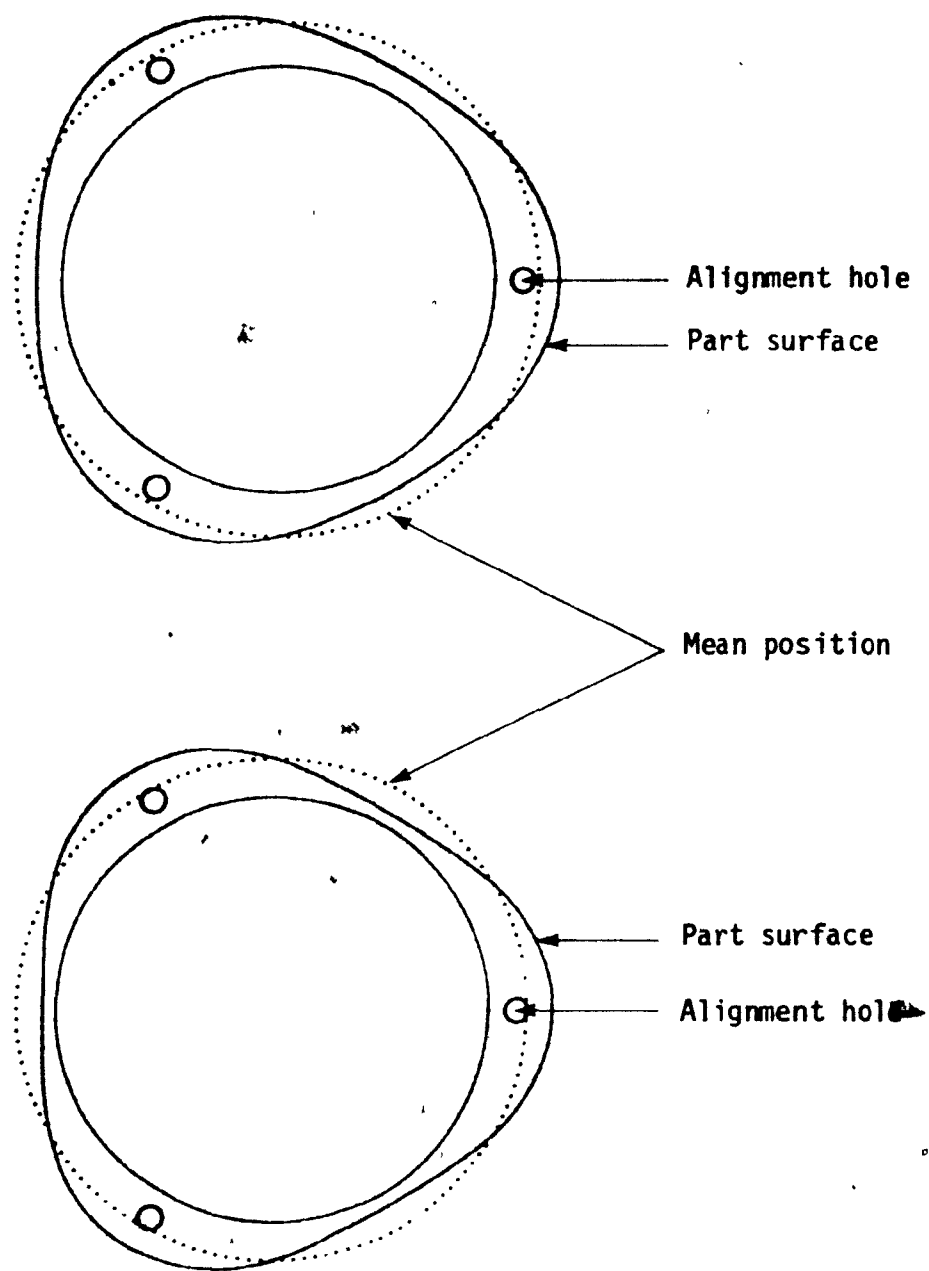


**Figure 7.2:** Cross-sectional view for the  $n=3$  mode model. The surface is described by  $R = 1.46 \cdot (1 + P \cos 3\theta) / (1 + P)$  where  $R = R(\theta)$  is the radius of curvature and  $P$  is a measure of the maximum radial displacement from the mean position. Top:  $P = 0.075$ ; bottom:  $P = 0.100$ .



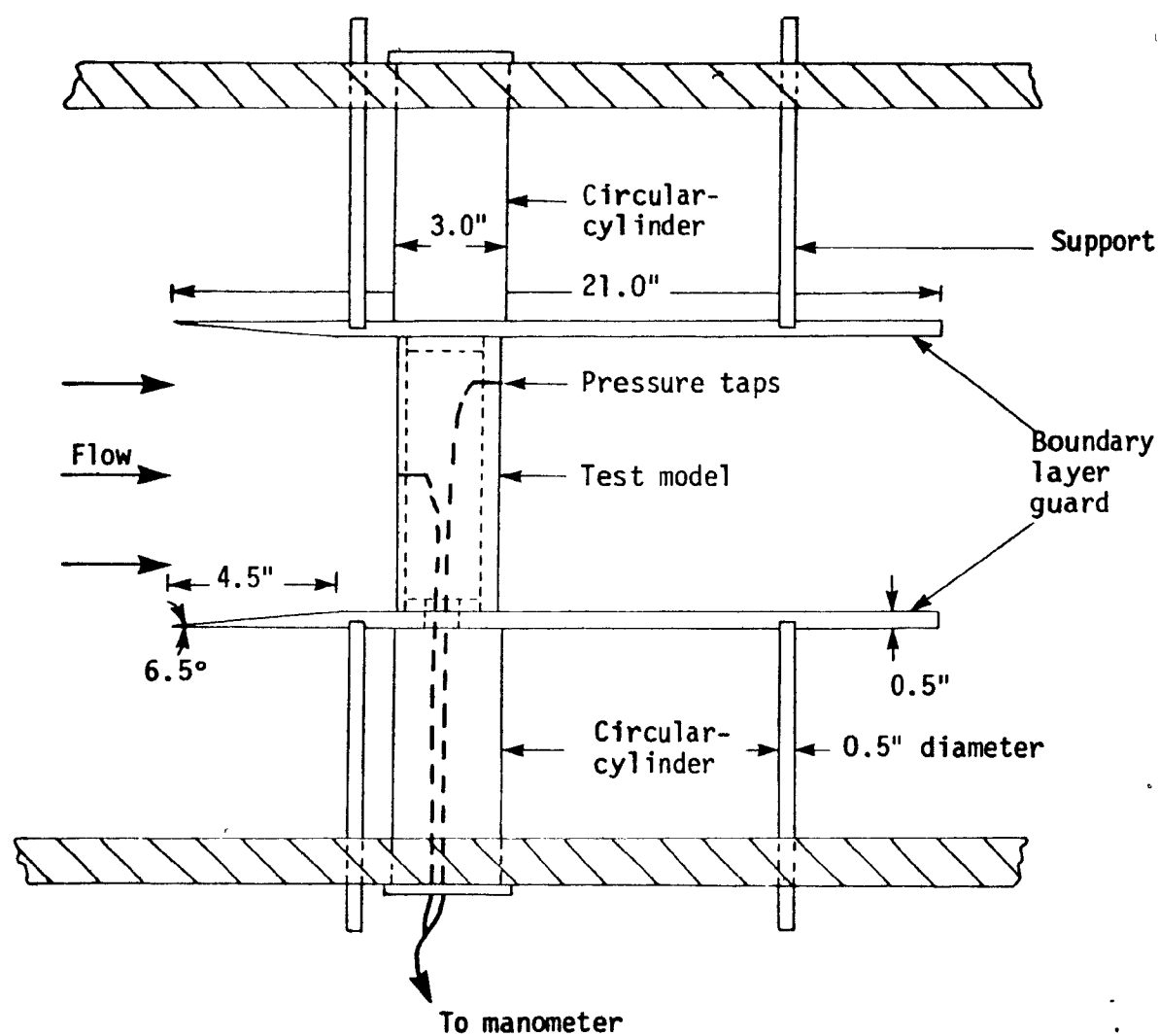


**Figure 7.3:** Side view of the test model with boundary layer guards in position in the wind-tunnel test section.

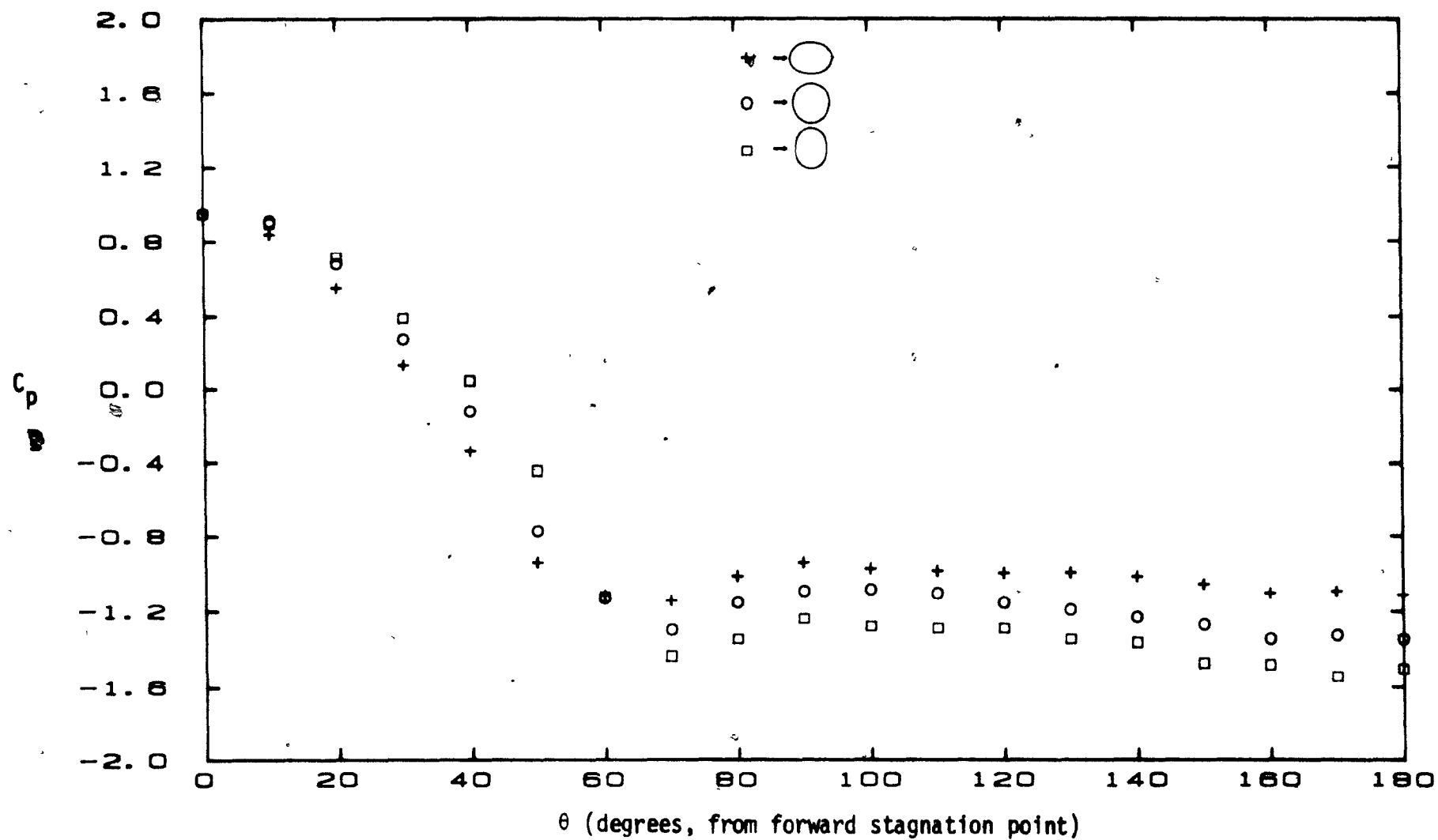


**Figure 7.4:** Pressure coefficient of the  $n=2$  mode model ( $a = 1.57$ ,  $b = 1.43$ ; less deformed) with an antinode facing the free-stream vector, at  $U = 7.5$  m/s ( $Re = 3.80 \times 10^4$ ).

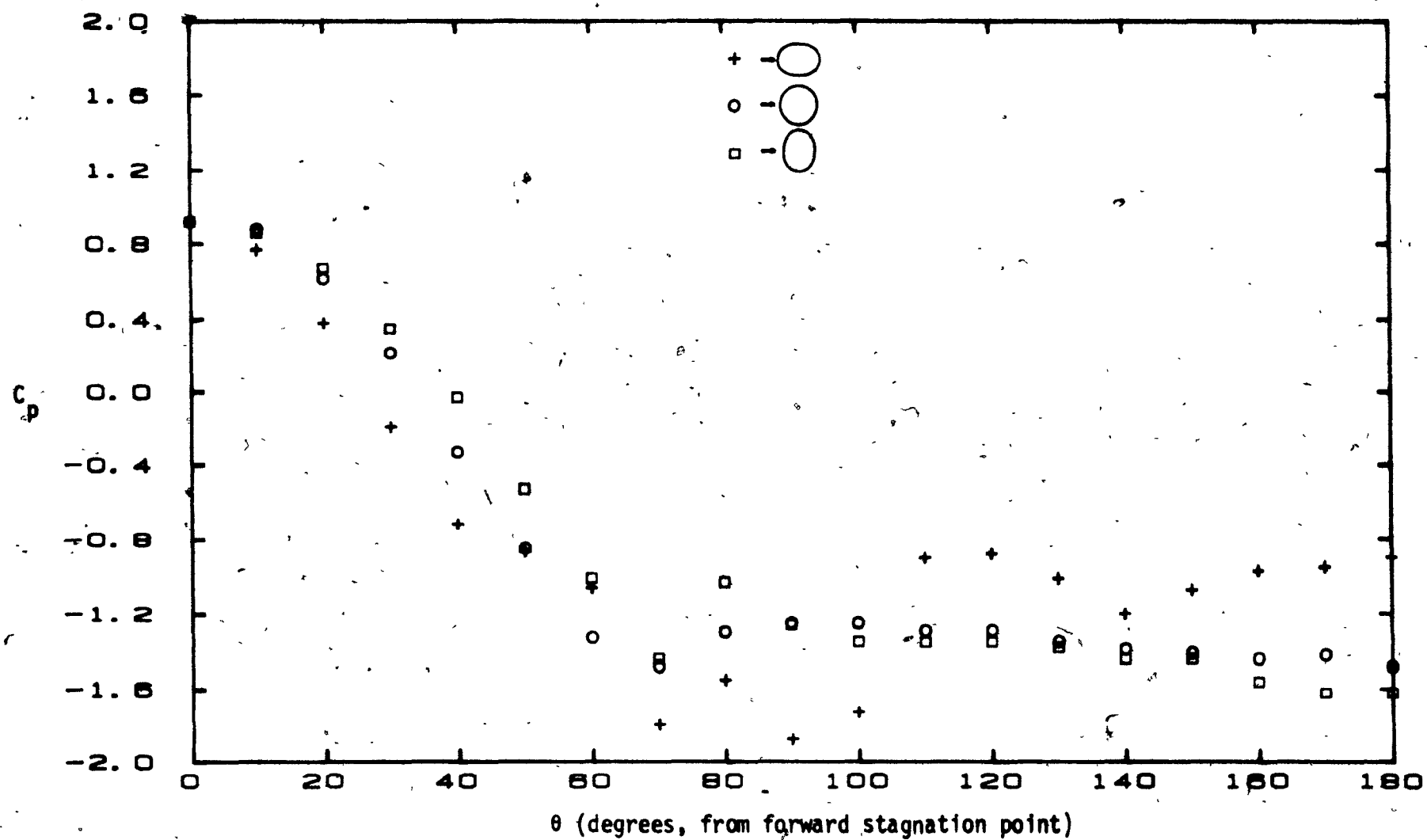


**Figure 7.5:** Pressure coefficient of the  $n=2$  mode model ( $a = 1.57$ ,  $b = 1.43$ ; less deformed) with an antinode facing the free-stream vector, at  $U = 23.5$  m/s ( $Re = 1.18 \times 10^5$ ).

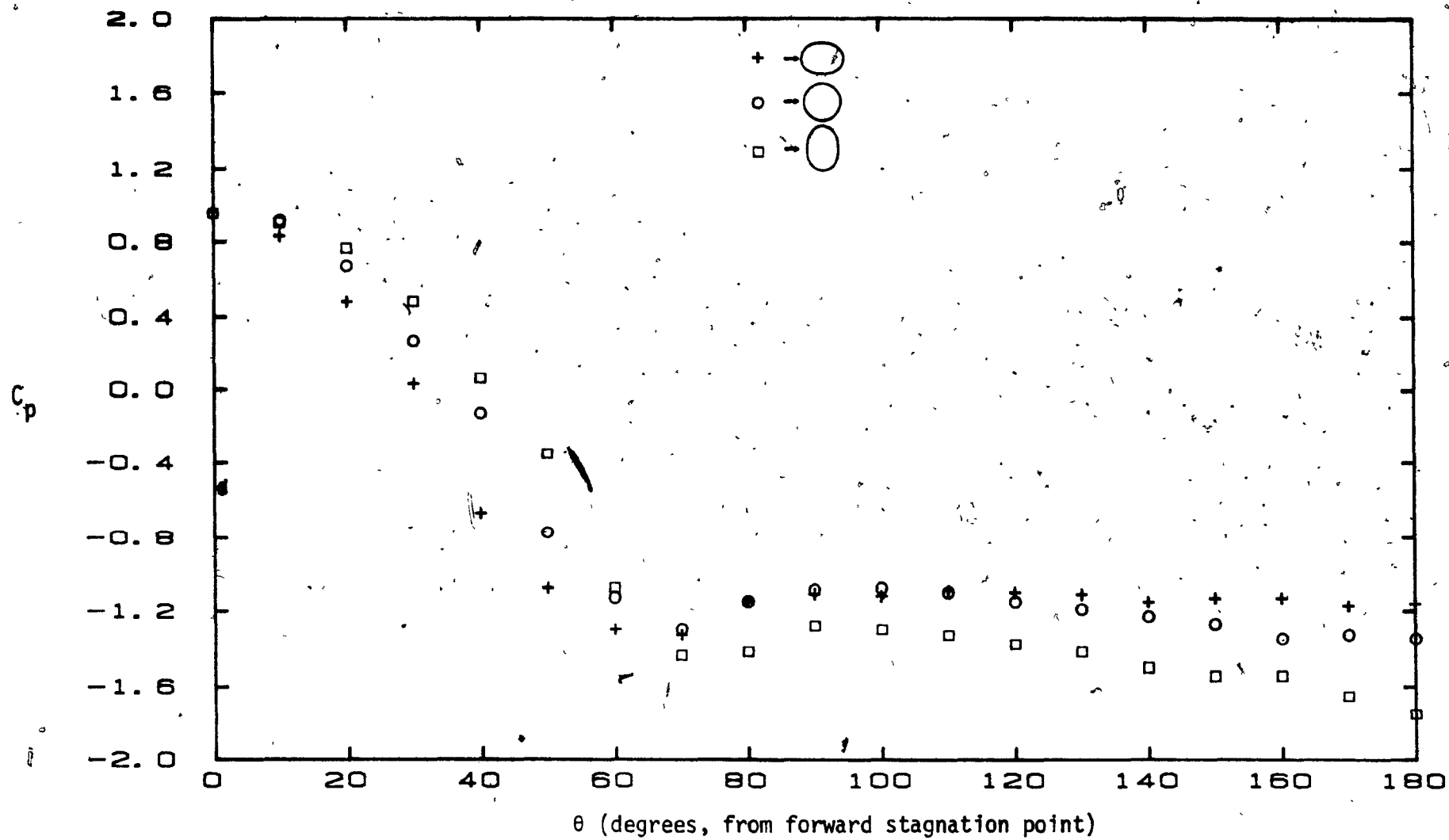


**Figure 7.6:** Pressure coefficient of the  $n=2$  mode model ( $a = 1.62$ ,  $b = 1.38$ ; more deformed) with an antinode facing the free-stream vector, at  $U = 7.5$  m/s ( $Re = 3.80 \times 10^4$ ).

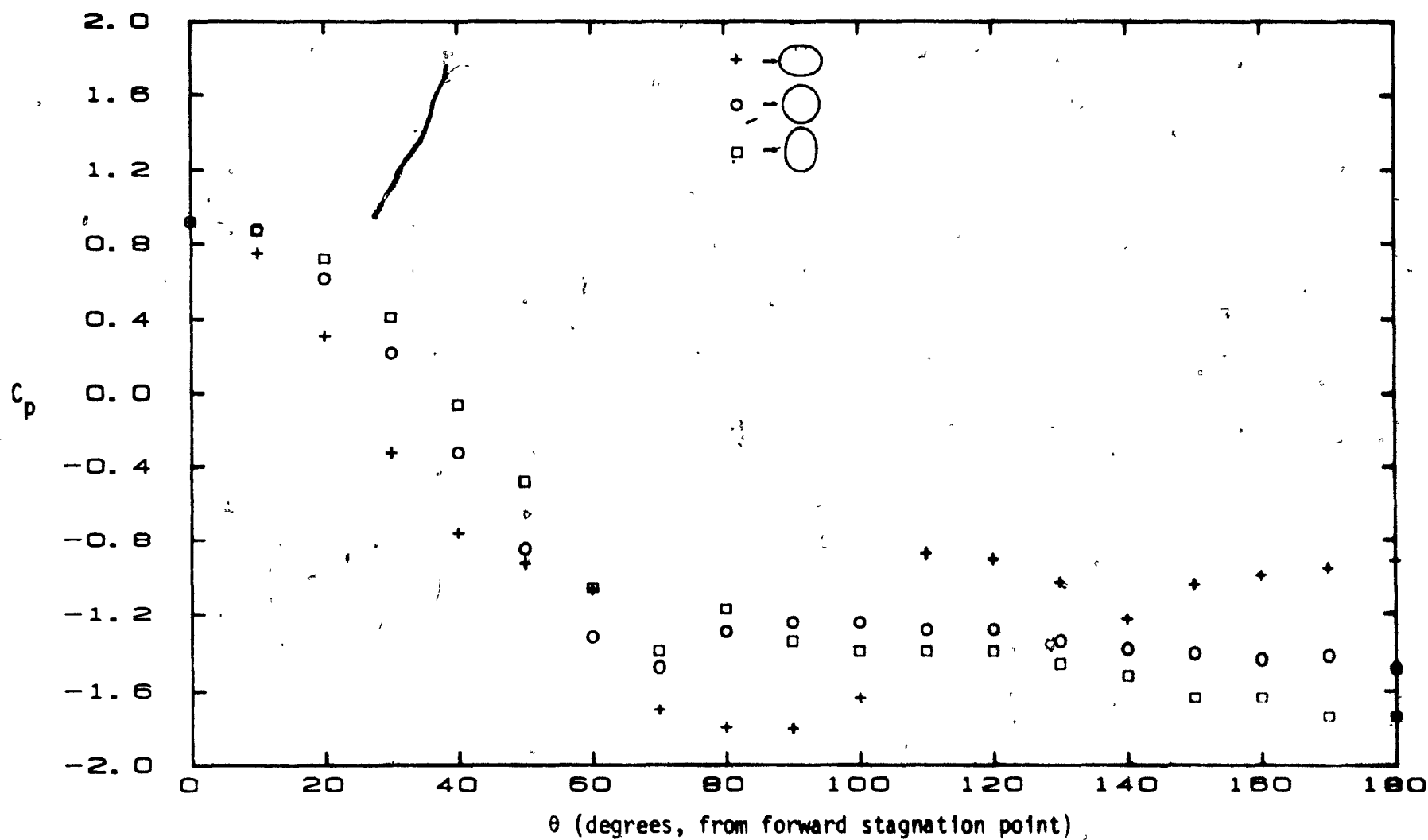


Figure 7.7: Pressure coefficient of the  $n=2$  mode model ( $a = 1.62$ ,  $b = 1.38$ ; more deformed) with an antinode facing the free-stream vector, at  $U = 23.5$  m/s ( $Re = 1.18 \times 10^5$ ).

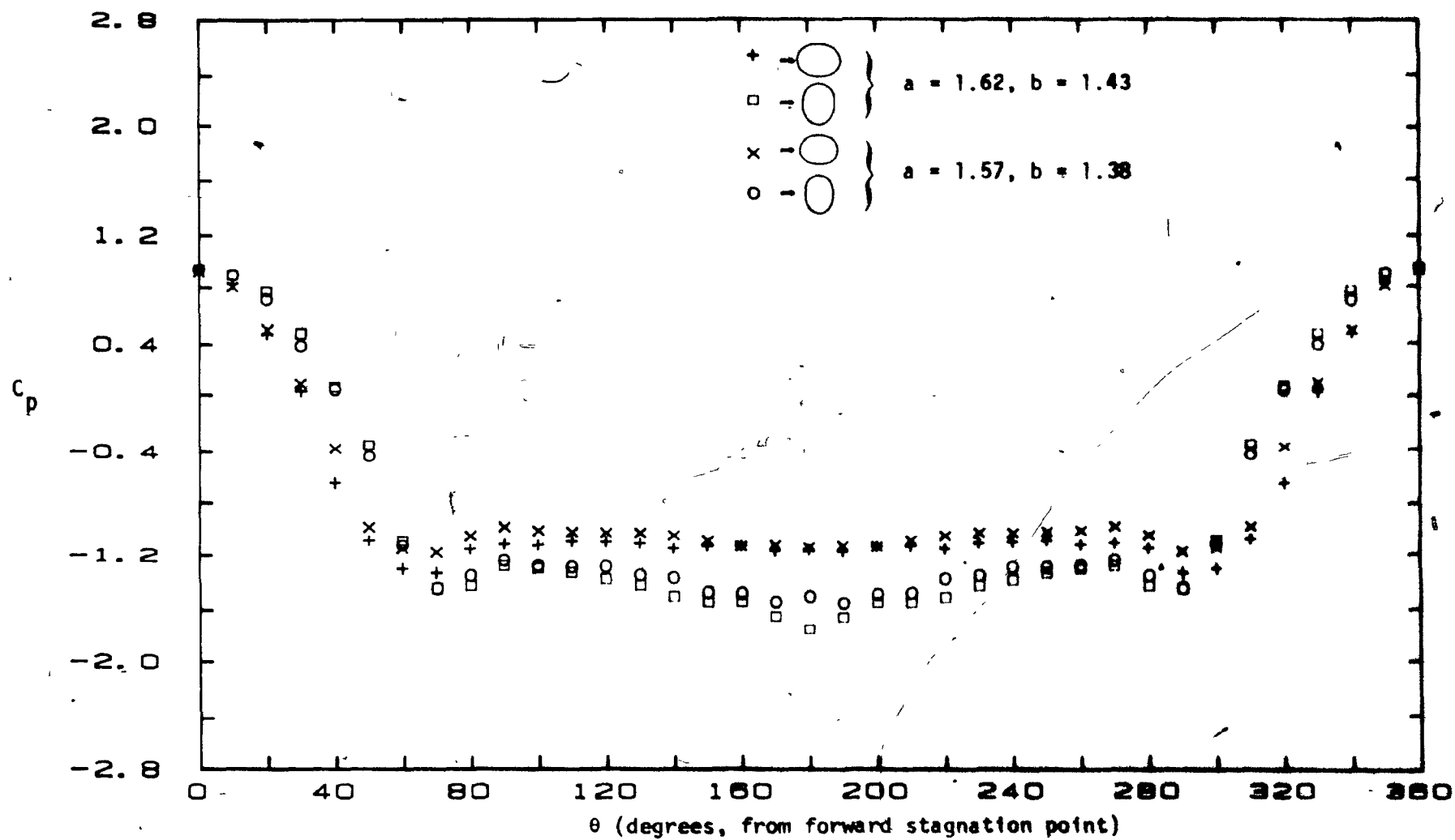


Figure 7.8: Comparison of the pressure coefficient for the two different models of the  $n=2$  mode at  $U = 7.5$  m/s ( $Re = 3.80 \times 10^4$ ).

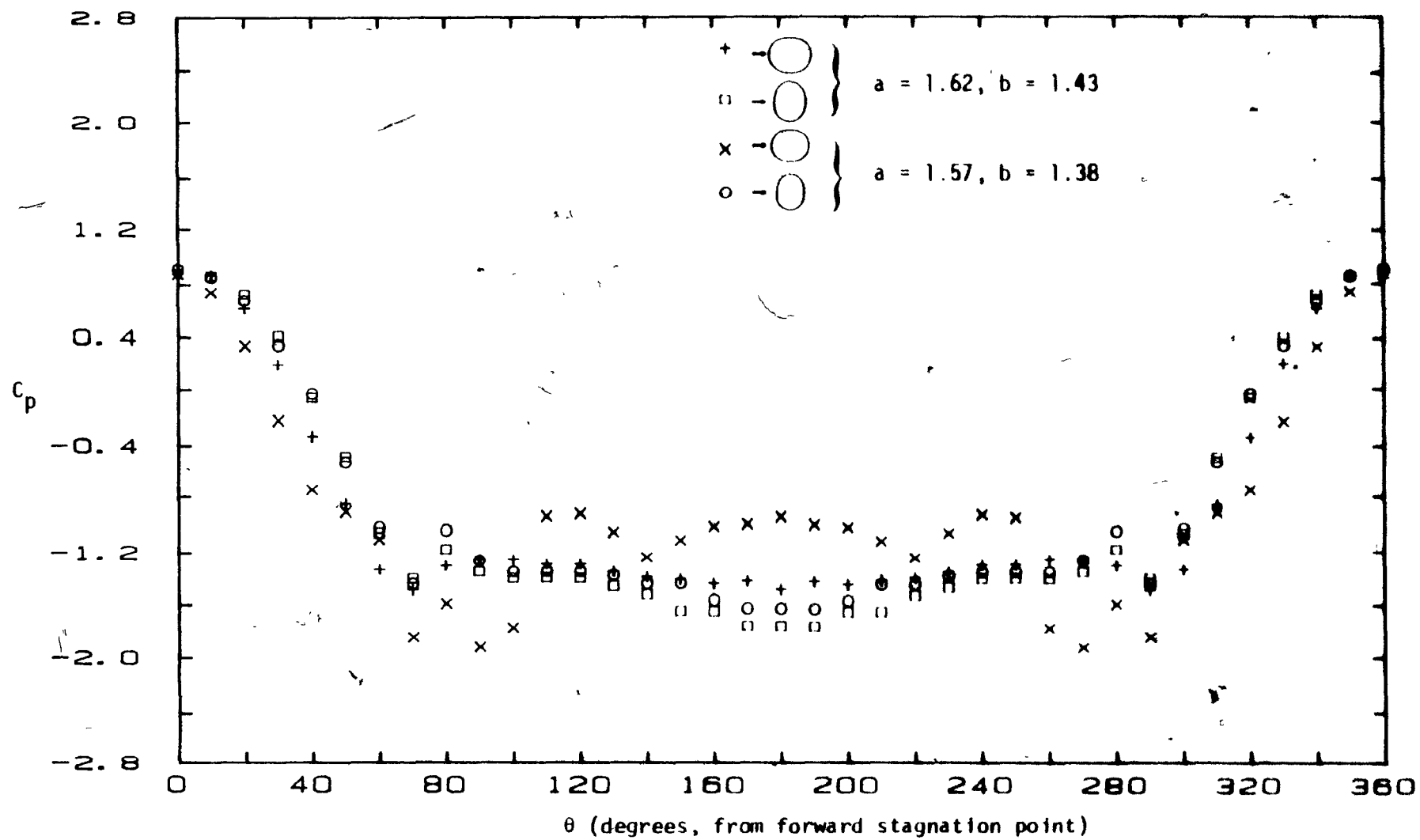


Figure 7.9: Comparison of the pressure coefficient for the two different models of the  $n=2$  mode at  $U = 23.5$  m/s ( $Re = 1.18 \times 10^5$ ).

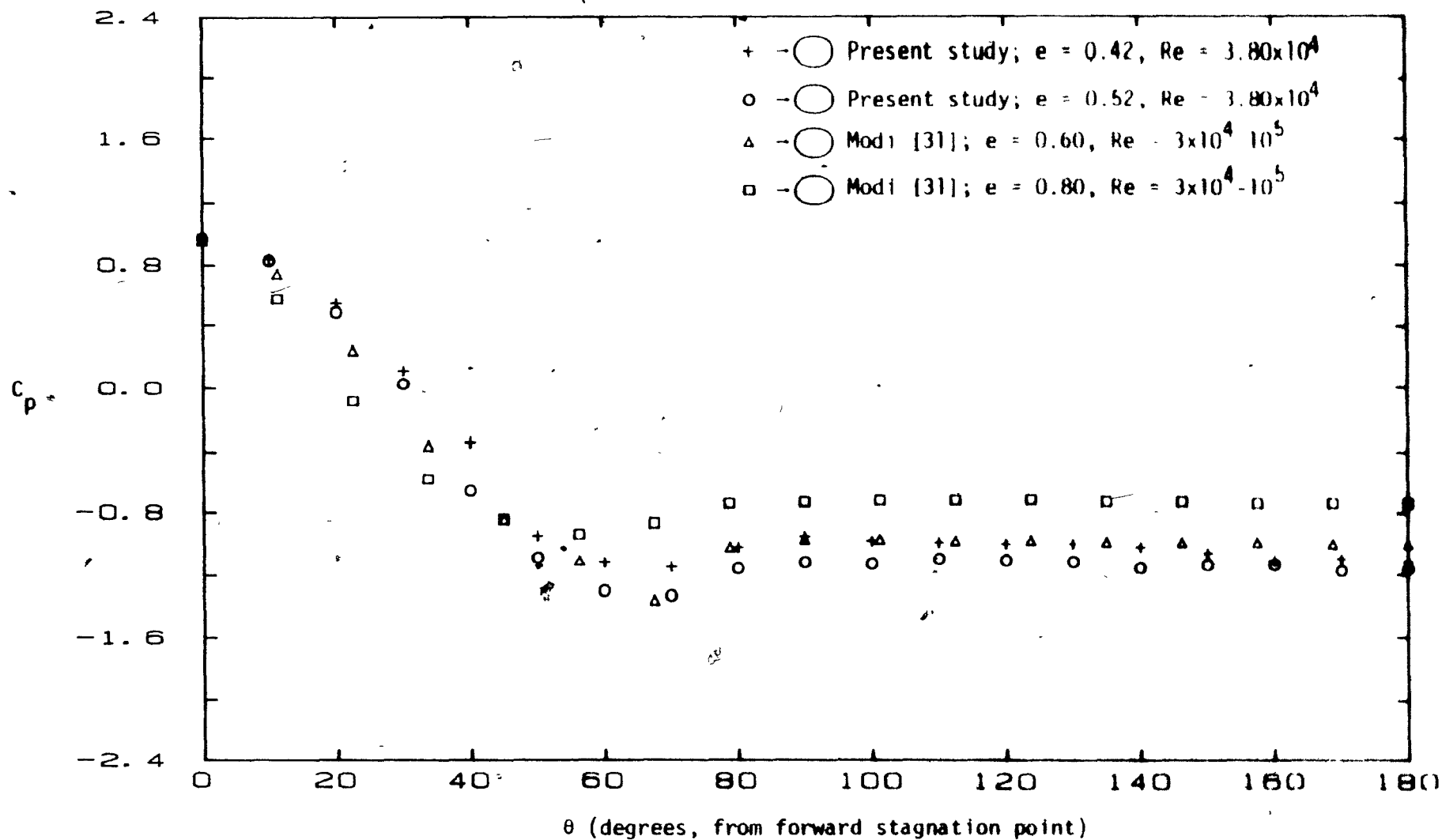


Figure 7.10: Pressure coefficient of the elliptic model for  $\alpha = 0^\circ$ , where  $\alpha$  is the angle between the major axis and the free stream,  $e$  is the eccentricity defined as  $\sqrt{1 - (b^2/a^2)}$ .



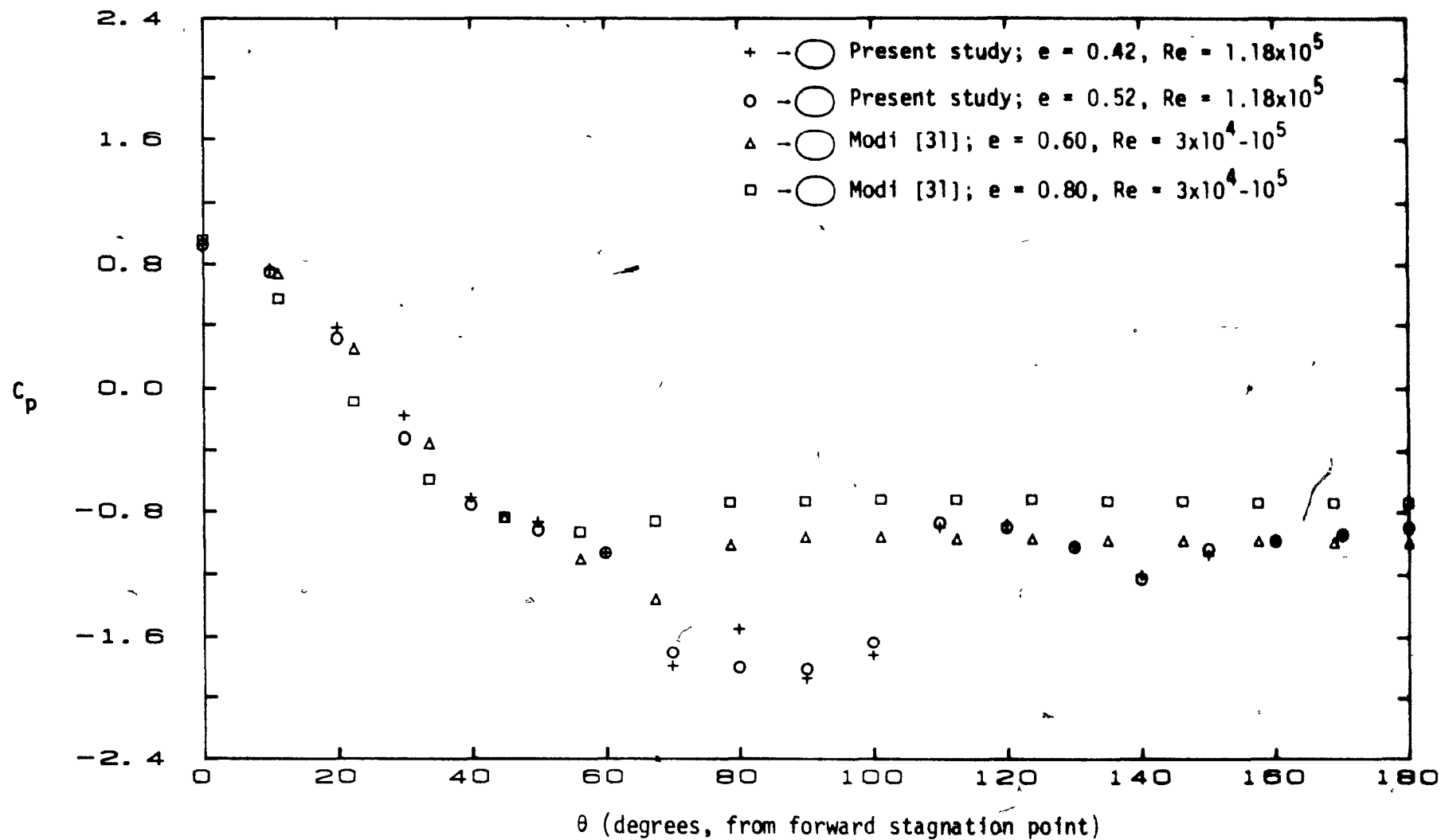


Figure 7.11: Pressure coefficient of the elliptic model for  $\alpha = 0^\circ$ , where  $\alpha$  is the angle between the major axis and the free stream,  $e$  is the eccentricity defined as  $\sqrt{1 - (b^2/a^2)}$ .

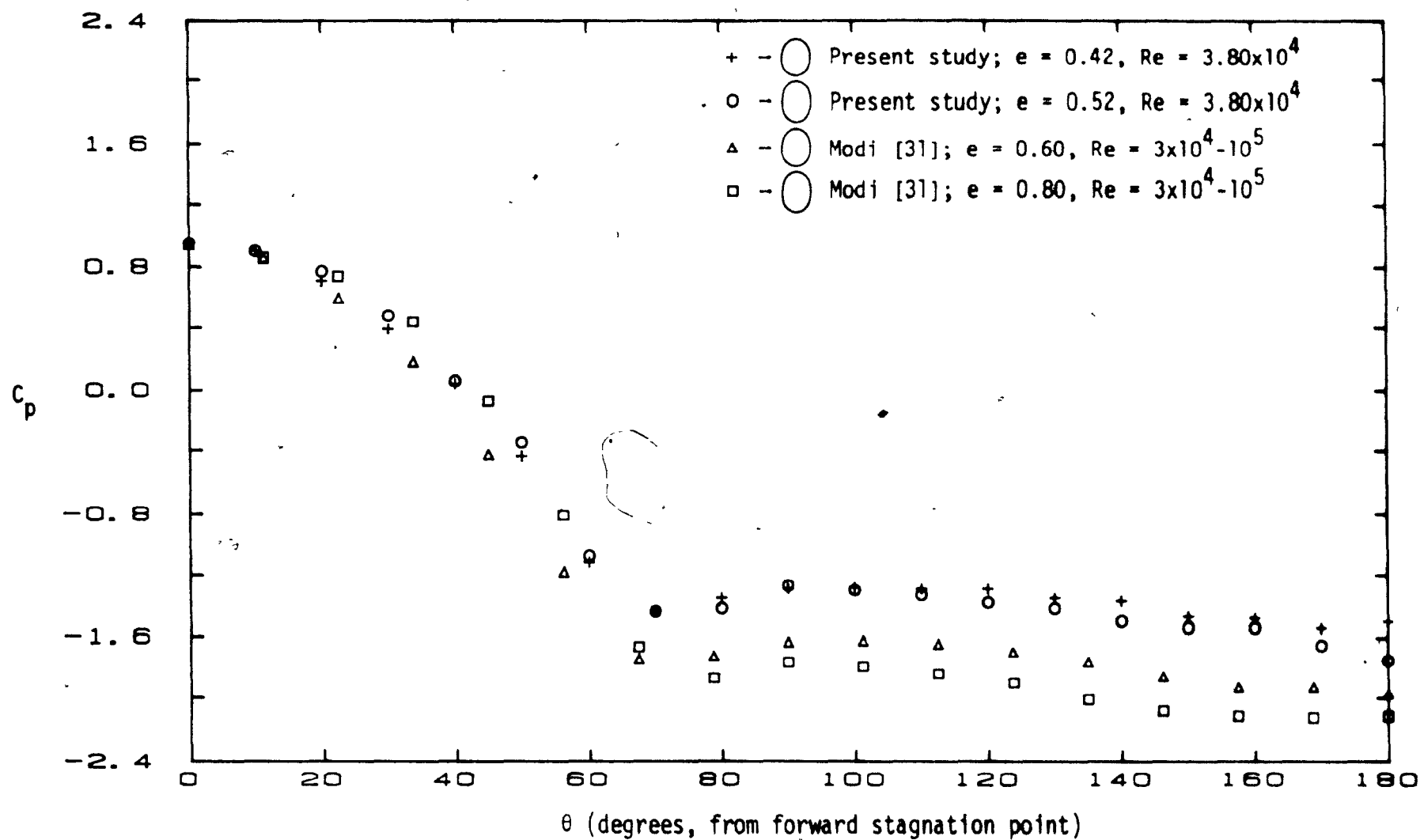


Figure 7.12: Pressure coefficient of the elliptic model for  $\alpha = 90^\circ$ , where  $\alpha$  is the angle between the major axis and the free stream,  $e$  is the eccentricity defined as  $\sqrt{1 - (b^2/a^2)}$ .

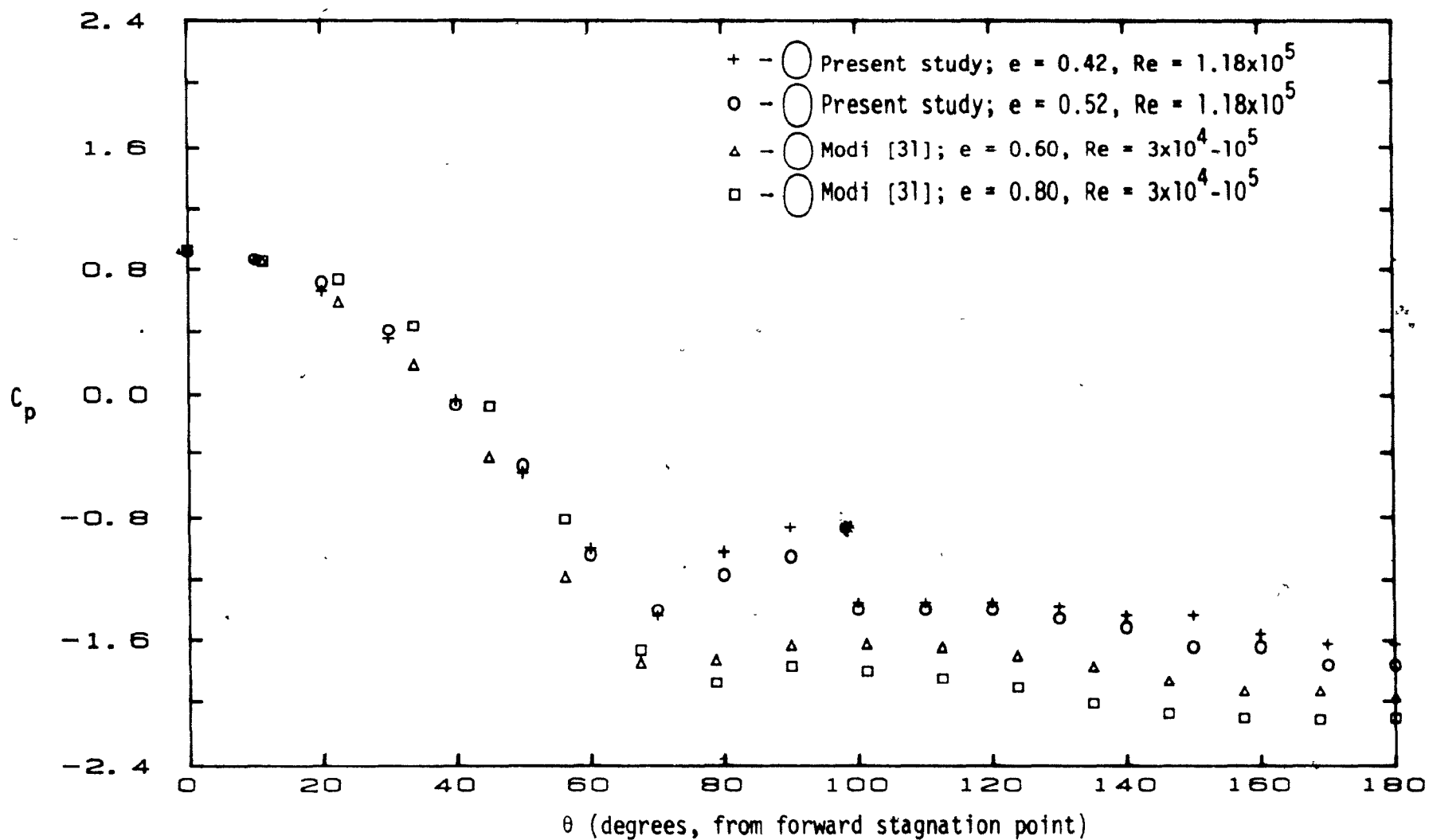
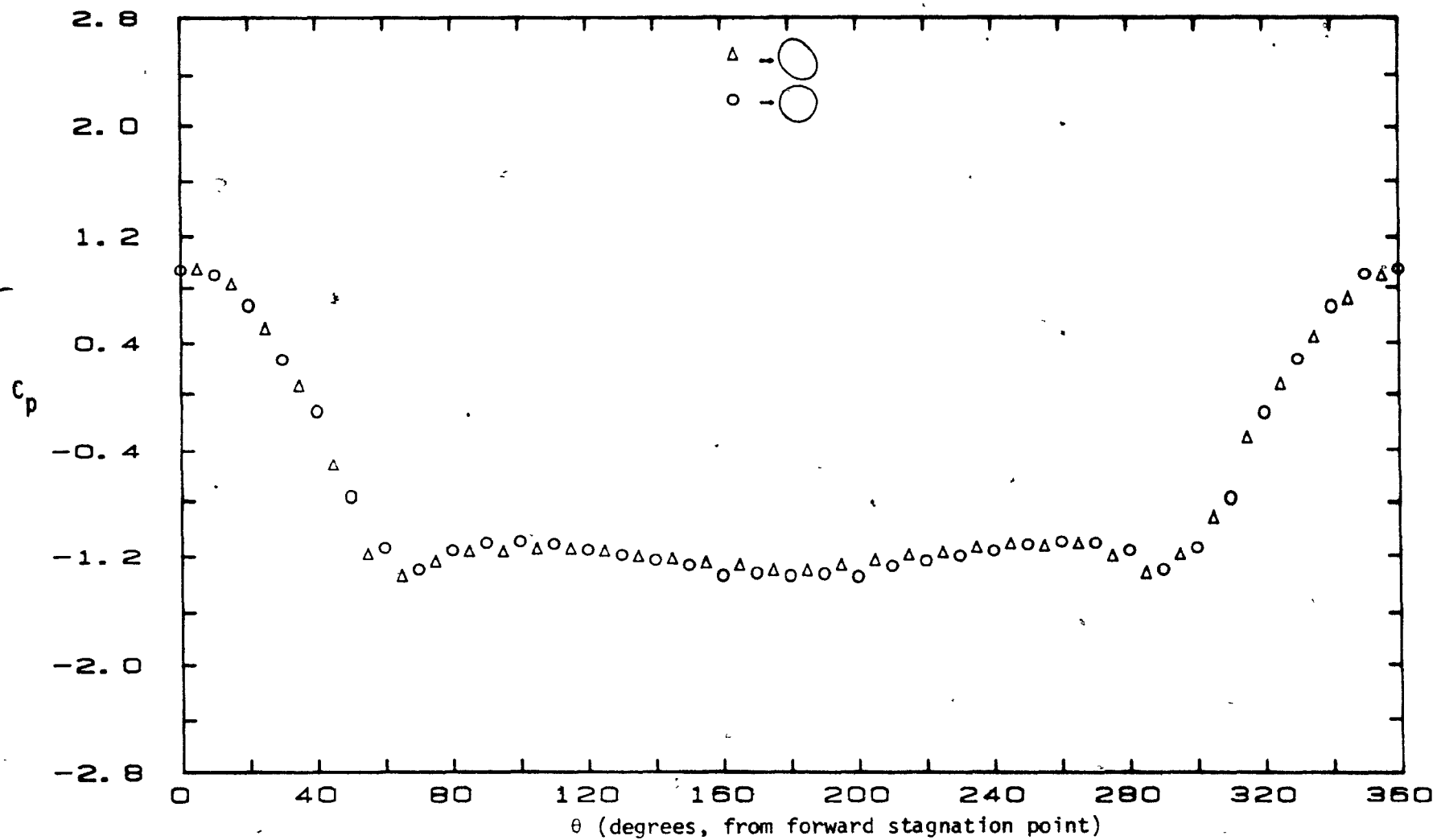


Figure 7.13: Pressure coefficient of the elliptic model for  $\alpha = 90^\circ$ , where  $\alpha$  is the angle between the major axis and the free stream,  $e$  is the eccentricity defined as  $\sqrt{1-(b^2/a^2)}$ .



**Figure 7.14:** Pressure coefficient of the  $n=2$  mode model ( $a = 1.57$ ,  $b = 1.43$ ; less deformed) with a node facing the free-stream vector, at  $U = 7.5$  m/s ( $Re = 3.80 \times 10^4$ ).

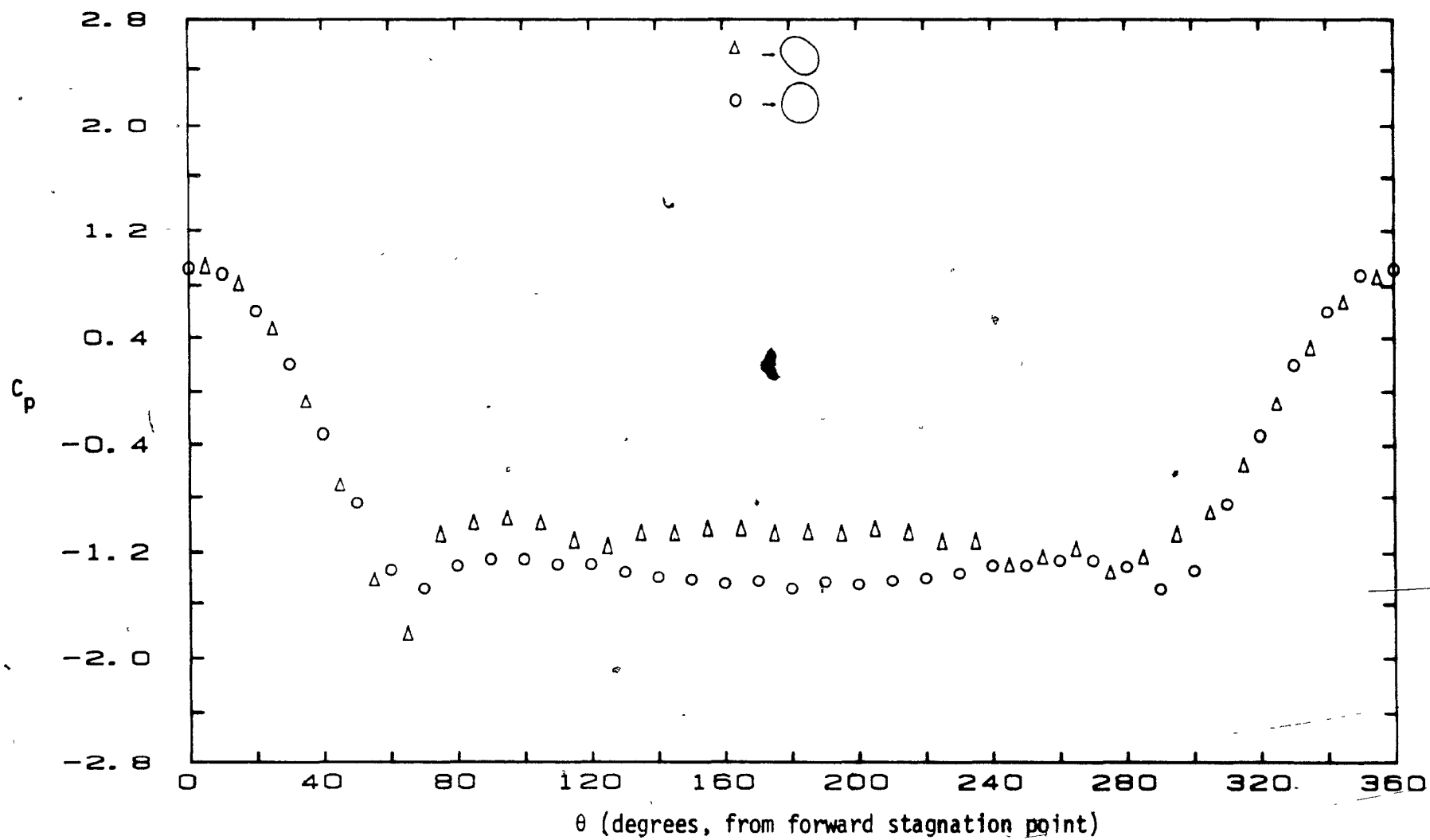


Figure 7.15: Pressure coefficient of the  $n=2$  mode model ( $a = 1.57$ ,  $b = 1.43$ ; less deformed) with a node facing the free-stream vector, at  $U = 23.5$  m/s ( $Re = 1.18 \times 10^5$ ).

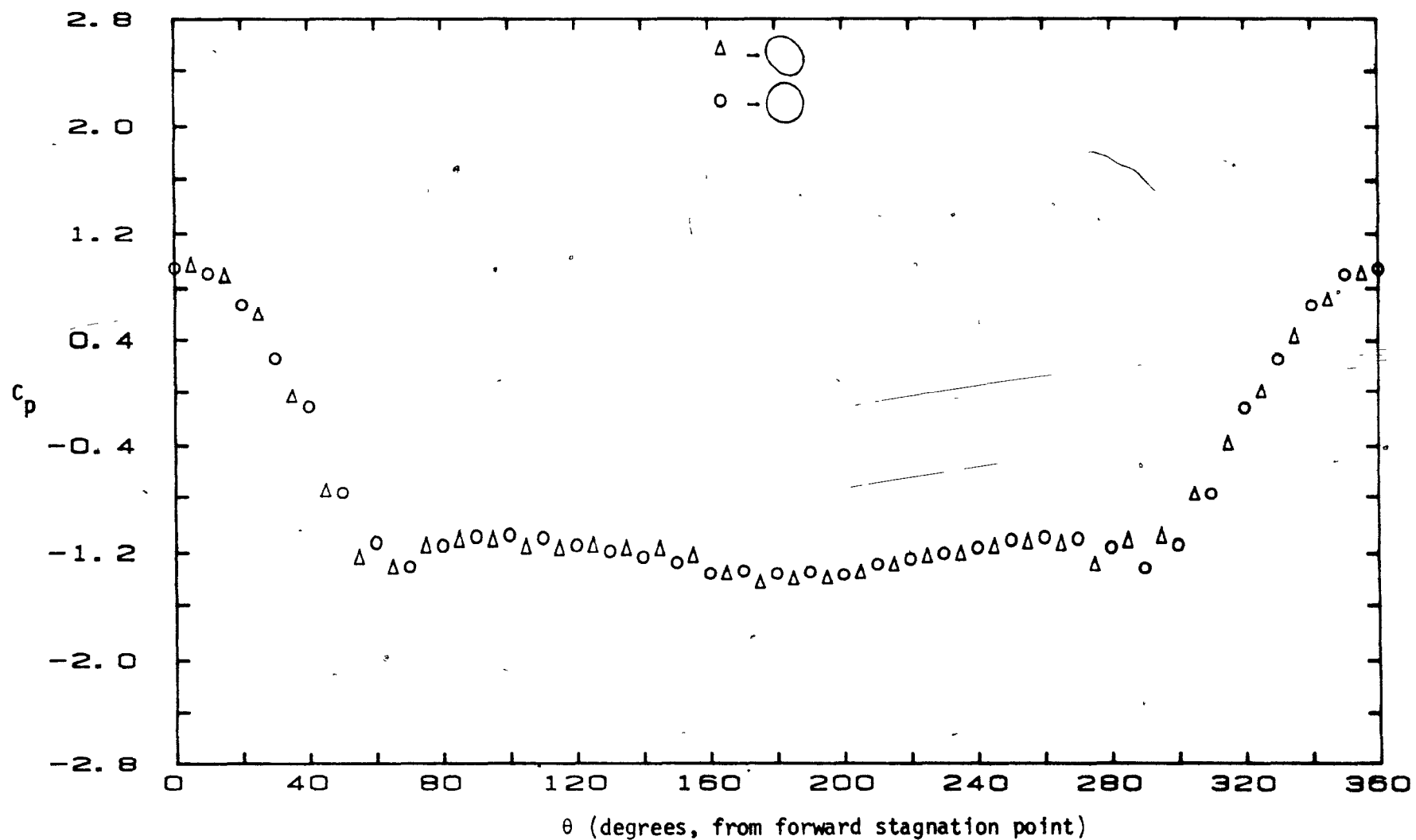


Figure 7.16: Pressure coefficient of the  $n=2$  mode model ( $a = 1.62$ ,  $b = 1.38$ ; more deformed) with a nose facing the free-stream vector, at  $U = 7.5$  m/s ( $Re = 3.80 \times 10^4$ ).

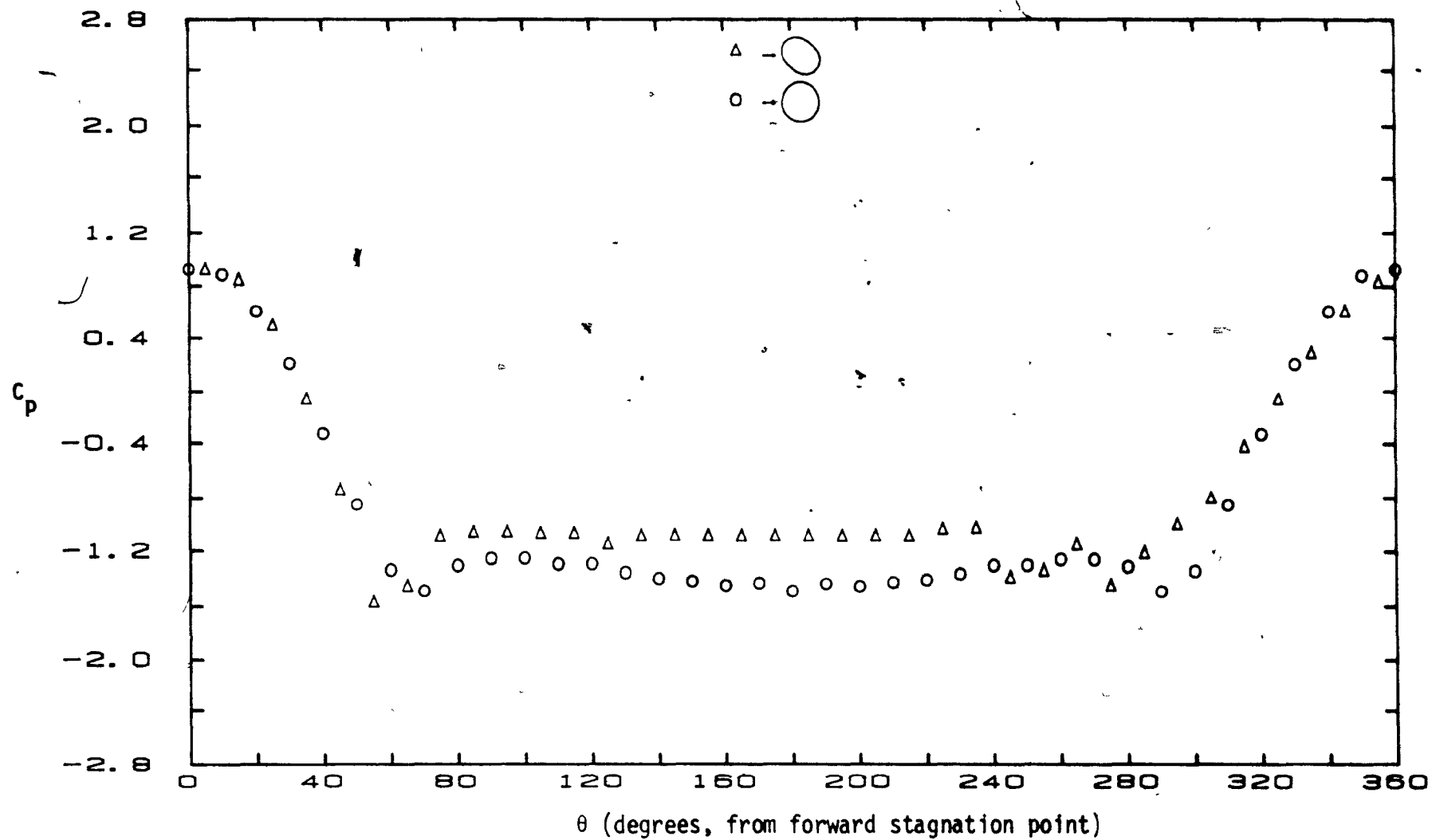


Figure 7.17: Pressure coefficient of the  $n=2$  mode model ( $a = 1.62$ ,  $b = 1.38$ ; more deformed) with a node facing the free-stream vector, at  $U = 23.5$  m/s ( $Re = 1.18 \times 10^5$ ).

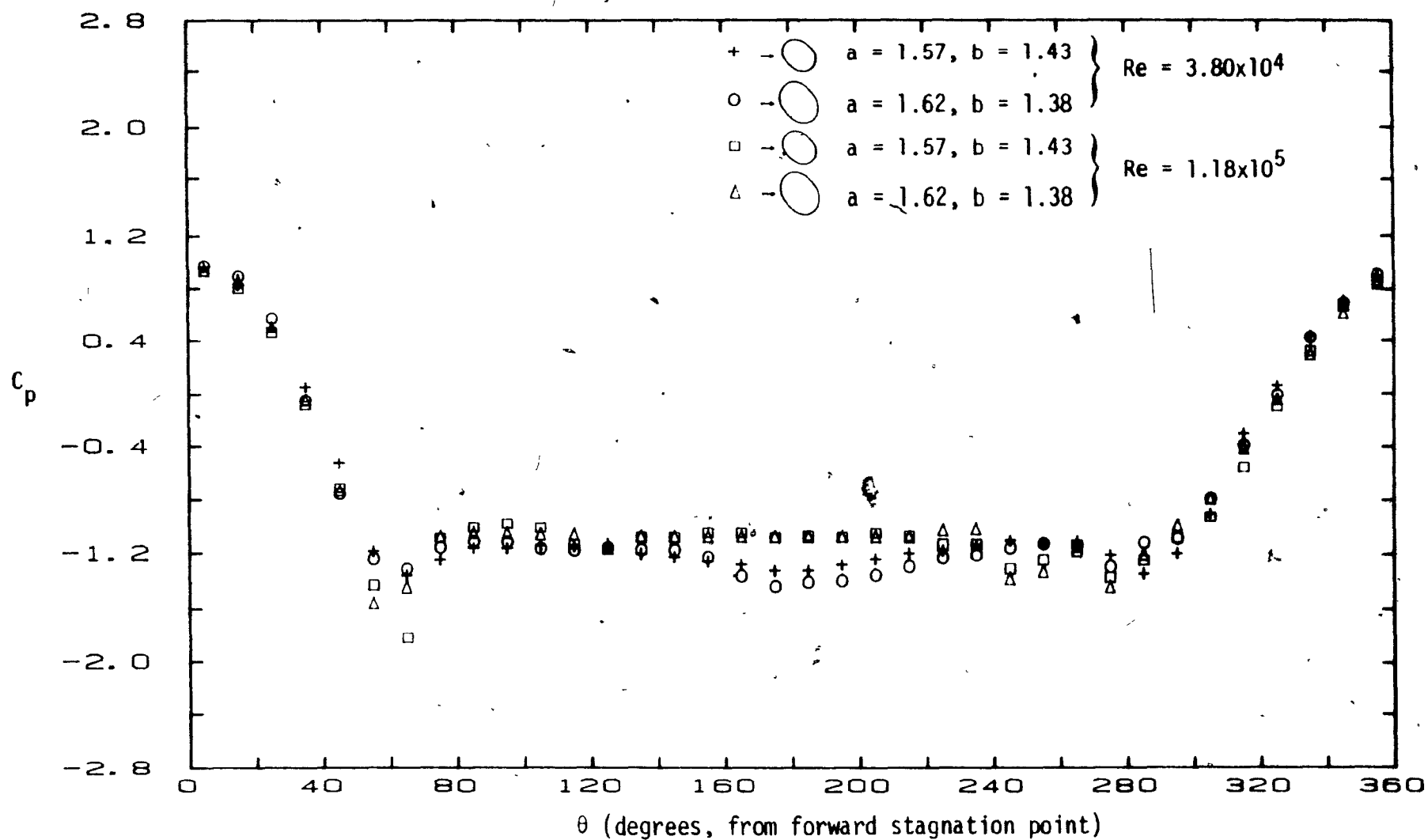


Figure 7.18: Comparison of the pressure coefficient for the two different models of the  $n=2$  mode at different flow velocities.



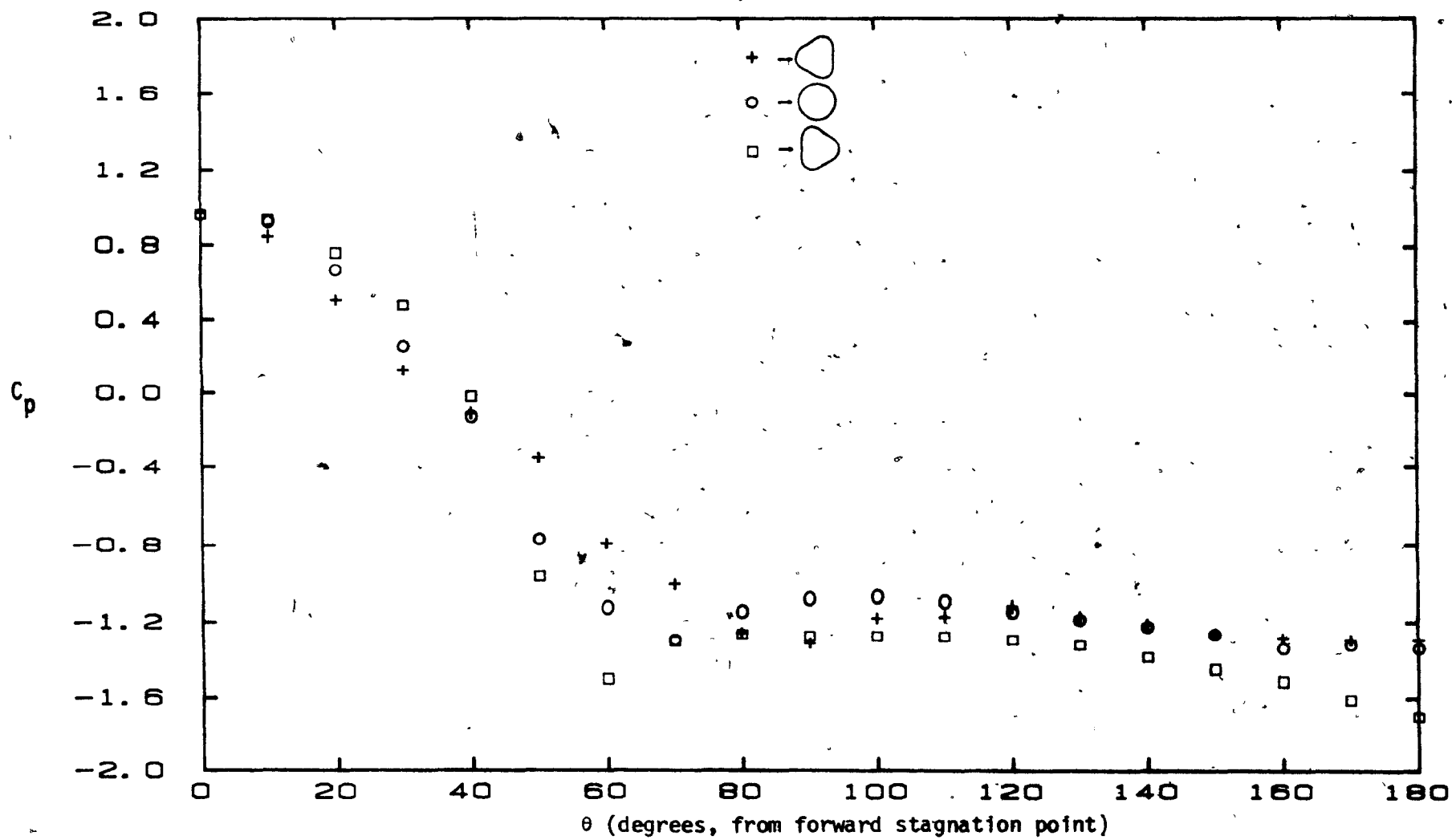
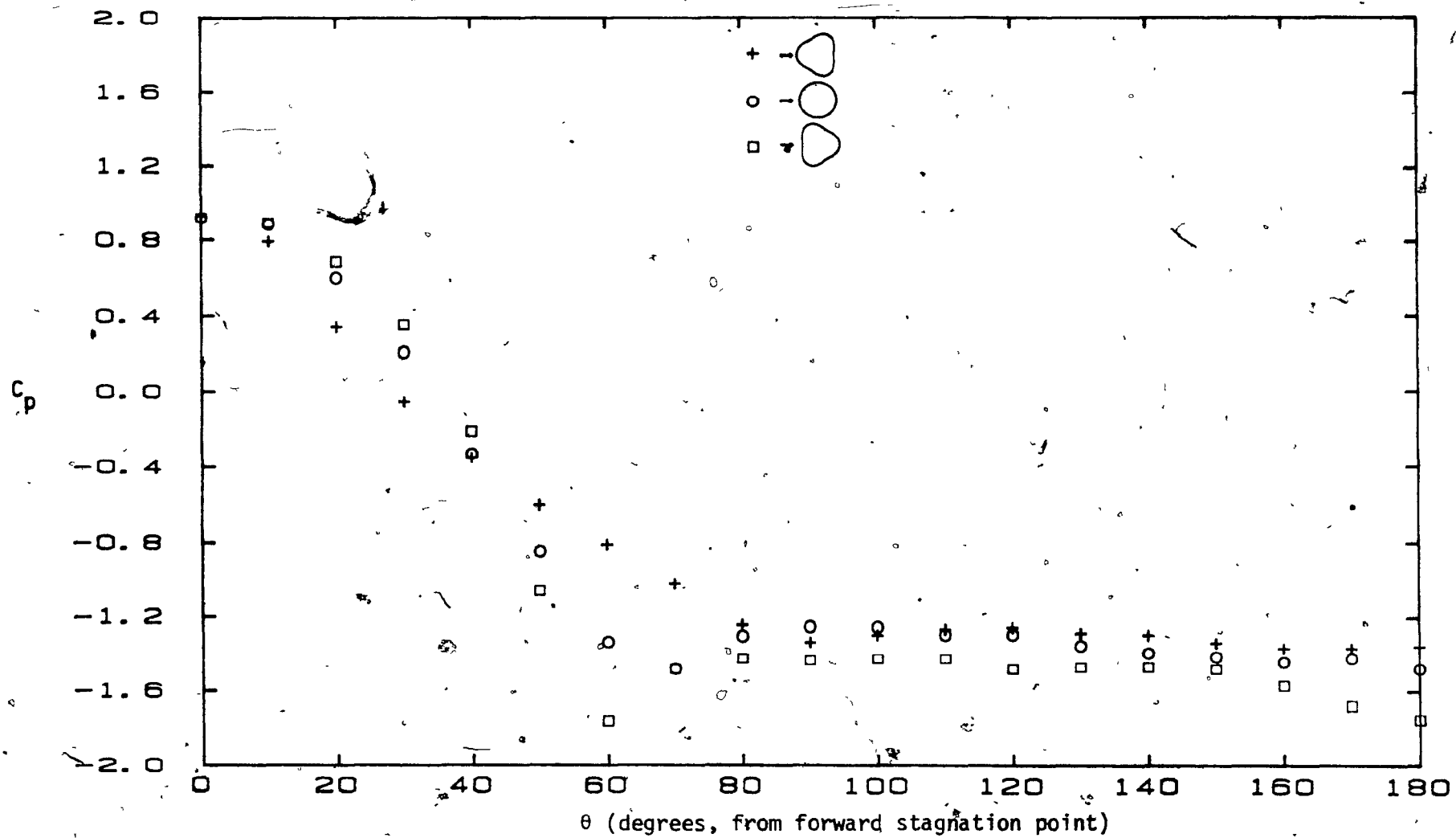
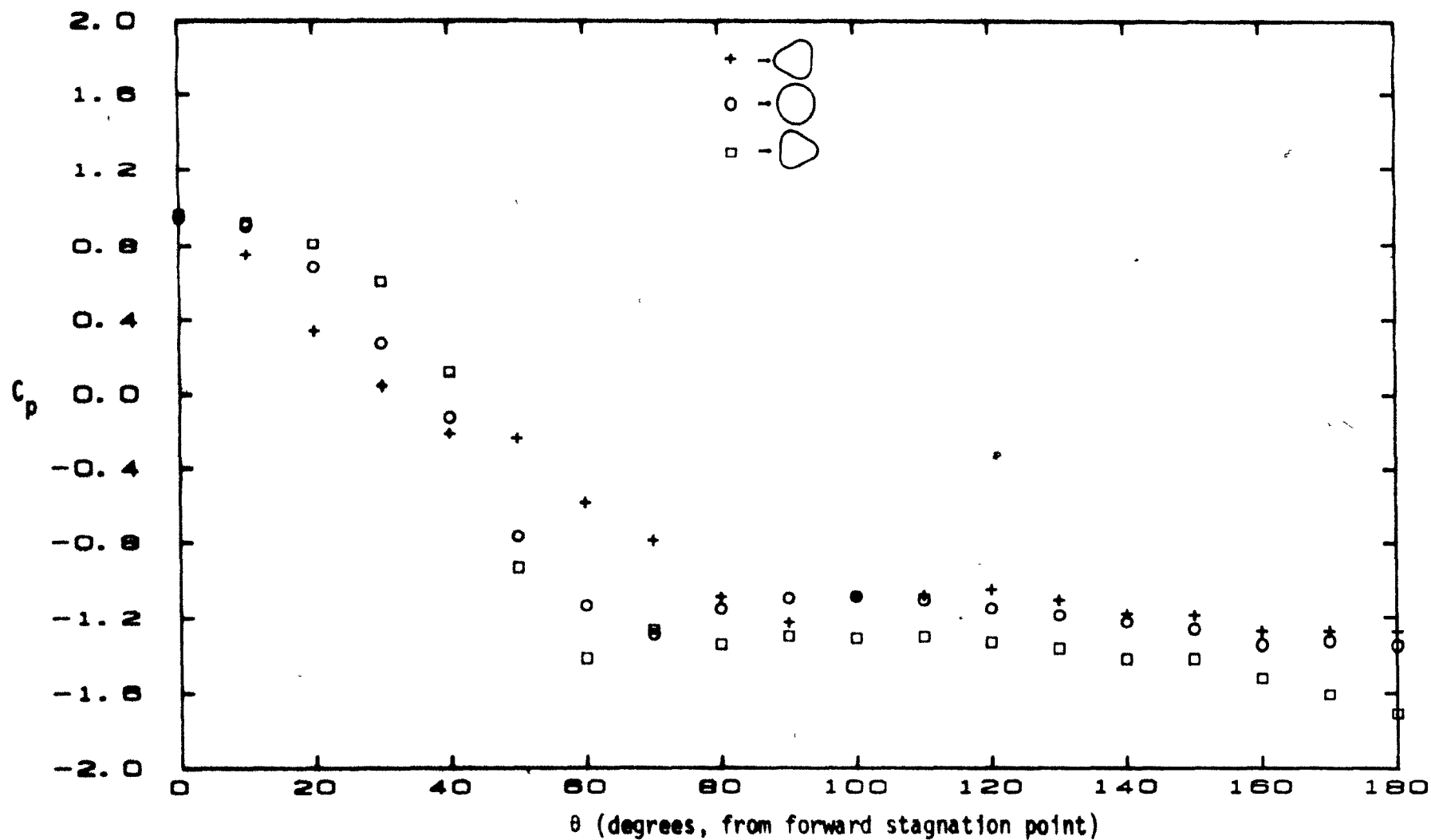


Figure 7.19: Pressure coefficient of the  $n=3$  mode model ( $P = 0.075$ ; less deformed) with an antinode facing the free-stream vector, at  $U = 7.5$  m/s ( $Re = 3.80 \times 10^4$ ).



**Figure 7.20:** Pressure coefficient of the  $n=3$  mode model ( $P = 0.075$ ; less deformed) with an antinode facing the free-stream vector, at  $U = 23.5$  m/s ( $Re = 1.18 \times 10^5$ ).



**Figure 7.21:** Pressure coefficient of the  $n=3$  mode model ( $P = 0.100$ ; more deformed) with an antinode facing the free-stream vector, at  $U = 7.5$  m/s ( $Re = 3.80 \times 10^4$ ).

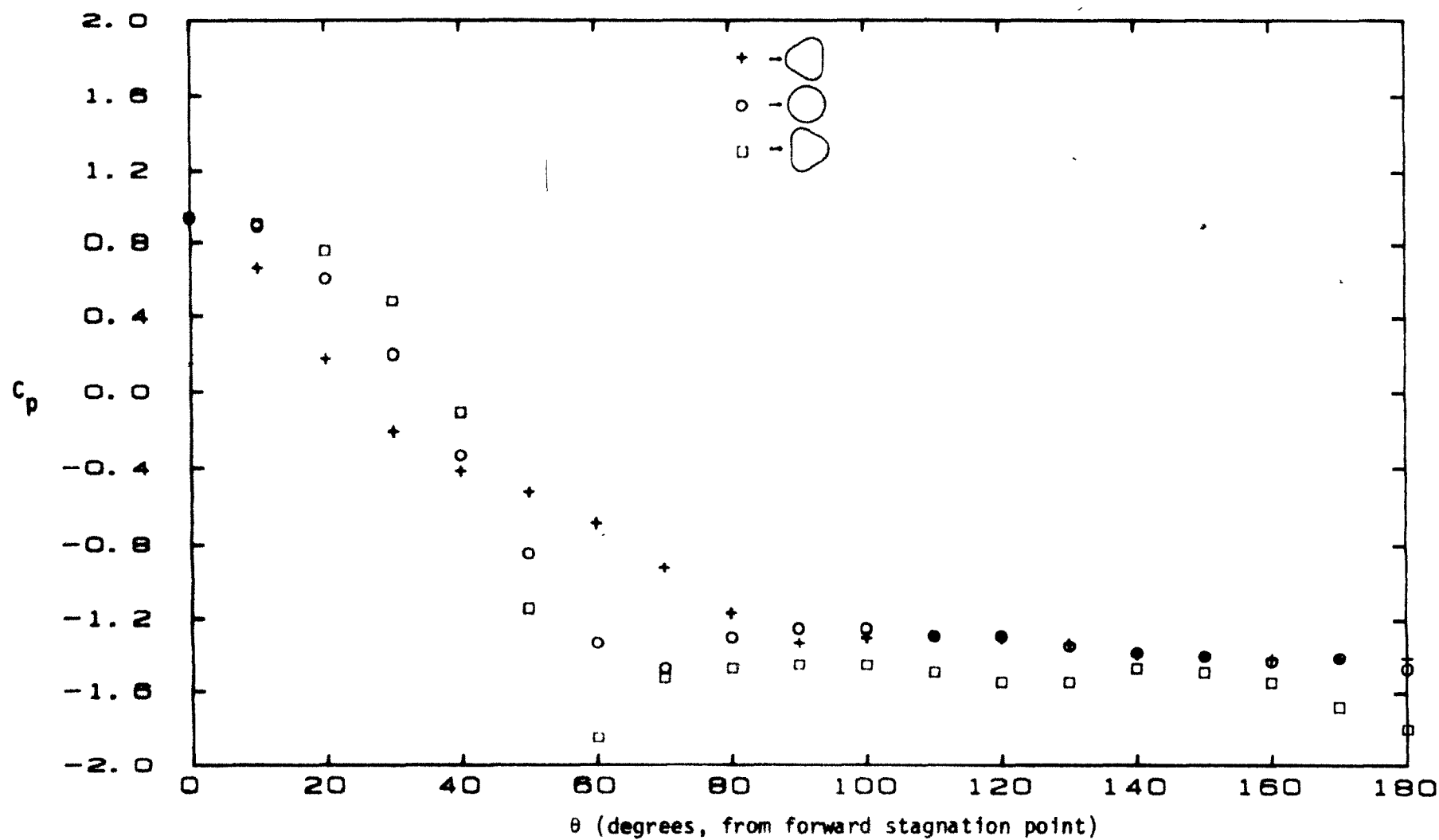


**Figure 7.22:** Pressure coefficient of the  $n=3$  mode model ( $P = 0.100$ ; more deformed) with an antinode facing the free-stream vector, at  $U = 23.5$  m/s ( $Re = 1.18 \times 10^5$ ).

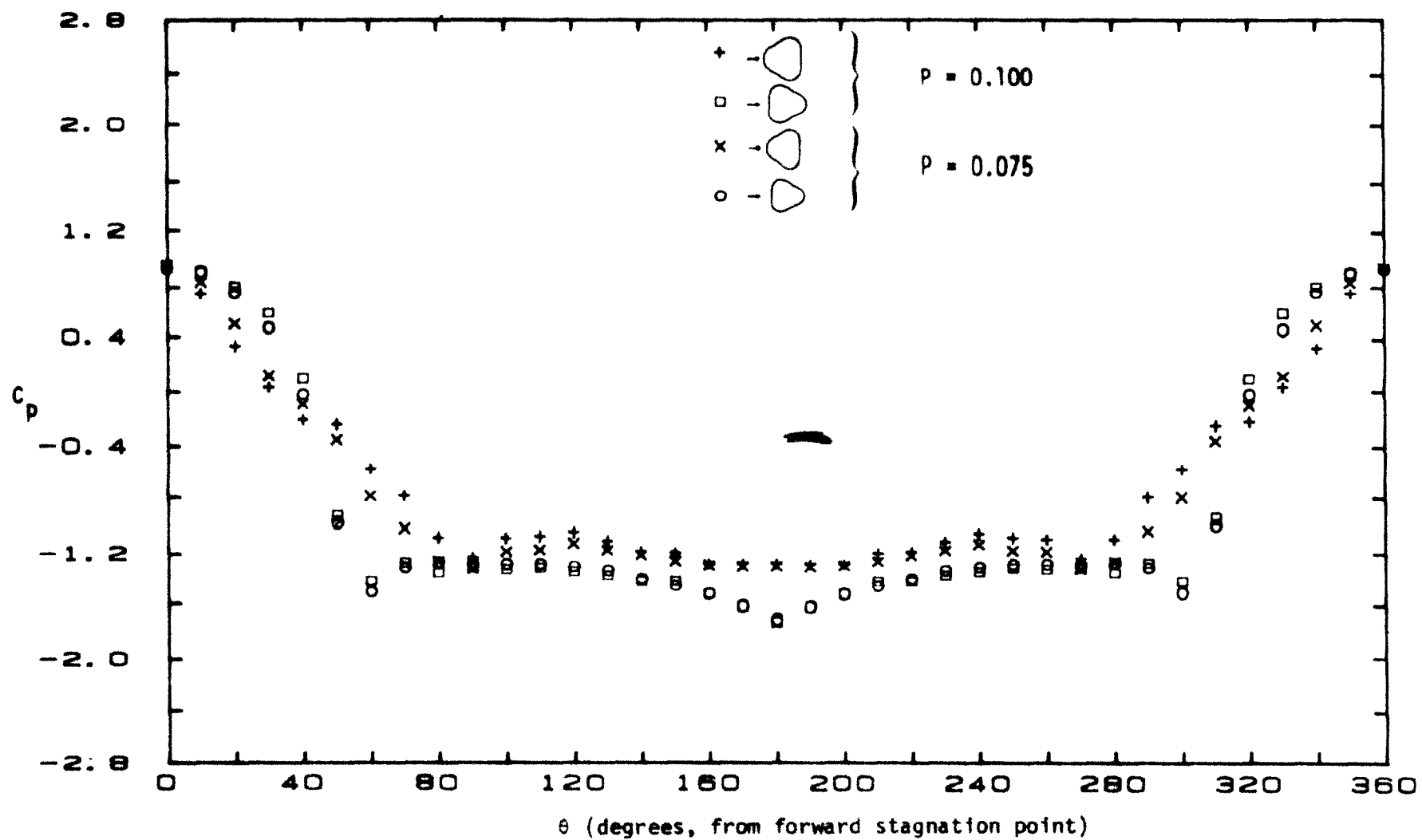


**Figure 7.23:** Comparison of the pressure coefficient for the two different models of the  $n=3$  mode at  $U = 7.5$  m/s ( $Re = 3.80 \times 10^4$ ).

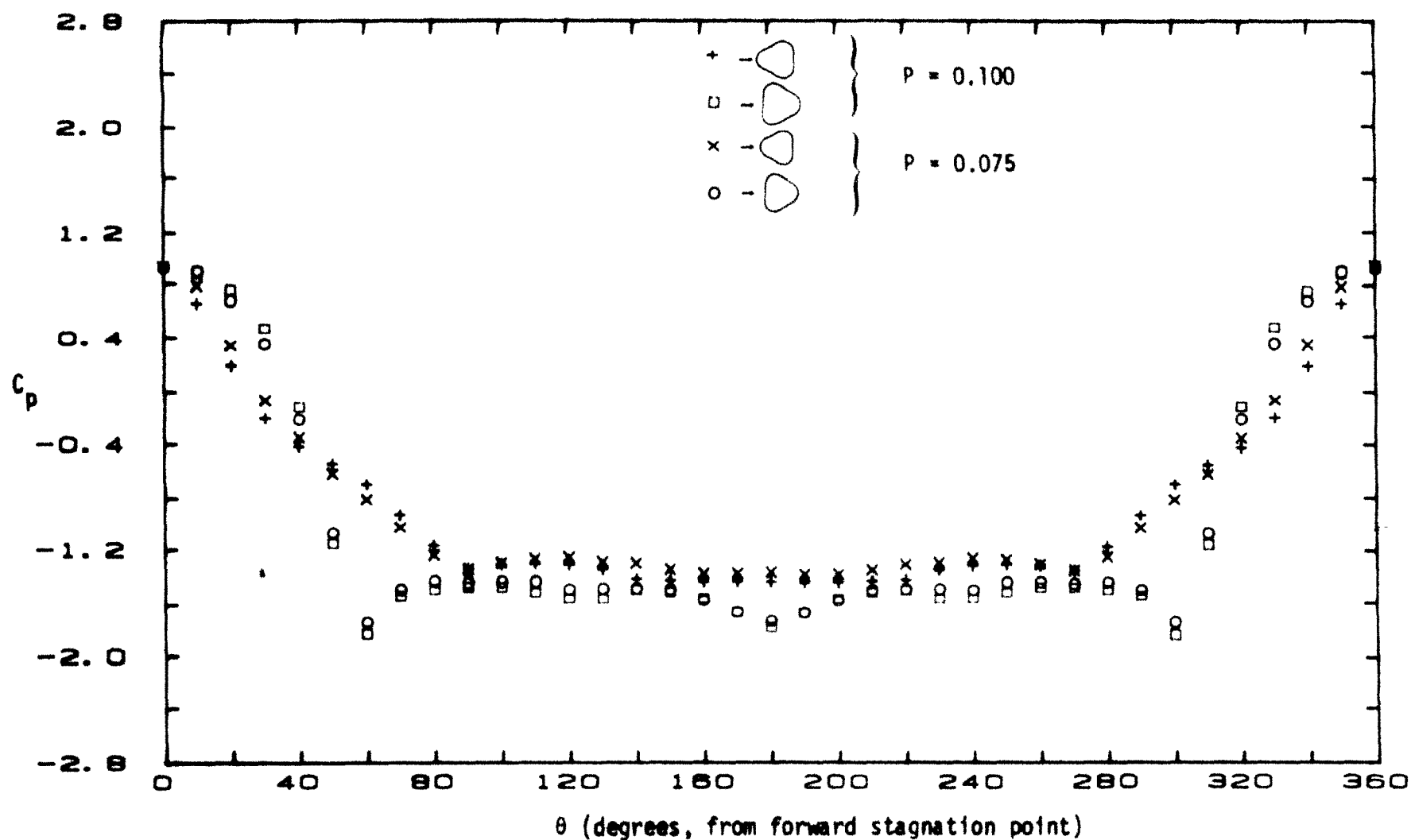


**Figure 7.24:** Comparison of the pressure coefficient for the two different models of the  $n=3$  mode at  $U = 23.5$  m/s ( $Re = 1.18 \times 10^5$ ).

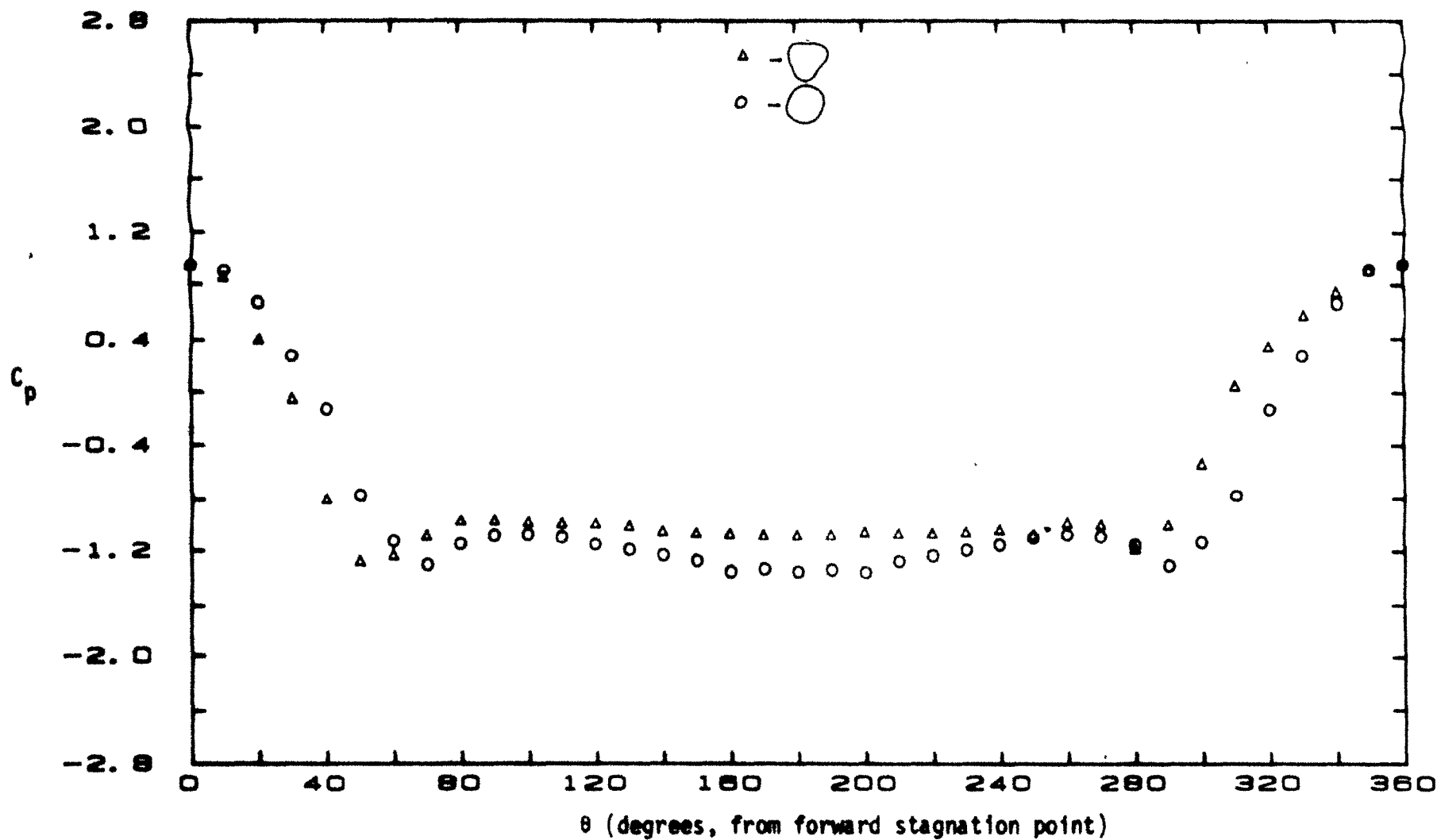


**Figure 7.25:** Pressure coefficient of the  $n=3$  mode model ( $P = 0.075$ ; less deformed) with a node facing the free-stream vector, at  $U = 7.5$  m/s ( $Re = 3.80 \times 10^4$ ).

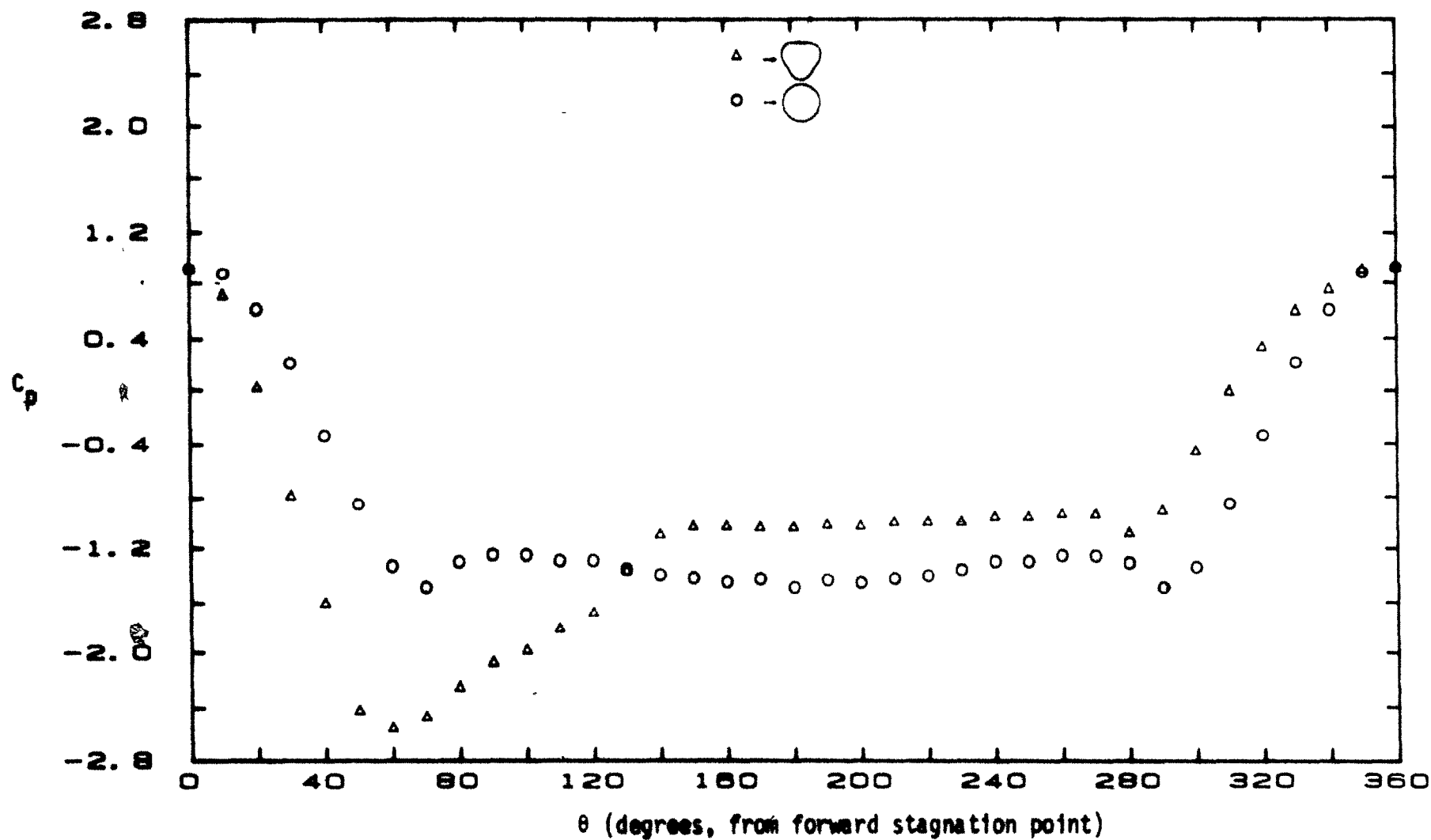


**Figure 7.26:** Pressure coefficient of the  $n=3$  mode model ( $P = 0.075$ ; less deformed) with a node facing the free-stream vector, at  $U = 23.5$  m/s ( $Re = 1.18 \times 10^5$ ).



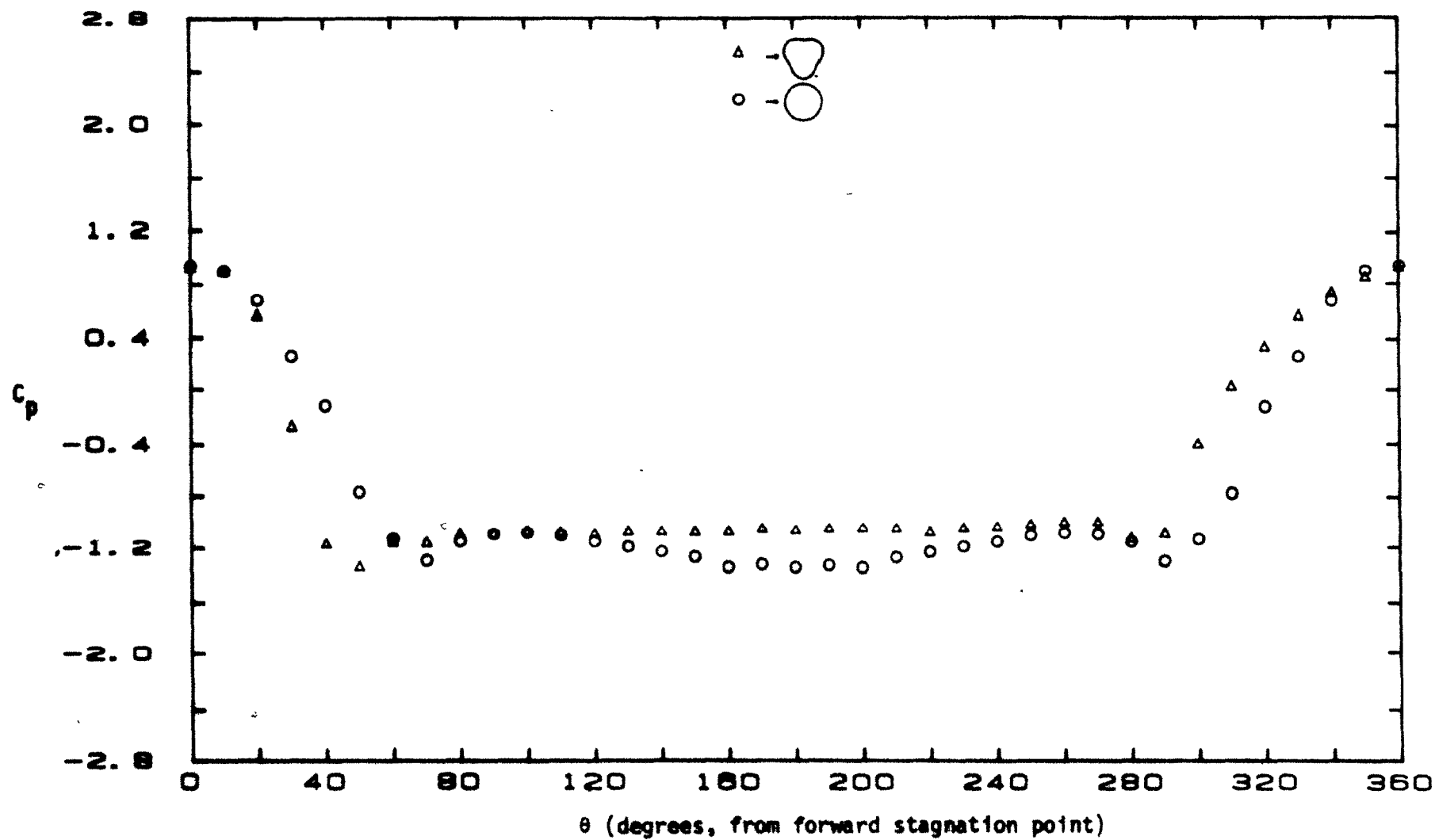


**Figure 7.27:** Pressure coefficient of the  $n=3$  mode model ( $P = 0.100$ ; more deformed) with a node facing the free-stream vector, at  $U = 7.5$  m/s ( $Re = 3.80 \times 10^4$ ).

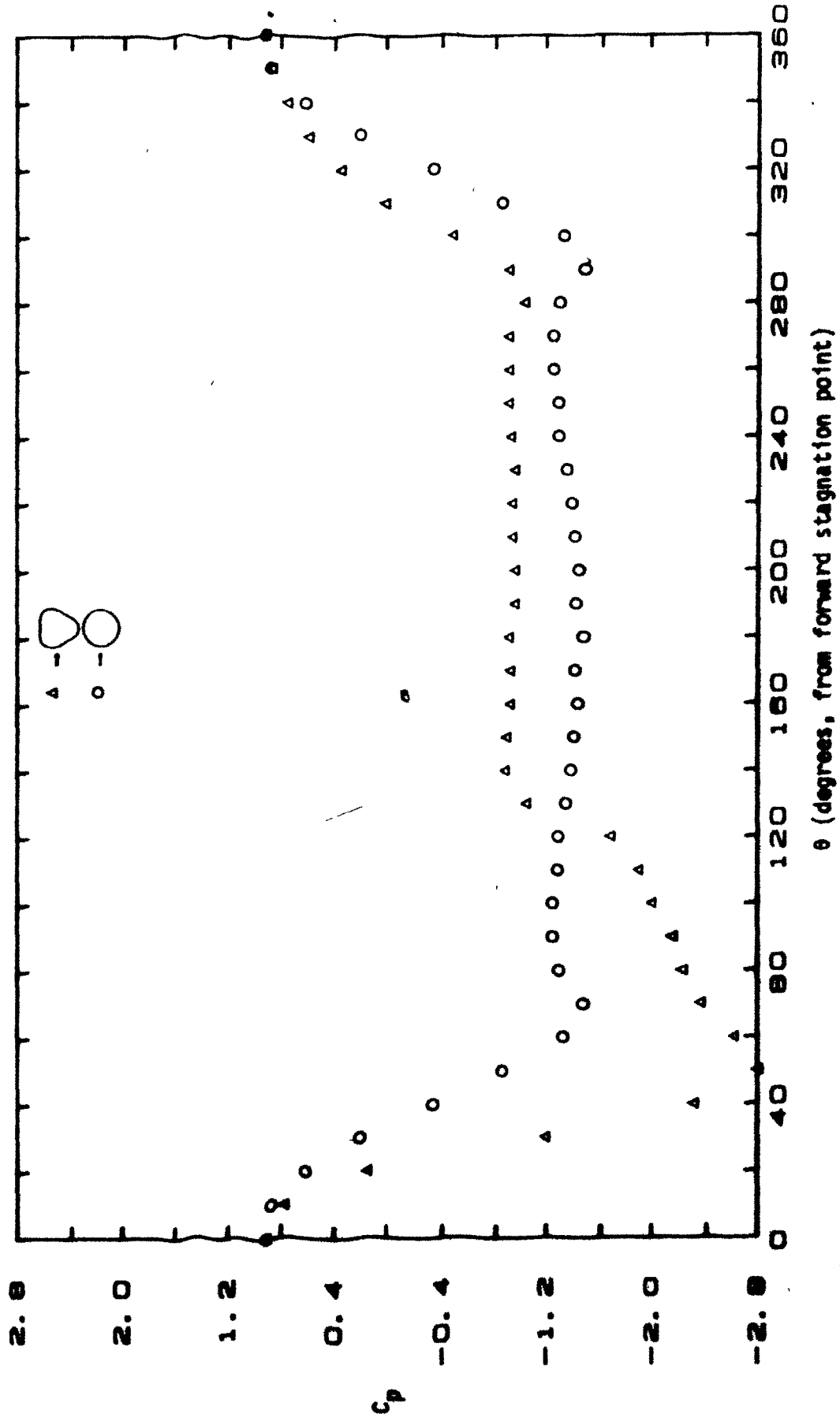
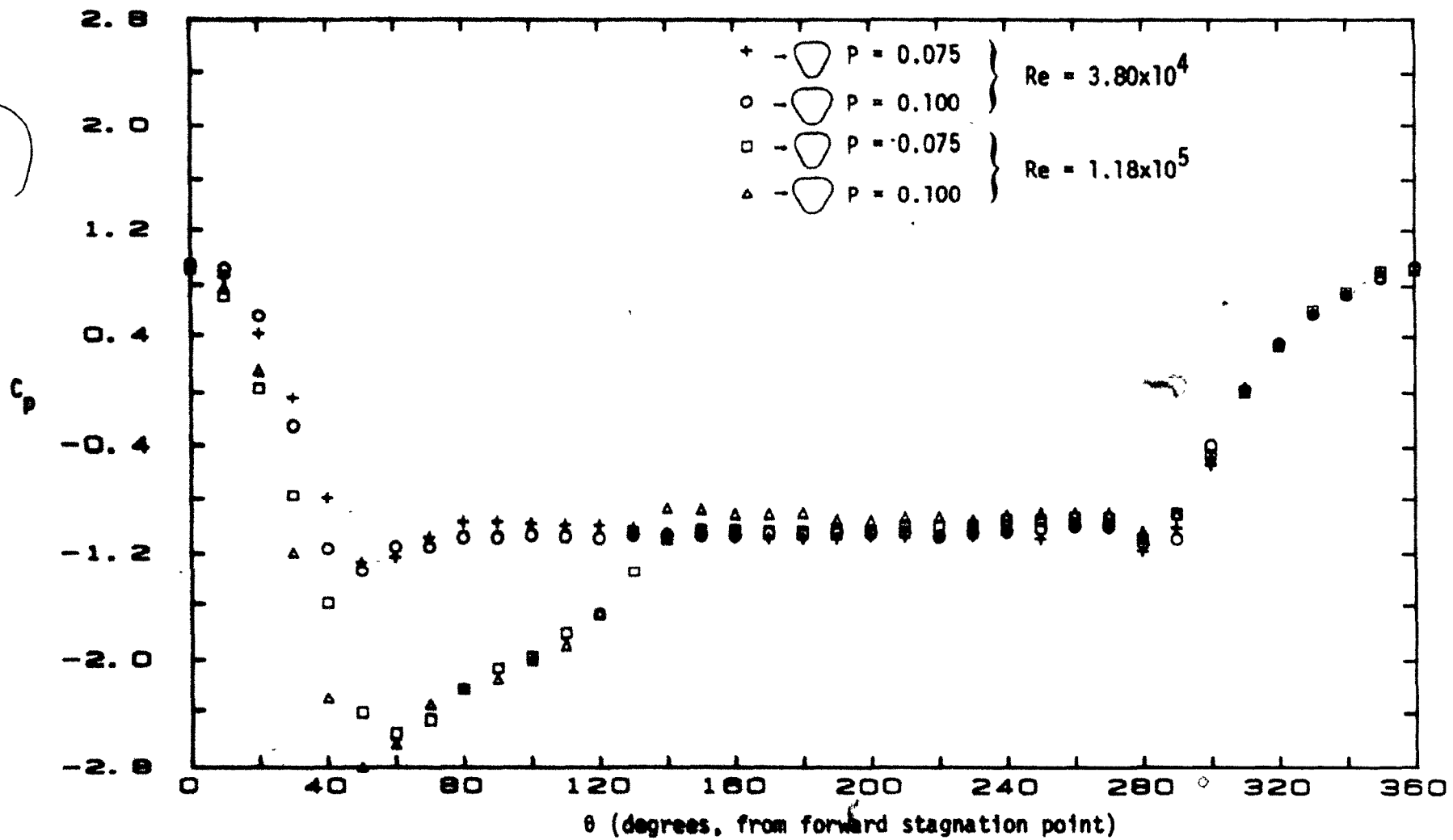
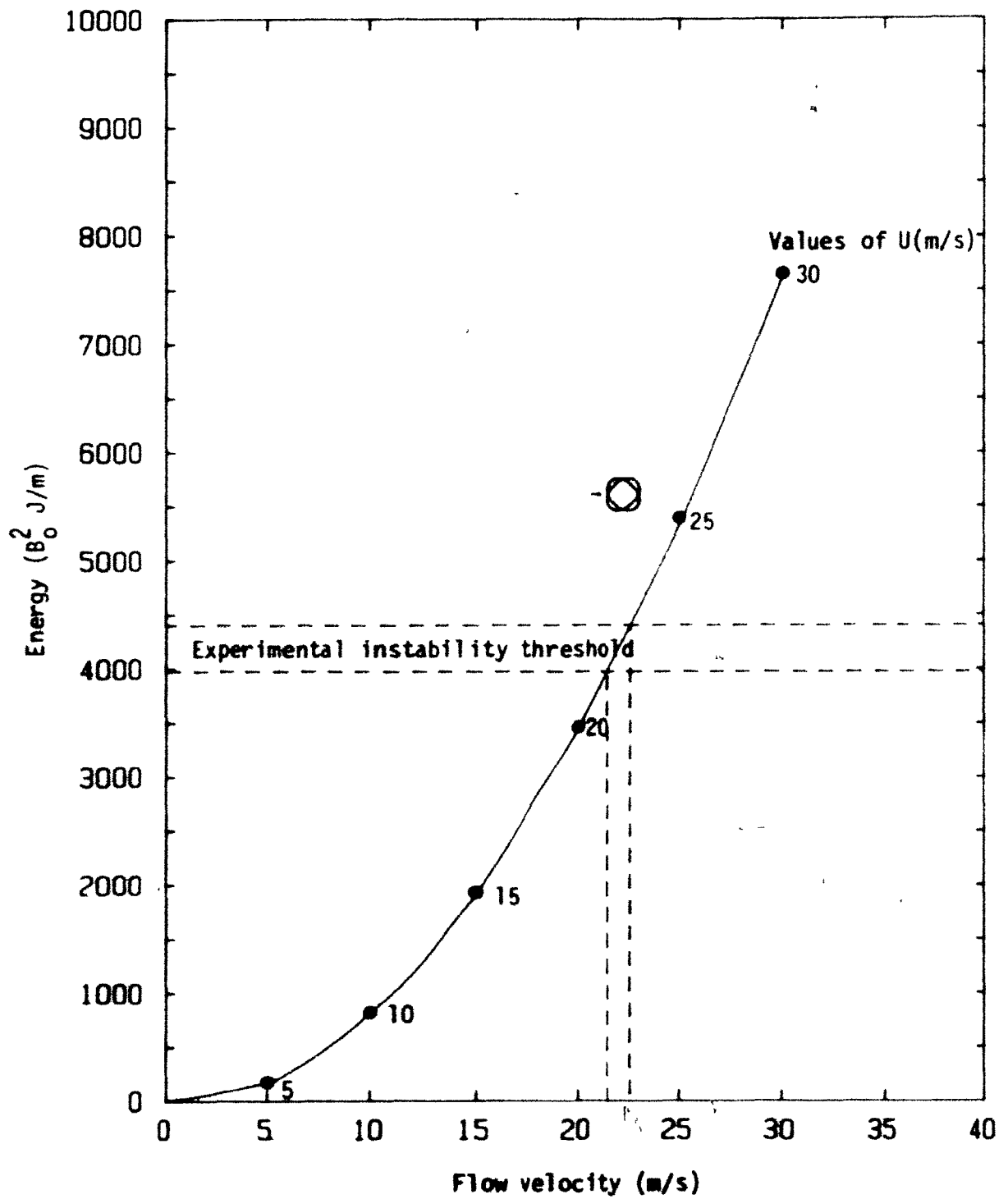


Figure 7.28: Pressure coefficient of the  $n=3$  mode model ( $P = 0.100$ ; more deformed) with a node facing the free-stream vector, at  $U = 23.5$  m/s ( $Re = 1.18 \times 10^5$ ).



**Figure 7.29:** Comparison of the pressure coefficient for the two different models of the  $n=3$  mode at different flow velocities.



**Figure 7.30:** Energy extracted from the free stream for the  $n=2$  mode vibrating with a node facing the free stream.

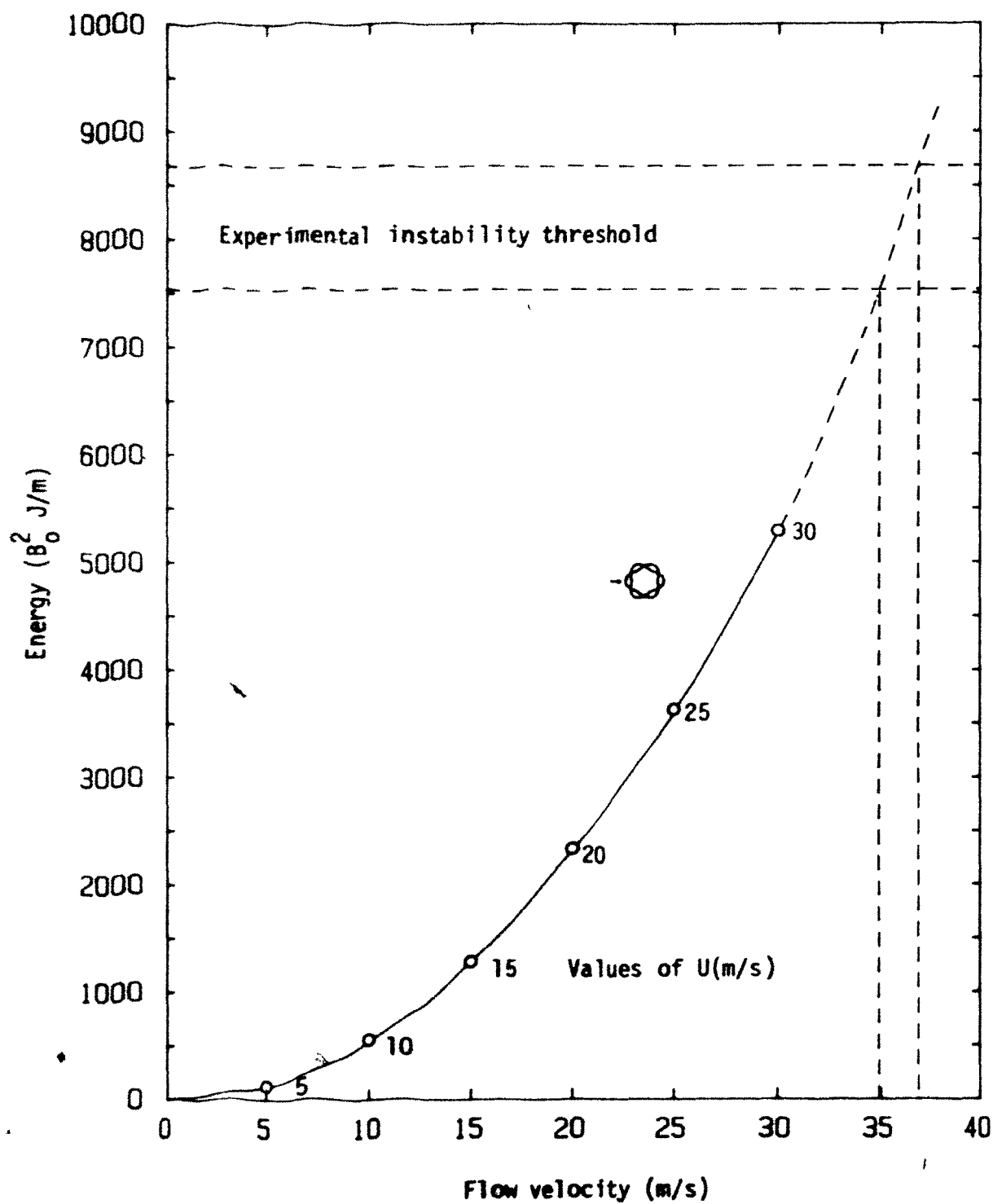


**Figure 7.31:** Energy extracted from the free stream for the  $n=3$  mode vibrating with an antinode facing the free stream.

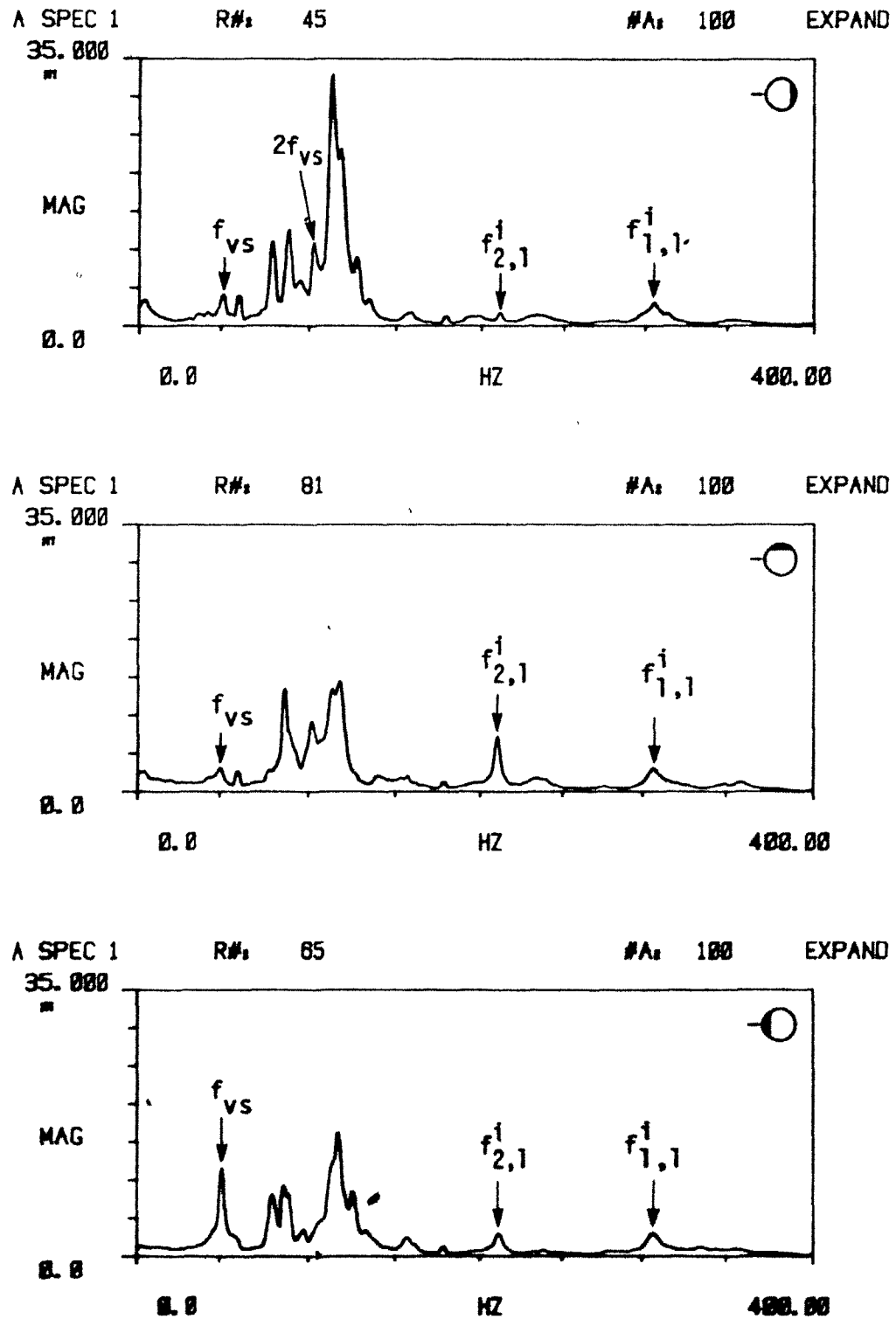


**Figure 8.1:** Frequency spectra of shell vibration of a clamped-clamped shell with an insert (shell B) for configurations I, II and III at  $U \approx 21.5$  m/s.

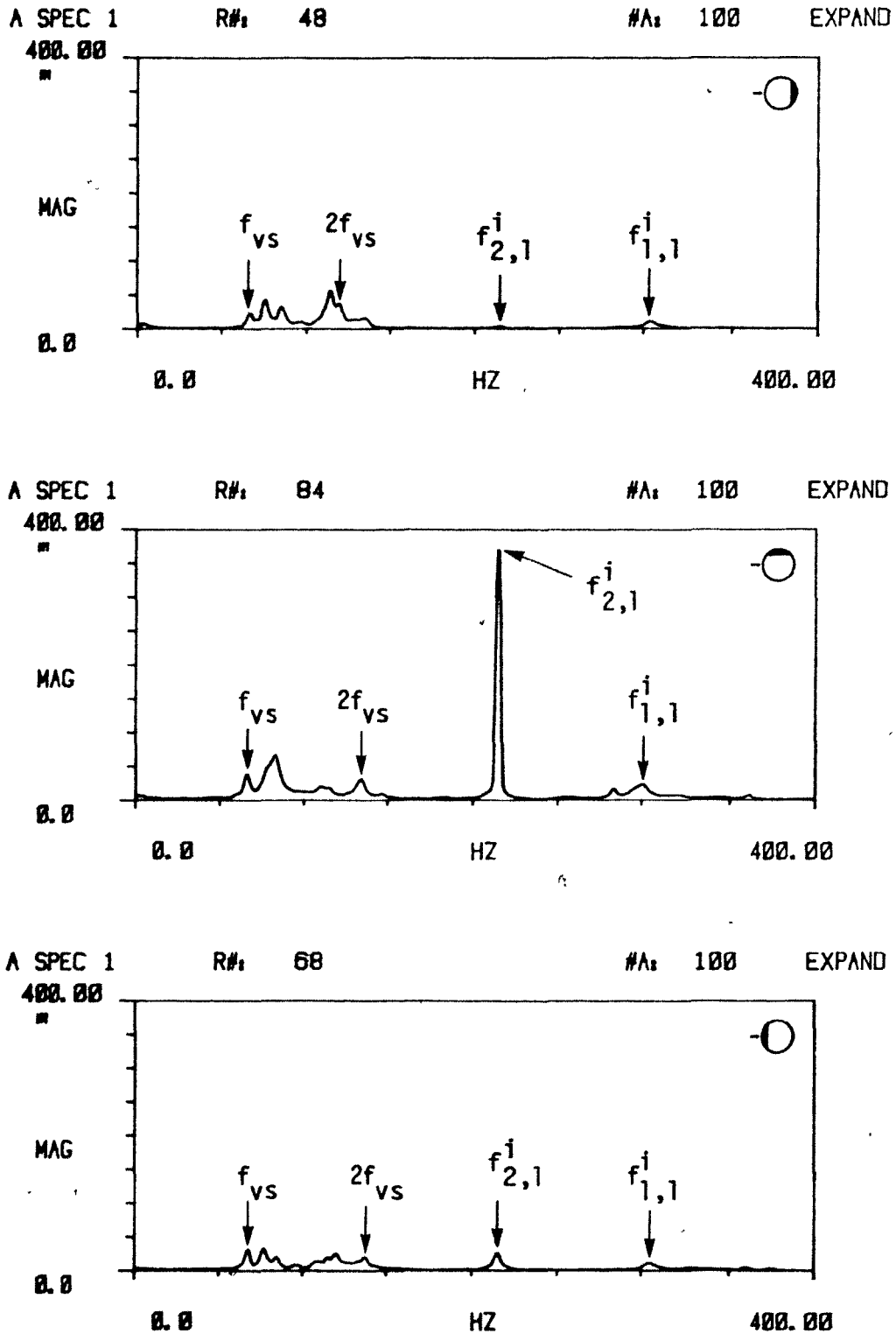
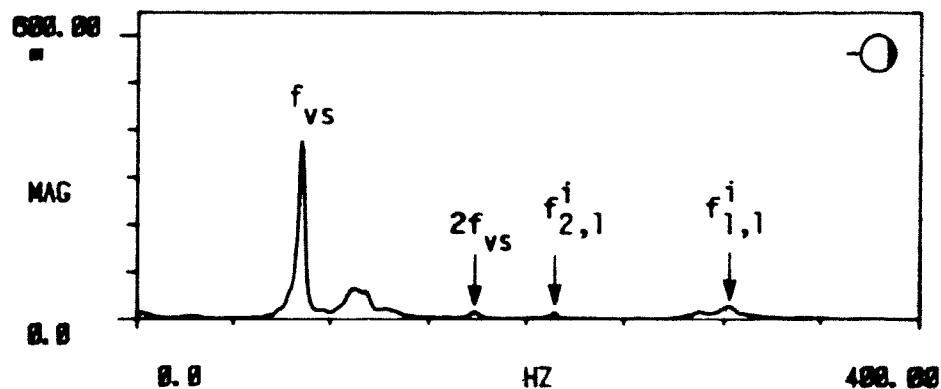
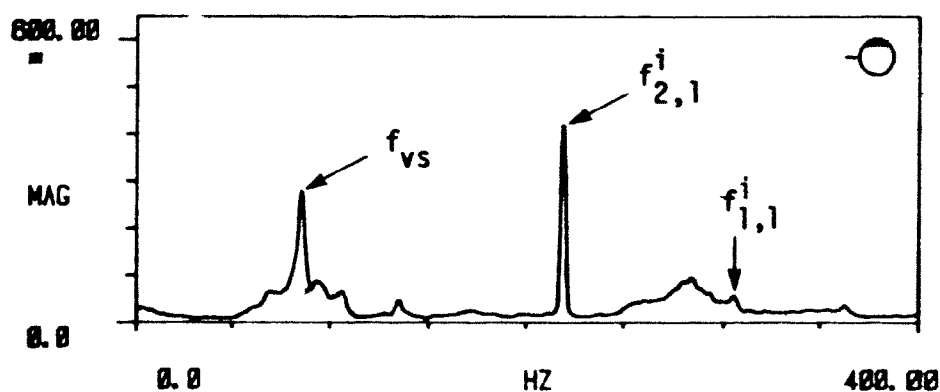


**Figure 8.2:** Frequency spectra of shell vibration of a clamped-clamped shell with an insert (shell B) for configurations I, II and III at  $U \approx 29.0$  m/s.

A SPEC 1 R# 51 #A: 100 EXPAND



A SPEC 1 R# 87 #A: 100 EXPAND



A SPEC 1 R# 72 #A: 100 EXPAND

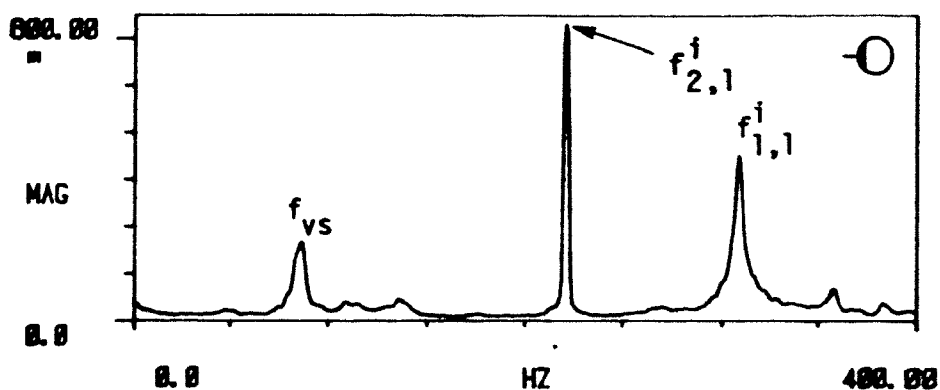


**Figure 8.3:** Frequency spectra of shell vibration of a clamped-clamped shell with an insert (shell B) for configurations I, II and III at  $U \approx 37.5$  m/s.



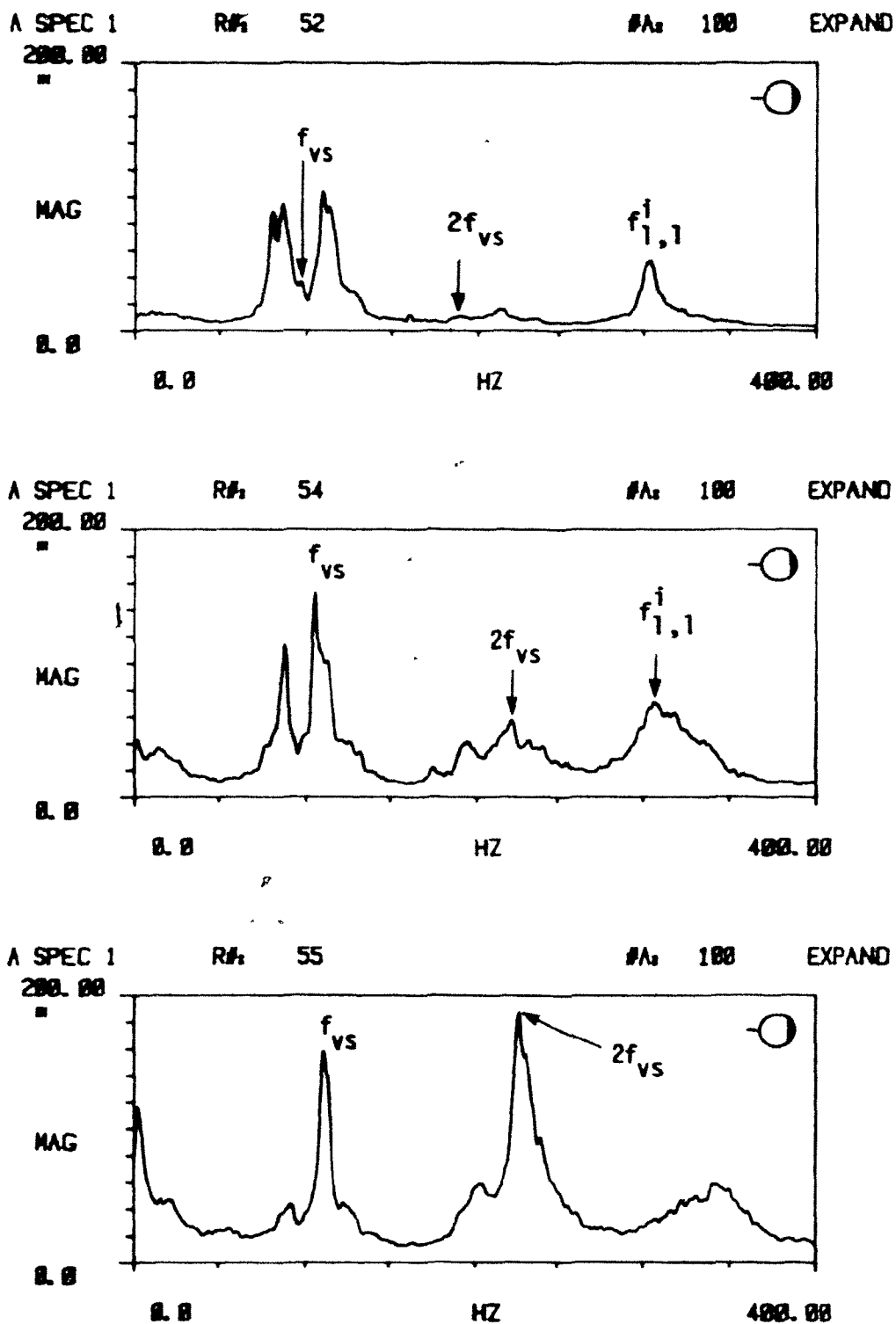


**Figure 8.4:** Frequency spectra of shell vibration of a clamped-clamped shell with an insert (shell B) for configuration I at different flow velocities. Top:  $U \sim 41.4$  m/s; center:  $U \sim 45.6$  m/s; bottom:  $U \sim 48.2$  m/s.

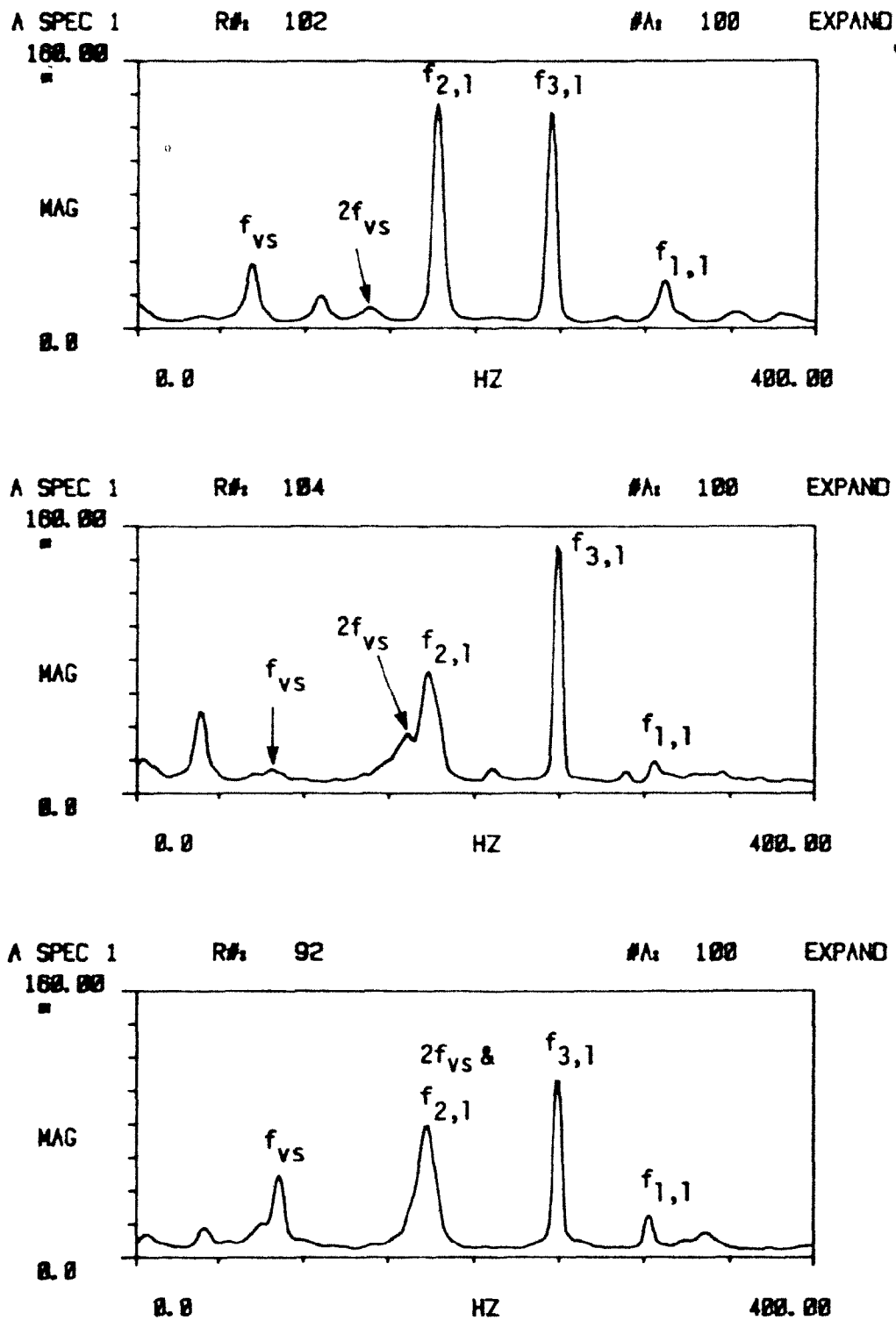


**Figure 8.5:** Frequency spectra of shell vibration of a clamped-clamped shell without an insert (shell A) at different flow velocities. Top:  $U \approx 32.0$  m/s,  $r \approx 2.5$ ; center:  $U \approx 36.9$  m/s,  $r \approx 2.1$ , bottom:  $U \approx 38.7$  m/s;  $r \approx 2.0$ .

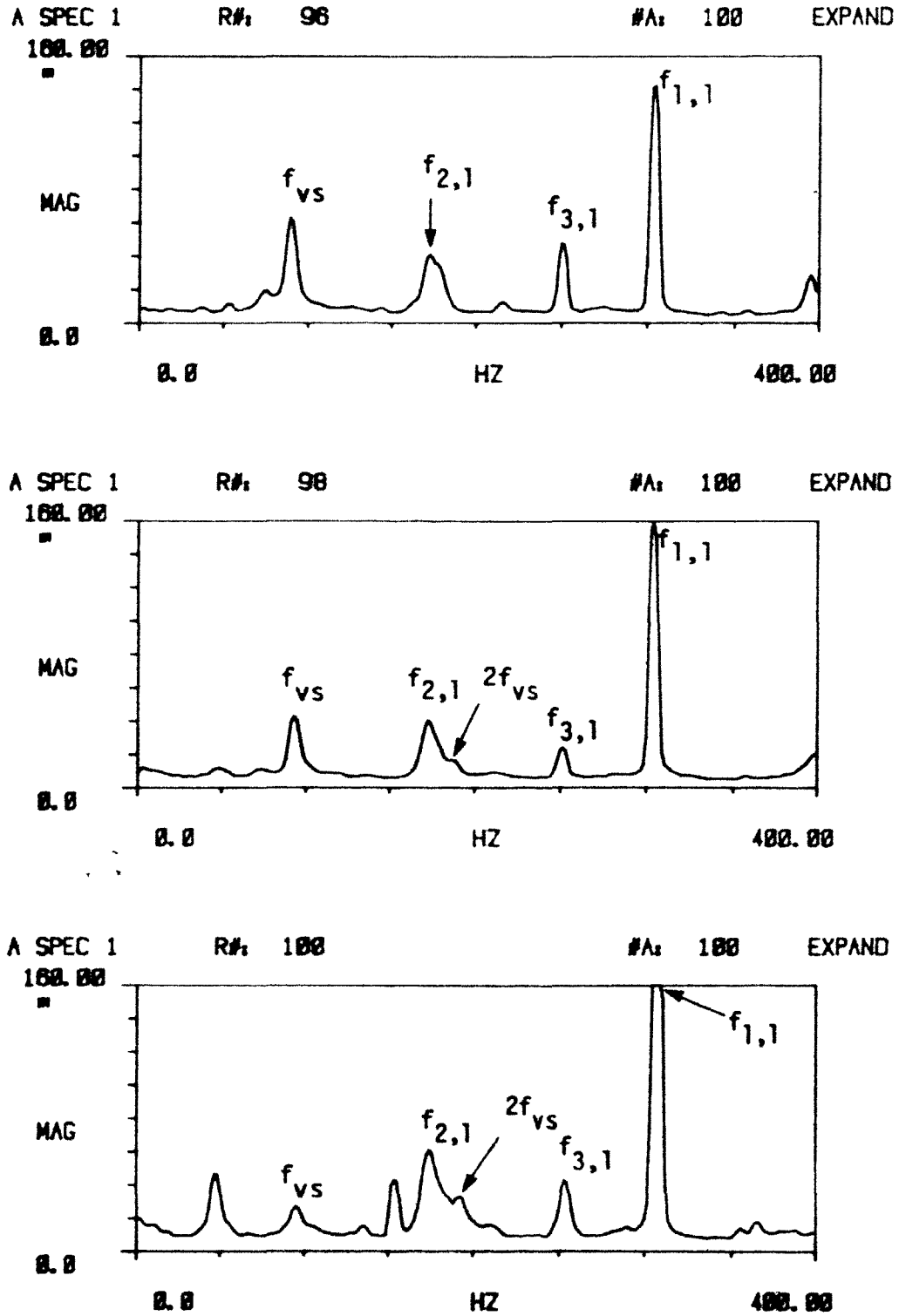


**Figure 8.6:** Frequency spectra of shell vibration of a clamped-clamped shell without an insert (shell A) at different flow velocities. Top:  $U \approx 40.5$  m/s,  $r \approx 1.9$ ; center:  $U \approx 41.9$  m/s,  $r \approx 1.8$ ; bottom:  $U \approx 43.4$  m/s,  $r \approx 1.8$ .

APPENDIX AAUXILIARY INSTRUMENTS

<u>FUNCTION</u>	<u>MAKE</u>	<u>MODEL</u>	<u>REMARKS</u>
Speaker	RADIO SHACK	40-248	8 ohms impedance
Beat frequency oscillator	B & K	1022	Range 20 Hz - 20 KHz
Condenser microphone	B & K	4145	Resonance frequency 9 KHz
Precision sound level meter	B & K	2203	"A", "B", "C" and "Lin" weighting
Fotonic sensor	MTI	KD-100	Resonance frequency 50 KHz
Constant temperature anemometer	DISA	55D01	
Hot wire probe	DISA	55P11	
Pressure transducer	PCB	112A22	Resonance frequency 250 KHz
Oscilloscope	TEKTRONIX	7313	
Digital multi-meter	HP	3438A	
Desktop computer	HP	9825A	
FFT analyser	HP	5420A	

## APPENDIX B

### THE NATURAL FREQUENCIES AND MODAL DAMPING OF SHELL A

The natural frequency of shell A (without an insert) for the second mode of ovaling is 171.0 Hz and the logarithmic decrement is 0.047 (see Figure B.1). Figure B.2 gives  $f_{3,1} = 232.1$  Hz and  $\delta_{3,1} = 0.046$ . Not too surprisingly, when the damping is light, the repeatability of the measurements is excellent (see Figures B.3 and B.4).

With the insert glued onto shell A, there is, approximately, a 28% increase in the second-mode natural frequency ( $f_{2,1}^i = 218.7$  Hz, see Figure B.5). The modal damping  $\delta_{2,1}^i$  for this mode is 0.058 (an increase of 20%). Figure B.6 presents the corresponding results for the  $n=3$  mode:  $f_{3,1}^i = 235.7$  Hz (a 1.5% increase) and  $\delta_{3,1}^i = 0.113$  (an increase of 145%). The measurements repeated on another date are shown on Figures B.7 and B.8.

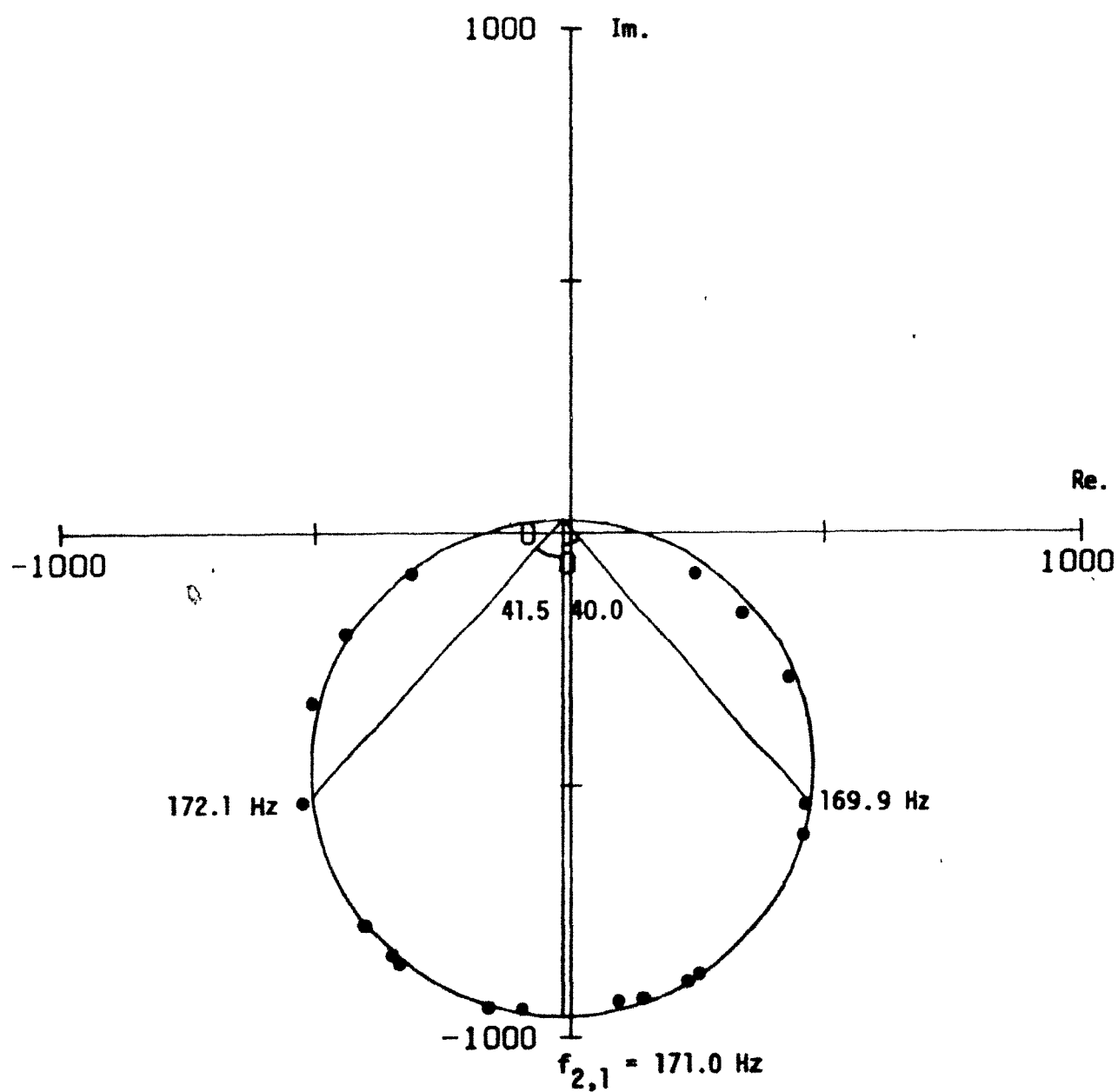


**Figure B.1:** Nyquist plot for shell A without an insert: (2,1)-mode;  
 $f_{2,1} = 171.0$  Hz,  $\delta_{2,1} = 0.047$ .

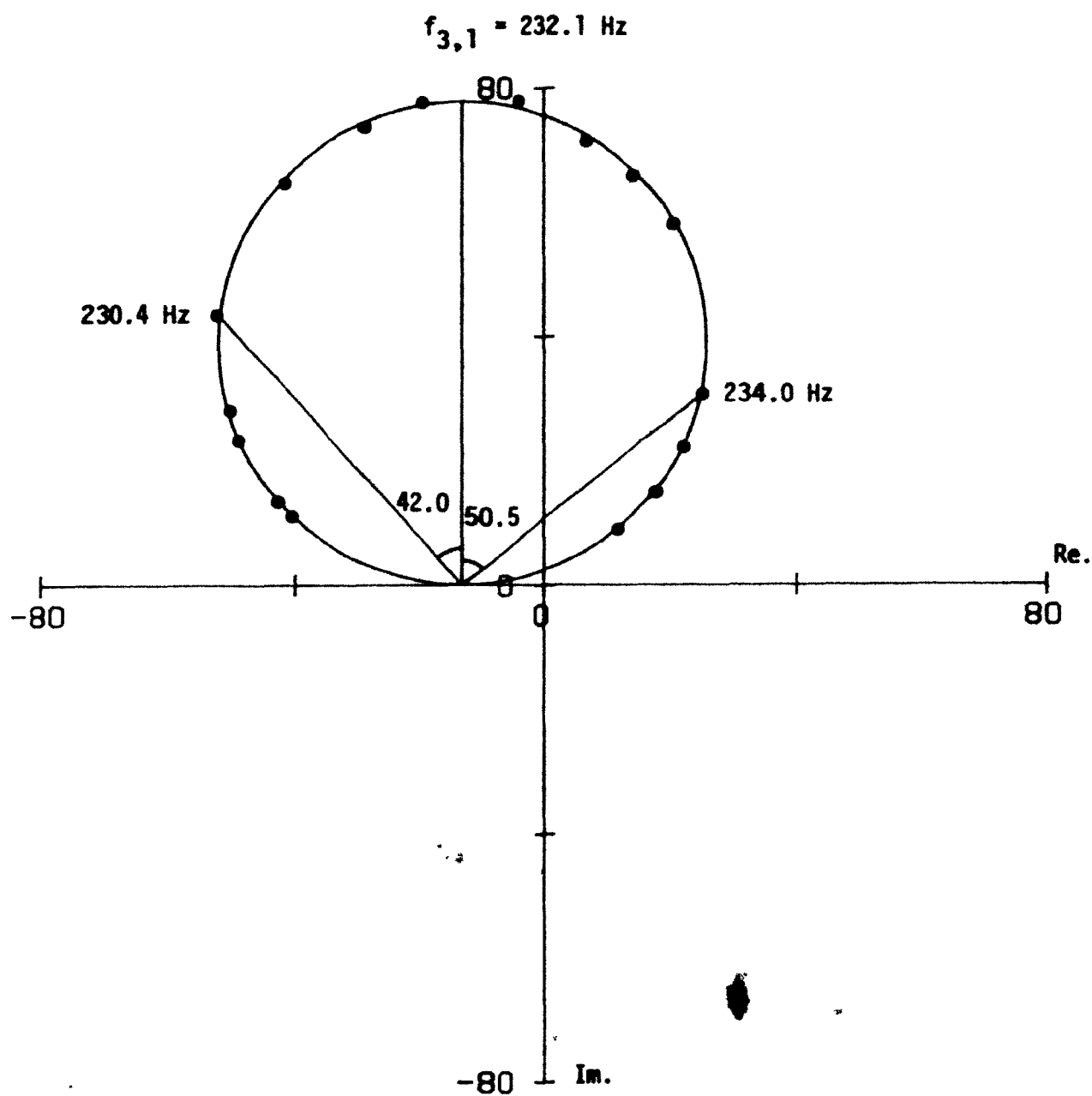


**Figure B.2:** Nyquist plot for shell A without an insert: (3,1)-mode;  
 $f_{3,1} = 232.1$  Hz,  $\delta_{3,1} = 0.046$ .

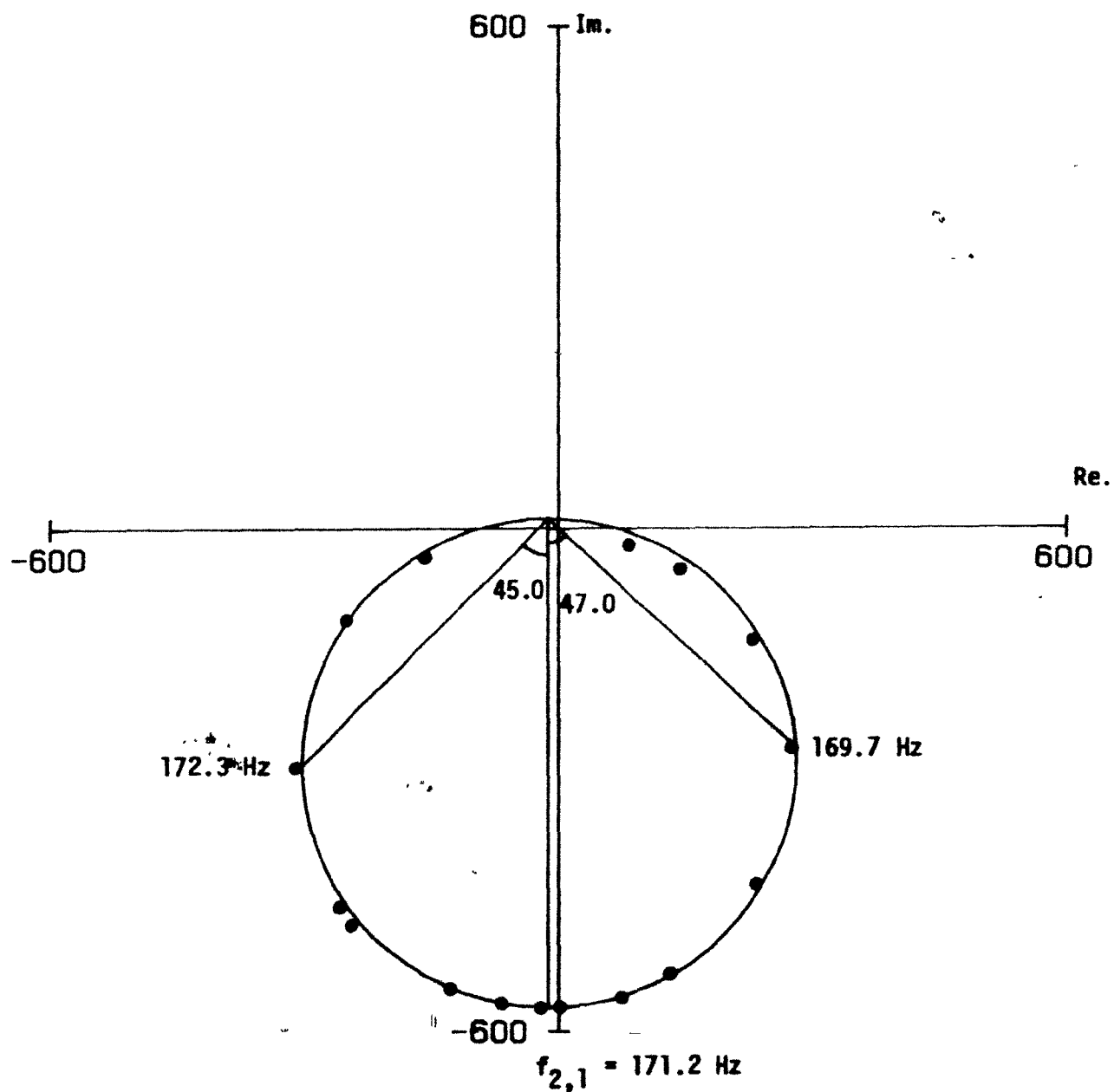


**Figure B.3:** Nyquist plot for shell A without an insert: (2,1)-mode;  
 $f_{2,1} = 171.2 \text{ Hz}$ ,  $\delta_{2,1} = 0.046$  - second set of measurements.



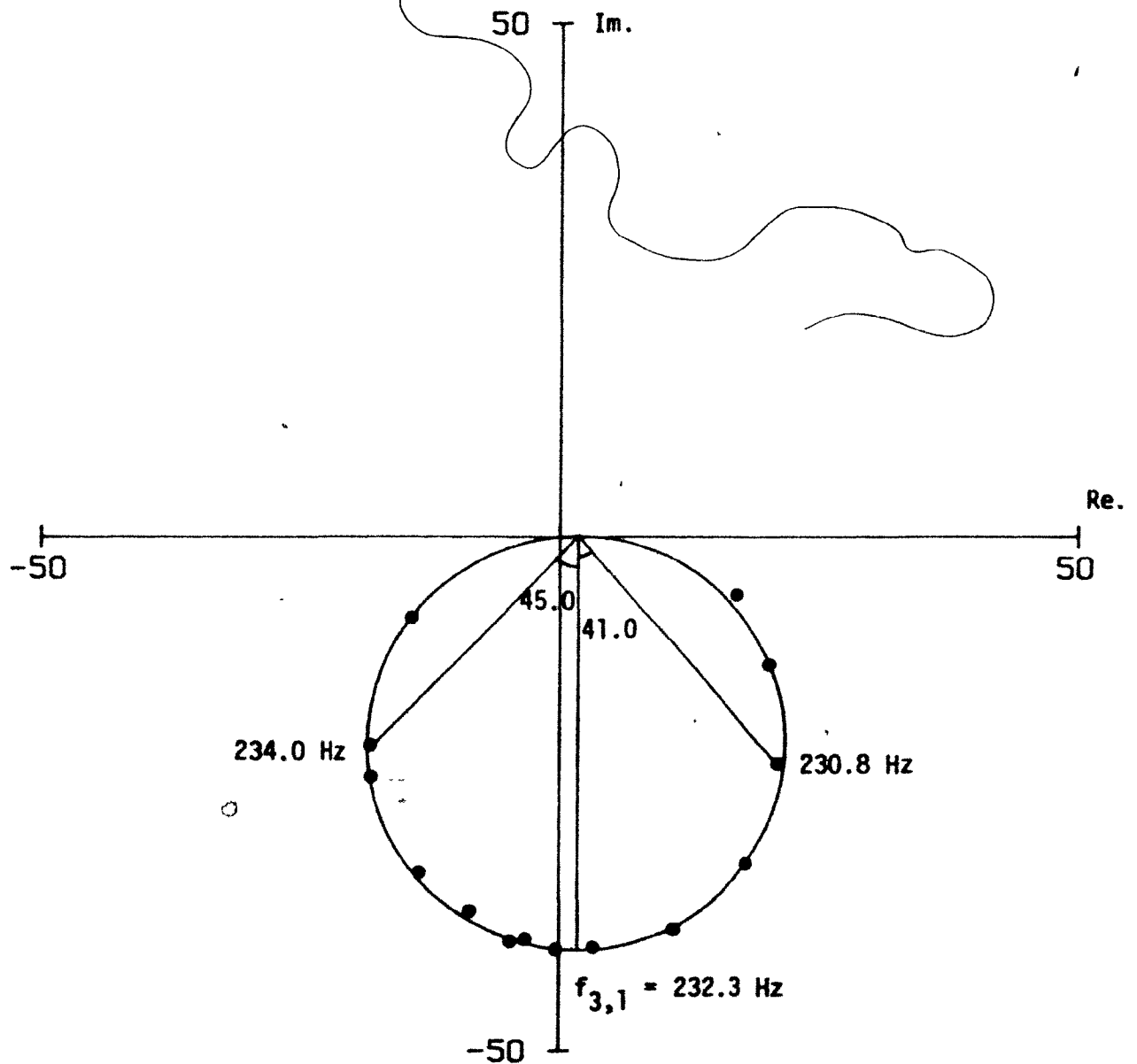


**Figure B.4:** Nyquist plot for shell A without an insert: (3,1)-mode;  $f_{3,1} = 232.3 \text{ Hz}$ ,  $\delta_{3,1} = 0.046$  - second set of measurements.

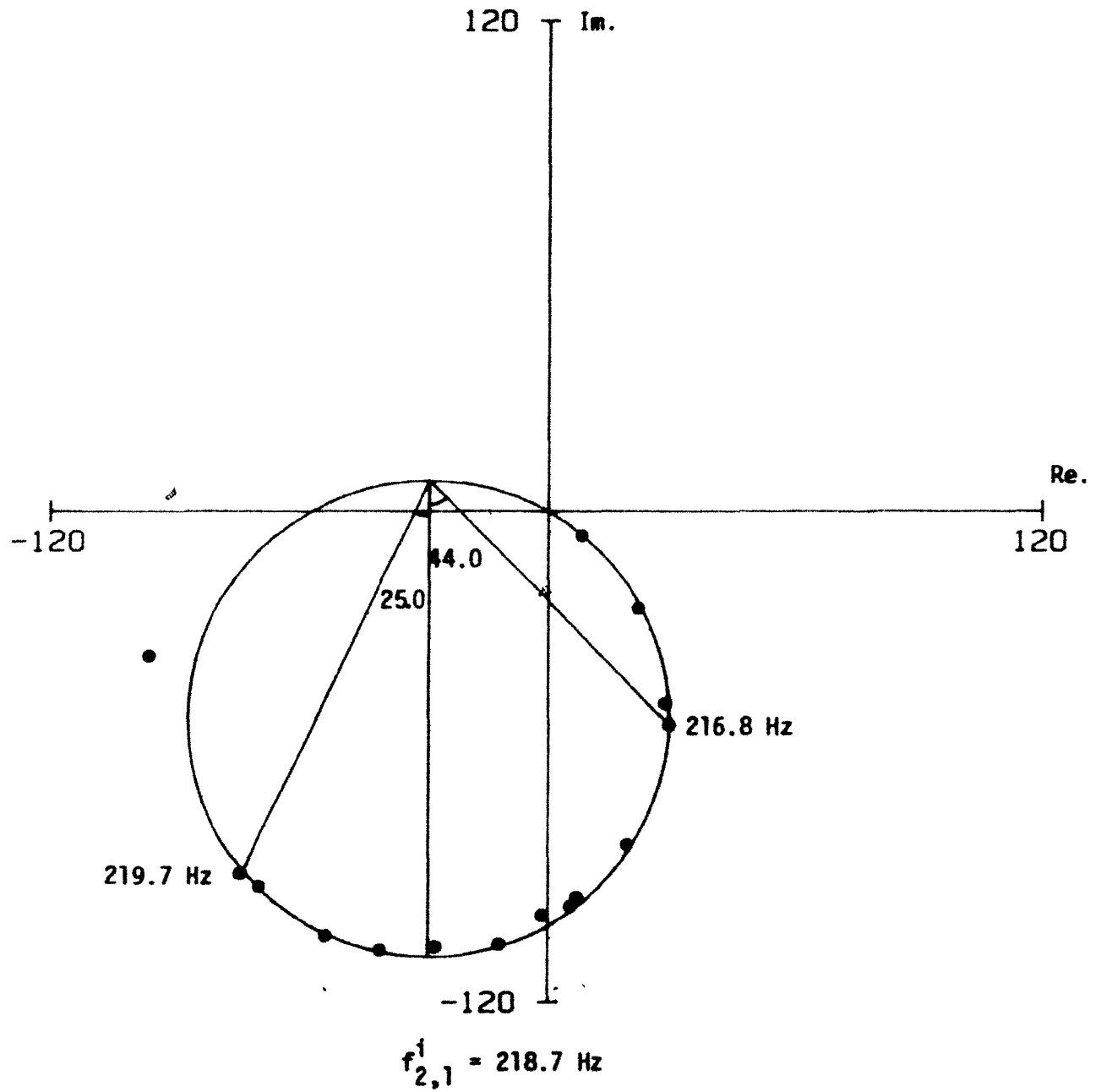


**Figure B.5:** Nyquist plot for shell A with an insert: (2,1)-mode;  
 $f_{2,1}^1 = 218.7 \text{ Hz}$ ,  $\delta_{2,1}^1 = 0.058$ .

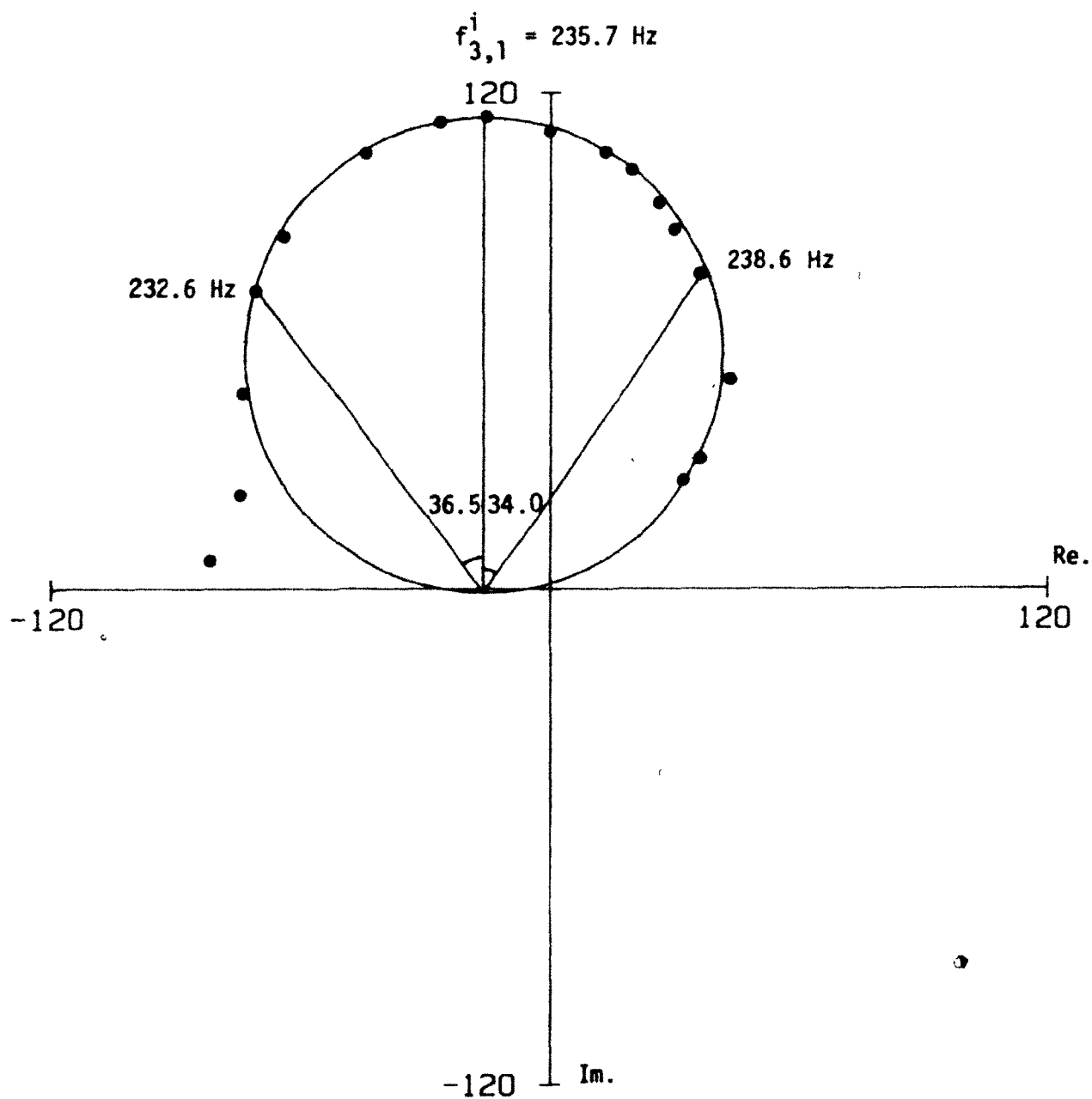


**Figure B.6:** Nyquist plot for shell A with an insert: (3,1)-mode;  
 $f_{3,1}^1 = 235.7 \text{ Hz}$ ,  $\delta_{3,1}^1 = 0.113$ .

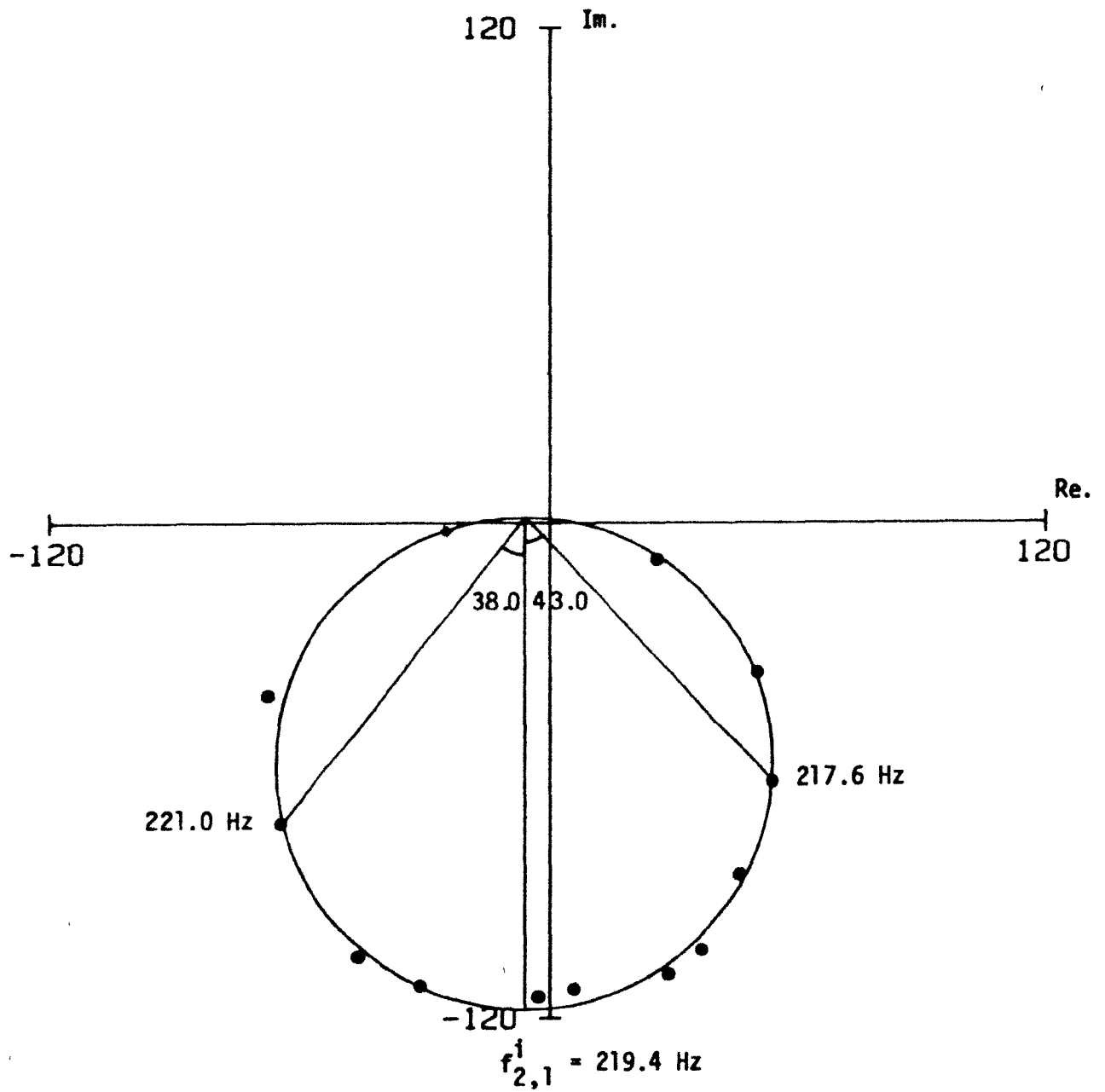


**Figure B.7:** Nyquist plot for shell A with an insert: (2,1)-mode;  
 $f_{2,1}^1 = 219.4 \text{ Hz}$ ,  $\delta_{2,1}^1 = 0.057$  - second set of measurements.

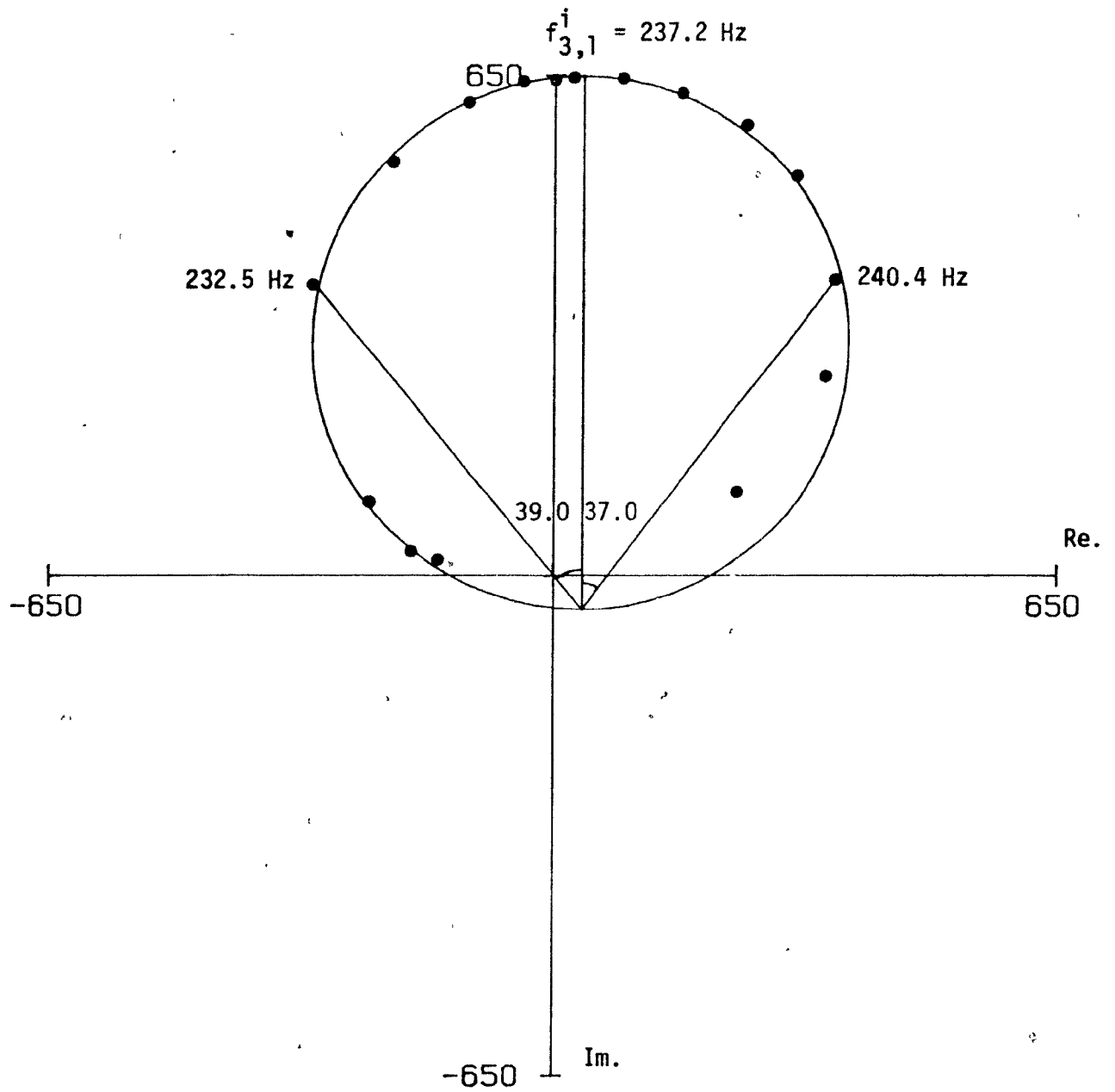


**Figure B.8:** Nyquist plot for shell A with an insert: (3,1)-mode;  
 $f_{3,1}^1 = 237.2 \text{ Hz}$ ,  $\delta_{3,1}^1 = 0.134$  - second set of measurements.

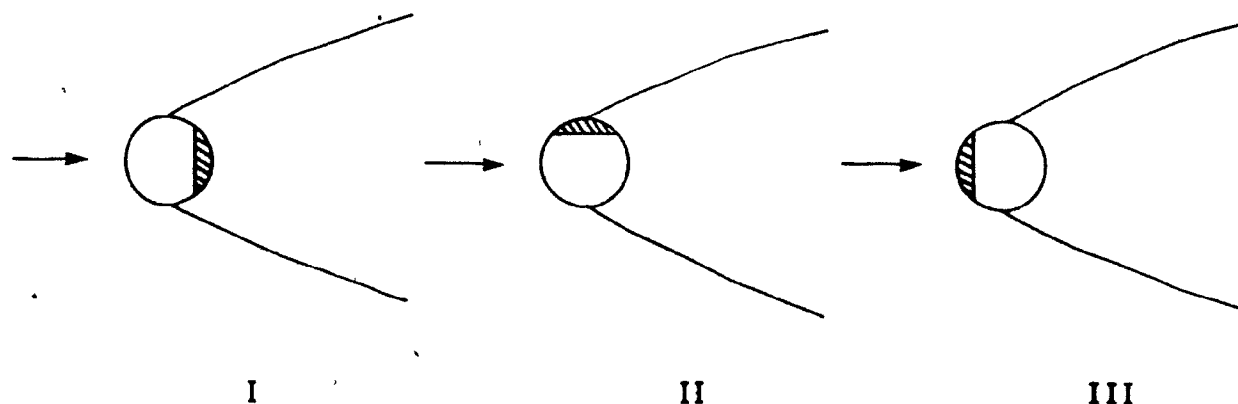
## APPENDIX C

### THE BEHAVIOUR OF SHELL A (WITHOUT AND WITH) AN INSERT

Shell A was used in the preliminary stage of wind tunnel experiments (see Chapter 4 for details), to study the shell response without and with an insert in cross wind.

A typical result for shell A without an insert is shown in Figure C.1. The average Strouhal number,  $S$ , is approximately 0.18 for  $0 < U < 35$  m/s. The first observed instability ( $n=2$  mode,  $\sim 174$  Hz) occurs at  $U_{cr} \simeq 21.7$  m/s and at this flow velocity the ratio  $r$  of ovalling frequency to vortex shedding frequency is from 3.4 to 3.5; the uncertainty in  $r$  arises from the corresponding difficulty in pinpointing  $U_{cr}$ . The  $n=3$  mode ovalling ( $\sim 236$  Hz) was precipitated at a slightly higher wind speed of  $U_{thr} \simeq 24.4$  m/s. The same experiment was repeated with the fotonic sensor monitoring the shell motion at  $\theta = 340^\circ$  (instead of  $\theta = 315^\circ$ ). The result is plotted in Figure C.2.

For shell A with an insert, the experiments were first conducted with the model orientated at configuration I. The fotonic probe was



positioned at different locations to monitor the shell response at different angular positions. It is seen (Figure C.3) that, at orientation I the system is stable at all flow velocities, up to  $U = 45$  m/s.

Figure C.4 shows that the system would become unstable at orientation III. The onset of instability for this configuration occurs at  $U_{cr}^I \approx 30.8$  m/s ( $f_{2,1}^I \sim 225$  Hz;  $r^I = 3.2-3.3$ ). The same experiment was repeated on another date and the result is presented in Figure C.5.

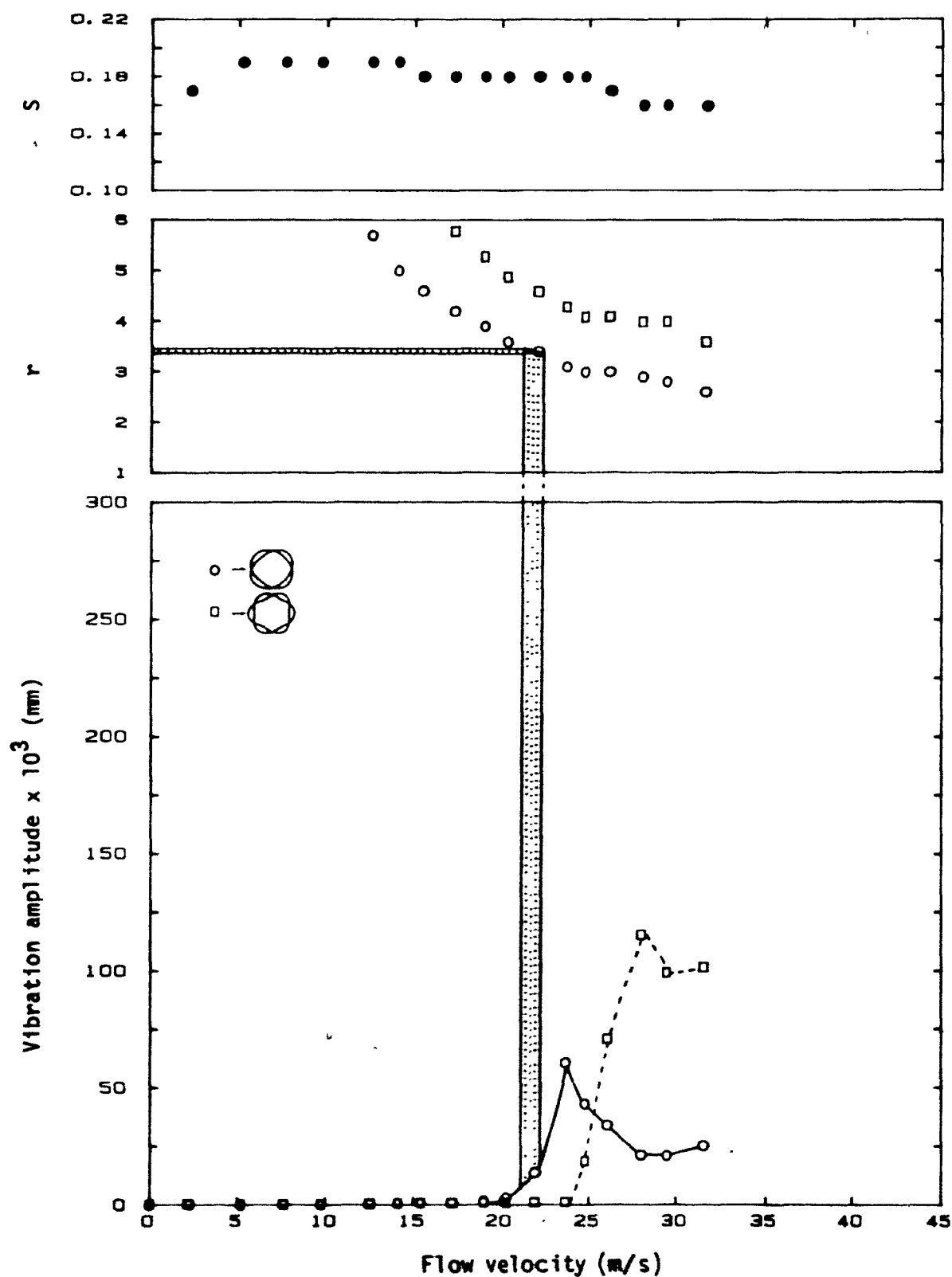
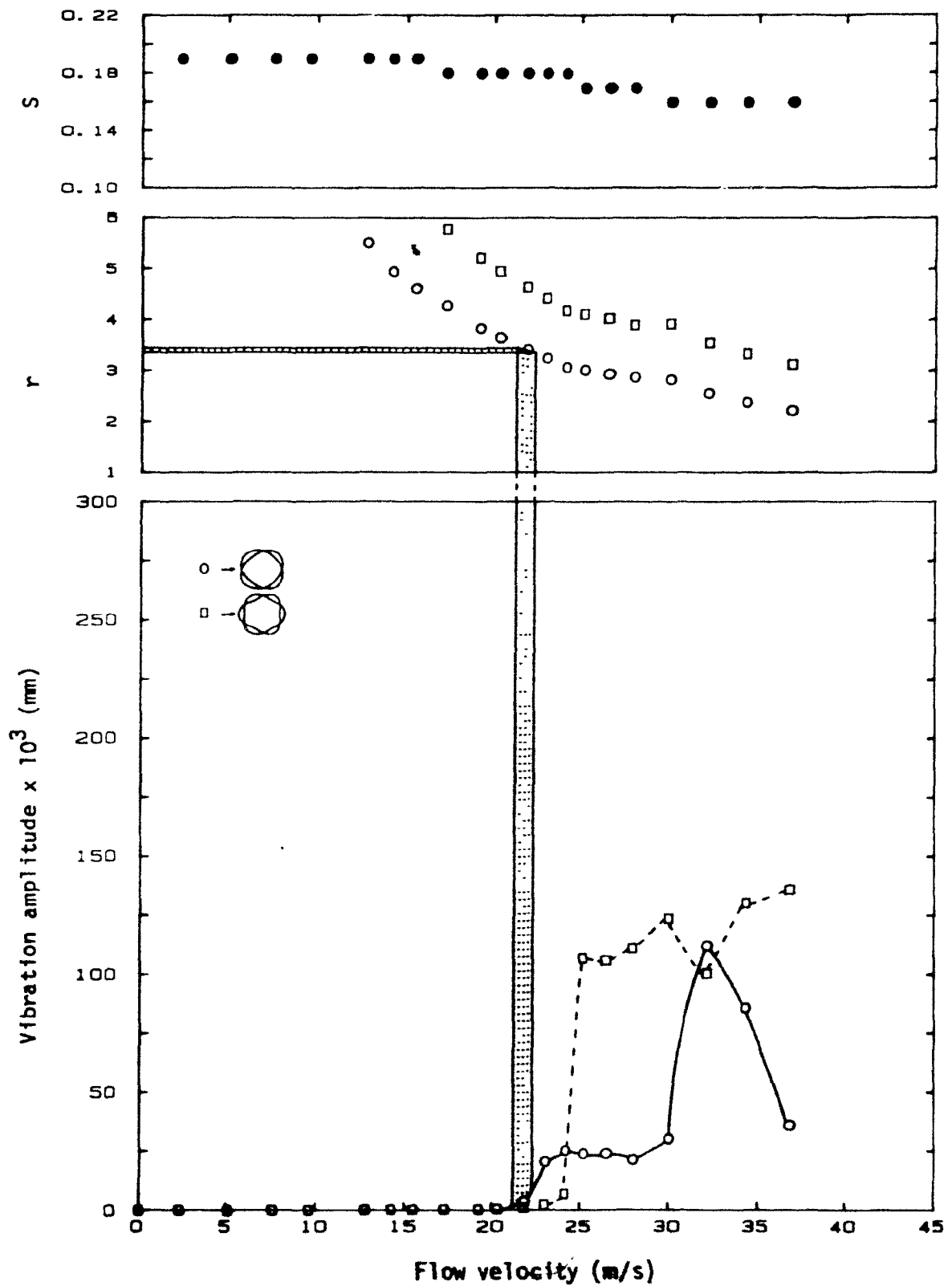
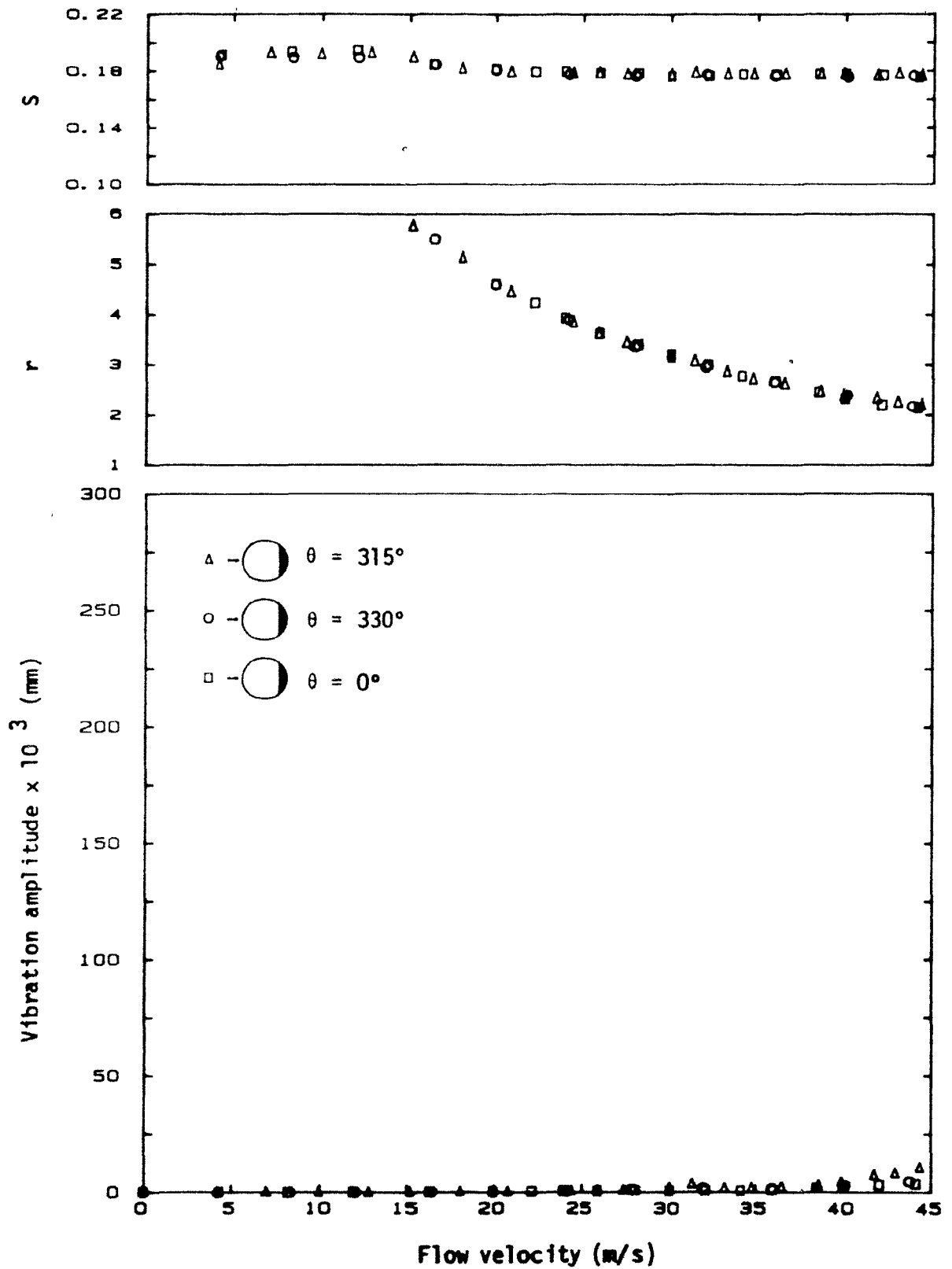


Figure C.1: Measured vibration amplitude [at  $\theta = 315^\circ$ ,  $h = 89$  mm (3.5 in.)], wake flow periodicity in terms of Strouhal number  $S$ , and  $r = f_{n,m}/f_{vs}$  for a clamped-clamped shell (shell A) in cross flow.





**Figure C.2:** Measured vibration amplitude [at  $\theta = 340^\circ$ ,  $h = 89$  mm (3.5 in.)], wake flow periodicity in terms of Strouhal number  $S$ , and  $r = f_{n,m}/f_{vs}$  for a clamped-clamped shell (shell A) in cross flow - repetition of test of Figure C.1.



**Figure C.3:** Measured vibration amplitude [at  $h = 89$  mm (3.5 in.) for  $n=2$  mode], wake flow periodicity in terms of Strouhal number  $S$ , and  $r = f_{n,m}/f_{vs}$  for shell A with an insert.  $\theta$  gives the angular position of photonic sensor ( $\theta = 0$  corresponds to the front stagnation point).

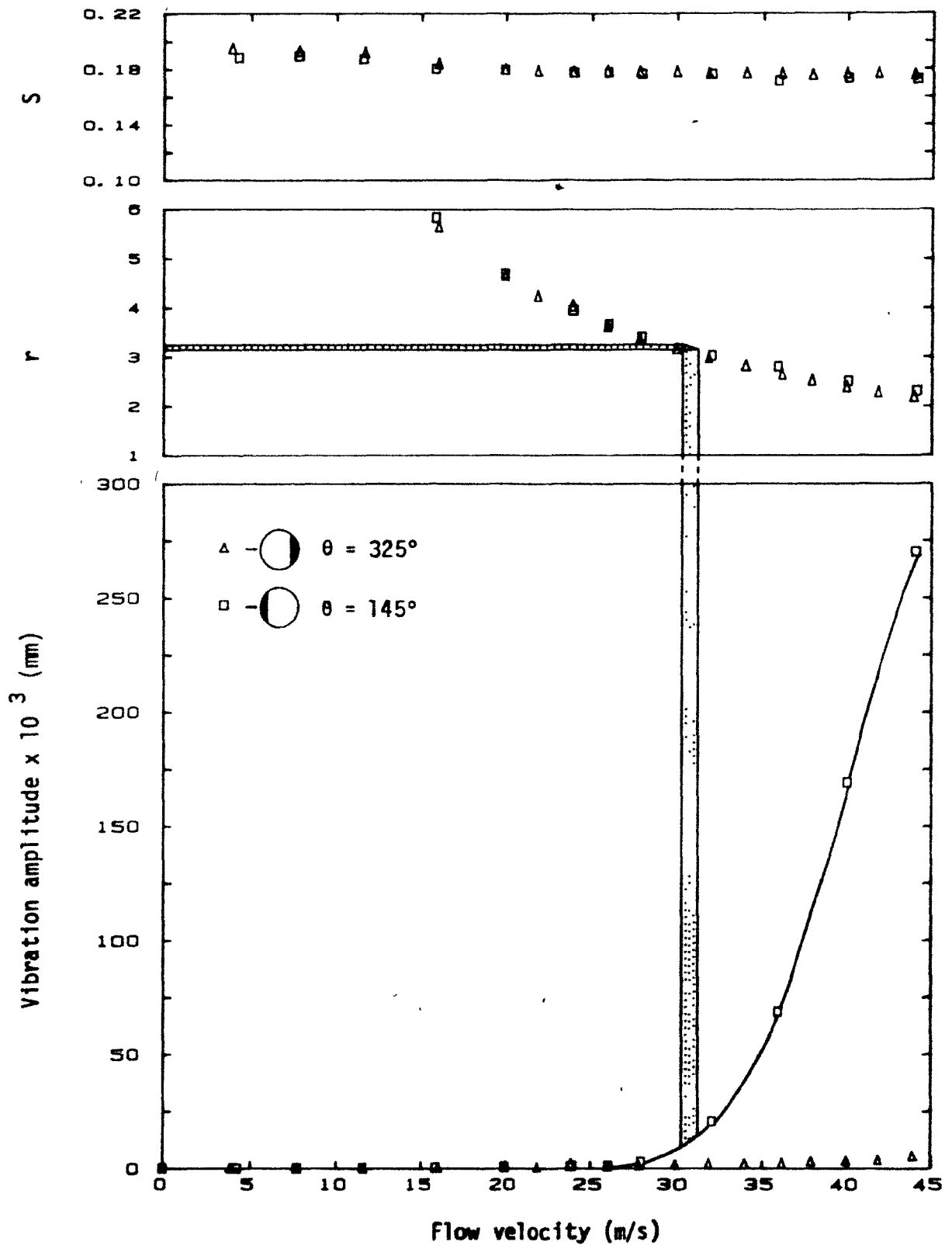


**Figure C.4:** Measured vibration amplitude [at  $h = 89$  mm (3.5 in.) for  $n=2$  mode], wake flow periodicity in terms of Strouhal number  $S$ , and  $r = f_{n,2}/f_{vs}$  for shell A with an insert.  $\theta$  gives the angular position of photonic sensor.

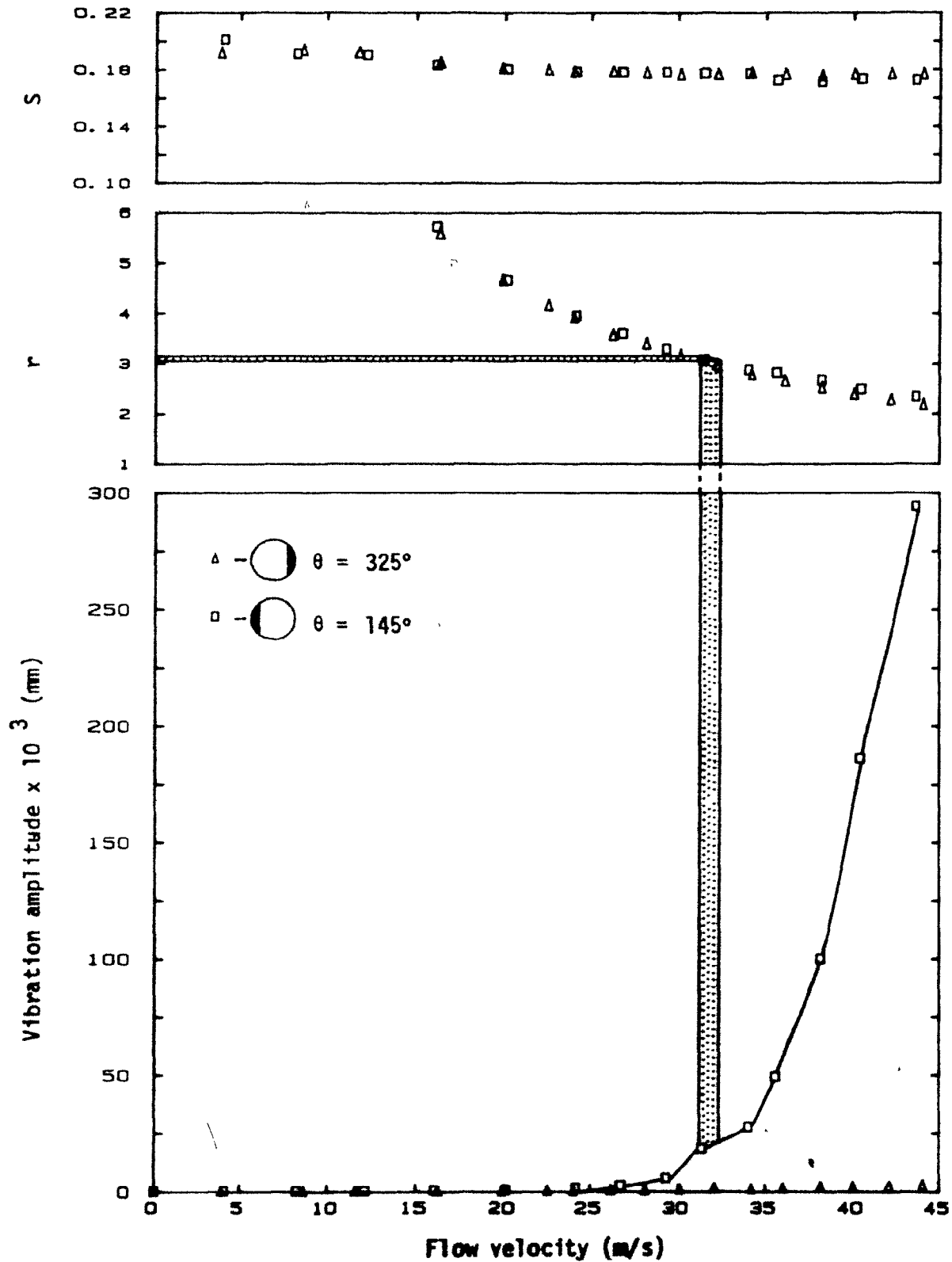


**Figure C.5:** Measured vibration amplitude at [ $h = 89$  mm (3.5 in.) for  $n=2$  mode], wake flow periodicity in terms of Strouhal number  $S$ , and  $r = f_{n,p}/f_{vs}$  for shell A with an insert.  $\theta$  gives the angular position of photonic sensor - repetition of test of Figure C.4.

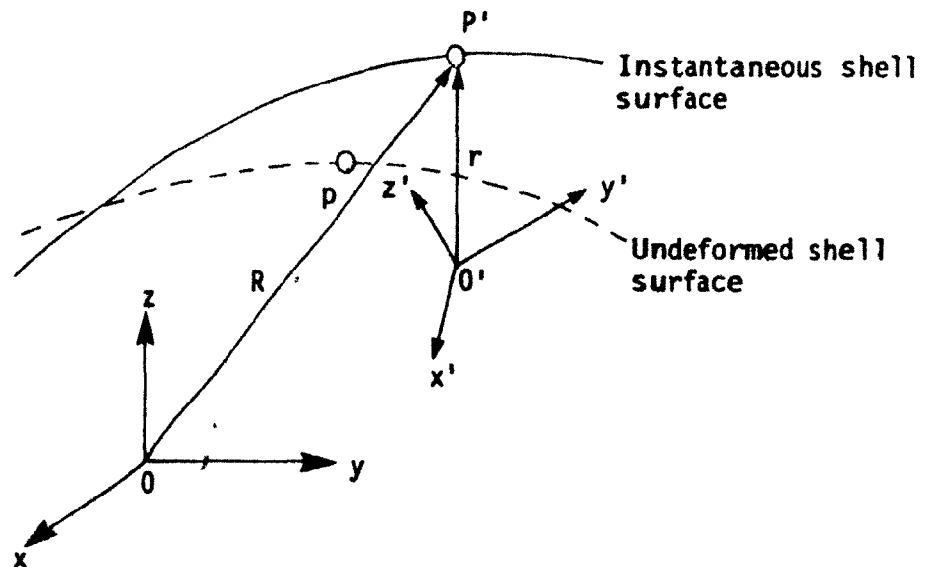
# APPENDIX D

## BERNOULLI EQUATION FOR A NON-STATIONARY SOLID-FLUID BOUNDARY

Owing to a moving fluid-solid boundary surface, the fluid properties are a function of position and time; hence, the unsteady Bernoulli equation should be written as

$$\frac{D\phi}{Dt} + \frac{v^2}{2} + \frac{p}{\rho} = \frac{p_0}{\rho},$$

where  $\frac{D}{Dt}$  is the substantial derivative.



Now consider two frames of reference  $oxyz$  or  $F$ , and  $o'x'y'z'$  or  $F'$ . At time  $t_0$ , both frames are coincident and  $F'$  is moving relative to  $F$  with a motion described in  $F$  as a velocity  $\underline{v}$  and an angular velocity  $\underline{\omega}$ .

Let  $\underline{\dot{R}}, \underline{\dot{r}}$  be the velocities of the fluid particle  $P$  as seen by an observer in  $F$  and  $F'$ , respectively. The term  $\frac{D}{Dt}$  may then be rewritten as

$$\begin{aligned}\frac{D\phi}{Dt} &= \frac{\partial\phi}{\partial t} + \underline{\dot{r}} \cdot \nabla\phi, \\ &= \frac{\partial\phi}{\partial t} + (\underline{\dot{R}} - \underline{v} - \underline{\omega} \times \underline{r}) \cdot \nabla\phi.\end{aligned}$$

To express the rate of change of  $\phi$  as seen by an observer in fixed space, one sets  $\underline{\dot{R}} = 0$ .

Hence, the unsteady Bernoulli equation reduces to

$$\frac{\partial\phi}{\partial t} - (\underline{v} + \underline{\omega} \times \underline{r}) \cdot \nabla\phi + \frac{v^2}{2} + \frac{p}{\rho} = \frac{p_0}{\rho}.$$

## APPENDIX E

### PHASE RELATION BETWEEN SHELL DEFORMATION AND THE INDUCED PRESSURE

It is presumed that due to viscous effects, there is a phase difference between the perturbation pressure field and shell deformation.

The experimental set-up allowed the phase to be measured only over a portion of the shell in the wake region ( $\theta = 120^\circ$  to  $240^\circ$ ). Hence, the phase from the forward stagnation point to the point where the flow is assumed to separate from the cylindrical shell is estimated analytically. The phase relation from  $\theta = 85^\circ$  to  $120^\circ$  lies in the so-called 'grey' region; phase values therein have been obtained by interpolation from those calculated and measured, respectively, fore and aft of this region.

#### E.1 Experimental Set-Up to Measure Phase

The experiment was set up in accordance with Figure E.1. The cylindrical test shell and the fibre optic probe were mounted in the same manner as described in Chapter 2. A PCB pressure transducer (type 112A22) was placed in the wake behind the shell to pick up the pressure signal induced by shell motion. The signals from the fotonic sensor and pressure transducer were then fed into a FFT signal analyser (HP 5420A). A transfer function was then used to find the phase and any other pertinent relation between the two signals.

The experiment was conducted with the wind speed set at 21.5 m/s and 25.5 m/s. At these respective flow velocities, the second and third mode of ovaling were seen to have large amplitudes of vibration.

## E.2 Experimental Results

It is reasonable to presume that the presence of the pressure transducer<sup>†</sup> in the region before the boundary layer separates from the body will disturb the mean flow and consequently the phase measured in that region would be unreliable. For this reason, the experiment was restricted to a small region of the wake where it was assumed that the pressure transducer had little effect on the measurement.

Initial tests were done with the pressure transducer traversing around the periphery of the shell from  $\theta = 120^\circ$  to  $240^\circ$ , at 15 degree intervals. The transducer was positioned such that the center of the sensing surface (diaphragm) was 9.50 mm (0.375 in.) away from the shell surface and was parallel to the mean flow velocity vector. The fonic sensor was set at  $\theta = 315^\circ$  and on the same height (120 mm (4.90 in.) above the tunnel floor) as the transducer.

Figures E.2 and E.4 show the frequency spectra of the shell vibration (top) and the induced pressure (bottom) for the second and third modes of ~~ovalling~~ <sup>vibration</sup>. It should be noted that the  $n=2$  mode is vibrating with a node facing the free stream vector, whilst the  $n=3$  mode has an antinode facing the flow.

The top diagrams of Figures E.3 and E.5 show the phase plot of the cross spectral density between the shell displacement and the perturbation pressure induced by shell motion. It is seen that there is a nice little plateau centered around the frequency of interest, which is approximately 167 Hz for the  $n=2$  mode and 235 Hz for the  $n=3$  mode - even

---

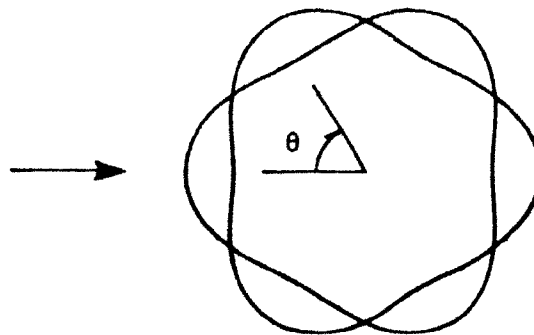
<sup>†</sup>The pressure transducer plus the holder has a dimension of 14 mm (0.55 in.) diameter.



though the pressure signal recorded is very weak and only just above the electrical noise level generated by the instrumentation. The validity of these results is enhanced by measuring the coherence between the two signals (see Figures E.3 and E.5, bottom): it is seen that it is close to one at the frequencies of interest. To further support this claim, a cross correlation function between a sinusoidal signal<sup>†</sup> and a random white noise was determined. In this case, it is found (see Figures E.6 to E.8) that at the frequency of interest there is no definite phase formed and the coherence between these two signals is practically zero.

The phase relation between the shell displacement measured at  $\theta = 315^\circ$  and the induced pressure at various angular positions are plotted on Figure E.9 for the second mode and on Figure E.10 for the third mode of ovaling.

In order to fully interpret the above results, some further measurements were needed. Firstly, it was necessary to express the phase between the induced pressure and the shell displacement at the point where the pressure was measured. For example, considering the  $n=3$  mode, in which the shell ovals with an antinode facing the wind, the shell motion on the part of the shell surface described by  $\theta = 330^\circ$  to  $30^\circ$  is in phase




---

<sup>†</sup>The sinusoidal signal is used here to simulate the shell vibration signal.

with that described by both  $\theta = 90^\circ$  to  $150^\circ$  and  $\theta = 210^\circ$  to  $270^\circ$ . However, it is 180 degrees out of phase with the parts of the shell for which  $\theta = 30^\circ$  to  $90^\circ$ ,  $\theta = 150^\circ$  to  $210^\circ$  and  $\theta = 270^\circ$  to  $330^\circ$ . Hence, it is possible to obtain the "actual phase" at any point on the shell from that measured with the fonic sensor set at  $\theta = 315^\circ$ . The above method of extrapolation was verified by performing another set of experiments, with the fonic sensor positioned at  $\theta = 0^\circ$ . It was found that, by making the appropriate compensation, the phase obtained is close to that measured in the earlier experiments.

Secondly, it was necessary to determine whether the phase measured by the analyser indicated that the induced pressure was leading or lagging the shell motion. This could be easily done by delaying a second signal by a certain fraction of time period with respect to the first signal. Both signals were then processed through the spectrum analyser. The conclusion drawn from this test is that the measured phase should be interpreted as a phase lag of the induced pressure with respect to the shell displacement.

Finally, the fully compensated phase angles *versus*  $\theta$  are presented in Figures E.11 and E.12. It is seen (in Figure E.11) that the measured phase for the second mode is not symmetric about the 0-180 degree line. However, the reliability of the measurements from  $\theta = 195^\circ$  to  $240^\circ$  is questionable, as indicated by the coherence in this region not being as good as that in the region  $\theta = 120^\circ$  to  $180^\circ$ . For instance, the measured phase at  $\theta = 210^\circ$  has a coherence of only 0.33. Hence, the phase measurements for  $\theta = 195^\circ$  to  $240^\circ$  are disregarded. For the third mode of ovaling (see Figure E.12), the amplitude of vibration is three times

larger than for the second mode and, consequently, the induced pressure signal is stronger. The coherence between shell vibration and the induced pressure is nearly one and the phase measured is symmetric about the 0-180 degree line.

### E.3 Calculation of Phase for $\theta = 0$ to 85 Degrees

The method used to estimate the phase for  $\theta = 0^\circ$  to  $85^\circ$  will briefly be outlined in this section. As suggested by experimental evidence, it is assumed that there is a phase lag  $\psi$  between the induced pressure and shell vibration. The expression for the induced pressure will be formulated analytically by utilizing strip theory aerodynamics, as described in Chapter 6. As will be seen in due course,  $\psi$  is determined, once the expression for the induced pressure is specified.

As a first approximation, equation<sup>†</sup> (6.11) and (6.12) may be simplified to

$$p \approx p_0 - \rho \left\{ \frac{\partial \phi^*}{\partial t} + \frac{1}{2} U^2 g^2(\theta) + \frac{U g(\theta)}{a} \frac{\partial \phi^*}{\partial \theta} \right\} \Big|_{r=a}, \quad (E.1)$$

and

$$\frac{\partial \phi^*}{\partial r} \Big|_{r=a} \approx \frac{\partial w^*}{\partial t} + \frac{U g(\theta)}{a} \frac{\partial w^*}{\partial \theta}; \quad (E.2)$$

for convenience,  $f(\theta)$  is replaced by  $g(\theta)$  and the effect of  $(\underline{v} + \underline{\omega} \times \underline{r}) \cdot \underline{\nabla} \phi$

<sup>†</sup>As shown in Chapter 6, the choice of an idealized fully potential flow for  $\phi_0$  tends to overestimate the effect of applying the boundary condition at  $r = a + w^*$ . For this reason, it was decided to apply the boundary condition at  $r = a$  in this analysis.

in equation (6.10) has been ignored.

Since the aim of this analysis is to estimate the phase ahead of the separation point, it is reasonable to ignore the flow within the wake and to assume  $g(\theta) = 0$  for  $\theta > \theta_s$ .

As the quasi-static pressure was measured by neglecting the axial deformation of the shell, and the energy calculations (in Chapter 7) are based on a shell of infinite length,  $w^*$  may be expanded in a series form

$$\begin{aligned} w^* &= e^{i\omega t} \sum_{\ell=0}^{\infty} B_{\ell} \cos(2\ell+1)n\theta \\ &= e^{i\omega t} B_0 \cos n\theta, \end{aligned} \quad (\text{E.3})$$

where the oscillations are symmetrically disposed about the  $(\theta=0, \theta=\pi)$ -plane; as suggested by the previous work [11],  $B_0 \gg B_1, B_2, \dots$ , etc. may safely be assumed.

Proceeding in a similar manner to that described in Chapter 6, it may be shown that for harmonic shell motion with an antinode facing the free stream, the external flow potential is given by

$$\phi_e^* = e^{i\omega t} \left[ D(0) + \sum_{j=1}^{\infty} D(j) r^{-j} \cos j\theta \right], \quad (\text{E.4})$$

where

$$D(j) = \left( \frac{a^{j+1}}{j} \right) \left[ -i\omega \delta_{nj} + 2 \frac{Un}{\pi a} G(n, j) \right] B_0, \quad (\text{E.5})$$

and

$$G(n, j) = \int_0^{\theta_s} g(\theta) \sin n\theta \cos j\theta d\theta. \quad (E.6)$$

Physically, one would expect  $\phi_e^* \rightarrow 0$  as  $r \rightarrow \infty$ . This implies  $D(0) = 0$  in equation (E.4), or

$$\phi_e^* = e^{i\omega t} \sum_{j=1}^{\infty} D(j) r^{-j} \cos j\theta. \quad (E.7)$$

Hence,

$$\begin{aligned} p_e^* &\simeq -\rho \left[ \frac{\partial \phi_e^*}{\partial t} + \frac{Ug(\theta)}{a} \frac{\partial \phi_e^*}{\partial \theta} \right] \Big|_{r=a} \\ &= -e^{i\omega t} \rho \theta_0 \left\{ \sum_{j=1}^{\infty} \omega^2 \delta_{nj} \frac{a}{j} \cos j\theta + 2 \frac{Un}{\pi} \omega i \sum_{j=1}^{\infty} \frac{\cos j\theta}{j} G(n, j) \right. \\ &\quad \left. - Ug(\theta) \left[ -\omega i \sum_{j=1}^{\infty} \sin j\theta \delta_{nj} + 2 \frac{Un}{\pi a} \sum_{j=1}^{\infty} \sin j\theta G(n, j) \right] \right\} \\ &= e^{i\omega t} \rho \theta_0 \left\{ -\frac{\omega^2 a}{n} \cos n\theta - i\omega \left[ 2 \frac{Un}{\pi} \sum_{j=1}^{\infty} \frac{\cos j\theta}{j} G(n, j) + Ug(\theta) \sin n\theta \right] \right. \\ &\quad \left. + 2 \frac{U^2 n}{\pi a} g(\theta) \sum_{j=1}^{\infty} \sin j\theta G(n, j) \right\}. \quad (E.8) \end{aligned}$$

In general,  $p_e^*$  may be expanded in a series form as

$$p_e^* = e^{i\omega t} \sum_{j=1}^{\infty} A(j) f(a, \theta) e^{-i\psi},$$

$$p_e^* = e^{i\omega t} \sum_{j=1}^{\infty} A(j) f(a, \theta) [\cos \psi - i \sin \psi], \quad (E.9)$$

where it is assumed that the induced pressure is lagging the shell vibration by an angle  $\psi$ .

Equating both real and imaginary parts of equations (E.8) and (E.9) gives

$$\sum_{j=1}^{\infty} A(j) f(a, \theta) \cos \psi = \rho \left\{ -\frac{\omega^2 a}{n} \cos n\theta + 2 \frac{U^2 n}{\pi a} g(\theta) \sum_{j=1}^{\infty} \sin j\theta G(n, j) \right\}, \quad (E.10)$$

and

$$-\sum_{j=1}^{\infty} A(j) f(a, \theta) \sin \psi = -\rho U \omega \left\{ g(\theta) \sin n\theta + 2 \frac{n}{\pi} \sum_{j=1}^{\infty} \frac{\cos j\theta}{j} G(n, j) \right\}. \quad (E.11)$$

Dividing (E.11) by (E.10) yields

$$-\tan \psi = U \omega \frac{\left( -g(\theta) \sin n\theta - 2 \frac{n}{\pi} \sum_{j=1}^{\infty} \frac{\cos j\theta}{j} G(n, j) \right)}{\left( -\frac{\omega^2 a}{n} \cos n\theta + 2 \frac{U^2 n}{\pi a} g(\theta) \sum_{j=1}^{\infty} \sin j\theta G(n, j) \right)}. \quad (E.12)$$

The foregoing analysis pertains to the case of oscillations with an antinode facing the free stream. Proceeding in a similar manner, the equivalent expression for oscillations with a node facing the free stream is given by

$$w^* \approx e^{i\omega t} B_0 \sin n\theta, \quad (E.13)$$

$$\phi_e^* = e^{i\omega t} \sum_{j=1}^{\infty} D(j) r^{-j} \sin j\theta, \quad (E.14)$$

where

$$D(j) = \left(\frac{a^{j+1}}{j}\right) [-i\omega \delta_{nj} - 2 \frac{Un}{\pi a} G(j,n)], \quad (E.15)$$

and

$$G(j,n) = \int_0^{\theta_s} g(\theta) \sin j\theta \cos n\theta d\theta. \quad (E.16)$$

The external fluctuating pressure and the phase lag, in terms of  $\tan \psi$ , may then be written as

$$\begin{aligned} p_e^* = e^{i\omega t} \rho B_0 \left\{ -\omega^2 a \frac{\sin n\theta}{n} + i\omega \left[ 2 \frac{Un}{\pi} \sum_{j=1}^{\infty} \frac{\sin j\theta}{j} G(j,n) + Ug(\theta) \cos n\theta \right] \right. \\ \left. + 2 \frac{U^2 n}{\pi a} g(\theta) \sum_{j=1}^{\infty} \cos j\theta G(j,n) \right\}, \quad (E.17) \end{aligned}$$

and

$$-\tan \psi = U\omega \frac{\left( +g(\theta) \cos n\theta + 2 \frac{n}{\pi} \sum_{j=1}^{\infty} \frac{\sin j\theta}{j} G(j,n) \right)}{\left( -\frac{\omega^2 a}{n} \sin n\theta + 2 \frac{U^2 n}{\pi a} g(\theta) \sum_{j=1}^{\infty} \cos j\theta G(j,n) \right)}. \quad (E.18)$$

#### E.4 Results

The phase angles were computed in  $10^\circ$  intervals from  $\theta = 5^\circ$  to  $85^\circ$ . The listing of a computer program for the calculation of  $\psi$  may be found in Appendix G.

Figures E.13 to E.15 show the results for the  $n=3$  mode vibrating with an antinode facing the free stream, for flow velocity  $U = 5$  to  $30$  m/s in steps of  $5$  m/s. The computation is based on an ovalling frequency of  $230$  Hz. To facilitate the presentation of the data, any phase lag  $\psi$  greater than  $360^\circ$  is reset to  $\psi - 360^\circ$ . The experimentally measured phases (from  $\theta = 120^\circ$  to  $180^\circ$ ) are also plotted on the same diagrams. The phases between  $\theta = 85^\circ$  to  $120^\circ$  may then be interpolated.

For the  $n=2$  node ovalling with a node facing the free stream, the ovalling frequency is assumed to be  $167$  Hz. The results are plotted in Figures E.16 to E.18.



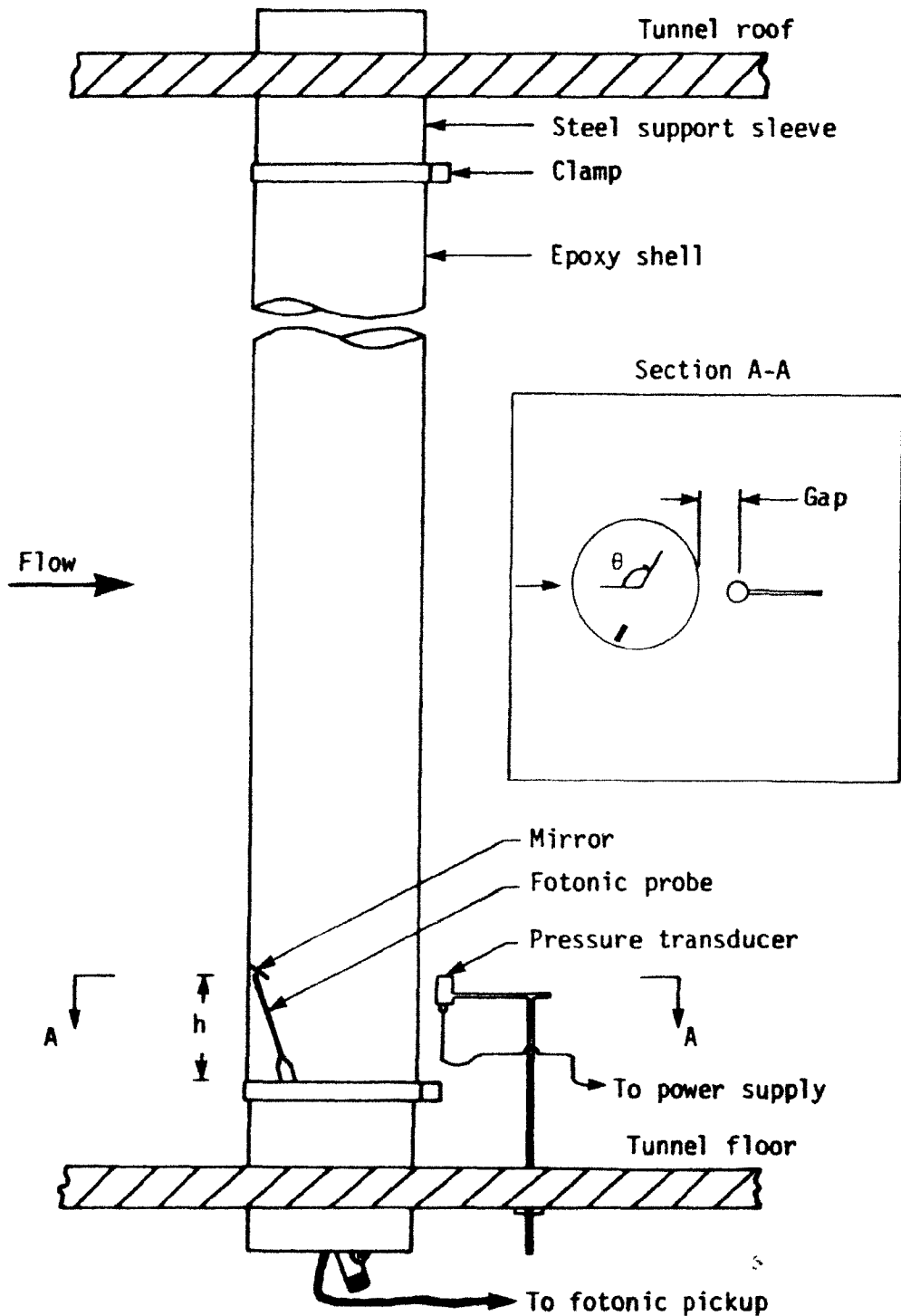


**Figure E.1:** Schematic of the cylindrical shell mounted in the wind tunnel test section, ancillary equipment and measuring apparatus for phase angle measurements.

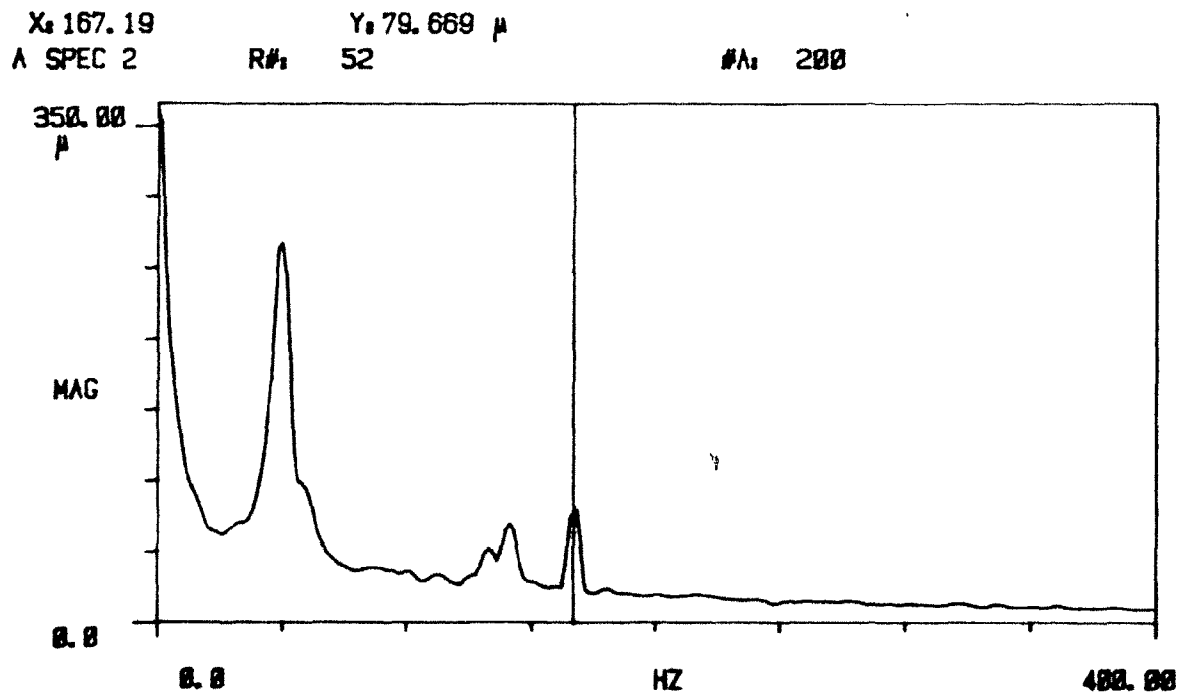
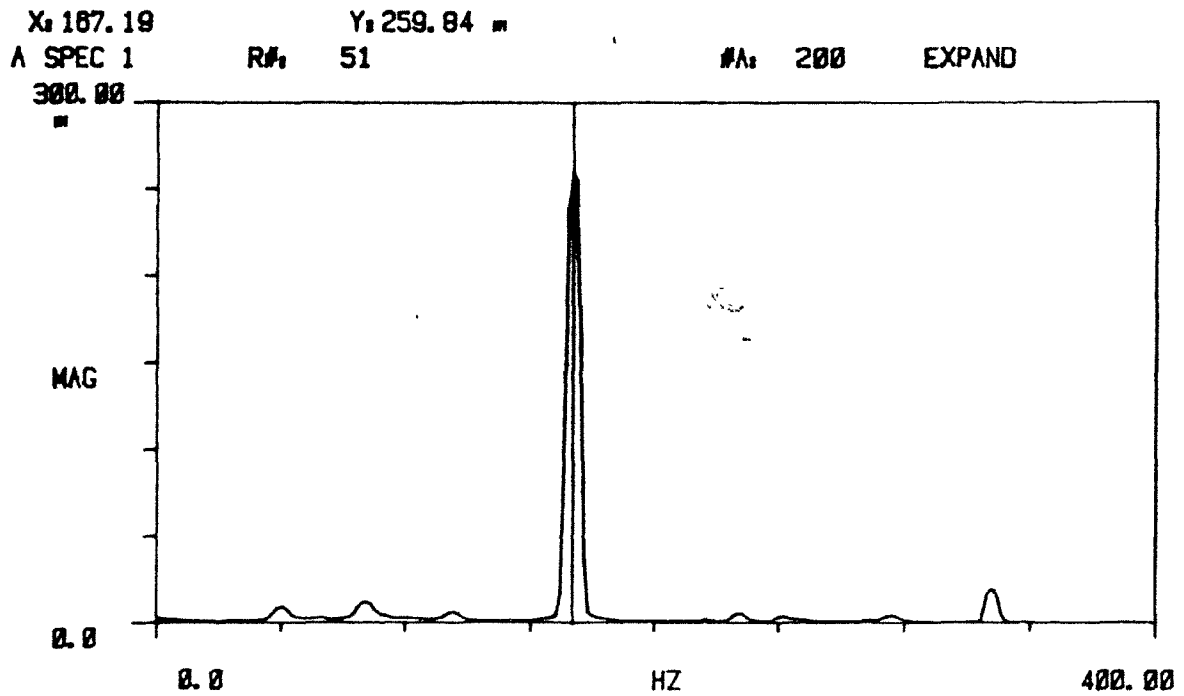


**Figure E.2:** Frequency spectra of shell vibration (top) at  $\theta = 315^\circ$  and induced pressure (bottom) at  $\theta = 135^\circ$  for the  $n=2$  mode ovalling at  $U = 21.5$  m/s.

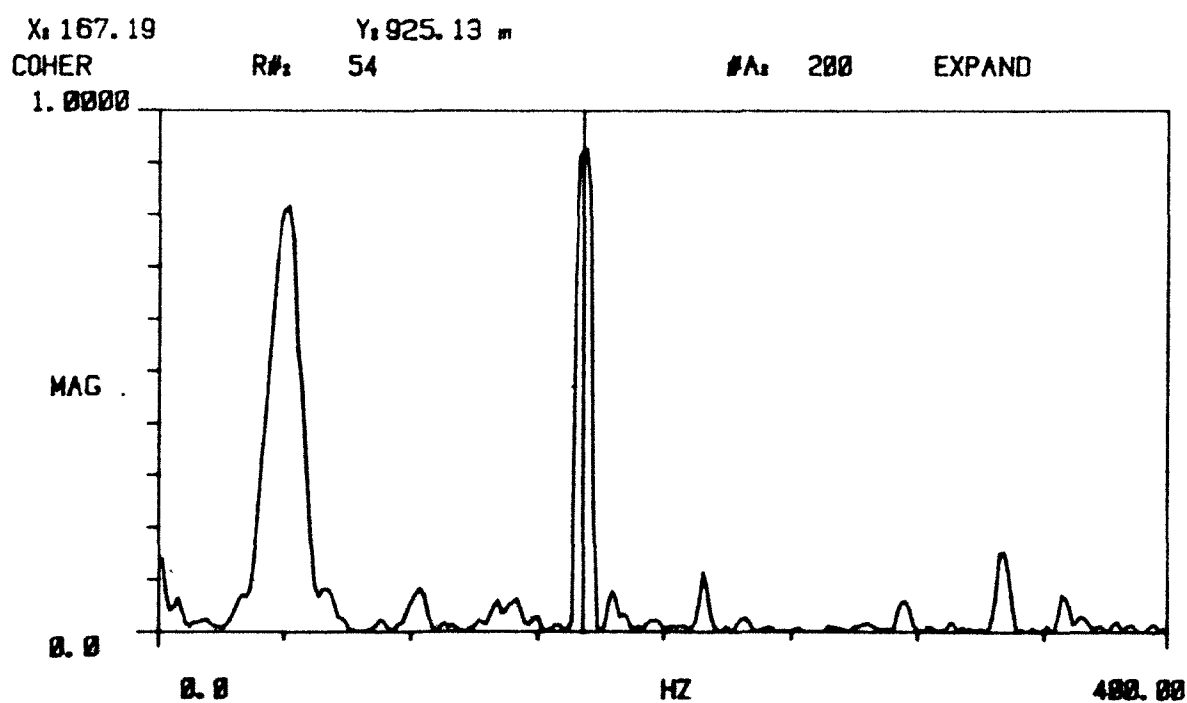
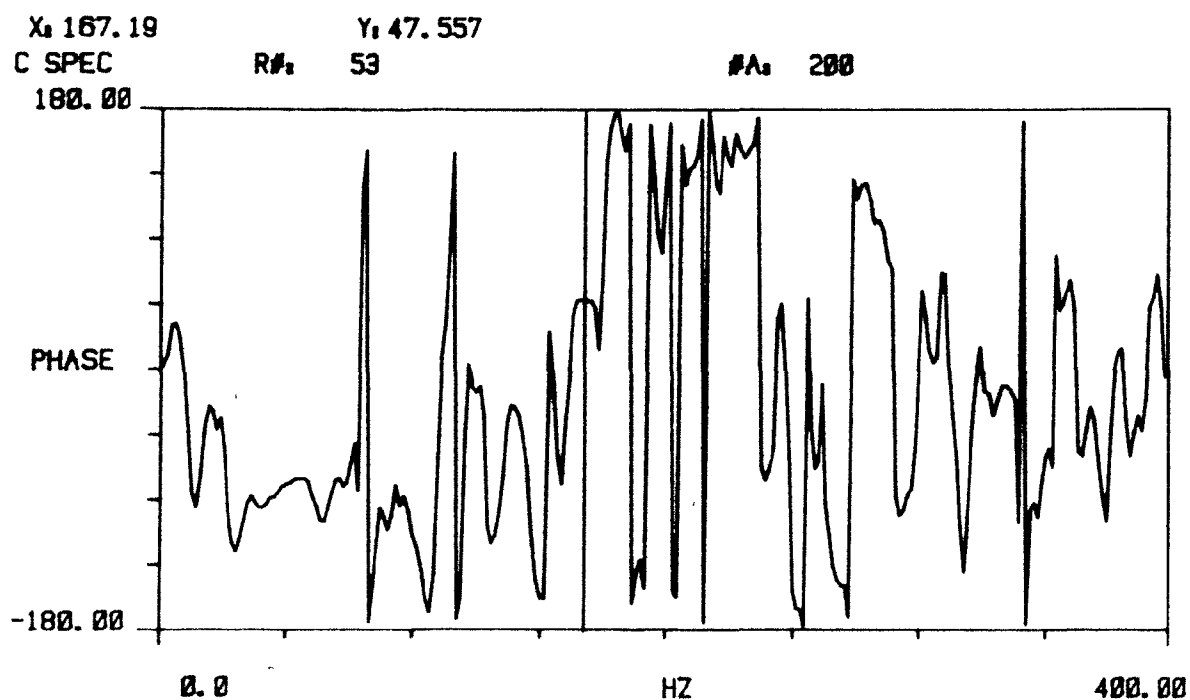


**Figure E.3:** Cross-correlation spectrum-phase (top) and coherence ratio (bottom) of shell vibration and induced pressure for the  $n=2$  mode at  $U = 21.5$  m/s.

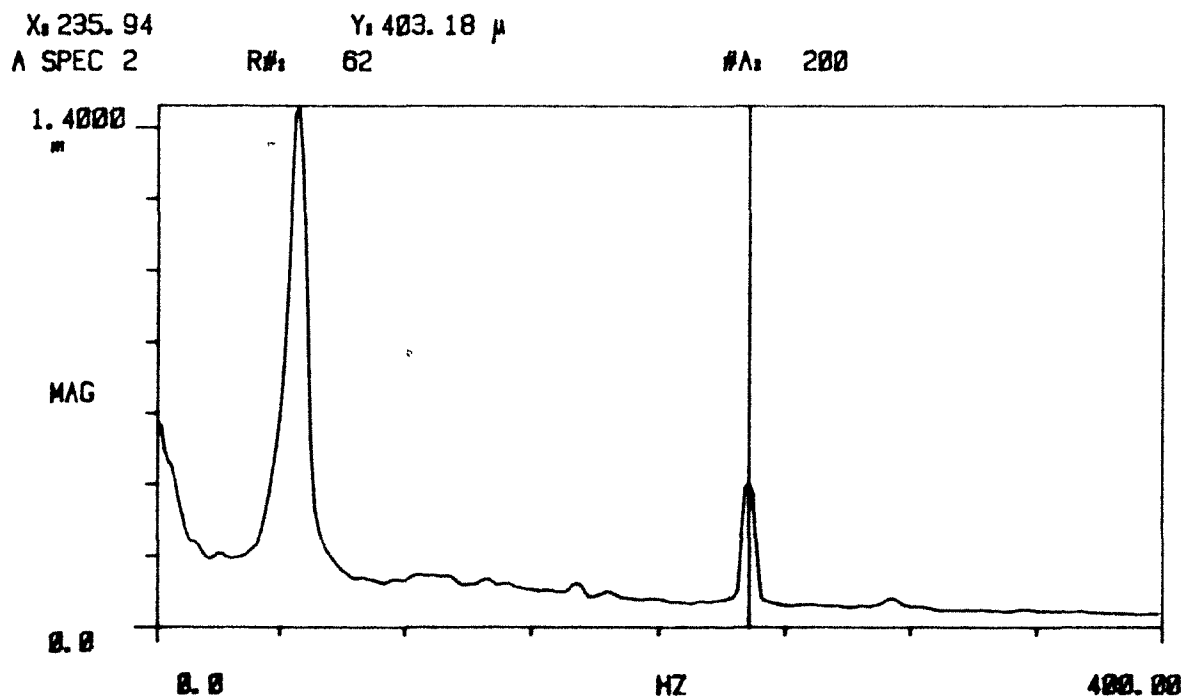
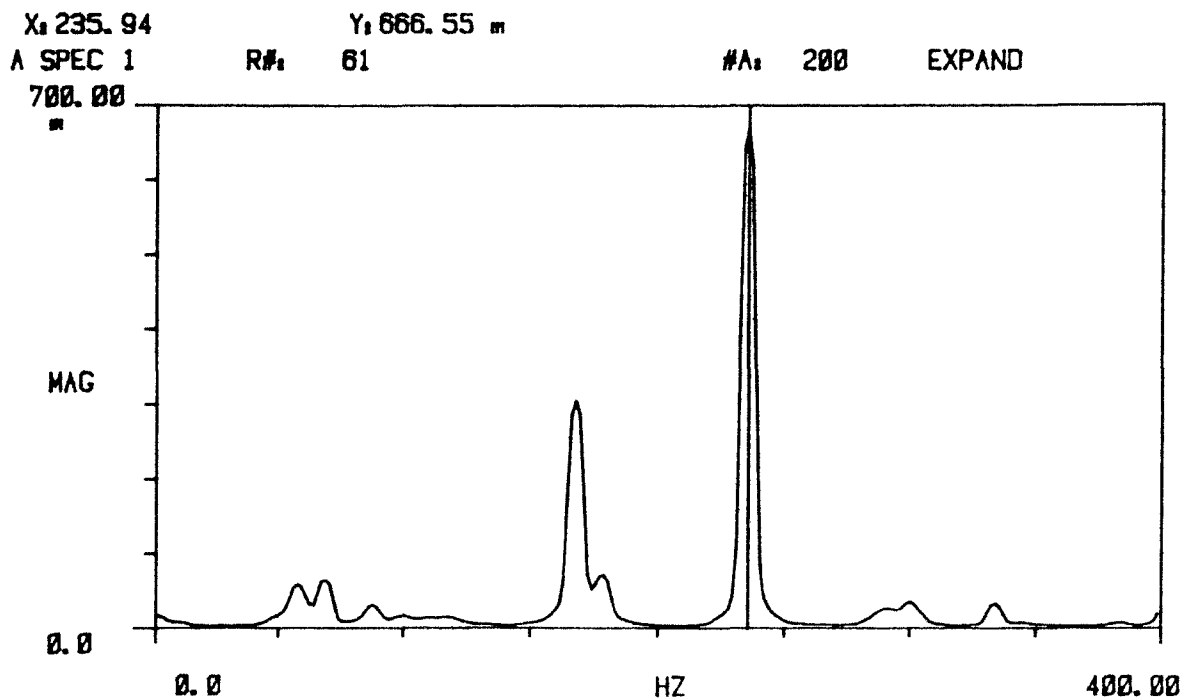
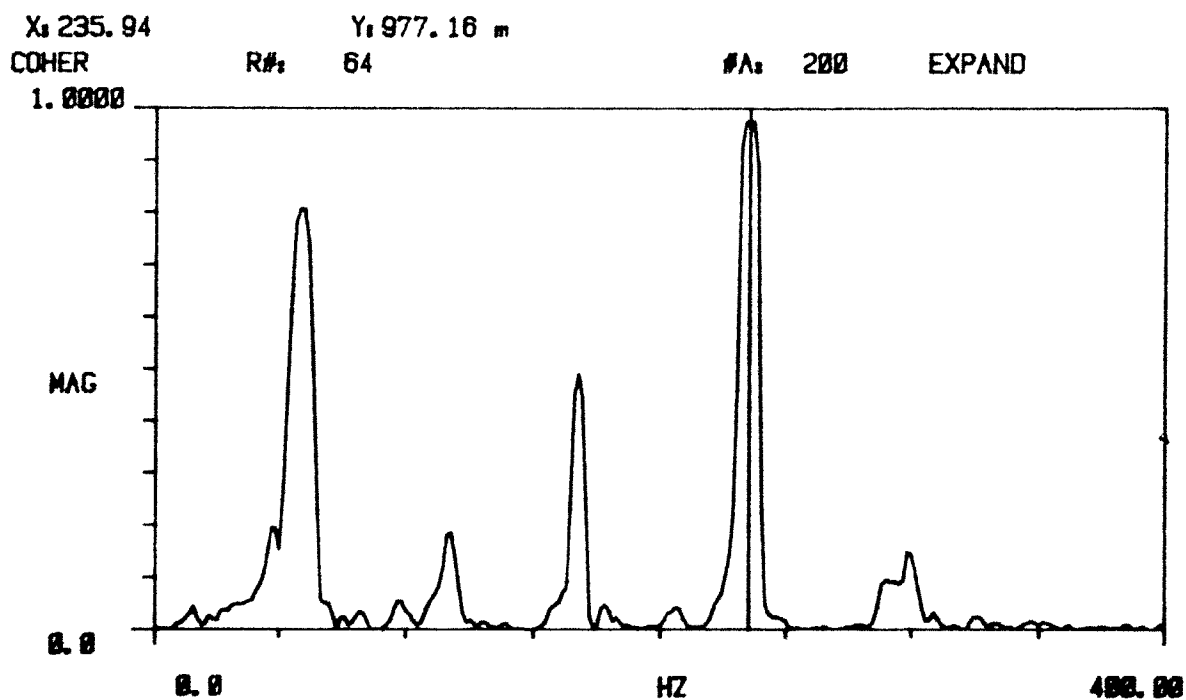
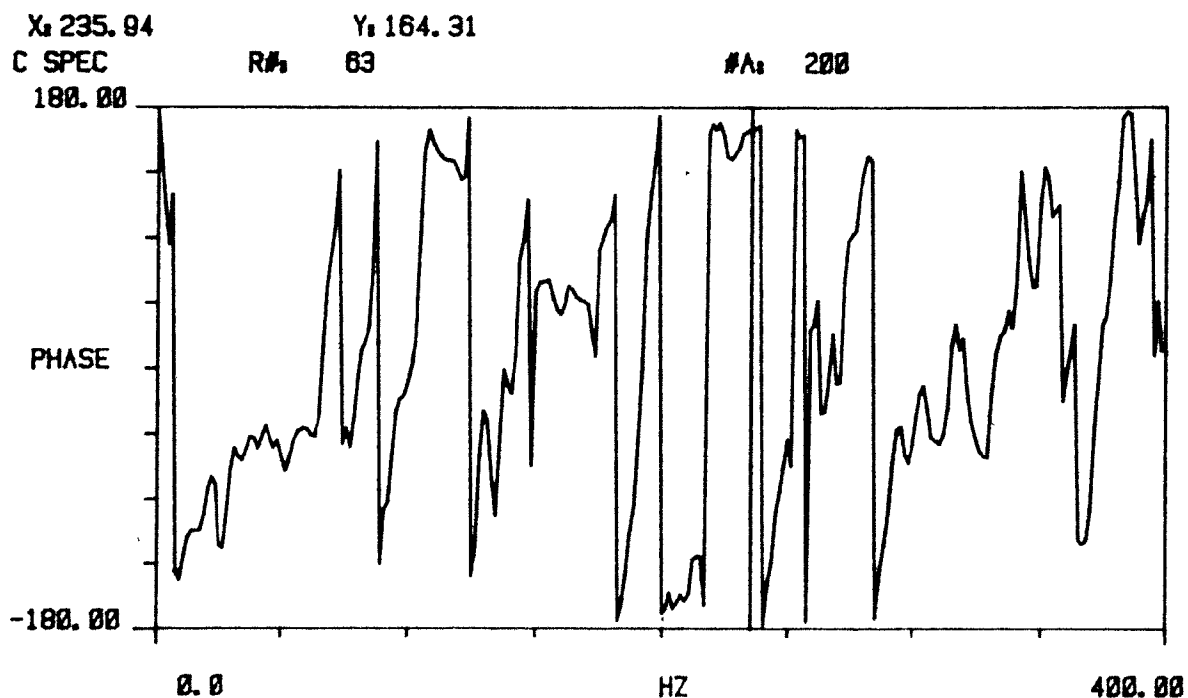


Figure E.4: Frequency spectra of shell vibration (top) at  $\theta = 315^\circ$  and induced pressure (bottom) at  $\theta = 135^\circ$  for the  $n=3$  mode ovalling at  $U = 25.5$  m/s.



**Figure E.5:** Cross-correlation spectrum-phase (top) and coherence ratio (bottom) of shell vibration and induced pressure for the  $n=3$  mode at  $U = 25.5$  m/s.

## SETUP STATE

MEASUREMENT : TRANSFER FUNCTION

AVERAGE : 200 , STABLE

SIGNAL : SINUSOIDAL

TRIGGER : FREE RUN , CHNL 1

CENT FREQ : 0.0 HZ

BANDWIDTH : 400.000 HZ

TIME LENGTH : 640.000 mS

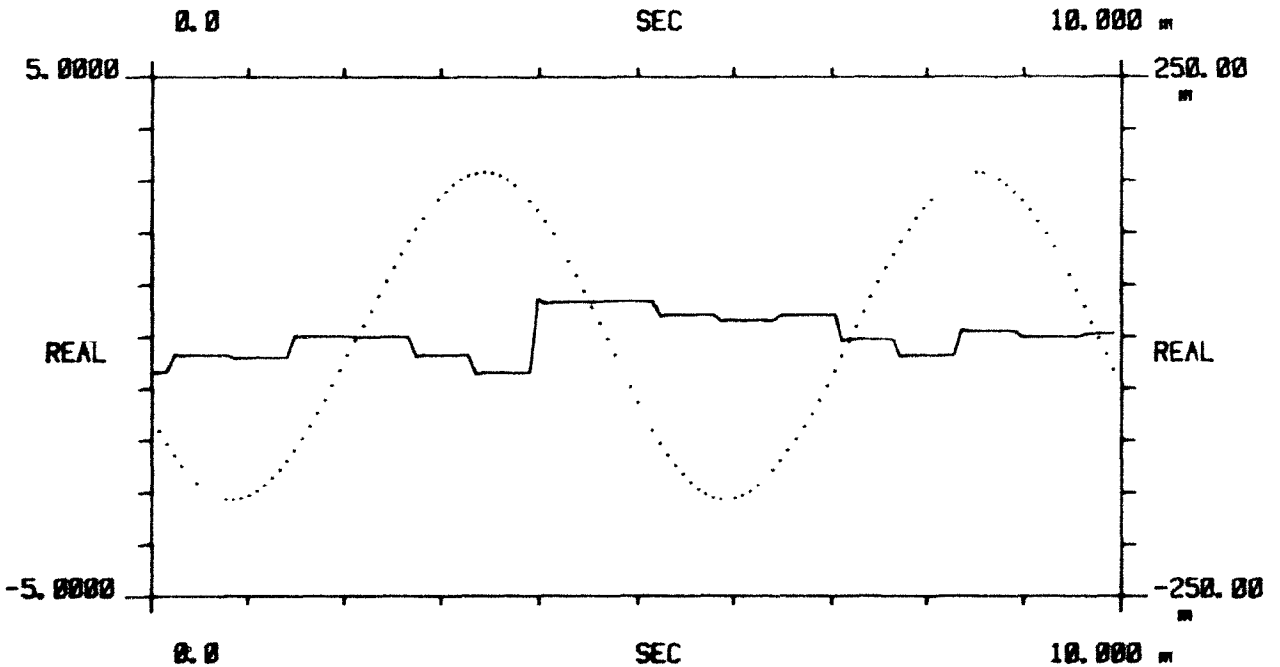
 $\Delta F$  : 1.56250 HZ $\Delta T$  : 625.000  $\mu$ S

ADC CHNL	RANGE	AC/DC	DELAY	CAL (C1/C2)
* 1	5 V	AC	0.0 S	1.00000
* 2	250 mV	AC	0.0 S	1.00000

INPT 1

#A<sub>1</sub> 1 EXPAND

INPT 2

#A<sub>2</sub> 1 EXPAND

**Figure E.6:** Typical setup state for phase measurements (top) and oscilloscope traces (bottom) of a sinusoidal signal (input 1) and a random white noise (input 2).

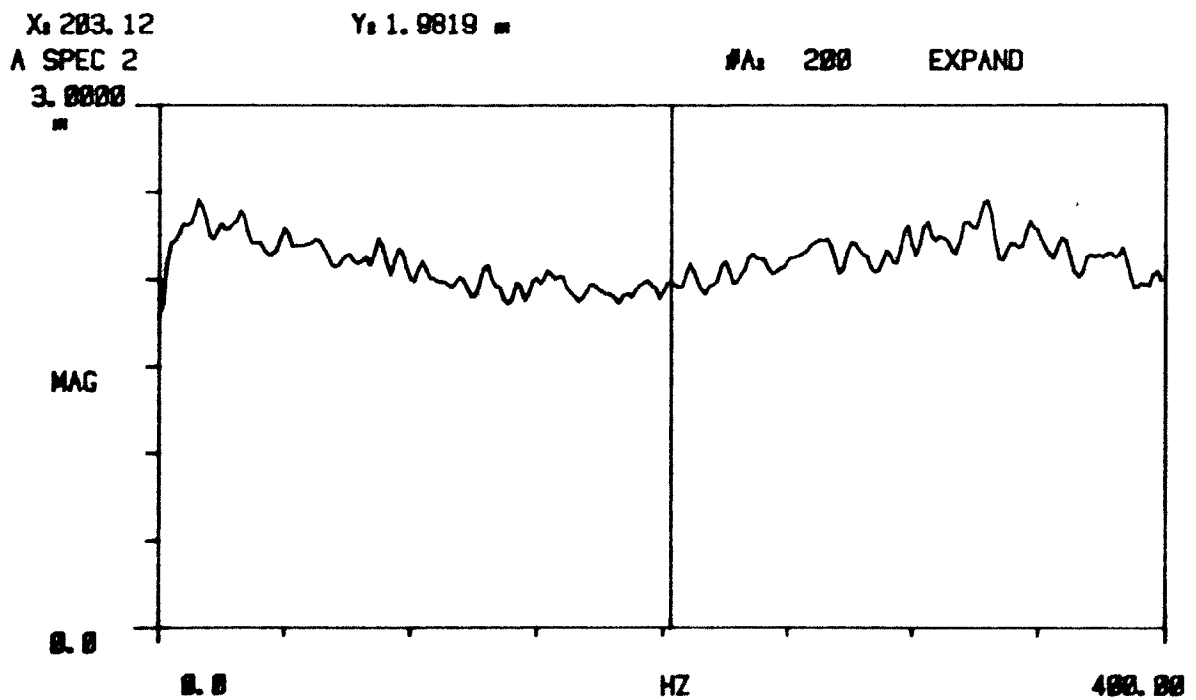
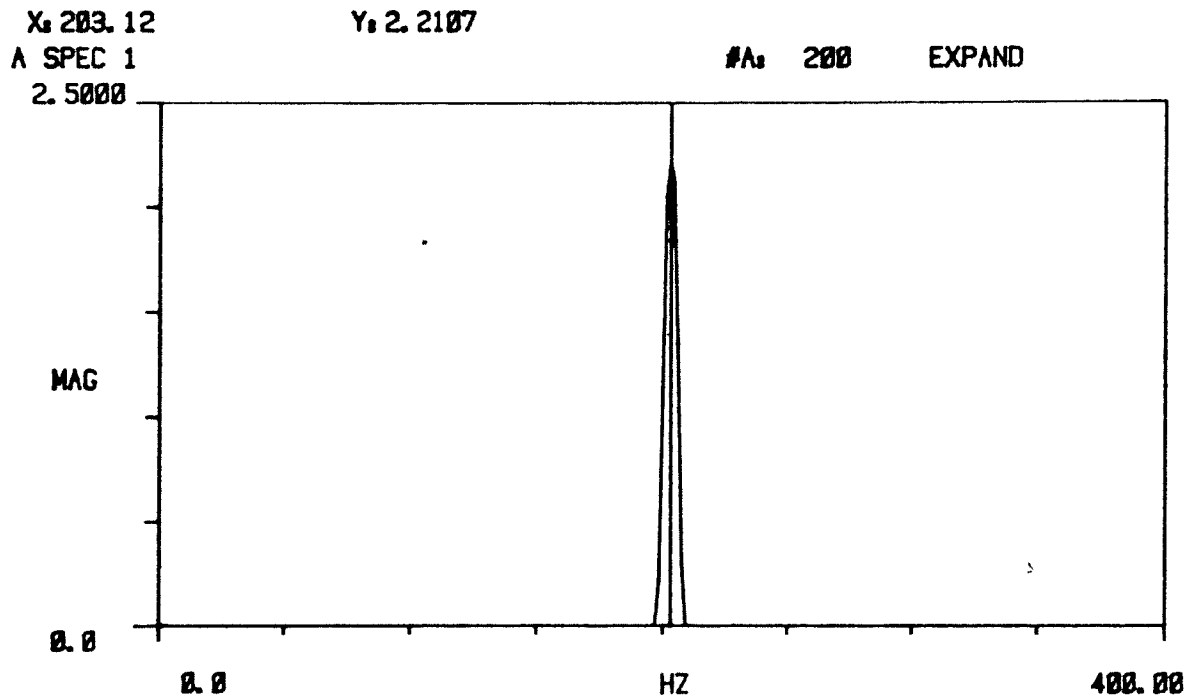


Figure E.7: Frequency spectra of a sinusoidal signal (top) and a random white noise (bottom).

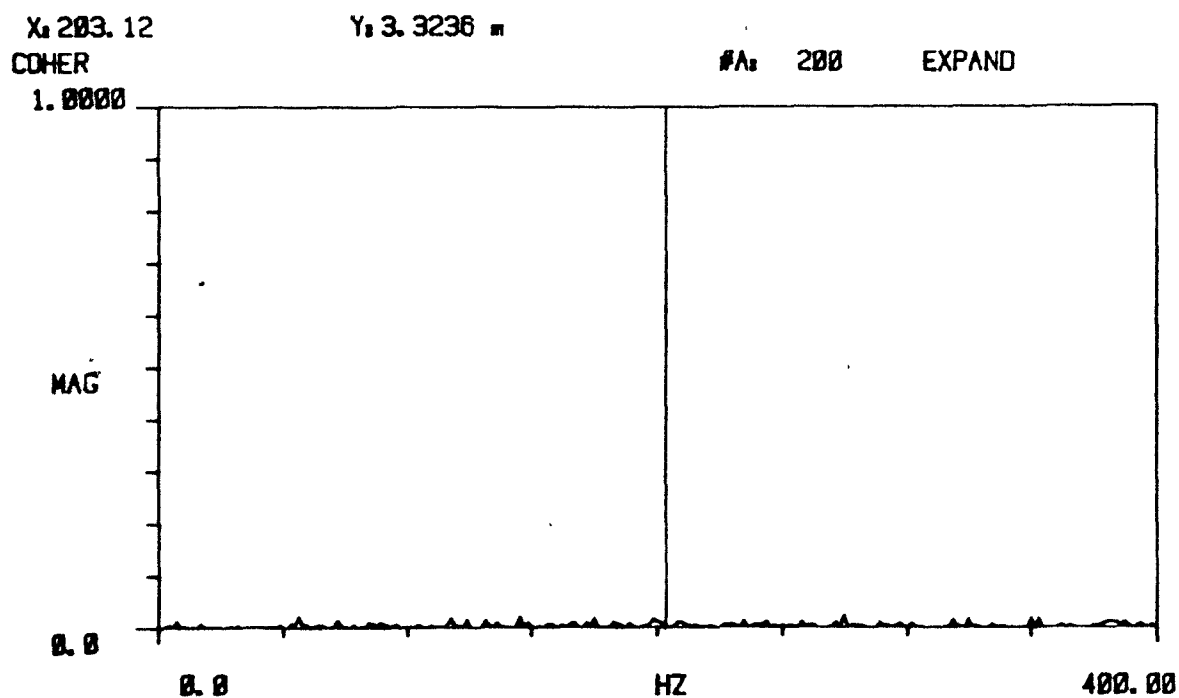
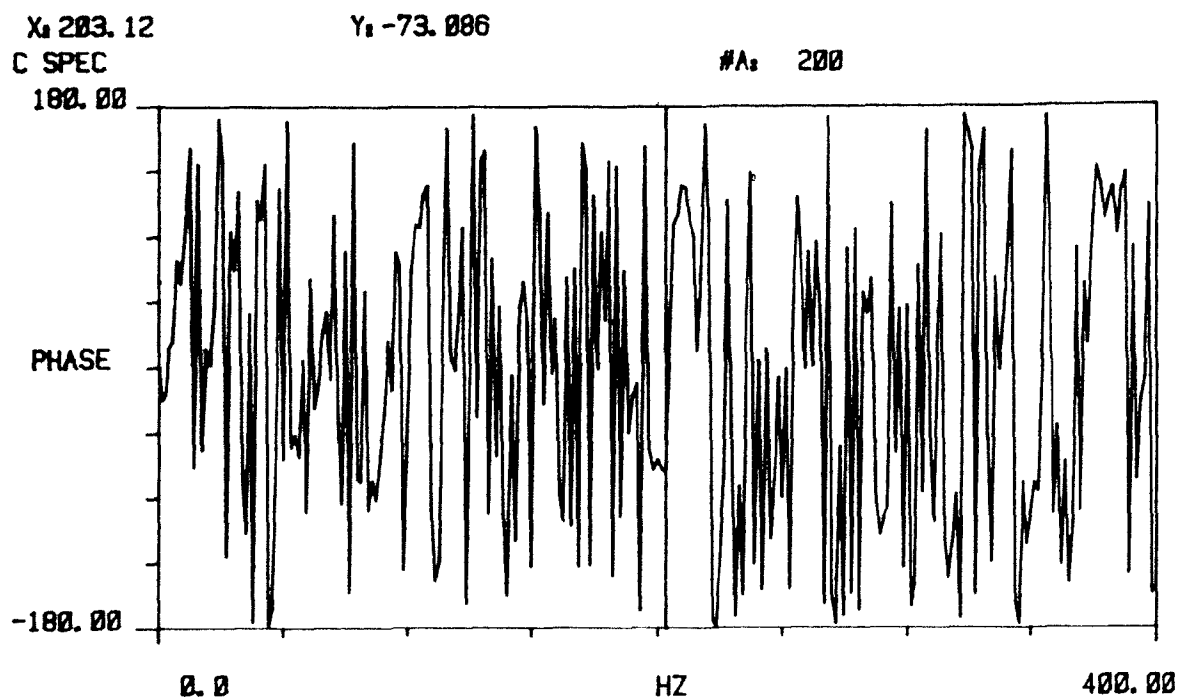
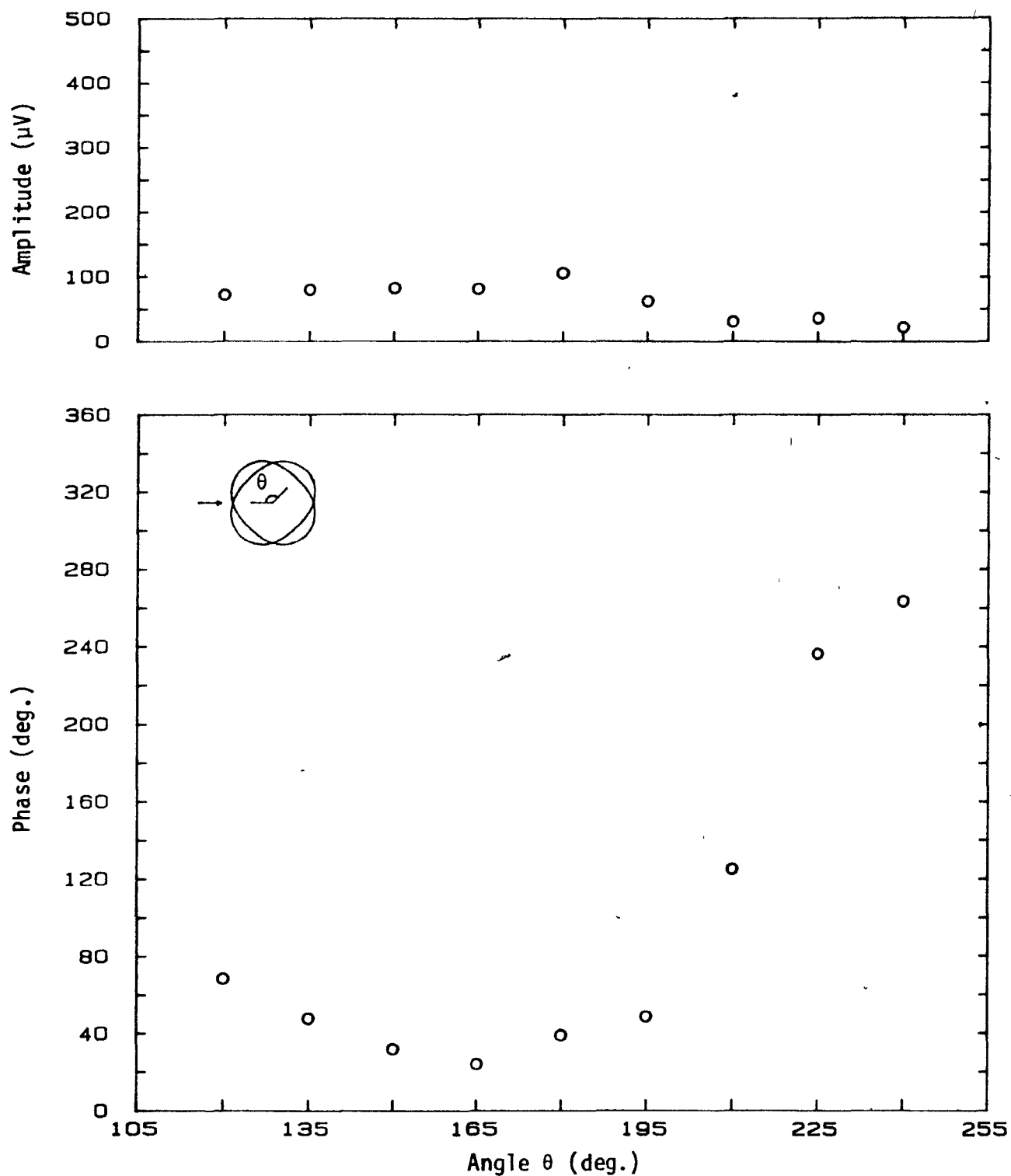
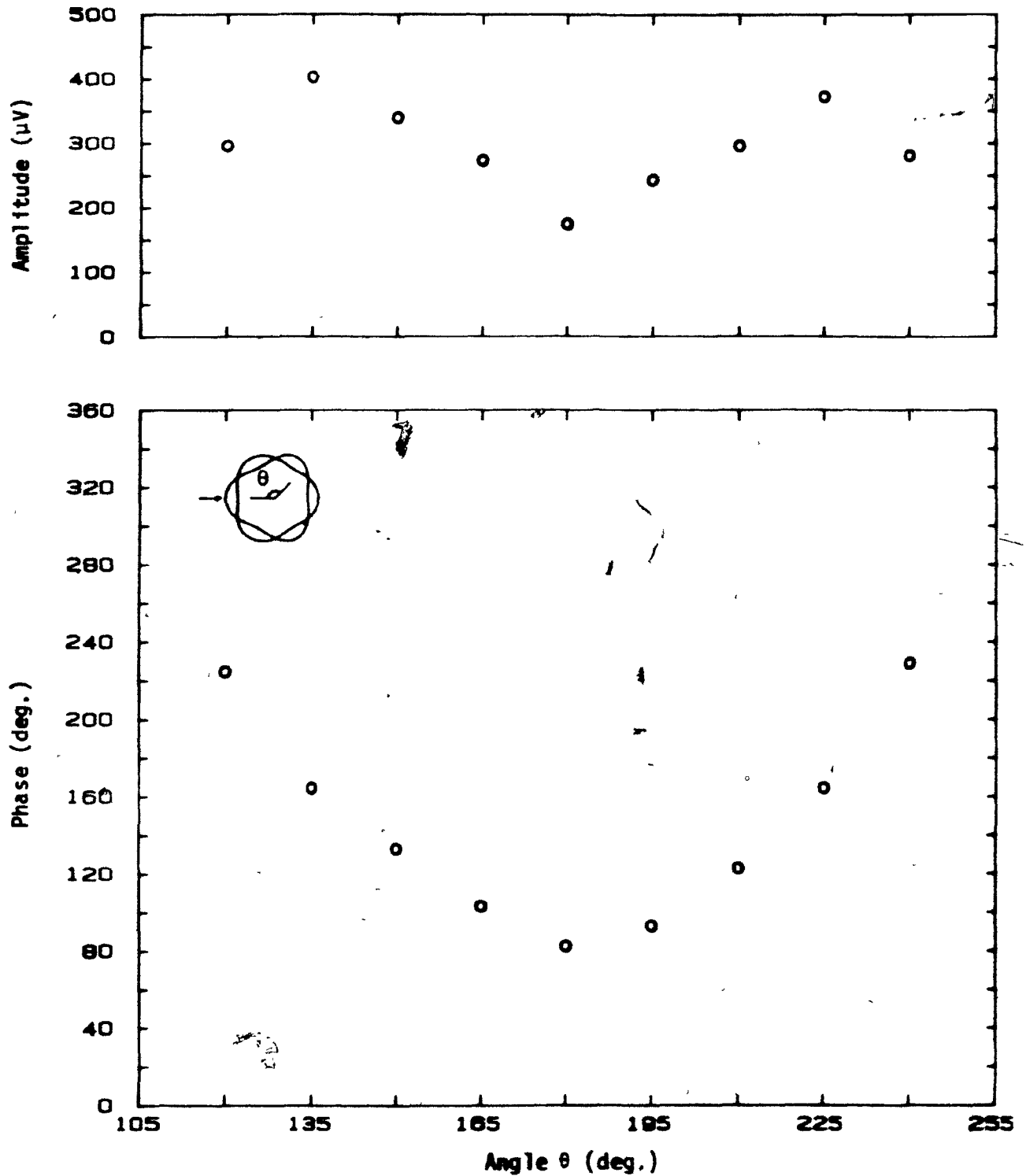


Figure E.8: Cross correlation spectrum-phase (top) and coherence ratio (bottom) of a sinusoidal signal correlated with random white noise.





**Figure E.9:** Measured magnitude of induced pressure (top) and the phase difference (bottom) between the shell displacement at  $\theta = 315^\circ$  and the induced pressure at various angular positions  $\theta$ , for the  $n=2$  mode at  $U = 21.5$  m/s.



**Figure E.10:** Measured magnitude of induced pressure (top) and the phase difference (bottom) between the shell displacement at  $\theta = 315^\circ$  and the induced pressure at various angular positions  $\theta$ , for the  $n=3$  mode at  $U = 25.5$  m/s.

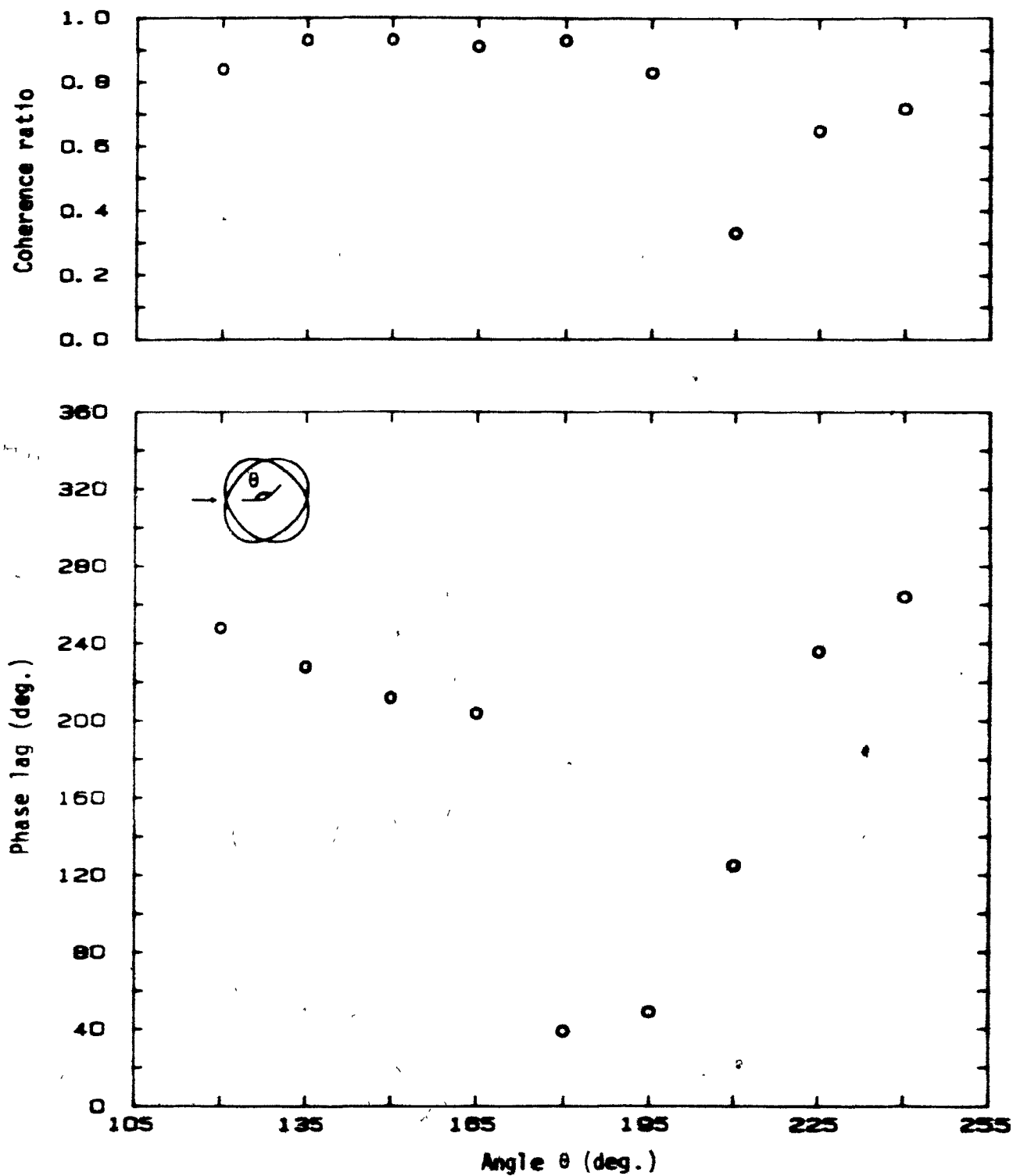


**Figure E.11:** Coherence ratio (top) and fully compensated phase lag (bottom) of induced pressure to shell displacement at various angular positions  $\theta$ , for the  $n=2$  mode at  $U = 21.5$  m/s.

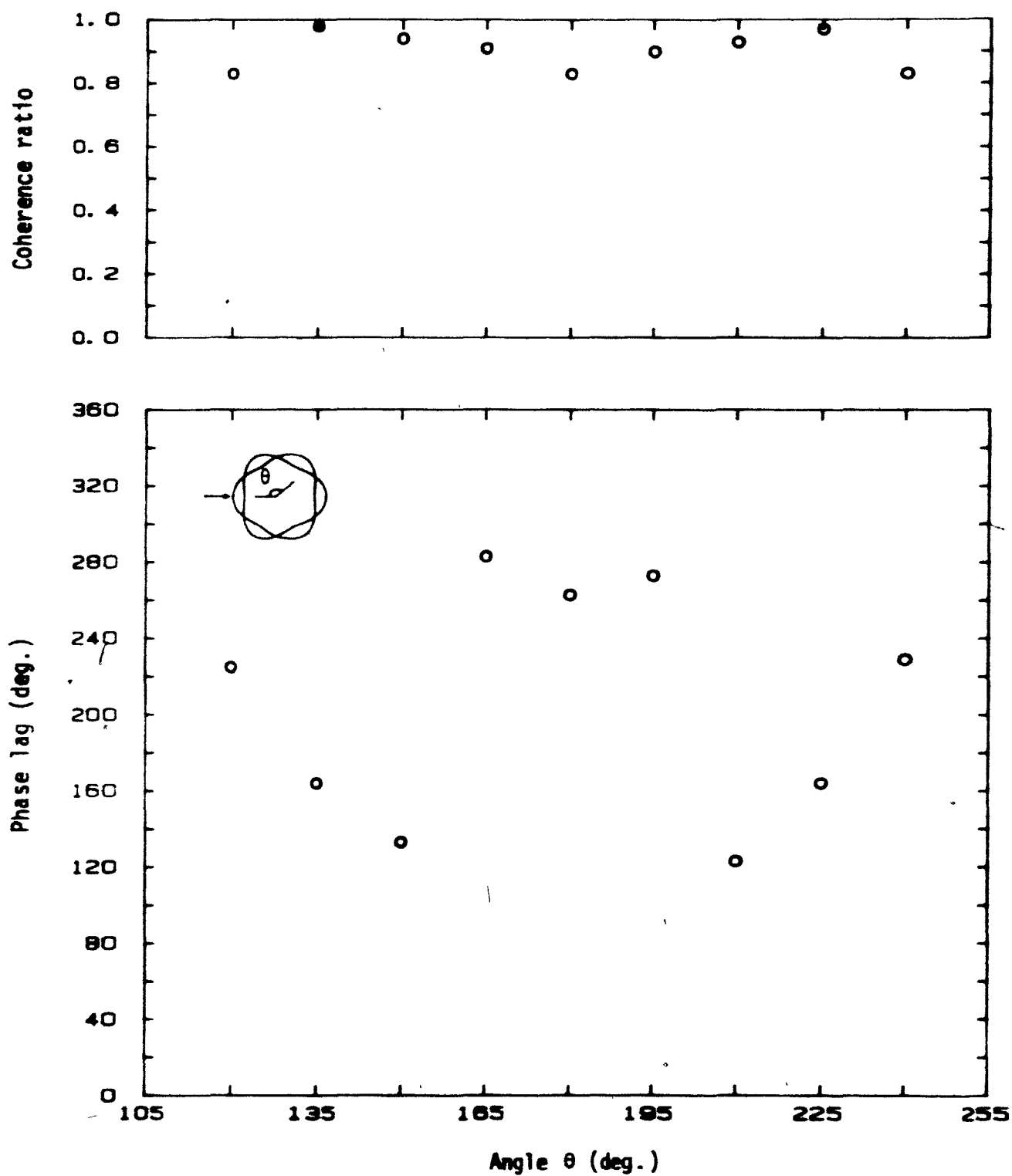


**Figure E.12:** Coherence ratio (top) and fully compensated phase lag (bottom) of induced pressure to shell displacement at various angular positions  $\theta$ , for the  $n=3$  mode at 25.5 m/s.

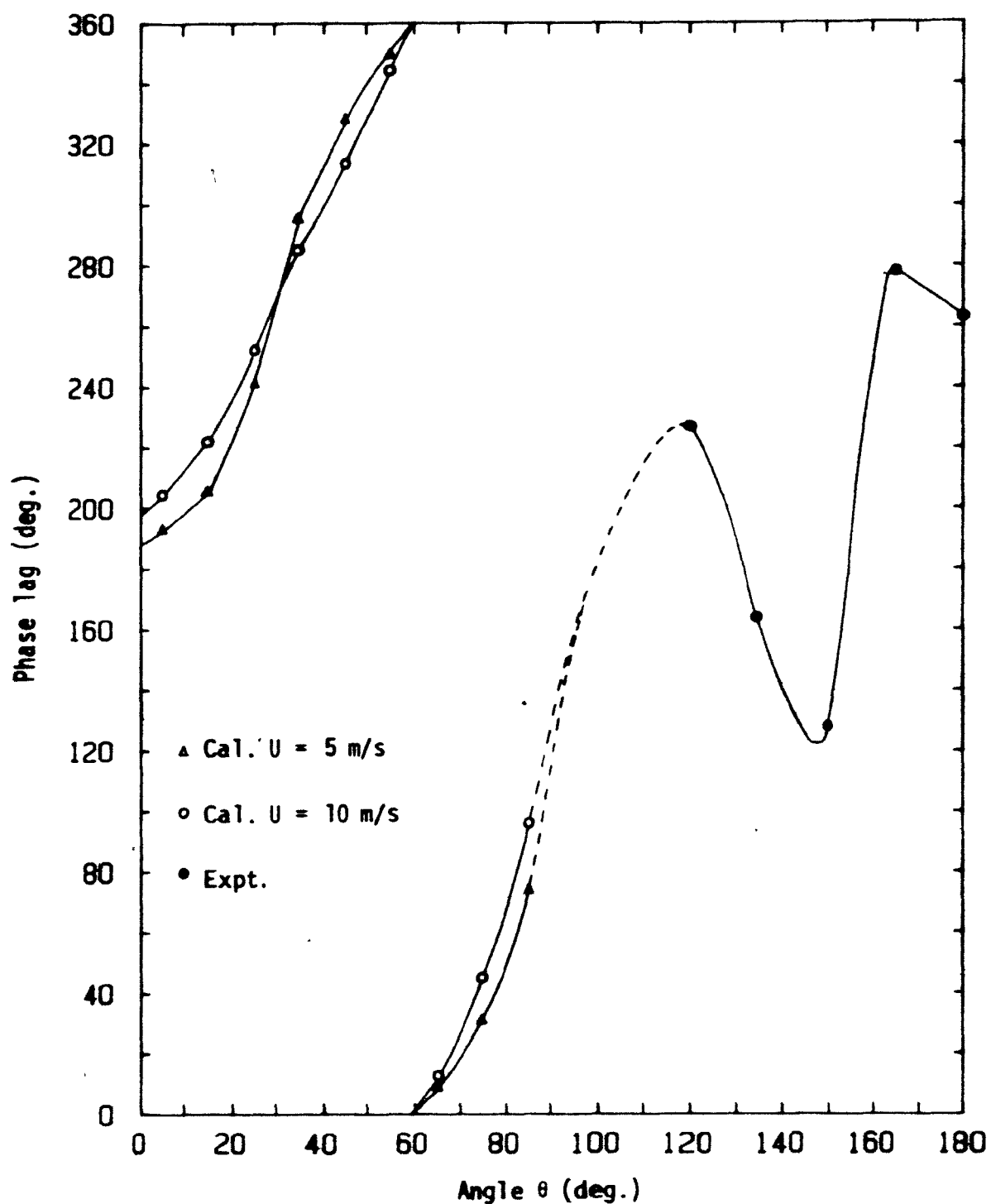


**Figure E.13:** Calculated and experimentally measured phase lag for the  $n=3$  mode vibrating with an antinode facing the free stream; calculations for  $U = 5$  and  $10$  m/s.

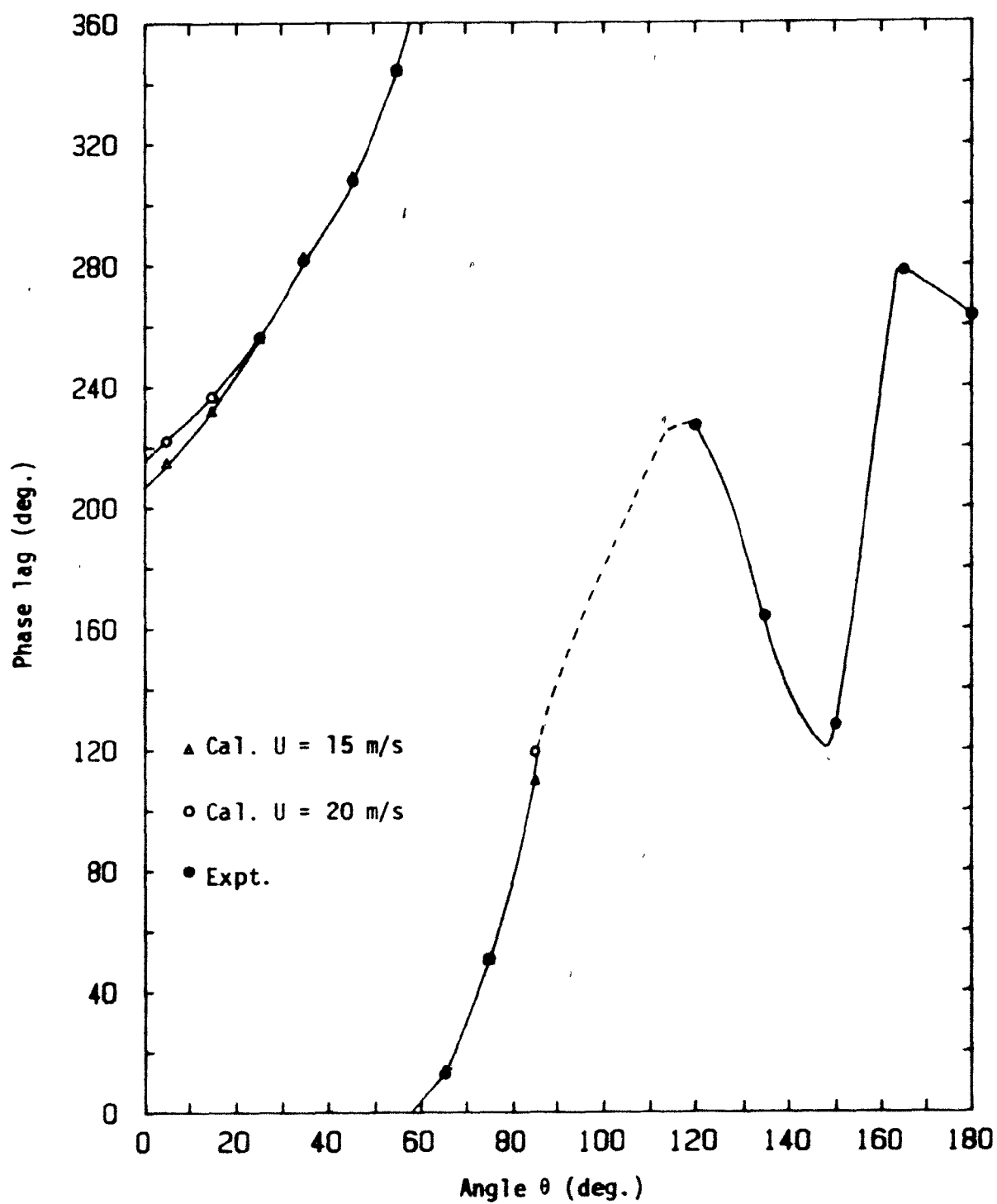


**Figure E.14:** Calculated and experimentally measured phase lag for the  $n=3$  mode vibrating with an antinode facing the free stream; calculations for  $U = 15$  and  $20$  m/s.

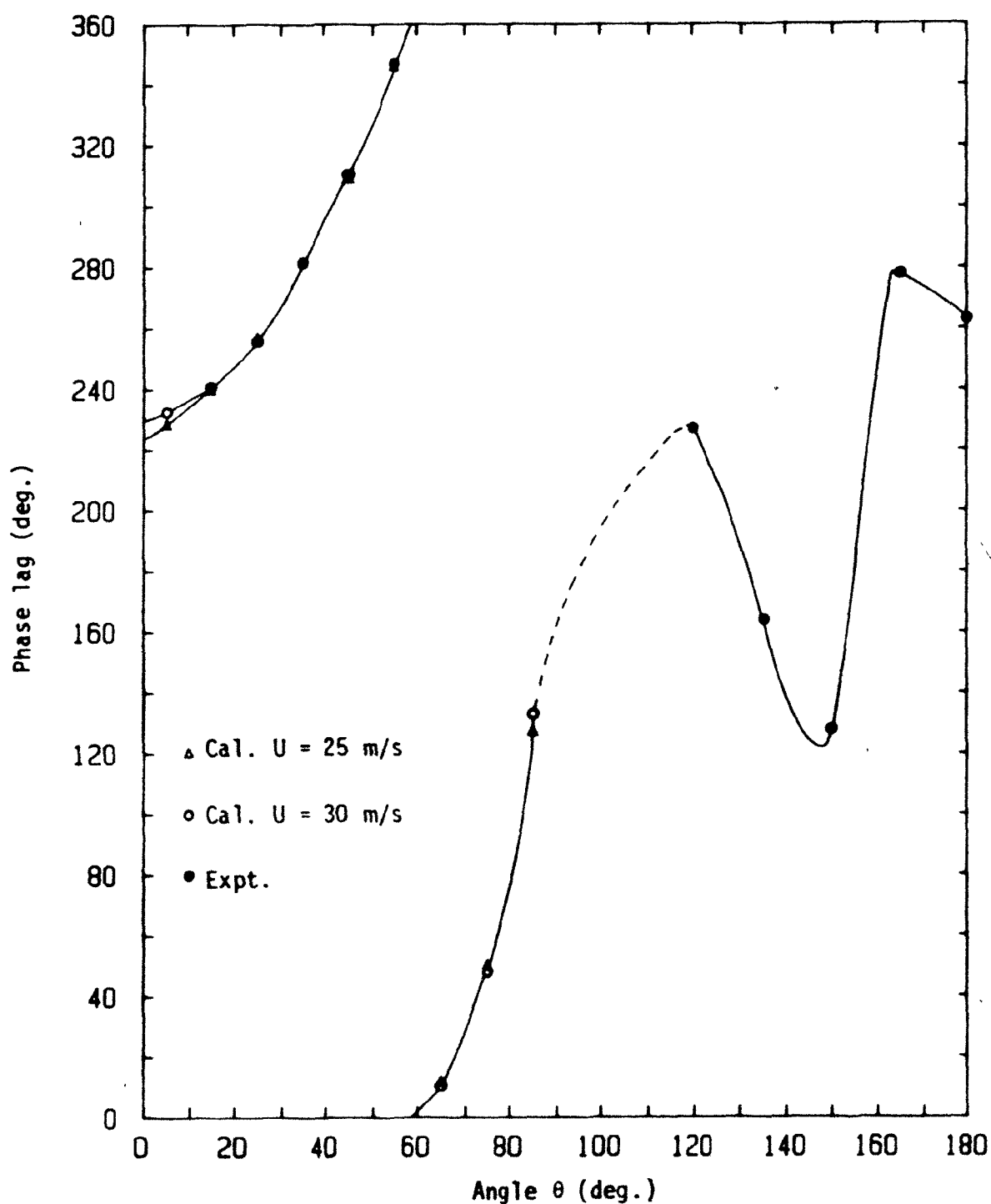


**Figure E.15:** Calculated and experimentally measured phase lag for the  $n=3$  mode vibrating with an antinode facing the free stream; calculations for  $U = 25$  and  $30$  m/s.

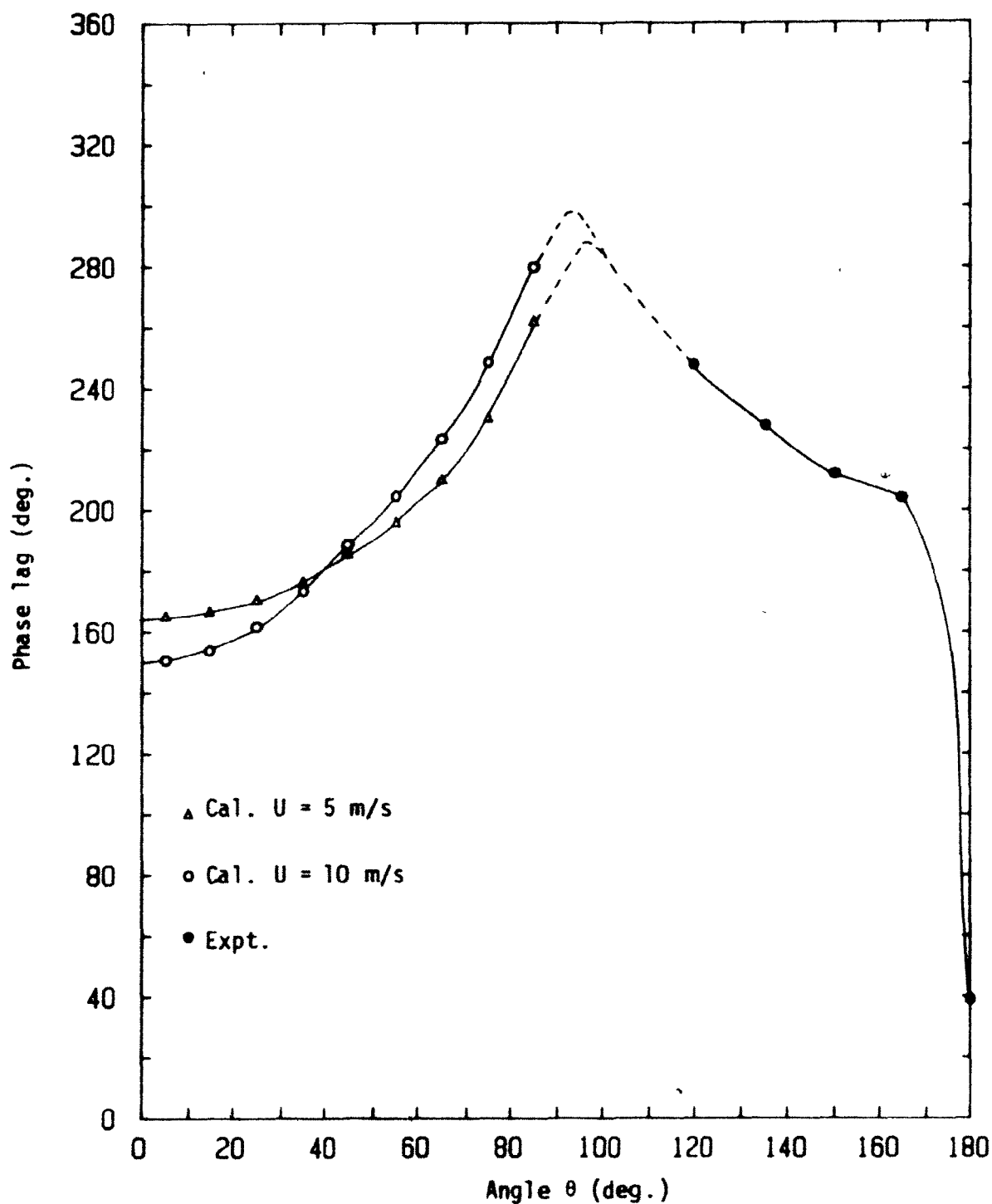


**Figure E.16:** Calculated and experimentally measured phase lag for the  $n=2$  mode vibrating with a node facing the free stream; calculations for  $U = 5$  and  $10$  m/s.



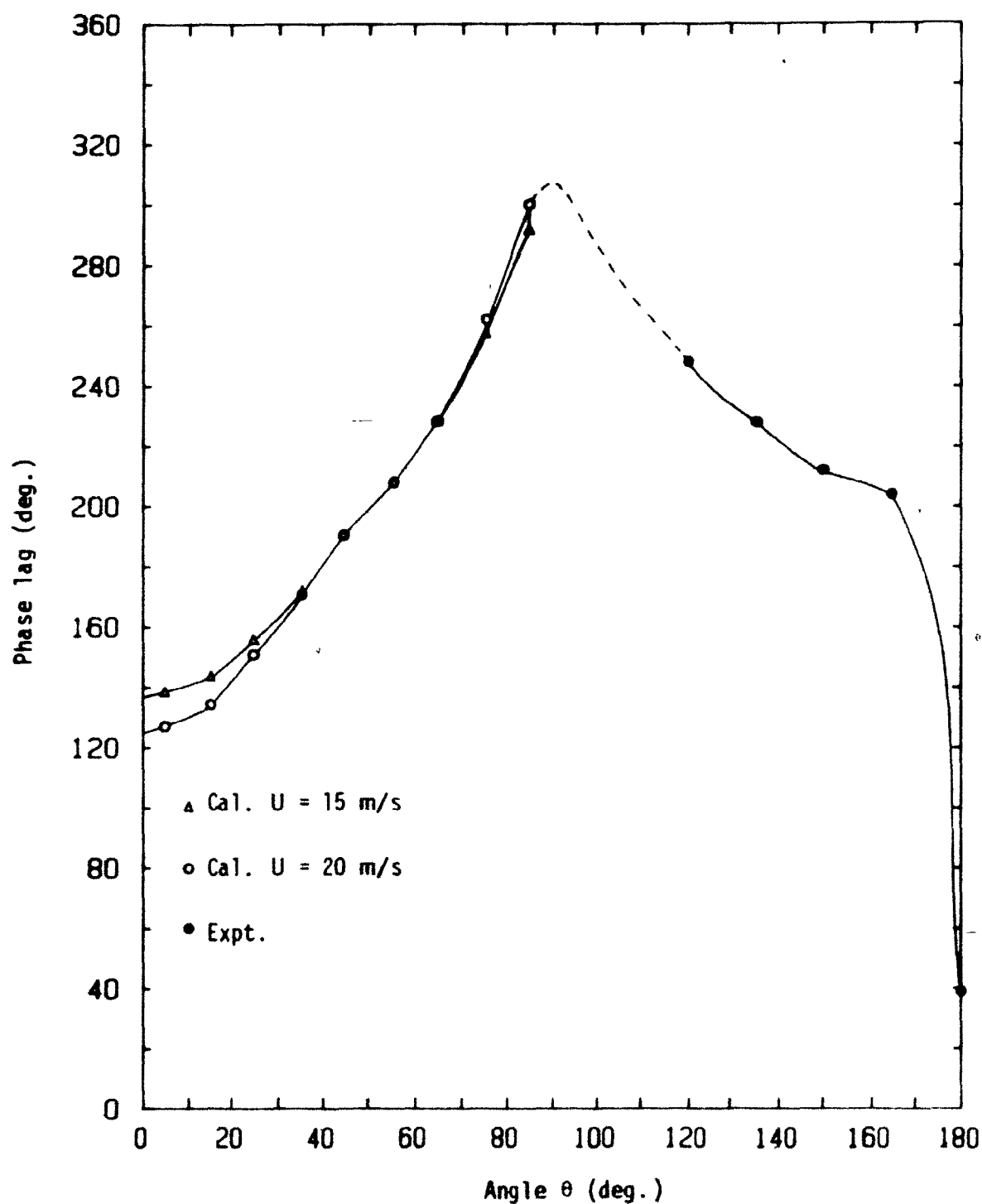


**Figure E.17:** Calculated and experimentally measured phase lag for the  $n=2$  mode vibrating with a node facing the free stream; calculations for  $U = 15$  and  $20$  m/s.

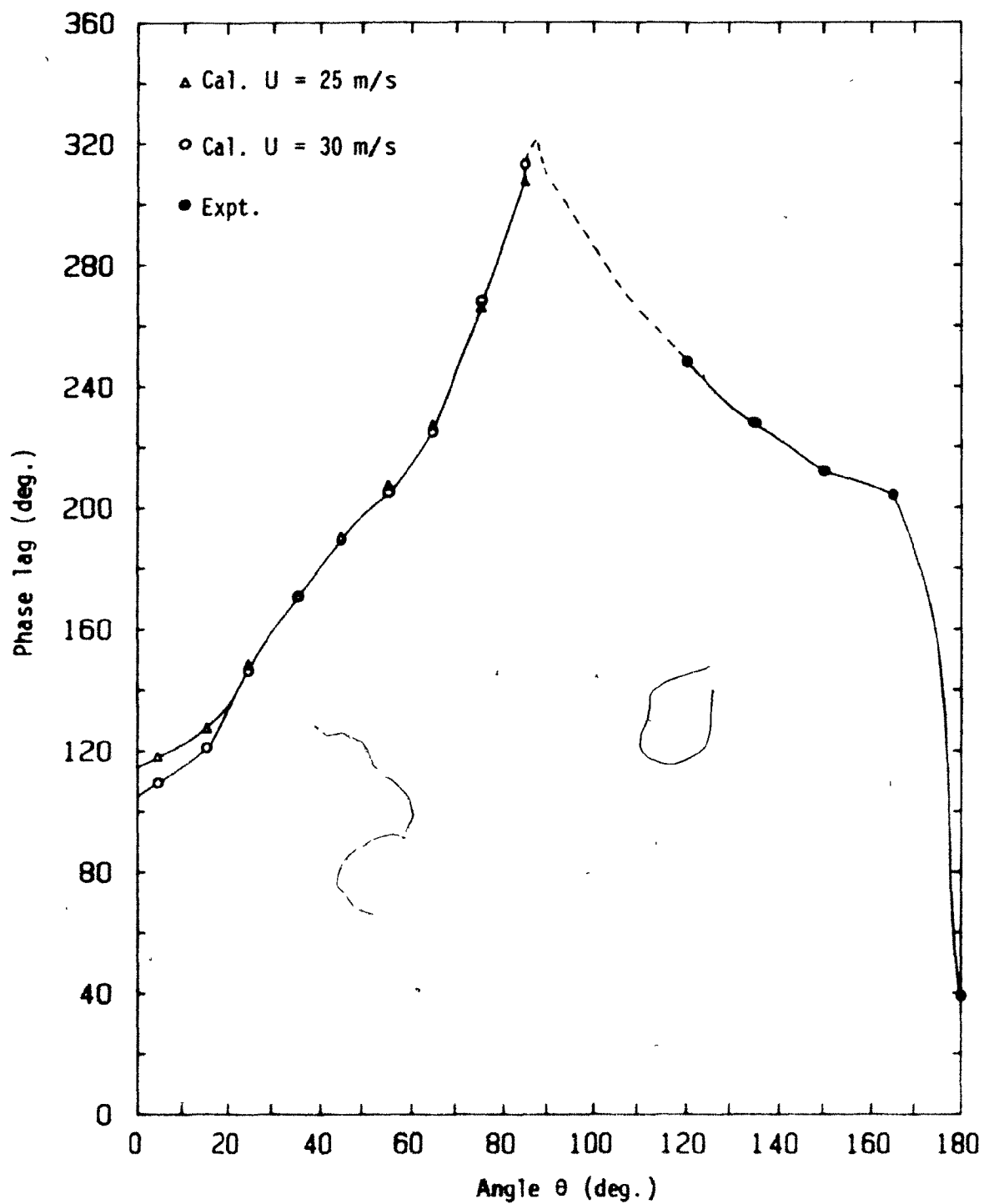


**Figure E.18:** Calculated and experimentally measured phase lag for the  $n=2$  mode vibrating with a node facing the free stream; calculations for  $U = 25$  and  $30$  m/s.

## APPENDIX F

### THEORY FOR OVALLING WITH A NODE FACING THE FREE STREAM

The analysis remains unaltered and as described in Chapter 6, except that the flow potentials and shell displacements assume different forms. Hence, only the major derivation procedures will be outlined and the final results will be presented directly.

For harmonic shell vibrations with a node facing the free stream, it may be shown that the external and internal perturbation flow potentials may be expressed as

$$\phi_e^* = e^{i\omega t} \sum_{\lambda=0}^{\infty} D(\lambda) r^{-\lambda} \sin \lambda \theta, \quad (\text{F.1})$$

$$\phi_i^* = e^{i\omega t} \sum_{\lambda=0}^{\infty} E(\lambda) r^{\lambda} \sin \lambda \theta, \quad (\text{F.2})$$

and the shell displacements may be assumed to have the forms

$$\begin{aligned} u^* &= e^{i\omega t} \sum_{m=1}^{\infty} A_m \sin n\theta \psi_m, \\ v^* &= e^{i\omega t} \sum_{m=1}^{\infty} B_m \cos n\theta \psi_m, \\ w^* &= e^{i\omega t} \sum_{m=1}^{\infty} C_m \sin n\theta \psi_m. \end{aligned} \quad (\text{F.3})$$

Substituting equations (F.1) and (F.2) into the boundary condition - equation (6.12) - an expression for  $D(\lambda)$  of  $\phi_e^*$  may be obtained:

$$D(j) = \left(\frac{a^{j+1}}{j}\right) \sum_{m=1}^{\infty} C_m \left\{ -i\omega \delta_{nj} - 2 \frac{U_n}{\pi a} F(j, n) + \frac{U}{\pi a} \left[ \frac{\sin(1+n+j)\theta_s}{1+n+j} - \frac{\sin(1+n-j)\theta_s}{1+n-j} - \frac{\sin(1-n+j)\theta_s}{1-n+j} + \frac{\sin(1-n-j)\theta_s}{1-n-j} \right] \right\} \psi_m. \quad (F.4)$$

Similarly,  $E(j)$  for  $\phi_i^*$  is given by

$$E(j) = \left(\frac{a^{1-j}}{j}\right) \sum_{m=1}^{\infty} i\omega C_m \delta_{nj} \psi_m. \quad (F.5)$$

Thus,  $\phi_e^*$  and  $\phi_i^*$  may be expressed as

$$\phi_e^* = e^{i\omega t} \left[ D(0) + \sum_{j=1}^{\infty} D(j) r^{-j} \sin j\theta \right], \quad (F.6)$$

$$\phi_i^* = e^{i\omega t} \left[ E(0) + \sum_{j=1}^{\infty} D(j) r^j \sin j\theta \right]. \quad (F.7)$$

With equations (F.6) and (F.7), in conjunction with (F.4) and (F.5), the external pressure  $p_e^*$  and internal pressure  $p_i^*$ , respectively, may be written as follows:

$$\begin{aligned}
p_e^* = & - \rho e^{i\omega t} \sum_{j=1}^{\infty} \left\{ c_m \left\{ \frac{\omega^2 a \sin n\theta}{n} - 2 \frac{U\omega i}{\pi} \left[ n \sum_{j=1}^{\infty} \frac{\sin j\theta}{j} F(j,n) \right. \right. \right. \\
& \left. \left. - \frac{1}{2} \left( \sum_{j=1}^{\infty} \frac{\sin j\theta}{j} \left( \frac{\sin(1+n+j)\theta_s}{1+n+j} - \frac{\sin(1+n-j)\theta_s}{1+n-j} - \frac{\sin(1-n+j)\theta_s}{1-n+j} + \frac{\sin(1-n-j)\theta_s}{1-n-j} \right) \right) \right] \right\} \\
& + U f(\theta) \delta_1 \left\{ -i\omega \cos n\theta [B_m + C_m] - 2 \frac{U}{\pi a} c_m \left[ n \sum_{j=1}^{\infty} F(j,n) \cos j\theta \right. \right. \\
& \left. \left. - \frac{1}{2} \left( \sum_{j=1}^{\infty} \cos j\theta \left( \frac{\sin(1+n+j)\theta_s}{1+n+j} - \frac{\sin(1+n-j)\theta_s}{1+n-j} - \frac{\sin(1-n+j)\theta_s}{1-n+j} + \frac{\sin(1-n-j)\theta_s}{1-n-j} \right) \right) \right] \right\} \\
& - 2 \frac{U^2}{a} c_m f(\theta) \sin\theta \sin n\theta \delta_2 - \frac{HU^2}{2a} e^{-i\psi} c_m \sin n\theta \delta_3 \left. \right\} \psi_m \\
& - \rho e^{i\omega t} i\omega D(0) , \tag{F.8}
\end{aligned}$$

where

$$f(\theta)\delta_1 = f(\theta) , \delta_2 = 1 \quad \text{and} \quad \delta_3 = 0 \quad \text{if} \quad 0 \leq |\theta| \leq \theta_s ,$$

$$f(\theta)\delta_1 = -f(\theta_s) , \delta_2 = 0 \quad \text{and} \quad \delta_3 = 1 \quad \text{if} \quad |\theta| > \theta_s ;$$

and

$$p_i^* = - \rho e^{i\omega t} \sum_{m=1}^{\infty} \left\{ - c_m \frac{\omega^2 a \sin n\theta}{n} \psi_m - \rho e^{i\omega t} E(0) \right\} . \tag{F.9}$$

Hence, the aerodynamic term  $q_r^* = p_i^* - p_e^*$  becomes

$$\begin{aligned}
q_r^* = & \rho e^{i\omega t} \sum_{m=1}^{\infty} \left\{ C_m \left\{ 2 \frac{\omega^2 a \sin n\theta}{n} + 2 \frac{U\omega l}{\pi} \left[ -n \sum_{j=1}^{\infty} \frac{\sin j\theta}{j} F(j,n) \right. \right. \right. \\
& + \left. \left. \frac{1}{2} \left( \sum_{j=1}^{\infty} \frac{\sin j\theta}{j} \left( \frac{\sin(1+n+j)\theta_s}{1+n+j} - \frac{\sin(1+n-j)\theta_s}{1+n-j} - \frac{\sin(1-n+j)\theta_s}{1-n+j} + \frac{\sin(1-n-j)\theta_s}{1-n-j} \right) \right) \right] \right\} \\
& - U f(\theta) \delta_1 \left\{ i\omega \cos n\theta [B_m + C_m] + 2 \frac{U}{\pi a} C_m \left[ n \sum_{j=1}^{\infty} F(j,n) \cos j\theta \right. \right. \\
& - \left. \left. \frac{1}{2} \left( \sum_{j=1}^{\infty} \cos j\theta \left( \frac{\sin(1+n+j)\theta_s}{1+n+j} - \frac{\sin(1+n-j)\theta_s}{1+n-j} - \frac{\sin(1-n+j)\theta_s}{1-n+j} + \frac{\sin(1-n-j)\theta_s}{1-n-j} \right) \right) \right] \right\} \\
& - 2 \frac{U^2}{a} C_m f(\theta) \sin\theta \sin n\theta \delta_2 - \frac{HU^2}{2a} e^{-i\psi} C_m \sin n\theta \delta_3 \left. \right\} \psi_m \\
& + \rho e^{i\omega t} i\omega \{D(0) - E(0)\} . \tag{F.10}
\end{aligned}$$

Substituting equations (F.3) and (F.10) into the shell equations, and using a variant of Galerkin's method (as in Chapter 6) yields the following set of equations:

$$\begin{aligned}
\sum_{m=1}^M \left\{ \{ a^2 g_{km} - \frac{1}{2} n^2 (1-\nu)(1+\kappa) f_{km} + \gamma \omega^2 f_{km} \} A_m + \{ -\frac{1}{2} a n (1+\nu) f_{km} \} B_m \right. \\
\left. + \{ a \nu f_{km} - a^3 \kappa g_{km} - \frac{1}{2} a n^2 \kappa (1-\nu) f_{km} \} C_m \right\} = 0 , \tag{F.11}
\end{aligned}$$

$$\sum_{m=1}^M \left\{ \{ \frac{1}{2} a n (1+\nu) c_{km} \} A_m + \{ -n^2 a_{km} + \frac{1}{2} a^2 (1+3\kappa)(1-\nu) c_{km} + \gamma \omega^2 a_{km} \} B_m \right.$$

continued

$$+ \{n a_{km} - \frac{1}{2} a^2 n \kappa (3-\nu) c_{km}\} c_m \} = 0, \quad (F.12)$$

$$\sum_{m=1}^M \left\{ \{-a \nu c_{km} + \frac{1}{2} a n^2 \kappa (1-\nu) c_{km} + a^3 \kappa e_{km}\} A_m + \{n a_{km} - \frac{1}{2} a^2 n \kappa (3-\nu) c_{km}\} B_m \right. \\ \left. \{-a_{km} - a^4 \kappa e_{km} + 2 a^2 n^2 \kappa c_{km} - (n^2-1)^2 \kappa a_{km} + \gamma \omega^2 a_{km} + \frac{\rho \gamma}{\rho_s h} \frac{2 \omega^2 a}{n} a_{km}\} c_m \right. \\ \left. + \frac{\rho \gamma}{\rho_s h} \frac{2U}{\pi} \omega_i \left\{ [-F(n,n) + \frac{1}{2} \left( \frac{\sin(1+2n)\theta_s}{n(1+2n)} - 2 \frac{\sin \theta_s}{n} + \frac{\sin(1-2n)\theta_s}{n(1-2n)} \right) \right\} a_{km} c_m \right. \\ \left. - F(n,n) a_{km} [B_m + C_m] \right\} - \frac{\rho \gamma}{\rho_s h} \left( \frac{4U^2}{\pi^2 a} \right) \left\{ n \sum_{j=1}^{\infty} F(n,j) F(j,n) \right. \\ \left. - \frac{1}{2} \left( \sum_{j=1}^{\infty} F(n,j) \left( \frac{\sin(1+n+j)\theta_s}{1+n+j} - \frac{\sin(1+n-j)\theta_s}{1+n-j} - \frac{\sin(1-n+j)\theta_s}{1-n+j} + \frac{\sin(1-n-j)\theta_s}{1-n-j} \right) \right) \right. \\ \left. + \pi F'(1,n,n) + \frac{\pi}{8} \text{He}^{-i\psi} [\pi - \theta_s + \frac{1}{2n} \sin 2n\theta_s] \right\} a_{km} c_m \Bigg\} = 0, \quad (F.13)$$

where

$$F(n,j) = \int_0^{\theta_s} f(\theta) \sin n\theta \cos j\theta d\theta - \int_{\theta_s}^{\pi} f(\theta_s) \sin n\theta \cos j\theta d\theta,$$

$$F(j,n) = \int_0^{\theta_s} f(\theta) \sin j\theta \cos n\theta d\theta - \int_{\theta_s}^{\pi} f(\theta_s) \sin j\theta \cos n\theta d\theta,$$

and

$$F'(1,n,n) = \int_0^{\theta_s} f(\theta) \sin\theta \sin n\theta \sin n\theta d\theta.$$

Let now

$$C_1^i = 2 \frac{\rho a}{\pi} ,$$

$$C_2^i = -4 \frac{\rho U}{\pi} F(n, n) ,$$

$$C_3^i = 4 \frac{\rho U^2}{\pi a} n \sum_{j=1}^{\infty} F(n, j) F(j, n) ,$$

$$C_4^i = \frac{\rho U}{\pi} \left[ \frac{\sin(1+2n)\theta_s}{n(1+2n)} - 2 \frac{\sin \theta_s}{n} + \frac{\sin(1-2n)\theta_s}{n(1-2n)} \right] ,$$

$$C_5^i = 2 \frac{\rho U^2}{\pi a} \sum_{j=1}^{\infty} F(n, j) \left[ \frac{\sin(1+n+j)\theta_s}{1+n+j} - \frac{\sin(1+n-j)\theta_s}{1+n-j} - \frac{\sin(1-n+j)\theta_s}{1-n+j} + \frac{\sin(1-n-j)\theta_s}{1-n-j} \right] ,$$

$$C_6^i = 4 \frac{\rho U^2}{\pi a} F'(1, n, n) ,$$

$$C_7^i = \frac{\rho U^2}{2\pi a} \text{He}^{-i\psi} \left[ \pi - \theta_s + \frac{1}{2n} \sin 2n\theta_s \right] .$$

Hence, the equations of motion (F.11)-(F.13) may be written in the following matrix form

$$-\omega^2 \begin{bmatrix} -\gamma f_{km} & 0 & 0 \\ 0 & -\gamma a_{km} & 0 \\ 0 & 0 & -\gamma a_{km} - \frac{\gamma}{\rho_s h} C_7^i a_{km} \end{bmatrix} \begin{bmatrix} A_m \\ B_m \\ C_m \end{bmatrix} +$$

continued



$$\frac{1}{2} \begin{bmatrix} 0 & 0 & 0 \\ 0 & 0 & 0 \\ 0 & \frac{\gamma}{\rho_s h} \frac{C_2'}{2} a_{km} & \frac{\gamma}{\rho_s h} (C_2' + C_4') a_{km} \end{bmatrix} \begin{bmatrix} A_m \\ B_m \\ C_m \end{bmatrix} +$$

$$\begin{bmatrix} a^2 g_{km} & -\frac{1}{2} a n (1+\nu) f_{km} & a \nu f_{km} - a^3 \kappa g_{km} \\ -\frac{1}{2} n^2 (1-\nu)(1+\kappa) f_{km} & & -\frac{1}{2} a n^2 \kappa (1-\nu) f_{km} \\ \frac{1}{2} a n (1+\nu) c_{km} & -n^2 a_{km} & n a_{km} \\ & + \frac{1}{2} a^2 (1+3\kappa)(1-\nu) c_{km} & -\frac{1}{2} a^2 n \kappa (3-\nu) c_{km} \\ -a \nu c_{km} & n a_{km} & -a_{km} - a^4 \kappa e_{km} + 2a^2 n^2 \kappa c_{km} \\ + \frac{1}{2} a n^2 \kappa (1-\nu) c_{km} & -\frac{1}{2} a^2 n \kappa (3-\nu) c_{km} & - (n^2 - 1)^2 \kappa a_{km} \\ + a^3 \kappa e_{km} & & - \frac{\gamma}{\rho_s h} [C_3' - C_5' + C_6' + C_7'] a_{km} \end{bmatrix} \begin{bmatrix} A_m \\ B_m \\ C_m \end{bmatrix}$$

= {0}

(F.14)

APPENDIX GLISTING OF THE COMPUTER PROGRAMSProgram I: AEROTERM

This program calculates the values of the aerodynamic terms

$$F(n,n), \sum_{j=1}^{\infty} F(n,j)F(j,n),$$

$$[\sin(1+2n)\theta_s/n(1+2n) + 2 \sin\theta_s/n + \sin(1-2n)\theta_s/n(1-2n)],$$

$$\sum_{j=1}^{\infty} \left[ \frac{\sin(1+n+j)\theta_s}{1+n+j} + \frac{\sin(1+n-j)\theta_s}{1+n-j} + \frac{\sin(1-n+j)\theta_s}{1-n+j} + \frac{\sin(1-n-j)\theta_s}{1-n-j} \right] F(j,n),$$

$$F(1,n,n) \text{ and } [\pi - \theta_s - \frac{1}{2n} \sin 2n\theta_s].$$

As defined in Chapter 6

$$F(n,j) = \int_0^{\theta_s} f(\theta) \sin n\theta \cos j\theta \, d\theta - \int_{\theta_s}^{\pi} f(\theta_s) \sin n\theta \cos j\theta \, d\theta,$$

$$F(j,n) = \int_0^{\theta_s} f(\theta) \sin j\theta \cos n\theta \, d\theta - \int_{\theta_s}^{\pi} f(\theta_s) \sin j\theta \cos n\theta \, d\theta,$$

$$F(1,n,n) = \int_0^{\theta_s} f(\theta) \sin\theta \cos n\theta \cos n\theta \, d\theta.$$

\*BATCH WATFIV ME15102 SYANG  
\$WATFIV ,TIME=60,PAGES=20

```

C-----*
C
C   TO EVALUATE THE AERODYNAMICS TERMS
C   COMMENT: F(N,N) FOR C2 & SUM F(N,U)*F2(U,N) FOR C3
C           --- WITH CONSTANT BACK FLOW ---
C           I.E. F(THETA-S)=CONSTANT / DEL2=1
C           : CONSTANTS FOR C4,C5 & C6
C           --- WITH MOVING BOUNDARY CONDITION ---
C           I.E. R=A+W*
C           : PI-(THETA-S - SIN(2N/THETA-S))/2N FOR C7
C           --- WITH BASE PRESSURE VARIATIONS ---
C           I.E. DP=B DIW* A * (W* A) * EXP(-I PHI)
C   FILE NAME=AEROTERM
C-----*

```

```

C   IMPLICIT REAL*8 A-H,O-Z)
C   DIMENSION B(8),C(9),BS(9)
C   COMMON C BS,FS,P:
C   DEL2=.0
C   PI=DARCS .DO.
C   ANGLE=85*PI/180
C-----*
C   INPUT COEFF OF FUNCTION F(THETA)
C   ANGLE OF BS : SEPERATION ANGLE
C-----*
C   READ (5,*) (C(I),I=1,5)
C   READ (5,*) (C(I),I=6,9)
C   PRINT 7
7   FORMAT(' ',2X,'THE COEFFICIENTS FOR THE POLYNOMIAL F(THETA)',
S//)
C   DO 10 I=1,9
C     BS(I)=ANGLE**I
C     K=I-1
C     PRINT ' ',K,C(I)
11   FORMAT(' ',12X,'C(',I1,')=' ,D20.12)
10  CONTINUE
C   F1=C(1)+C(2)*BS(1)+C(3)*BS(2)+C(4)*BS(3)+C(5)*BS(4)+C(6)*BS(5)
C   F2=C(7)+C(8)*BS(6)+C(9)*BS(7)+C(9)*BS(8)
C   FS=F1+F2
C   PRINT 12 FS
12  FORMAT(' ',2X,'F(THETA-S) =',F10.5)
C   DO 300 N=2,3
C     PRINT 5,N
5     FORMAT(' ',10X,'N=',I3)
C
C   EVALUATION OF F(N,N) FOR C2
C
C     RN=N
C     TWON=N*2
C     CON=(DCOS(TWON*PI)-DCOS(TWON*BS(1)))*FS/4/N
C     FNN=FSIN(TWON)*0.5+CON*DEL2
C     PRINT 1,FNN
1     FORMAT(' ',2X,'F(N,N) FOR C2 =',F10.5)
C
C   EVALUATION OF SUMMATION F(N,U)*F(U,N) FOR C3
C

```

```

SUM=0.0
U=1.
N1=N-1
DO 56 J=1,N1
  X1=0.50*(FSIN(N+U)+FSIN(N-U))+CONST(RN,U)*DEL2
  X2=0.50*(FSIN(U+N)+FSIN(U-N))+CONST(U,RN)*DEL2
  X=X1*X2
  SUM=SUM+X
  4      FORMAT(' ',//,12X,'NO. OF TERMS=',F6.2,5X,'SUMMATION OF C3 =',
S          F20.5)
56      U=U+1.
C
  X1=0.50*FSIN(TWON)+CON*DEL2
  X2=0.50*FSIN(TWON)+CON*DEL2
  X=X1*X2
  SUM=SUM+X
  U=U+1.
C
55  CONTINUE
  X1=0.50*(FSIN(N+U)+FSIN(N-U))+CONST(RN,U)*DEL2
  X2=0.50*(FSIN(U+N)+FSIN(U-N))+CONST(U,RN)*DEL2
  X=X1*X2
  OLDSUM=SUM
  SUM=SUM+X
  TOL=SUM-OLDSUM
  IF(DABS(TOL).LE.'.0D-05) GOTO 65
  U=U+1
  IF (U.GE.300) GOTO 66
  GOTO 55
65  PRINT 4,U,SUM
  GOTO 100
66  PRINT 67
67  FORMAT(' ',//,5X,'THE SERIES DOES NOT CONVERGE')
  PRINT 4,U,SUM
100  CONTINUE
C
C  EVALUATION OF  $\frac{\sin((1+2N)(\theta-S))/N(1+2N) + 2*\sin(\theta-S)/N + \sin((1-2N)(\theta-S))/N(1-2N)}{\sin((1+N+U)*\theta)/((1+N+U)) + \sin((1+N-U)*\theta)/((1+N-U)) + \sin((1-N+U)*\theta)/((1-N+U)) + \sin((1-N-U)*\theta)/((1-N-U))}$  FOR C4
C
  CFOR1=DSIN((1+TWON)*BS(1))/N(1+TWON)+2*DSIN(BS(1))/N
  CFOR2=DSIN((1-TWON)*BS(1))/N(1-TWON)
  CFOR=CFOR1+CFOR2
  PRINT 3 CFOR
  3  FORMAT(' ',12X,'CONSTANTS FOR C4 =',F10.5)
C
C  EVALUATION OF  $\frac{\sin((1+N+U)*\theta)/((1+N+U)) + \sin((1+N-U)*\theta)/((1+N-U)) + \sin((1-N+U)*\theta)/((1-N+U)) + \sin((1-N-U)*\theta)/((1-N-U))}{F(U,N)}$  FOR C5
C
  SUM=0.0
  U=1.
  DO 106 J=1,N1
    Y1=DSIN((1+N+U)*BS(1))/((1+N+U))+DSIN((1+N-U)*BS(1))/((1+N-U))
    IF(J.EQ.N1) GOTO 98
    Y2=DSIN((1-N+U)*BS(1))/((1-N+U))+DSIN((1-N-U)*BS(1))/((1-N-U))
    GOTO 99
98    Y2=BS(1)+DSIN((1-N-U)*BS(1))/((1-N-U))
99    Y3=0.50*(FSIN(U+N)+FSIN(U-N))+CONST(U,RN)*DEL2

```

```

      Y=(Y1+Y2)*Y3
      SUM=SUM+Y
      U=U+1.
106 C
      Y1=DSIN((1+N+U)*BS(1))/(1+N+U)+DSIN((1+N-U)*BS(1))/(1+N-U)
      Y2=DSIN((1-N+U)*BS(1))/(1-N+U)+DSIN((1-N-U)*BS(1))/(1-N-U)
      Y3=0.50*(FSIN(TWON))+CON*DEL2
      Y=(Y1+Y2)*Y3
      SUM=SUM+Y
      U=U+1.
C
      Y1=DSIN((1+N+U)*BS(1))/(1+N+U)+BS(1)*
      Y2=DSIN((1-N+U)*BS(1))/(1-N+U)+DSIN((1-N-U)*BS(1))/(1-N-U)
      Y3=0.50*(FSIN(U+N)+FSIN(U-N))+CONST(U,RN)*DEL2
      Y=(Y1+Y2)*Y3
      SUM=SUM+Y
      U=U+1.
C
105 CONTINUE
      Y1=DSIN((1+N+U)*BS(1))/(1+N+U)+DSIN((1+N-U)*BS(1))/(1+N-U)
      Y2=DSIN((1-N+U)*BS(1))/(1-N+U)+DSIN((1-N-U)*BS(1))/(1-N-U)
      Y3=0.50*(FSIN(U+N)+FSIN(U-N))+CONST(U,RN)*DEL2
      Y=(Y1+Y2)*Y3
      OLDSUM=SUM
      SUM=SUM+Y
      TOL=SUM-OLDSUM
      IF(DABS(TOL).LE.1.0D-05) GOTO 115
      U=U+1
      IF(U.GE.300) GOTO 116
      GOTO 105
115 PRINT 120,U,SUM
120 FORMAT(' ',//,12X,'NO. OF TERMS=',F6.2,5X,'SUMMATION OF C5 =',
      $      F20.5)
      GOTO 150
116 PRINT 67
      PRINT 120,U,SUM
150 CONTINUE
C
C EVALUATION OF FINN FOR C6
C
      FINN=0.5*(FSIN(1.0D0)+0.5*FSIN(1.0+TWON)+0.5*FSIN(1.0-TWON))
      PRINT 175,FINN
175 FORMAT(' ',//,12X,'F(1,N,N) FOR C6 =',F10.5)
C
C EVALUATION OF PI-(THETA-S)-SIN(2N(THETA-S))/2N
C
      CSEVEN=PI-BS(1)-DSIN(2*N*BS(1))/2/N
      PRINT 180,CSEVEN
180 FORMAT(' ',//,12X,'CONSTANT FOR C7 =',F10.5)
300 CONTINUE
      PRINT 101
101 FORMAT(' ')
      STOP
      END
C-----*
C *
C FUNCTION SUB-PROGRAMME TO EVALUATE THE INTEGRAL *
C FROM 0 TO THETA-S SIN(A*THETA)*F(THETA) *

```

```

C   AND FROM THEAT-S TO PI :-
C   THETA-S*F(BS(1))*SIN(N*THETA)*COS(U*THETA)
C
C-----
      REAL FUNCTION FSIN*8(A)
      IMPLICIT REAL*8(A-H,O-Z)
      DIMENSION B(8),C(9),BS(9)
      COMMON C,BS,FS,PI
      APhi=A*BS(1)
      A2=A**2
      A3=A**3
      A4=A**4
      A5=A**5
      A6=A**6
      A7=A**7
      A8=A**8
      A9=A**9
      SIN21=(C(2)+2*C(3)*BS(1)+3*C(4)*BS(2)+4*C(5)*BS(3))/A2
      SIN22=(5*C(6)*BS(4)+6*C(7)*BS(5)+7*C(8)*BS(6)+8*C(9)*BS(7))/A2
      SIN41=-(6*C(4)+24*C(5)*BS(1)+60*C(6)*BS(2))/A4
      SIN42=-(120*C(7)*BS(3)+210*C(8)*BS(4)+336*C(9)*BS(5))/A4
      SIN6=(120*C(6)+720*C(7)*BS(1)+2520*C(8)*BS(2)+6720*C(9)*BS(3))/A6
      SIN8=-(5040*C(8)+40320*C(9)*BS(1))/A8
      SIN=SIN21+SIN22+SIN41+SIN42+SIN6+SIN8
      COS11=-(C(1)+C(2)*BS(1)+C(3)*BS(2)+C(4)*BS(3)+C(5)*BS(4))/A
      COS12=-(C(6)*BS(5)+C(7)*BS(6)+C(8)*BS(7)+C(9)*BS(8))/A
      COS31=(2*C(3)+6*C(4)*BS(1)+12*C(5)*BS(2)+20*C(6)*BS(3))/A3
      COS32=(30*C(7)*BS(4)+42*C(8)*BS(5)+56*C(9)*BS(6))/A3
      COS51=-(24*C(5)+120*C(6)*BS(1)+360*C(7)*BS(2)+840*C(8)*BS(3))/A5
      COS52=-(1680*C(9)*BS(4))/A5
      COS7=(720*C(7)+5040*C(8)*BS(1)+20160*C(9)*BS(2))/A7
      COS=COS11+COS12+COS31+COS32+COS51+COS52+COS7-40320*C(9)/A9
      CONST=C(1)/A-2*C(3)/A3+24*C(5)/A5-720*C(7)/A7+40320*C(9)/A9
      FSIN=DSIN(APhi)*SIN+DCOS(APhi)*COS+CONST
      RETURN
      END
      REAL FUNCTION CONST*8(RI,RJ)
      IMPLICIT REAL*8(A-H,O-Z)
      DIMENSION B(8),C(9),BS(9)
      COMMON C,BS,FS,PI
      C1=(DCOS((RI+RJ)*PI)-DCOS((RI+RJ)*BS(1)))/(RI+RJ)
      C2=(DCOS((RI-RJ)*PI)-DCOS((RI-RJ)*BS(1)))/(RI-RJ)
      CONST=FS*(C1+C2)/2
      RETURN
      END
$DATA
0.DO,1.6073D0,0.5700D0,-0.9394D0,0.1714D0
0.DO,0.DO,0.DO,0.DO
$

```

## THE COEFFICIENTS FOR THE POLYNOMIAL P(THETA)

C(0)= 0.000000000000D 00  
 C(1)= 0.160730000000D 01  
 C(2)= 0.570000000000D 00  
 C(3)= -0.939400000000D 00  
 C(4)= 0.171400000000D 00  
 C(5)= 0.000000000000D 00  
 C(6)= 0.000000000000D 00  
 C(7)= 0.000000000000D 00  
 C(8)= 0.000000000000D 00

F(THETA-S) = 1.40201

N= 2

F(N,N) FOR C2 = -0.17526

NO. OF TERMS= 48.00      SUMMATION OF C3 = -1.62763

CONSTANTS FOR C4 = 0.92584

NO. OF TERMS= 32.00      SUMMATION OF C5 = 0.39354

F(1,N,N) FOR C6 = 0.47440

CONSTANT FOR C7 = 1.74357

N= 3

F(N,N) FOR C2 = 0.31774

NO. OF TERMS= 72.00      SUMMATION OF C3 = -3.18603

CONSTANTS FOR C4 = 0.68554

NO. OF TERMS= 24.00      SUMMATION OF C5 = 0.27018

F(1,N,N) FOR C6 = 0.63744

CONSTANT FOR C7 = 1.57473



Program II: ACOM3DFILTER

This program calculates the eigenvalues and aerodynamic damping of the theory presented in Chapter 6, for different flow velocities and different circumferential mode shapes of a clamped-clamped shell.

```
//ME15102 JOB (ME15,102,008,0050,0000,20,,1),'SYANG'
//STEP1 EXEC FORTRAN
//FORT.SYSIN DD *
```

```
C-----*
C
C FLUTTER ANALYSIS OF 3D (CL-CL,L=21") SHELL IN CROSS FLOW
C VIBRATING WITH AN ANTINODE FACING THE FREE STREAM
C COMMENT: CASE 1: EFFECT OF (V+(OMEGA) CROSS (R)) DOT GRAD(PHI)
C IN BERNOULLI EQUATION
C I.E. -UF(THETA) DV/DT |: DEL1=1
C PLUS ---
C CASE 2: EFFECT OF CONSTANT BACK FLOW IN THE WAKE
C I.E. F(THETA-S)=CONST. FOR (THETA).GT.(THETA-S)
C |: DEL2=1
C PLUS ---
C CASE 3: EFFECT OF MOVING BOUNDARY CONDITION
C I.E. R=A+W* |: DEL3=1
C PLUS --
C CASE 4: EFFECT OF BASE PRESSURE VARIATIONS
C I.E. DP-B/D(W*A) * (W/A) * EXP(-I PHI)
C WHERE PHI=PHASE LAG |:DEL4=1
C FOR N=2, PHI=270; N=3, PHI=270
C FILE NAME : ACOM3DFILTER
C-----*
```

```
C
C IMPLICIT REAL*8 (A-H,O-Z)
C DIMENSION D(6)
C COMPLEX*16 RA(3,3),RB(3,3),RC(3,3),Y(6,6),YY(6,6)
C COMPLEX*16 WK(6,12),V(6,6),EIGA(6),EIGB(6),IMAG,C7
C
C PROPERTIES INPUT
C READ(5,*) A,TH,RHS,POI,YUN,RHO,RL
C
C PRINT 1
C 1 FORMAT('1',///,8X,'PROPERTIES OF THE SHELL')
C PRINT 2,A
C 2 FORMAT(' ',/,5X,'MEAN RADIUS =',F10.5,' M')
C PRINT 3,TH
C 3 FORMAT(' ',4X,'THICKNESS =',F10.5,' M')
C PRINT 4,POI
C 4 FORMAT(' ',4X,'POISSONS RATIO =',F10.3)
C PRINT 5,YUN
C 5 FORMAT(' ',4X,'YOUNGS MODULUS =',D10.3,' N/M**2')
C PRINT 9,RHS
C 9 FORMAT(' ',4X,'DENSITY =',F10.1,' KG/M**3')
C PRINT 8,RHO
C 8 FORMAT(' ',4X,'DENSITY OF AIR =', F10.4,' KG/M**3')
C PRINT 11,RL
C 11 FORMAT(' ',4X,'LENGTH =',F10.5,' M')
C PRINT 12
C 12 FORMAT(' ',4X,'NO. OF COMPARISON FUNCTION = 1',/)
C
C DEFINE THE CONSTANTS
C
C DEL1=1.0
C DEL3=1.0
C DEL4=1.0
C IMAG=(0.0,1.0)
```

BETAJ=4.73004074/RL  
 ALFAJ=0.982502215  
 AJJ=RL  
 CJJ=ALFAJ\*BETAJ\*(2.-ALFAJ\*BETAJ\*RL)  
 EJJ=BETAJ\*\*4\*RL  
 FJJ=-CJJ  
 GJJ=-EJJ

C

PI=DARCOS(-1.0D0)  
 RK=(TH/A)\*\*2/12.0  
 GAMA=RHS\*A\*\*2\*(1.0-POI\*\*2)/YUN  
 Z=(1.D0-POI)/2.D0

C

100

CONTINUE

READ(5,78) N

78

FORMAT(I3)

IF(N.EQ.0) GOTO 999

PRINT 77,N

77

FORMAT(' ',///,8X,'MODE NO. N = ',I5)

IF(N.EQ.2) GO TO 51

IF(N.EQ.3) GO TO 52

IF(N.EQ.4) GO TO 53

IF(N.EQ.5) GO TO 54

C

C

CONSTANTS FROM PROGRAME FILE: AEROTERM

C

51

G2=-0.17526

G3=-1.62763

G4=0.92584

G5=0.39354

G6=0.47440

G7=1.74357

H=3.7879

PHI=270\*PI/180

GO TO 56

52

G2=0.31774

G3=-3.18603

G4=0.68554

G5=0.27018

G6=0.63744

G7=1.57473

H=-2.3776

PHI=270\*PI/180

GO TO 56

53

G2=0.0

G3=0.0

G4=0.0

G5=0.0

G6=0.0

G7=0.0

H=0.0

PHI=0.0

GO TO 56

54

G2=0.0

G3=0.0

G4=0.0

G5=0.0

G6=0.0

```

G7=0.0
H=0.0
PHI=0.0
56 PRINT 32,G2
32 FORMAT(' ',/,5X,'F(N,N) FOR C2 : ',F10.5)
PRINT 33,G3
33 FORMAT(' ',4X,'SUM OF F(N,J)*F(J,N) FOR C3 : ',F10.5)
PRINT 34,G4
34 FORMAT(' ',4X,'CONSTANT FOR C4 : ',F10.5)
PRINT 35,G5
35 FORMAT(' ',4X,'SUM OF SIN (N,J)*F(J,N) FOR C5 : ',F10.5)
PRINT 36,G6
36 FORMAT(' ',4X,'F(1,N,N) FOR C6 : ',F10.5)
PRINT 38,G7
38 FORMAT(' ',4X,'PI-(THETA-S)-SIN(2N(THETA-S)/2N FOR C7 : ',
$ F10.5)
PRINT 39,H,PHI
39 FORMAT(' ',4X,'H FOR BASE PRESSURE VARIATION : ',F10.5,/,
$ 16X,'WITH PHASE LAG PHI : ',F5.2,' RAD.')
C
C INITIALIZE THE MATRICES RA,RB,RC,Y,YY
C
DO 24 I=1,3
DO 24 J=1,3
RA(I,J)=(0.0,0.0)
RB(I,J)=(0.0,0.0)
RC(I,J)=(0.0,0.0)
24 CONTINUE
DO 29 I=1,6
DO 29 J=1,6
Y(I,J)=(0.0,0.0)
YY(I,J)=(0.0,0.0)
29 CONTINUE
C
C CALCULATE MATRICES RA,RB,RC
C
RA(1,1)=-GAMA*FJJ
RC(1,1)=A**2*GJJ-Z*N**2*FJJ-RK*Z*N**2*FJJ
RC(1,2)=A*(1.+POI)/2.*N*FJJ
RC(1,3)=POI*A*FJJ-RK*A**3*GJJ-RK*Z*N**2*FJJ*A
RC(2,1)=-A*(1.+POI)/2.*N*CJJ
RA(2,2)=-GAMA*AJJ
RC(2,2)=-N**2*AJJ+A**2*Z*CJJ+3.*RK*Z*A**2*CJJ
RC(2,3)=-N*AJJ+(3.-POI)/2.*RK*A**2*N*CJJ
RC(3,1)=-POI*A*CJJ+RK*A*Z*N**2*CJJ+RK*A**3*EJJ
RC(3,2)=-N*AJJ+RK*(3.-POI)/2.*A**2*N*CJJ
C
U=0.0
DO 58 KKK=1,16
10 FORMAT(' ',///,5X,'FREESTREAM VELOCITY =',F5.2,' M/S',4X,
$ 'PERFORMANCE INDEX =',F6.3,/)
C
C1=2.0*RHO*A/N'
C2=4.0*RHO*U*G2/PI
C3=4.0*RHO*U*U*N*G3/PI/PI/A
C4=RHO*U*G4/PI*DEL3
C5=2.0*RHO*U*U*G5/PI/PI/A*DEL3
C6=4*RHO*U*U*G6/PI/A*DEL3

```

```

C       C7=RHO*U*U*H*(DCOS(PHI)-IMAG*DSIN(PHI))*G7/2.0/PI/A*DEL4

      RA(3,3)=-GAMA*AJJ-C1*GAMA*AJJ/RHS/TH
      RB(3,2)=-GAMA*C2*AJJ/2.0/RHS/TH*DEL1
      RB(3,3)=GAMA*(C2-C4)*AJJ/RHS/TH
      RC(3,3)=-AJJ-RK*A**4*EJJ+2.*A**2*RK*N**2*CJJ-RK*N**4*AJJ
      $      +2.*RK*N**2*AJJ-RK*AJJ-(C3-C5+C6+C7)*GAMA*AJJ/RHS/TH
C  TRANSFER TO MATRICES Y & YY
      DO 49 I=1,3
        K=I+3
        DO 49 J=1,3
          KK=J+3
          Y(I,KK)=RA(I,J)
          Y(K,J)=RA(I,J)
          Y(K,KK)=RB(I,J)
          YY(I,J)=RA(I,J)
          YY(K,KK)=-RC(I,J)
49      CONTINUE
C
C  FIND THE EIGENVALUES
C
      CALL EIGZC(YY,6,Y,6,6,2,EIGA,EIGB,V,6,WK,INFER,IER)
      PER=DREAL(WK(1,1))
      PRINT 10,U,PER
      DO 94 I=1,6
        EIGA(I)=EIGA(I)/EIGB(I)/2.0/PI
        EIGA(I)=-IMAG*EIGA(I)
        REAL=DREAL(EIGA(I))
        IF(REAL.EQ.0.0) GOTO 94
        D(I)=2.*PI*DIMAG(EIGA(I))/DABS(REAL)
        PRINT 6,EIGA(I),D(I)
94      CONTINUE
6      FORMAT(' ',6X,2F15.4,8X,'DAMP.=' ,F8.4)
      U=U+2.
58      CONTINUE
C
      GOTO 100
999      CONTINUE
      STOP
      END
//GO.SYSIN DD *
0.0381,0.00051,1290,0.4,.28D10,1.204,.53340
2
3
0
//

```

# PROPERTIES OF THE SHELL

MEAN RADIUS = 0.03810 M  
 THICKNESS = 0.00051 M  
 POISSONS RATIO = 0.400  
 YOUNGS MODULUS = 0.280D+10 N/M\*\*2  
 DENSITY = 1290.0 KG/M\*\*3  
 DENSITY OF AIR = 1.2040 KG/M\*\*3  
 LENGTH = 0.53340 M  
 NO. OF COMPARISON FUNCTION = 1

MODE NO. N = 2

F(N,N) FOR C2 : -0.17526  
 SUM OF F(N,J)\*F(J,N) FOR C3 : -1.62763  
 CONSTANT FOR C4 : 0.92584  
 SUM OF SIN (N,J)\*F(J,N) FOR C5 : 0.39354  
 F(1,N,N) FOR C6 : 0.47440  
 PI-(THETA-S)-SIN(2N(THETA-S)/2N FOR C7 : 1.74357  
 H FOR BASE PRESSURE VARIATION : 3.78790  
 WITH PHASE LAG PHI : 4.71 RAD.

FREESTREAM VELOCITY = 0.0 M/S PERFORMANCE INDEX = 0.053

14993.8765	-0.0000	DAMP. = -0.0000
7873.4100	0.0000	DAMP. = 0.0000
-14993.8765	0.0000	DAMP. = 0.0000
-7873.4100	-0.0000	DAMP. = -0.0000
166.1963	0.0	DAMP. = 0.0
-166.1963	0.0	DAMP. = 0.0

FREESTREAM VELOCITY = 2.00 M/S PERFORMANCE INDEX = 0.091

-14993.8765	0.0140	DAMP. = 0.0000
-7873.4100	0.0008	DAMP. = 0.0000
14993.8765	0.0140	DAMP. = 0.0000
7873.4100	0.0008	DAMP. = 0.0000
-166.1875	0.1145	DAMP. = 0.0043
166.1875	0.1378	DAMP. = 0.0052

FREESTREAM VELOCITY = 4.00 M/S PERFORMANCE INDEX = 0.975

-14993.8764	0.0279	DAMP. = 0.0000
-7873.4100	0.0017	DAMP. = 0.0000
14993.8764	0.0281	DAMP. = 0.0000
7873.4100	0.0017	DAMP. = 0.0000
-166.1610	0.2058	DAMP. = 0.0078

166.1610

0.2988

DAMP. = 0.0113

FREESTREAM VELOCITY = 6.00 M/S

PERFORMANCE INDEX = 0.679

-14993.8763	0.0417
-7873.4100	0.0025
14993.8763	0.0423
7873.4100	0.0026
-166.1168	0.2739
166.1168	0.4830

DAMP. = 0.0000
DAMP. = 0.0000
DAMP. = 0.0000
DAMP. = 0.0000
DAMP. = 0.0104
DAMP. = 0.0183

FREESTREAM VELOCITY = 8.00 M/S

PERFORMANCE INDEX = 0.971

-14993.8761	0.0555
-7873.4100	0.0033
14993.8761	0.0565
7873.4100	0.0034
-166.0550	0.3186
166.0550	0.6906

DAMP. = 0.0000
DAMP. = 0.0000
DAMP. = 0.0000
DAMP. = 0.0000
DAMP. = 0.0121
DAMP. = 0.0261

FREESTREAM VELOCITY = 10.00 M/S

PERFORMANCE INDEX = 1.224

-14993.8759	0.0693
-7873.4100	0.0042
14993.8759	0.0708
7873.4100	0.0043
-165.9756	0.3400
165.9756	0.9215

DAMP. = 0.0000
DAMP. = 0.0000
DAMP. = 0.0000
DAMP. = 0.0000
DAMP. = 0.0129
DAMP. = 0.0349



FREESTREAM VELOCITY = 30.00 M/S

PERFORMANCE INDEX = 0.470

14993.8714	0.2167
7873.4096	0.0132
-14993.8714	0.2034
-7873.4096	0.0122
164.2183	4.5370
-164.2183	-0.7525

DAMP. = 0.0001
DAMP. = 0.0000
DAMP. = 0.0001
DAMP. = 0.0000
DAMP. = 0.1736
DAMP. = -0.0288

MODE NO. N = 3

$P(N,N)$  FOR C2 : 0.31774  
 $\text{SUM OF } P(N,J) * F(J,N)$  FOR C3 : -3.18603  
 CONSTANT FOR C4 : 0.68554  
 $\text{SUM OF } \sin(N,J) * F(J,N)$  FOR C5 : 0.27018  
 $P(1,N,N)$  FOR C6 : 0.63744  
 $\pi - (\text{THETA} - S - \sin(2N(\text{THETA} - S)) / 2N)$  FOR C7 : 1.57473  
 H FOR BASE PRESSURE VARIATION : -2.37760  
 WITH PHASE LAG PHI : 4.71 RAD.

FREESTREAM VELOCITY = 0.0 M/S PERFORMANCE INDEX = 1.600

21247.4735	0.0000	DAMP. = 0.0000
11375.1295	0.0000	DAMP. = 0.0000
-21247.4735	-0.0000	DAMP. = -0.0000
-11375.1295	-0.0000	DAMP. = -0.0000
208.1264	0.0	DAMP. = 0.0
-208.1264	0.0	DAMP. = 0.0

FREESTREAM VELOCITY = 2.00 M/S PERFORMANCE INDEX = 0.727

-21247.4735	0.0119	DAMP. = 0.0000
-11375.1295	0.0001	DAMP. = 0.0000
21247.4735	0.0119	DAMP. = 0.0000
11375.1295	0.0001	DAMP. = 0.0000
-208.0950	-0.0578	DAMP. = -0.0017
208.0950	-0.0698	DAMP. = -0.0021



FREESTREAM VELOCITY = 30.00 M/S PERFORMANCE INDEX = 0.068

21247.4663	0.1772	DAMP. = 0.0001
11375.1292	0.0008	DAMP. = 0.0000
-21247.4663	0.1799	DAMP. = 0.0001
-11375.1292	0.0009	DAMP. = 0.0000
200.9289	-2.3586	DAMP. = -0.0738
-200.9289	0.4438	DAMP. = 0.0139



Program III: APHASE3

This program calculates the phase between shell deformation and the induced pressure, for  $\theta = 0^\circ$  to  $85^\circ$  at different flow velocities.

The phase angle  $\psi$  is as defined in Appendix E (equations (E.12) and (E.18)).

\*BATCH WATFIV ME15102 SYANG

\$WATFIV ,TIME=60,PAGES=20

```

C-----*
C
C  PROGRAMME : EVALUATION OF PHASE LAG PHI
C              FOR N=3 MODE(ANTINODE) VIBRATION
C              -- PHASE FROM 0 TO 85 DEG. --
C  FILE NAME=APHASE3
C-----*

```

```

      IMPLICIT REAL*8(A-H,O-Z)
      DIMENSION B(8),C(9),BS(9)
      DIMENSION STOP(9),SBOT(9)
      COMMON C,BS,PI
      PI=DARCOS(-1.D0)
      ANGLE=85*PI/180

```

```

C-----*
C  INPUT COEFF. OF FUNCTION G(THETA)
C  ANGLE OR BS(1):SEPERATION ANGLE
C-----*

```

```

      READ (5,*) (C(I),I=1,5)
      READ (5,*) (C(I),I=6,9)
      PRINT 7
7  FORMAT('1',///,1X,'THE COEFFICIENTS FOR THE POLYNOMIAL G(THETA)',
$//)
      DO 10 I=1,9
        STOP(I)=0.0
        SBOT(I)=0.0
        BS(I)=ANGLE**I
        K=I-1
        PRINT 11,K,C(I)
11  FORMAT(' ',11X,'C(',I1,')=',F10.5)
10  CONTINUE
      PRINT 14
14  FORMAT(' ',/,1X,'THE PHASE LAG PHI FOR N=3 MODE(ANTINODE) VIBRATIO
$N',/,3X,'OVALLING FREQUENCY = 230 HZ',/)
      N=3

```

```

C
C  DEFINE THE CONSTANTS
C

```

```

      W=2*PI*230
      V=5
      Q=5

```

```

C
C  EVALUATION OF NUMERATOR : TOP
C      -G(THETA)*SIN(N-THETA) - 2*N/PI* SUM COS(J-THETA)/J*G(N,J)
C      AND
C  EVALUATION OF DENOMERATOR : BOT
C      2*V*V*N/PI/A*G(THETA)* SUM SIN(J-THETA)*G(N,J) -
C      W**2*A/N*COS(N-THETA)
C

```

```

      DO 100 J=1,9
        T=Q*PI/180
        TOLTOP=1.0
        TOLBOT=1.0
        SUMTOP=0.0
        SUMBOT=0.0
        U=1.

```

```

N1=N-1
DO 56 KJ=1,N1
  GNJ=0.50*(GSIN(N+U)+GSIN(N-U))
  XTOP=GNJ*DCOS(U*T)/U
  XBOT=GNJ*DSIN(U*T)
  SUMTOP=SUMTOP+XTOP
  SUMBOT=SUMBOT+XBOT
56  U=U+1.
C
  TWON=2*N
  GNJ=0.50*(GSIN(TWON))
  XTOP=GNJ*DCOS(U*T)/U
  XBOT=GNJ*DSIN(U*T)
  SUMTOP=SUMTOP+XTOP
  SUMBOT=SUMBOT+XBOT
  U=U+1.
C
55  CONTINUE
  GNJ=0.50*(GSIN(N+U)+GSIN(N-U))
  IF(DABS(TOLTOP).LE.1.D-05) GOTO57
  XTOP=GNJ*DCOS(U*T)/U
  OLDST=SUMTOP
  SUMTOP=SUMTOP+XTOP
  TOLTOP=SUMTOP-OLDST
57  IF(DABS(TOLBOT).LE.1.D-05) GOTO58
  XBOT=GNJ*DSIN(U*T)
  OLDSB=SUMBOT
  SUMBOT=SUMBOT+XBOT
  TOLBOT=SUMBOT-OLDSB
58  IF(DABS(TOLTOP).LE.1.D-05.AND.DABS(TOLBOT).LE.1.D-05) GOTO 65
  U=U+1.
  IF(U.GE.250) GOTO66
  GOTO55
66  PRINT 67,Q
67  FORMAT(' ',//,5X,'WARNING ! THE SERIES DOES NOT CONVERGE',5X,
$    'FOR THE ANGLE THETA=' ,F5.1)
65  STOP(J)=SUMTOP
  SBOT(J)=SUMBOT
  Q=Q+10
100 CONTINUE
  DO 200 L=1,6
    Q=5
    PRINT 5,V
5    FORMAT(///,3X,'FLOW VELOCITY =' ,F5.2)
    PRINT 2
2    FORMAT(' ',/,5X,'ANGLE THETA',3X,'PHASE LAG IN DEG.',5X,'NUMERAT
$OR',6X,'DENOMERATOR',/)
    DO 150 J=1,9
      T=Q*PI/180
      G1=C(1)+C(2)*T+C(3)*T**2+C(4)*T**3+C(5)*T**4+C(6)*T**5
      G2=C(7)*T**6+C(8)*T**7+C(9)*T**8
      G=G1+G2
      TOP=W*V*(-G*DSIN(N*T)-2*N*STOP(J)/PI)
      BOT=2*V*V*N*G*SBOT(J)/PI/0.0381-W*W*0.0381*DCOS(N*T)/N
      TANPHI=TOP/BOT
      PHI=DATAN(TANPHI)
      PHI=PHI*180/PI
      PRINT 82,Q,PHI,TOP,BOT

```

```

82      FORMAT(' ',8X,F5.1,8X,F8.2,9X,F12.4,6X,F12.4)
      Q=Q+10
150     CONTINUE
      V=V+5
200     CONTINUE
      PRINT 220
220     FORMAT('1')
      STOP
      END

```

```

C-----*
C  FUNCTION SUB-PROGRAMME TO EVALUATE THE INTEGRAL      *
C  FROM 0 TO THETA-S SIN(A*THETA)*G(THETA)              *
C  WHERE THETA-S=ANGLE OF SEPERATION                    *
C-----*

```

```

      REAL FUNCTION GSIN*8(A)
      IMPLICIT REAL*8(A-H,O-Z)
      DIMENSION B(8),C(9),BS(9)
      COMMON C,BS,PHI
      A*PHI=A*BS(1)
      A2=A**2
      A3=A**3
      A4=A**4
      A5=A**5
      A6=A**6
      A7=A**7
      A8=A**8
      A9=A**9
      SIN21=(C(2)+2*C(3)*BS(1)+3*C(4)*BS(2)+4*C(5)*BS(3))/A2
      SIN22=(5*C(6)*BS(4)+6*C(7)*BS(5)+7*C(8)*BS(6)+8*C(9)*BS(7))/A2
      SIN41=(-(6*C(4)+24*C(5)*BS(1)+60*C(6)*BS(2))/A4
      SIN42=(-(120*C(7)*BS(3)+210*C(8)*BS(4)+336*C(9)*BS(5))/A4
      SIN6=(120*C(6)+720*C(7)*BS(1)+2520*C(8)*BS(2)+6720*C(9)*BS(3))/A6
      SIN8=(-(5040*C(8)+40320*C(9)*BS(1))/A8
      SIN=SIN21+SIN22+SIN41+SIN42+SIN6+SIN8
      COS11=-(C(1)+C(2)*BS(1)+C(3)*BS(2)+C(4)*BS(3)+C(5)*BS(4))/A
      COS12=-(C(6)*BS(5)+C(7)*BS(6)+C(8)*BS(7)+C(9)*BS(8))/A
      COS31=(2*C(3)+6*C(4)*BS(1)+12*C(5)*BS(2)+20*C(6)*BS(3))/A3
      COS32=(30*C(7)*BS(4)+42*C(8)*BS(5)+56*C(9)*BS(6))/A3
      COS51=-(24*C(5)+120*C(6)*BS(1)+360*C(7)*BS(2)+840*C(8)*BS(3))/A5
      COS52=-(1680*C(9)*BS(4))/A5
      COS7=(720*C(7)+5040*C(8)*BS(1)+20160*C(9)*BS(2))/A7
      COS=COS11+COS12+COS31+COS32+COS51+COS52+COS7-40320*C(9)/A9
      CONST=C(1)/A-2*C(3)/A3+24*C(5)/A5-720*C(7)/A7+40320*C(9)/A9
      GSIN=DSIN(A*PHI)*SIN+DCOS(A*PHI)*COS+CONST
      RETURN
      END

```

```

$DATA
0.DO,1.6073D0,0.5700D0,-0.9394D0,0.1714D0
0.DO,0.DO,0.DO,0.DO
$

```

## THE COEFFICIENTS FOR THE POLYNOMIAL G(THETA)

C(0)= 0.00000  
 C(1)= 1.60730  
 C(2)= 0.57000  
 C(3)= -0.93940  
 C(4)= 0.17140  
 C(5)= 0.00000  
 C(6)= 0.00000  
 C(7)= 0.00000  
 C(8)= 0.00000

## THE PHASE LAG PHI FOR N=3 MODE(ANTINODE) VIBRATION

OVALLING FREQUENCY = 230 HZ

FLOW VELOCITY = 5.00

ANGLE THETA	PHASE LAG IN DEG.	NUMERATOR	DENOMERATOR
5.0	12.99	-5919.9679	-25663.1126
15.0	25.37	-9043.4614	-19073.3405
25.0	61.12	-13117.1710	-7235.6741
35.0	-64.63	-15185.5590	7200.1310
45.0	-31.84	-12422.0794	20001.9532
55.0	-10.46	-5314.8362	28790.5288
65.0	8.77	4473.6352	29004.9831
75.0	30.87	11976.2206	20035.7538
85.0	73.79	14958.8870	4349.6933

FLOW VELOCITY = 30.00

ANGLE THETA	PHASE LAG IN DEG.	NUMERATOR	DENOMERATOR
5.0	52.55	-35519.8074	-27205.5286
15.0	60.87	-54260.7681	-30234.8015
25.0	75.59	-78703.0263	-20223.1951
35.0	-78.25	-91113.3539	18943.6433
45.0	-49.50	-74532.4765	63664.8592
55.0	-12.85	-31889.0169	139792.5112
65.0	10.31	26841.8111	147512.8651
75.0	47.92	71857.3238	64881.6832
85.0	-47.01	89753.3219	-83672.1117

## APPENDIX H

### EFFECT OF BOUNDARY LAYER GUARDS

Some initial tests of a cylinder both with and without boundary layer guards were conducted to check the effects of the *plates* on the symmetry of the pressure distribution with respect to the velocity vector and the two dimensionality of the measurements. The results show that the measured pressure is the same on both sides of the cylinder and is uniform over most of the span.

Figure H.1 compares the pressure coefficient,  $(p-p_\infty)/\frac{1}{2}\rho U^2$ , of a circular cylinder with and without end plates at  $Re = 3.80 \times 10^4$  ( $U = 7.5$  m/s); Roshko's [27]<sup>†</sup> experimental data at a lower Reynolds number are also plotted on the same graph, for reference. It is seen that the measured pressure distribution for a cylinder (without end plates) vertically spanning the working section resembles closely that reported by Roshko, whereas the pressure coefficient of a cylinder with end plates is lower than the "classical" value in the wake region, but in this area  $C_p$  is also known to be strongly  $Re$ - and surface-roughness-dependent.

The pressure distribution for the cylinder at a higher flow velocity is shown in Figure H.2. Again the suction coefficient in the base region of the cylinder with end plates is substantially lower than that of a cylinder without end plates. Comparison of Figures H.1 and H.2 shows that the pressure coefficient in the wake of a cylinder with end plates increases with  $Re$ , but the opposite effect is found for the cylinder

---

<sup>†</sup>End plates or boundary layer guards were not used in Roshko's experiment.

without end plates.

Since boundary layer guards were used for the pressure measurements of the "deformed" circular shape models (see Chapter 7), it was necessary to check the validity of the experimental set-up. It was thought (referring to Figure 7.3) that because of the orientation of the bevelled plates<sup>†</sup> in the present set-up, the flow might be accelerating towards the test models, explaining thereby the discrepancy of the pressure measured in the wake.

To study this effect, the end plates were inverted such that the flow would not be accelerating towards the model. The pressure coefficient in the wake region (see Figure H.3) at an intermediate  $Re = 9.1 \times 10^4$  ( $U = 18.0$  m/s) lies between the value measured from earlier (original) experiments at a lower  $Re = 3.8 \times 10^4$  ( $U = 7.5$  m/s) and a higher  $Re = 1.18 \times 10^5$  ( $U = 23.5$  m/s). This suggests the orientation of the end plates does not influence the pressure measurements.

Another two parameters which may affect the results were the roughness of the cylinder surface and the length to diameter ratio of the cylinder. To study these, the original cylinder of length 609.6 mm (24.00 in.) was re-surfaced, so as to have a smoother surface. The test (see Figure H.4) shows that roughness of the cylinder does not play a crucial role in the pressure distribution in the wake.

Recalling that the length of the cylinder used in the experiments with end plates was 292.1 mm (11.50 in.), to study the aspect ratio effect, the pressure distribution around a cylinder of length 508.0 mm (20.00 in.) was measured, with the end plates in position. It is seen (Figure H.4)

---

<sup>†</sup> A bevelled plate is needed to avoid flow separation at the leading edge.

that even though the ratio  $l/D$  was now almost double that in the previous test, the pressure coefficient does not change significantly.

Thus, it may be concluded that the experimental set-up is good and that the orientation of the end plates, the roughness of the cylinder surface, and the aspect ratio, all within the ranges of these experiments, do not play an important role in determining the pressure coefficient. Perhaps the above findings are not too surprising; they support experimental evidence by Stansby [24] where suitably designed end plates added to a circular cylinder spanning a wind tunnel remove the effects of the tunnel wall boundary layers and enhance the two-dimensionality of the flow. The addition of such plates, in Stansby's measurements also, caused a substantial reduction of base pressure.



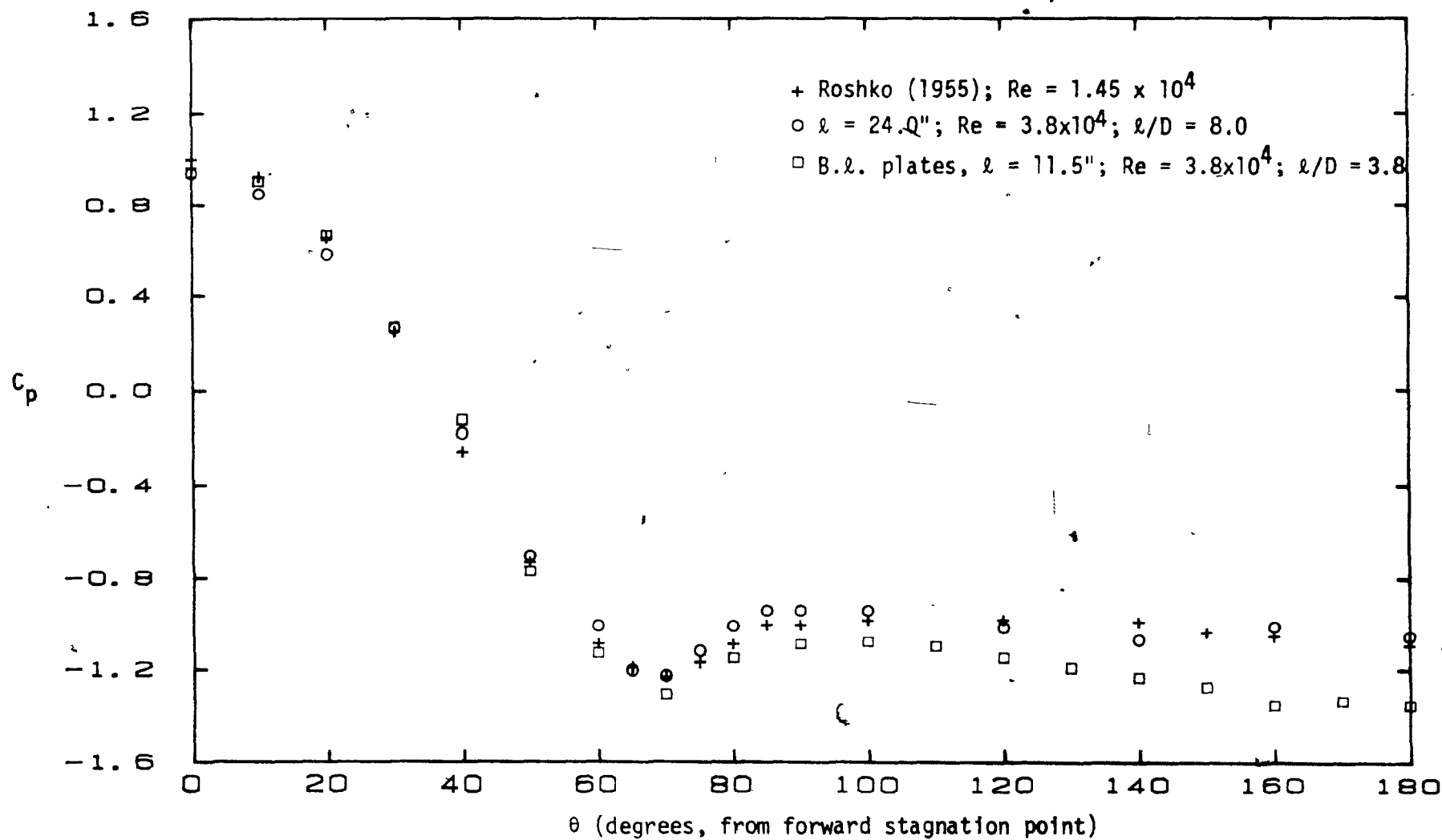


**Figure H.1:** Comparison of the pressure distribution around a circular cylinder with and without boundary layer guards in position;  $\ell$  is the length of the cylinder.

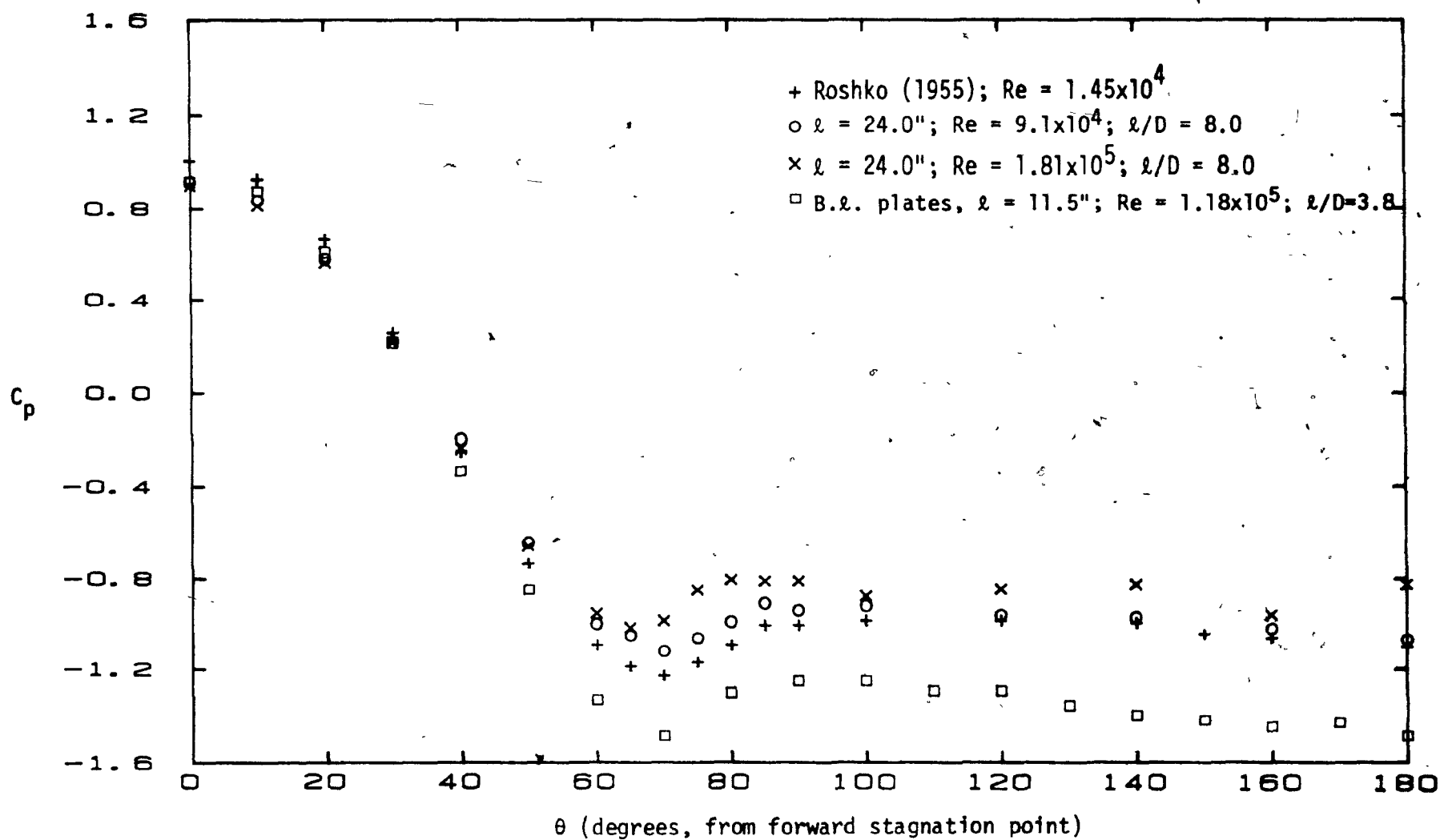


Figure H.2: Comparison of the pressure distribution around a circular cylinder with and without boundary layer guards in position;  $\ell$  is the length of the cylinder.

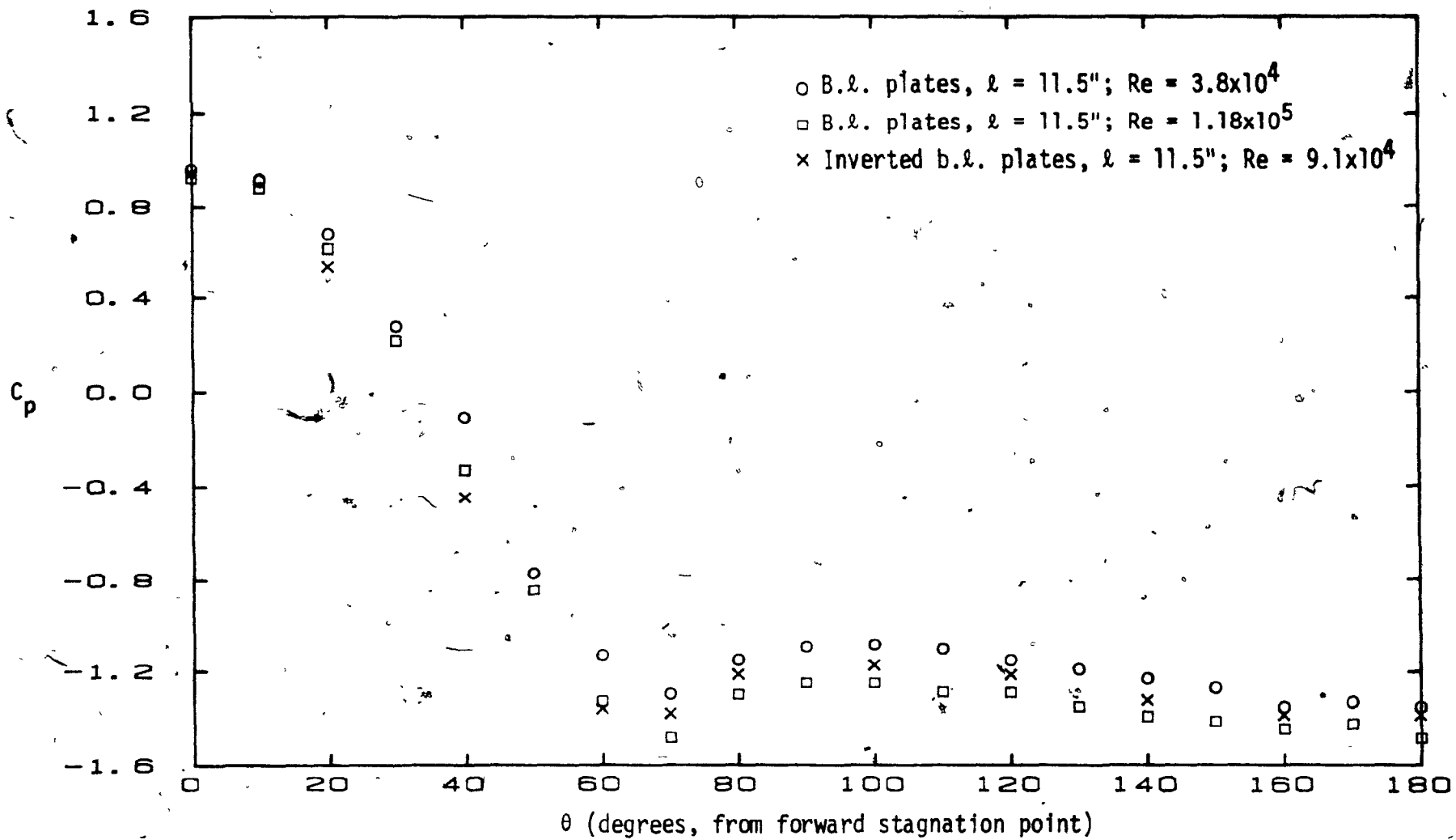
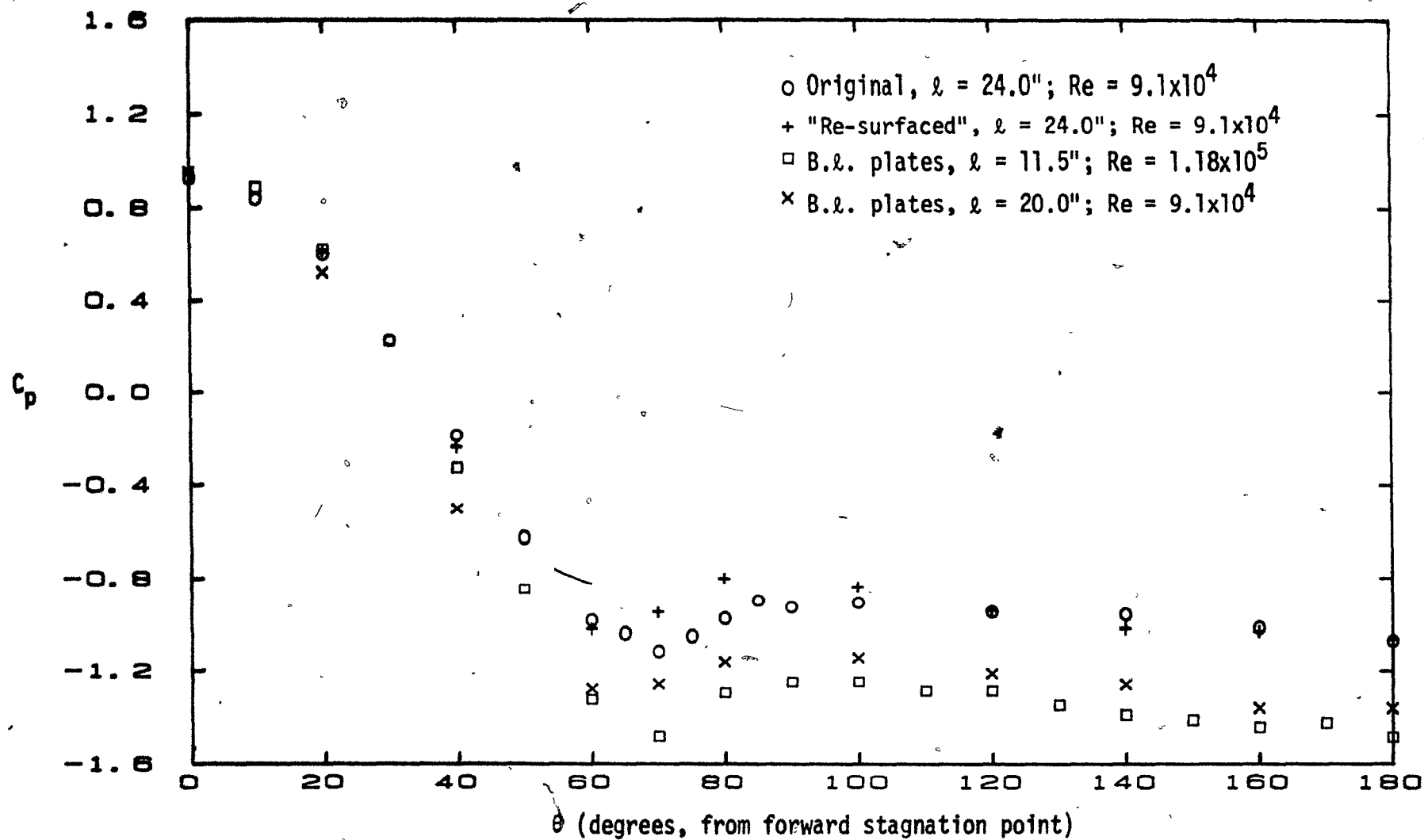


Figure H.3: Pressure distribution around a circular cylinder with the boundary layer guards in original and inverted configuration;  $l$  is the length of the cylinder.



**Figure H.4:** Comparison of pressure distribution of a smooth cylinder with no end plates and the effect of aspect ratio on the pressure coefficient for a cylinder with end plates;  $\ell$  is the length of the cylinder.